

THE ORIGINS OF SUPEROXIDE AND HYDROGEN PEROXIDE PRODUCTION
BY THE MAMMALIAN MITOCHONDRIAL ELECTRON TRANSPORT CHAIN:
A COMPUTATIONAL AND EXPERIMENTAL APPROACH

By

Quynh Van Duong

A DISSERTATION

Submitted to
Michigan State University
in partial fulfillment of the requirements
for the degree of

Biochemistry and Molecular Biology—Doctor of Philosophy

2021

ABSTRACT

THE ORIGINS OF SUPEROXIDE AND HYDROGEN PEROXIDE PRODUCTION BY THE MAMMALIAN MITOCHONDRIAL ELECTRON TRANSPORT CHAIN: A COMPUTATIONAL AND EXPERIMENTAL APPROACH

By

Quynh Van Duong

The mitochondrial electron transport chain (ETC) produces reactive oxygen species (ROS) as by-products of cellular respiration. Certain pathological conditions including ischemia-reperfusion (IR) injury disrupts mitochondrial ROS homeostasis, causing oxidative stress which can lead to cell death. Despite research efforts in the past few decades, an incomplete understanding of how mitochondria orchestrate ROS production and elimination prevails and hinders the development of efficacious therapeutic measures against oxidative stress. A major impediment is the lack of a quantitative framework capable of identifying site-specific sources of mitochondrial ROS production. Many mathematical models of mitochondria have been developed to tackle this challenge. Unfortunately, none is comprehensive and able to quantitatively reproduce a variety of bioenergetic data.

The work presented in this dissertation culminates in a mathematical model of ROS production by the ETC complexes coupled with substrate metabolism. First, a variety of bioenergetic data are generated in-house using isolated mitochondria. Generating in-house data permits precise control over experimental conditions, which minimizes hidden variables in model simulations. Second, a biophysically detailed model of the ETC complex II is developed. Finally, the complex II model is integrated with the models developed by Beard and colleagues. These include the bioenergetic model, the kinetic model of complex I and the functional bc1

dimer model. The integrated model is biophysically detailed, mass-and-charge balanced and thermodynamically consistent. The modelling process involves an iterative process of model calibration and validation to ensure the quality of model predictions.

Using this model, the flavin mononucleotide of complex I is identified as the primary source of superoxide and hydrogen peroxide in forward electron transport. The model predicts that, under conditions that favor highly reduced quinol and NADH pools in uninhibited mitochondria, both sites I_F and I_Q produce significant amounts of ROS. The model also reveals that hydrogen peroxide (H₂O₂) production by site I_F underlies the substrate-specific monotonic dependence between net ROS production and oxygen concentrations. When electron flux is perturbed such as in the presence of an inhibitor, the topology of ROS production is altered. Thus, the model can be used to quantify the effects of changes to mitochondrial environment on ROS production, an application that, today, is experimentally limited. The model also highlights the importance of furthering our understanding of the scavenging system under different conditions to establish a complete picture of mitochondrial ROS homeostasis.

ACKNOWLEDGEMENTS

The author thanks Drs. Jason N. Bazil, Shelagh M. Ferguson-Miller, Erik Martinez-Hackert, John J. Lapres and Jianping Hu for mentorship and advice over the course of the PhD training. The author also thanks Mr. Jasiel O. Strubbe, Ms. Maria J. Dessinger, Ms. Adrianna L. Hoffman, Ms. Katie Zhong, Dr. Yizhu Zhang, Dr. Sathyavani Malyala and Dr. Neeraj Manhas for their companionship and assistance with various aspects of laboratory experiments. The author is indebted to the DO/PhD Program – especially Dr. Justin J. McCormick, Ms. Bethany Heinlen, Dr. Brian Schutte, and Ms. Michelle Volker – for the training opportunity and their ongoing support. The author is grateful for Ms. Jessica Lawrence from the Department of Biochemistry and Molecular Biology for helping the author navigate the administrative complexity of being a dual-degree student during the PhD training.

Special thanks go to the author's spouse, Dr. Daniel B. Lybrand, for his unconditional love and support. He sends flowers frequently and provides a pair of objective lenses on the written language of this dissertation. The author's sister, Ms. Quynh Thu Van Duong, accompanies the author to local bakery shops and favorite Vietnamese restaurant when "Elvish bread" becomes an essential. Last but not least, the author's forever puppy, Meiji, is always a constant source of joy and an anchor all these years. A bad day in the lab can be cured by a walk into the woods with Meiji, who happens to be another kind of lab.

This research was made possible by the Michigan State University College of Osteopathic Medicine, the Michigan State University College of Natural Science and the National Institute of Health Grant R00-HL121160 (to J. N. B.).

PREFACE

In this dissertation, an integrated model of mitochondrial bioenergetics is constructed, calibrated and validated. The model presented is the first of its kind that is capable of simulating substrate metabolism and free radical homeostasis in non-phosphorylating and phosphorylating mitochondria. The work presented herein demonstrates that computational models are powerful tools to study mitochondrial bioenergetics. The model both checks for consistency in existing data and enables extrapolations beyond the experimental space. Each chapter in the dissertation is dedicated to an aspect crucial to the final model and is briefly summarized below.

The introductory chapter serves a dual purpose of an exploratory guide to computational modeling and a literature survey of mainstream kinetic models of mitochondria. In my early days working on this project, the computational aspect was elusive to me. Most reviews on mitochondrial models, unfortunately, tend to focus on only the results presented by some of the mainstream models. The technical aspects are often forgone presumably out of the fear of losing the reader's interest. However, without the technical understanding, it is impossible for the reader to form his or her own critique of a modeling work. Thus, a major part of the introductory chapter was devoted to key concepts in computational modeling. Although the technical aspects of modeling are often expressed in mathematical language, an intuitive understanding can be accomplished without resorting to mathematical expressions. The literature survey of several mainstream kinetic models of mitochondria was subsequently

provided. My hope is to create a document that is useful to those unfamiliar with this line of work like I did a few years ago.

The modeling process can be broken down into model construction, verification, calibration and validation phases. Each phase requires a large number of data sets, especially the calibration phase. Thus, I dedicated the first part of my PhD work to generating bioenergetic data for the model. Generating data in-house also enables precise control over experimental conditions, which helps to minimize hidden variables that can complicate data interpretation. Representative data are the oxygen consumption rates, the net hydrogen peroxide emission rates and the reduction state of the nicotinamide adenine dinucleotide pool in non-phosphorylating and phosphorylating mitochondria energized with a variety of substrate combinations and calcium levels. The data set of fatty acid substrates (palmitoylcarnitine/malate) indicates that mitochondria energized with fatty acid substrates are increasingly sensitive to calcium, which led to the decision to reserve beta-oxidation for a future version of mitochondrial model. The other data sets generated using NADH-linked and QH₂-linked substrates in the absence of RET were used to calibrate the integrated model.

A primary goal in developing the model is to unearth mechanistic insights underlying the origin of superoxide and hydrogen peroxide produced by the electron transport chain (ETC) complexes. The goal necessitates that a biophysically detailed model of the ETC complexes capable of producing superoxide and hydrogen peroxide be first developed. Previous works in our groups have led to the kinetic models of complexes I and III. Therefore, the next part of my PhD project was to develop the model for complex II. This model can simulate a variety of literature data of succinate oxidation and net hydrogen peroxide emission rates at 1) increasing

succinate concentrations, 2) in the presence of other TCA cycle dicarboxylates, 3) at different pH conditions and 4) in the presence of ETC complex inhibitors. To my knowledge, no other models of complex II are able to faithfully recapitulate these behaviors. The complex II model suggests that the [4Fe-4S] cluster near the Q reductase site is an important source of superoxide production by complex II. It also suggests that the accessibility of the flavin site is necessary for free radical production, which explains the decreased net hydrogen peroxide emission rate at high succinate or other dicarboxylate concentrations.

Finally, the complex II model was integrated into a single, unified framework of mitochondria model. In addition to the biophysically detailed models of complexes I and III, the integrated model also includes a simplified TCA cycle, the activity of malic enzyme and relevant substrate transport. The model does not include beta oxidation or the effects of calcium on substrate metabolism. Moreover, the scavenging system is modelled using a rather simple Michaelis-Menten like expression. Thus, the integrated model is capable of explaining substrate metabolism and free radical homeostasis in forward and reverse electron transport (FET and RET) modes excluding fatty acid substrates. No other existing mitochondrial models are able to quantitatively reproduce these behaviors. Nevertheless, a complete model will need to include beta-oxidation, hash out the scavenging system and incorporate calcium buffering. It is also necessary to replace the simplified TCA cycle model with a more detailed model. All these modifications require additional data.

In conclusion, the work presented herein culminates an integrated computational model of mitochondria which can quantitatively reproduce substrate metabolism and free radical homeostasis. The model quantifies superoxide and hydrogen peroxide production by ETC redox

centers under a variety of conditions. Some of the simulations such as in the absence of inhibitors are still experimentally infeasible. The model is also ideal for future expansions of other mitochondrial processes and integration into larger-scale models (such as cardiomyocytes) to elucidate mechanistic insights in a system-based approach.

TABLE OF CONTENTS

LIST OF TABLES.....	xii
LIST OF FIGURES.....	xiii
KEY TO ABBREVIATIONS.....	xv
CHAPTER 1 – EXISTING MODELS OF MITOCHONDRIA.....	1
INTRODUCTION.....	2
Myocardial Ischemia/Reperfusion Injury Overview	2
Mathematical Modeling as a Tool to Understand Mitochondrial Oxidative Stress in Myocardial I/R Injury	5
KEY ASPECTS IN MATHEMATICAL MODELING	9
Model Construction & Verification	9
Model Training.....	14
Important Considerations.....	18
EXISTING MATHEMATICAL MODELS OF MITOCHONDRIA.....	21
Achs-Garfinkel-Kohn Models	21
Korzeniewski-Zoladz Models.....	22
Cortassa-Aon Models	25
Markevich-Hoek Models.....	30
Beard-Bazil-Vinnakota Models.....	32
CONCLUSION.....	35
REFERENCES.....	37
CHAPTER 2 – CALCIUM OVERLOAD DECREASES NET FREE RADICAL EMISSION IN CARDIAC MITOCHONDRIA.....	46
INTRODUCTION.....	47
MATERIALS AND METHODS.....	50
Mitochondria Isolation.....	50
Experimental Set-up.....	51
Oxygen Consumption Rates and Hydrogen Peroxide Emission Rates.....	53
High Amplitude Swelling Assay	53
Membrane Potential Measurement	54
Buffer Calcium Measurement.....	54
Data Analysis and Statistical Testing.....	55
RESULTS	56
DISCUSSION.....	76
Mitochondrial respiration depends on the fuel source.....	76
Oxaloacetate accumulation depresses maximal succinate-supported respiration	78
Respiratory changes are driven by membrane potential	80
Increased calcium concentrations do not increase ROS emission rates	80

Net hydrogen peroxide emission rates are driven by membrane potential	81
Electron flux does not appreciably influence hydrogen peroxide emission rates	83
Hydrogen peroxide emission rates are non-linearly dependent on oxygen concentration	83
Strengths and Limitations of Study	87
SUMMARY	90
APPENDIX	92
REFERENCES	107
CHAPTER 3 – COMPUTATIONALLY MODELING MAMMALIAN SUCCINATE DEHYDROGENASE	
KINETICS IDENTIFIES THE ORIGINS AND PRIMARY DETERMINANTS OF ROS PRODUCTION	114
INTRODUCTION	115
MATERIALS AND METHODS	120
Model Construction	120
Experimental Data	124
Experimental Details	125
Model Simulations	127
RESULTS	128
Model Simulations of Succinate Oxidation Rates Under Different Conditions Are Faithful to	
Experimental Data	134
Model Simulations Are Consistent with Experimental ROS Production Rates	138
Model Testing and Corroboration	146
Model Predicts the [3Fe-4S] ISC is the Primary Source of ROS	154
DISCUSSION	158
APPENDIX	165
REFERENCES	185
CHAPTER 4 – COMPUTATIONAL MODELING IDENTIFIES SITE-SPECIFIC SUPEROXIDE AND	
HYDROGEN PEROXIDE PRODUCTION OF THE MITOCHONDRIAL ELECTRON TRANSPORT CHAIN	
.....	192
INTRODUCTION	193
MATERIALS AND METHODS	197
General Approach to Modeling and Processes Included	197
Model Simulations	197
Data Sets	200
Model Parameters	202
Oxygen Consumption and Net Hydrogen Peroxide Emission Rates	204
NADH Fluorescence Measurement	205
RESULTS	206
Oxygen Consumption and Net Hydrogen Peroxide Emission Rates	206
NADH Reduction States	209
Oxygen Consumption, Net Hydrogen Peroxide Production Rates, and Oxygen	
Concentration Dynamics Under Both NADH- and QH ₂ -linked Substrate Metabolism	212
Monotonic Relationship Between J _{H₂O₂} and [O ₂]	212

Hydrogen Peroxide Production by Site I _F Underlies the Kinetics of Net ROS Emission Rates at Low [O ₂]	214
Site-Specific Superoxide Fluxes.....	219
Site-Specific Hydrogen Peroxide Fluxes.....	223
Effects of the NADH and Q pools' Reduction States on ROS Production	225
Effects of Substrate Utilization and Electron Transport Mode on Scavenging Activity	227
DISCUSSION.....	229
Model Predictions of Site-Specific ROS from the ETS Complexes	229
CONCLUSIONS.....	232
APPENDIX	233
REFERENCES	237
CONCLUDING REMARKS	243
REFERENCES	248

LIST OF TABLES

Table 2.1 Statistical significance between respiratory rates	60
Table S2.1 Comprehensive table of statistical results from Table 2.1	101
Table S2.2 The inhibitory effect of oxaloacetate on complex II can be relieved by adding glutamate	102
Table S2.3 Calcium affects the ETC at complex I	103
Table S2.4 Irreversible mPT does not occur in our experimental conditions.....	104
Table S2.5 Comprehensive table of statistical values for net hydrogen peroxide emission rates	105
Table S2.6 Mitochondria were able to maintain membrane potential at the maximal experimental calcium conditions.....	106
Table 3.1 Experimental data used for model fitting.....	131
Table 3.2 Model adjustable parameters.....	133
Table 3.3 Integrated model simulation results.....	155
Table S3.2 Environmental parameters	170
Table 4.1 Description of the ETS redox centers included in the model	199
Table 4.2 Summary of data used in this study.....	201
Table 4.3 Model adjustable parameters.....	203
Table 4.4 Comparison of experimental and model J_{O_2} (pmol/mg/min).....	208
Table 4.5 Comparison of experimental and model $J_{H_2O_2}$	210
Table 4.6 Model predictions of site-specific superoxide production (J_{SO} , nmol/mg/min) during leak and oxphos states supported by different substrates	221

LIST OF FIGURES

Figure 2.1 Calcium inhibits respiration for P/M, PC/M, and S but not S/R fueled mitochondria	57
Figure 2.2 Calcium affects both leak and oxphos state respiration rates	58
Figure 2.3 Effects of glutamate addition on oxphos J_{O_2} during succinate-fueled respiration.....	62
Figure 2.4 Calcium does not significantly affect the electron transport system downstream of Complex I	63
Figure 2.5 Moderate calcium overload does not trigger mitochondrial permeability transition	65
Figure 2.6 Relative absorbance (%) following calcium addition.....	66
Figure 2.7 Net hydrogen peroxide emission rates are inhibited by calcium.....	67
Figure 2.8 Mitochondria remain energized during moderate calcium overload	69
Figure 2.9 Mitochondrial membrane potential is affected by calcium loading	70
Figure 2.10 Buffer and steady-state matrix calcium.....	72
Figure 2.11 Hydrogen peroxide emission rates are dependent on oxygen concentration.....	74
Figure 2.12 Hydrogen peroxide emission rate is independent of oxygen consumption rate	75
Figure 2.13 Schematic of resorufin formation.....	84
Figure S2.1 Effects of buffer sodium on leak-state oxygen consumption rates (J_{O_2}).....	93
Figure S2.2 Effects of buffer sodium on sodium/calcium cycling oxygen consumption rates (J_{O_2})	94
Figure S2.3 Effects of buffer sodium on oxphos-state net oxygen consumption rates (J_{O_2}).....	95
Figure S2.4 Effects of buffer sodium on leak-state net hydrogen peroxide emission rates ($J_{H_2O_2}$)	96
Figure S2.5 Effects of buffer sodium on sodium/calcium cycling net hydrogen peroxide emission rates ($J_{H_2O_2}$).....	97
Figure S2.6 Effects of buffer sodium on oxphos-state net hydrogen peroxide emission rates ($J_{H_2O_2}$).....	98

Figure S2.7 Glutamate-dependent respiration is significantly inhibited by calcium.....	99
Figure S2.8 Pathway diagram for succinate +/- rotenone supported respiration.....	100
Figure 3.1 Overview of the SDH model.....	129
Figure 3.2 Succinate oxidation rates at varied concentrations of different electron acceptors	135
Figure 3.3 Succinate oxidation kinetics in the presence of SDH inhibitors using bovine heart SMP	137
Figure 4.1 Schematic of explicitly modeled phenomena.....	198
Figure 4.6. Schematic that relates the resorufin formation to steady-state net matrix H ₂ O ₂ ...	216
Figure S4.1 L-malate is able to support respiration during leak state and oxphos	234
Figure S4.2 NADH redox state was determine during leak and oxphos states using fluorimetry	235

KEY TO ABBREVIATIONS

[ADP]	molar concentration of adenine diphosphate
[ATP]	molar concentration of adenine triphosphate
$[\text{H}_2\text{O}_2]_{\text{buffer}}$	buffer hydrogen peroxide concentration in molar unit
$[\text{H}_2\text{O}_2]_{\text{m}}$ or $[\text{H}_2\text{O}_2]_{\text{matrix}}$	matrix hydrogen peroxide concentration in molar unit
[NAD ⁺]	molar concentration of nicotinamide dinucleotide in the oxidized form
[NADH]	molar concentration of nicotinamide dinucleotide in the reduced form
[NADH] _{tot}	nicotinamide adenine dinucleotide pool as the sum of the oxidized and reduced forms
ADP	adenosine diphosphate
ANT	adenine nucleotide transporter
ATP	adenosine triphosphate
ATP ⁴⁻	free ionic form of adenine triphosphate
β_{atpenin}	atpenin inhibitory factor
BP	binding polynomial
BSA	bovine serum albumin
CaGreen-5N	Calcium Green, a fluorescent indicator
CS	cardioplegic solution
CS	citrate synthase
DCC	dicarboxylate carrier
DQ	decylubiquinone
EGTA	ethylene glycol-bis(b-aminoethyl ether)-N,N,N',N'-tetracetic acid
$E_{\text{m}}^{\text{Q/Q}\cdot-}$	midpoint potential of the quinone/semiquinone pair
E_{R}	total capacity of electron donors in their reduced states

ETC	electron transport chain
EtOH	ethanol
Etot _{C_I}	complex I content
Etot _{C_{II}}	complex II content
Etot _{C_{III}}	complex III content
ETS	electron transport system
ETS-ROS	name of the integrated computational model with a focus on reactive oxygen species produced by the electron transport system
F	fluorescence
FAD	flavin adenine dinucleotide
FADH ₂	flavin adenine dinucleotide, fully reduced form
FCCP	2-[2-[4-(trifluoromethoxy)phenyl]hydrazinylidene]-propanedinitrile
FET	forward electron transport
F _{max}	maximal fluorescence
F _{min}	minimal fluorescence
FMN	flavin mononucleotide
G/M	glutamate/ malate
GPX	glutathione peroxidase
GR	glutathione reductase
H ₂ O ₂	hydrogen peroxide
HATP ³⁻	ionic form of adenine triphosphate bound to a proton
HrP	horseradish peroxidase
IB	isolation buffer
IDH	isocitrate dehydrogenase
IF	flavin site of complex I (general)

$I_{FMNH\bullet-}$	flavin radical of complex I
I_{FMNH_2}	fully reduced flavin of complex I
$II_{[3Fe-4S]}$	the iron-sulfur cluster near the quinone reductase site in complex II
$II_{FADH\bullet-}$	flavin radical of complex II
II_{FADH_2}	fully reduced flavin of complex II
II_Q	quinone reductase site of complex II
IMAC	inner membrane ion channel
I_Q	quinone reductase site of complex I
IR injury or I/R injury	ischemia/reperfusion injury
ISC	iron-sulfur center
ISP	iron-sulfur protein
$J_{H_2O_2}$	hydrogen peroxide emission rate
J_{O_2}	oxygen consumption rate
J_{ROS}	total flux of reactive oxygen species, defined as the sum of the hydrogen peroxide flux and half the superoxide flux
J_{SO}	superoxide flux
K_2HPO_4	potassium monophosphate
K_{ad}	atpenin dissociation constant at the distal quinone-binding site of complex II
K_{ap}	atpenin dissociation constant at the Q_p site of complex II
$KATP^{3-}$	ionic form of adenine triphosphate bound to a potassium ion
KCl	potassium chloride
K_d	dissociation constant
K_{DH}	ATPase feedback constant on dehydrogenase activity
k_e	elimination rate

$k_{\text{Emission_H2O2}}$	H_2O_2 permeability rate constant
k_{ME}	rate constant of malic enzyme
$k_{\text{fo}}^{3\text{Fe-4S}}$	rate constant for superoxide production by the [3Fe-4S] cluster near the quinone reductase site of complex II
$k_{\text{fo}}^{\text{FADH}\bullet}$	rate constant for superoxide production by the flavin radical of complex II
$k_{\text{fo}}^{\text{FADH}_2}$	rate constant for hydrogen peroxide production by the fully reduced flavin of complex II
$k_{\text{fo}}^{\text{QH}_2}$	rate constant of quinol production
$k_{\text{fo}}^{\text{SUC}}$	rate constant of succinate oxidation
k_{f}^{P}	rate constant of phenazine reduction
$k_{\text{f}}^{\text{TMPD}}$	rate constant of TMPD reduction
K_{FUM}	fumarate dissociation constant
K_{H}	proton dissociation constant at the Q_p site of complex II
K_{m}	Michaelis-Menten constant, the substrate concentration corresponding to half of the maximal turn-over rate
$K_{\text{m_scavenging}}$	molar concentration of hydrogen peroxide at half maximal scavenging capacity
K_{MAL}	malate dissociation constant at the flavin site of complex II
K_{MALO}	malonate dissociation constant at the flavin site of complex II
K_{OAA}	oxaloacetate dissociation constant at the flavin site of complex II
k_{off}	dissociation rate
k_{p}	production rate
K_{Q}	quinone dissociation constant
K_{QH_2}	quinol dissociation constant from complex II
K_{SUC}	succinate dissociation constant
k_{t}	rate of hydrogen peroxide transported from the matrix

$\lambda_{\text{emission}}$	emission wavelength
$\lambda_{\text{excitation}}$	excitation wavelength
L-M	L-malate
MCU	mitochondrial calcium uniporter
ME	malic enzyme
MgATP ²⁻	ionic form of adenine triphosphate bound to a magnesium ion
MgCl ₂	magnesium chloride
Mn-SOD	superoxide dismutase using Mn ²⁺ as a cofactor, found in mitochondrial matrix
MOPS	3-(N-morpholino)propanesulfonic acid
N ₂	molecular nitrogen
Na ⁺ /Ca ²⁺ cycling state	sodium/calcium cycling state
NaCl	sodium chloride
NADH	nicotinamide adenine dinucleotide
NCLX	sodium calcium exchanger
NDH	NADH/NAD ⁺ feedback constant on dehydrogenase activity
NHE	sodium hydrogen exchanger
O ₂	molecular oxygen
O ₂ ^{•-}	superoxide
OAA	oxaloacetate
ODE	ordinary differential equation
oxphos	oxidative phosphorylation
P/M	pyruvate/L-malate
P/M/S	pyruvate/L-malate/succinate
PC/M	palmitoylcarnitine/L-mate

PDH	pyruvate dehydrogenase
P _i	inorganic phosphate
P _i /H ⁺ co-transporter	transporter of inorganic phosphate and proton
P _i C	phosphate carrier
PMS	phenazine methosulfate
Prx	peroxiredoxin
Q	ubiquinone (quinone)
Q pool	quinol pool
QH ₂	ubiquinol (quinol)
Q-linked substrates	substrates that feed electrons to the quinol pool
Q _N	quinone binding site on the matrix side (complex III)
Q _o	quinone oxidase site of complex III, also known as the Q _p site
Q _p , or III _{QP}	quinone binding site on the intermembranous space (complex III)
RCR	respiratory control ratio
RET	reverse electron transport
ROS	reactive oxygen species
S/R	succinate/rotenone
S/R	succinate
SDH	succinate dehydrogenase
SDHA	subunit A of succinate dehydrogenase
SDHB	subunit B of succinate dehydrogenase
SDHC	subunit C of succinate dehydrogenase
SDHD	subunit D of succinate dehydrogenase
SMP	submitochondrial particles

SOD	superoxide dismutase
SQ	semiquinone
TCA	tricarboxylic acid
TDH	transhydrogenase
TMPD	N,N,N',N'-tetramethyl-p-phenylenediamine
TMRM	tetramethylrhodamine, methyl ester
TRX	thioredoxin
V_{\max}	maximal enzyme turn-over rate
V_{\max_DCC}	maximal capacity of dicarboxylate carrier
V_{\max_FH}	maximal capacity of fumarate hydratase
$V_{\max_scavenging}$	maximal scavenging
V_{O_2}	oxygen consumption rate
X_{DH}	dehydrogenase activity
α KDH	α -ketoglutarate dehydrogenase

CHAPTER 1 – EXISTING MODELS OF MITOCHONDRIA

INTRODUCTION

Myocardial Ischemia/Reperfusion Injury Overview

Cardiovascular disease is the leading cause of death in the U.S. This disease encompasses a wide variety of cardiac pathologies with coronary artery disease (CAD) singly responsible for 42.1% of deaths [1]. Severe CAD typically leads to a heart attack, an unfortunate event that happens every 36 seconds in the U.S. This frightening rate translates into more than 800,000 heart attacks every year that result in approximately 114,000 deaths. Despite recent improvement on the mortality rate, survivors gradually develop heart failure and eventually require heart transplant as the definitive treatment or are faced with demise [2]. The short- and long-term consequences of heart attacks have cost the healthcare and economy a staggering \$363.4 billion between 2016 and 2017 [1]. The motivation to mitigate such dire consequences has led to intensive research efforts to hash out the pathophysiology underlying heart attacks. Unfortunately, results of these studies are not forthcoming [3,4].

In severe CAD, occlusion of the coronary artery leads to ischemia and requires timely reperfusion to salvage the tissue [2,5]. Timely reperfusion alone, however, reduces the infarction size to only 50% [6]. Even when adjunct therapies are used, approximately 25% of area at risk for infarction cannot be saved [6]. Because these statistical numbers were obtained in a laboratory setting where a heart attack is planned and fully prepared for, they are likely worse in real-life clinical situations. These observations of residual infarction despite timely reperfusion suggest reperfusion-induced damages which lead to the term myocardial ischemia/reperfusion (I/R) injury [7]. The pathophysiology underlying I/R injury is complex and can be temporally divided into acute- and delayed-phase responses [8]. Acute responses occur at the

onset of reperfusion and include alterations in calcium handling, free radical homeostasis and metabolic activities. Delayed responses arise in a few days and can last for months to years wherein the immune system removes dead cardiomyocytes and replace them with fibrotic tissue [9–11]. In the delayed phase, microvascular dysfunction has also been observed and is linked to the no-reflow phenomenon, which is one of the four phenotypes of myocardial I/R injury [8]. The other types of injury are reentrant arrhythmia, myocardial stunning and lethal reperfusion injury. It is lethal reperfusion injury that is responsible for the residual 25% of infarction despite timely reperfusion and adjunct therapies [5].

Mitochondrial dysfunctions of the ischemic myocardium have been implicated in the acute responses of myocardial I/R injury. Many excellent reviews exist on this topic [12,13], and only key details are summarized here. During ischemia, hypoxia or anoxia ceases the activity of the electron transport chain (ETC) and leads to ATP depletion. Metabolic switch to glycolysis due to anoxia and net ATP hydrolysis acidifies the cytosol. Cytosolic pH maintenance happens at the expense of cytosolic calcium overload. The Na^+/H^+ exchanger extrudes H^+ by allowing Na^+ to accumulate in the cytosol, and the sodium/calcium/lithium exchanger (NCLX) removes cytosolic Na^+ by importing Ca^{2+} [14]. Cytosolic calcium is subsequently taken up by mitochondria, resulting in mitochondrial calcium overload. Upon reperfusion, a burst of reactive oxygen species (ROS) is observed and causes oxidative stress [15]. Mitochondrial calcium overload and oxidative stress have been suggested to create a vicious cycle and triggers the phenomenon termed the mitochondrial permeability transition (mPT) phenomenon [16,17]. Irreversible mPT has been shown to contribute to apoptotic cell death by releasing cytochrome c and other pro-apoptotic factors into the cytosol. Thus, many of the current adjunct therapies are designed to

prevent mPT by targeting mitochondrial calcium overload and oxidative stress [18–20]. However, clinical studies that are successful in animals have not produced enthusiastic outcomes when translated onto humans [2,3,21].

A survey of current literature reveals that conflicting experimental results constitutes a major impediment contributing to the discrepancy between research effort and clinical improvement. One particular area that is fraught with controversies is mitochondrial oxidative stress. Despite the consensus that the mitochondrial ETC complexes are responsible for most reactive oxygen species (ROS), the relative contributions of the ETC redox centers to species-specific ROS production remain debatable. For example, Kussmaul and Hirst reported that the fully reduced flavin mononucleotide of complex I produces most ROS as superoxide [22]. In this study, purified complex I from bovine heart mitochondria was used. Galkin and Brandt, using complex I purified from yeasts, agreed that superoxide is the main ROS produced by the flavin radical of complex I [23]. Lambert and Brand, however, contend that the quinone reductase site is responsible for most superoxide produced by this enzyme complex. The conclusion was obtained using intact mitochondria isolated from the skeletal muscle of rats. The capacity of complex II to produce ROS has also been questioned. While the mainstream perspective does not consider complex II as a significant source of ROS [24], several studies suggest that it can contribute significantly to total mitochondrial ROS under the right conditions [25,26]. Most studies on oxidative stress also overlook the mitochondrial scavenging enzymes. Studying mitochondrial ROS homeostasis is further challenging because ROS production and elimination processes are integrated into a metabolic network that is affected by matrix calcium content [27,28].

Mathematical Modeling as a Tool to Understand Mitochondrial Oxidative Stress in Myocardial I/R Injury

The interdependent nature of mitochondrial ROS homeostasis and other processes makes mitochondria a particularly suitable target for mathematical modeling, which has been widely applied to study biochemical systems of varying complexity levels. A classic example of mathematical modeling is the Michaelis-Menten enzyme rate equation. This equation relates the enzyme turnover with substrate concentrations [29]. In another example, microbiologists predict microbial growth under varying conditions using logistic growth models [30–32]. Over the years, mathematical modeling significantly contributed to our collective understanding of underlying mechanisms associated with physical systems. From the well-known Hodgkin and Huxley's ion channel models [33], Huxley cross-bridge theory [34], the Onsager's reciprocal relation applied to metabolism [35–37], excitation contraction coupling models [38–40] and cardiac electrophysiological models [41–44], scientists have gained unprecedented insights into biological phenomena.

These examples demonstrate the extremely important role of using mathematical modeling to understand complex systems, including biological systems. Without a model, data can take us only so far due to the non-linear nature of biological systems. Biological systems are very often non-linear and consist of numerous interacting components each of which often performs multiple functions. As such, a perturbation to one component due to an experimental procedure can affect other components (including their functions) in any combination. Yet experimentally quantifying these effects in a comprehensive manner is constrained by technological, financial and time resources. While assuming these collateral effects are

negligible is often the first choice when interpreting data, this practice has led to many conflicting experimental results. The unresolved discrepancies of existing data have hindered the elucidation of mechanistic relationships of biological systems under physiological conditions and compromised our understanding of how such a system behaves under a stressor (such as a pathological condition).

In contrast, the effects of a perturbation on various aspects of a system can be executed efficiently using a model. The advent of computers creates a powerful platform to simulate mathematical models and perform uncertainty analysis on the model inputs and outputs, leading to “mathematical model” and “computer model” often being used interchangeably. Some, however, prefer one term over the other. In this review, these terminology words are used interchangeably. In addition to improved efficiency, another major advantage of computer modeling is the ability to uncover mechanistic relationships among the system’s constituents and how they shape the system’s behaviors. This ability naturally arises from the modeling process as constructing a mathematical model involves not only deconstructing the system into its parts but also, and more importantly, *reconstituting* these parts into a single framework. This *integrative* modeling approach enables a robust, quantitative analysis of the system’s components both at an individual level and a systems level. The importance of a system-level understanding was formally emphasized by Henrik Kacser, one of the pioneers of metabolic control analysis [45].

The motivation to mathematically model mitochondria originated from the desire to understand how metabolite transport, substrate metabolism, ionic fluxes and oxidative phosphorylation are related and regulated [46–48]. Some of them are formulated to settle

discrepancies among experimental studies [49,50]. In recent years, mitochondrial models have been expanded to study human diseases which involve mitochondrial dysfunctions [51–54]. Ischemia-reperfusion (IR) injury is a broad pathological phenomenon in which mitochondrial dysfunctions are implicated to result in cell death [55,56]. The dysfunctions include metabolic shift, disrupted calcium buffering and imbalanced free radical homeostasis. The changes are interrelated and affect the ability of mitochondria to maintain the protonmotive force and synthesize ATP. Unfortunately, intensive research efforts aimed to rectify these dysfunctions in IR injury have not been fruitful [3,4]. The situation arose from an incomplete understanding of mitochondrial physiology and, to a larger extent, how mitochondria interact with other organelles in the absence of pathologies. Consequently, our understanding of how normal mitochondrial behaviors are altered under pathological conditions are likely less accurate than we desire. Evident to this incomplete understanding of normal and abnormal mitochondrial physiology are the unsettled origins of superoxide and hydrogen peroxide produced by mitochondria [22,23,25,57–60]. The interplay between the mitochondrial free radical production and scavenging systems, and the effects of calcium on substrate metabolism and free radical homeostasis also remain a mystery.

The very first models involving mitochondria, developed by Achs and Garfinkel in the late 1970s and [61,62] and Korzeniewski-Zolald in the 1980s-early 1990s [46], have inspired many groups to develop their own models. Some of the models are focused exclusively on mitochondria [46,47,49,63–66] while others are interested in mitochondria as a part of the cell [52,67,68]. The goal often dictates the modeling process and results in models of different levels of granularity. Most models were initially built on the tricarboxylic cycle (TCA) reactions

and oxidative phosphorylation with varying degree of focus on metabolite trafficking and ionic interactions in the mitochondrial matrix [46,47,49,63,66]. Later on, models focused on free radical homeostasis were developed once free radicals are recognized as important signaling molecules instead of merely by-products of cellular respiration [64,65]. While there are quite a handful of mitochondrial models, only a few are comprehensive. This review will focus on major models that comprehensively address more than one aspect of mitochondrial physiology – substrate utilization which includes transport and metabolism, oxidative phosphorylation (oxphos), calcium buffering and free radical homeostasis. These are models developed by the groups of 1) Cortassa and Aon [47,63–65], 2) Markevich and Hoek [69–71] and 3) Beard, Bazil and Vinnakota [49,50,66,72,73]. The Achs-Garfinkel-Kohn [61,62] and Korzeniewski-Zoladz models [46,67] are included to provide a frame of reference and comparison as they were among pioneering works. In addition to providing a concise survey on existing models, our goal is also to equip those unfamiliar with this line of work a systemic approach to understand and evaluate mathematical models. As such, we devote the next section to key aspects involved in modeling before discussing the specific models.

KEY ASPECTS IN MATHEMATICAL MODELING

A primary goal in constructing mathematical models is to gain mechanistic insights that are not amenable to experimental techniques. This appealing outcome necessitates that the model must first be able to reproduce existing data as being able to reproduce experimental data verifies that the model is an *in-silico* replica of the system. The process of modeling also checks for the internal consistency of existing data. To fulfill these goals, the modeling process is naturally iterative and evolutionary. The modeling workflow includes model construction, verification, calibration and validation.

Model Construction & Verification

Model construction transforms the system of interest from mathematical expressions to computer code replicating those mathematical functions *in silico*. Verification is the step whereby you make sure the construction phase was completed successfully. In the initial model construction, biophysical constraints given an experimental condition are imposed on the model. A modeling approach also needs to be chosen. Although modeling approaches are often shown as binary choices, as below, this presentation is for the sake of conveniently present the information. In practice, combining approaches is often necessary, a practice guided by both theoretical knowledge and practice-informed intuition.

In the simplest scenario in which an enzyme converts a single substrate to a single product, the system can be “reduced” to the rate law of the enzyme, which is the product of the reaction rate constant and substrate concentration. Despite the simplicity of the system, it is subject to biophysical laws – the law of conservation, its derivative and the laws of thermodynamics. These laws confer the biophysical properties of the system being modeled to

an otherwise ordinary set of mathematical equations. They ensure that all the reactions included in mathematical models, especially those comprised of more than one reaction, are mass and charge balanced individually and together and that the reactions proceed in accordance with thermodynamics. Mathematical models lacking these constraints operate in unchecked theoretical space, and the mechanisms proposed are not necessarily valuable insights. Thus, it is imperative to check for constraints in mathematical models of biochemical systems.

In mitochondrial matrix, metabolites and nucleotides exist in interconverting ionic forms and interact with other ionic species in the environment. In observance with the law of conservation, a metabolite or nucleotide is often treated as a metabolite or nucleotide pool, i.e., the sum of all the ionic forms of that metabolite or nucleotide. For example, NADH can be expressed as the sum of its reduced and oxidized forms as in $[\text{NADH}]_{\text{tot}} = [\text{NAD}^+] + [\text{NADH}]$. Similarly, ATP can be expressed as the sum of free ATP and ATP bound to other ions such as in $[\text{ATP}] = [\text{ATP}^{4-}] + [\text{HATP}^{3-}] + [\text{KATP}^{3-}] + [\text{MgATP}^{2-}]$ [66]. The bound ATP species can be all expressed in terms of free ATP by using the equilibrium constants, a practice formally put forward by Alberty [74]. The equilibrium constant associated with the binding of ATP and protons is simply an acid-base equilibrium constant. Expressing all bound forms in term of the free form is done not only for mathematical conveniences but also for the sake of computational cost. Thus, this practice has been implemented in some models although the reason behind the decision is often implied [63,66].

The choice of modeling approach is immensely important. Model evolution is inevitable as new experimental data are generated daily. Processes that were once considered trivial such

as free radical homeostasis may become of significant interests [75–77]. Technological progress has also made available data that were once unattainable. Existing models need to incorporate new experimental data to better emulate the system being modeled. Thus, there should be room for changes in the model, and the modeling approach either facilitates or hinders the process.

One of the most common changes made to an existing model is to explicitly model processes that were once phenomenologically modeled. This approach arises from the desire to impart mechanistic details on previously unexplained phenomenon. Explicit models are, thus, described as more granular. The advent of the high-resolution respirometry systems, new generations of inhibitors and enzyme assays has resulted in a growing body of experimental data informative of mitochondrial free radical homeostasis. Thus, it became feasible to explicitly model superoxide and hydrogen peroxide production by mitochondrial enzymes. Yet phenomenological or empirical modeling remains necessary when data are unsubstantial or associated with high uncertainty level. Combining processes that are not rate-limiting steps in a lump-sum function, also known as a “forcing function”, also helps to reduce computational cost. For example, the TCA cycle can be explicitly modeled in which all the reactions are mathematically described. Some of the reactions, in contrast, can be lumped together in a single reaction that depends on the $[NAD^+]$, $[NADH]$, and concentrations of allosteric modulators. The factors that govern this method of model reduction are often found after a thorough analysis of the initial model.

In the bottom-up approach, building blocks (model constituents) are assembled to explain system behaviors. A common way to define the model building blocks is to divide the

system into functional modules, each of which focuses on a single function of the system.

Deconstruction often arises from the need to reduce the complexity of the system in order to identify its properties at the level of its constituents. Once the modules have gone through the entire workflow (construction, verification, calibration and validation), they are united in a single framework. For instance, a mitochondrial model can be deconstructed into the TCA cycle and oxphos modules. Deconstruction enables using experimental data on enzyme kinetics to calibrate the TCA cycle and oxphos modules. Then the calibrated components are reconstituted and calibrated at the system level (mitochondria). Models developed using this approach is often described as being “modular.” In contrast, mechanisms are derived from observations in the top-down approach. Social network and epidemiological studies often employ top-down approach. Some modelers consider the metabolic control theory as following the “top-down” approach wherein the control contributed by a whole branch of pathway is determined [78,79].

Assumptions are important in constructing models because not all information necessary for model building is available. A common assumption is that an enzyme’s kinetic properties (other than V_{max}) are not significantly dependent on tissue- and species-specific. This assumption allows an initial model to be constructed using data from other tissue or species as they may be all available information. In these models, V_{max} terms are identified using the calibration data the model is built from. For example, Kohn and Garfinkel used data from isolated enzymes in lieu of information collected from tissue homogenates or intact organs to develop an initial model of the ischemic rat heart purine metabolism [80]. The authors stated that the V_{max} values are increased in some instances to account for the loss of enzymatic activity due to the isolation process. Another common assumption is that enzyme catalytic

processes are in the steady state. This greatly simplifies the model and reduces computational complexity up to several orders of magnitude. Similarly, certain steps in a pathway may be combined into a lumped function or omitted when they do not significantly contribute to the model output. In the ischemic excised dog heart model, the TCA cycle is simplified by excluding enzymes that become inactive under ischemia, and matrix pH is expressed as a forcing function to keep it at a predetermined level [61]. It is worth reiterating that these assumptions are necessary to build the initial model and do get tested during the model training process and integrating into larger-scale models. Nevertheless, they must not violate biophysical laws.

The essence of the parsimonious principle is that the simplest model capable of explaining (reproducing) the largest sets of data is most likely “correct” given existing literature for lack of a better word. Model simplicity includes the smallest set of assumptions, smallest set of adjustable parameters and simplest mathematical expressions. Although the parsimonious principle is integral to the entire modeling workflow, it is included in this section because the initial model construction presents many opportunities to violate this principle. For example, using module-specific adjustable parameters often arises from the desire to fit data in the absence of a mechanistic explanation. This practice becomes troublesome when the model gets integrated into a larger-scale model [64]. Because such a model relies on unphysiological instead of true biophysical model details to fit data, the model does not operate as a biophysical entity. In other cases, the parsimonious principle improves the consistency between model outputs and data by reducing the model complexity. Malyala and colleagues found that simplifying the mathematical expressions for the mitochondrial calcium uniporter (MCU) and sodium calcium exchanger (NCLX) was necessary to fit the experimental data [81]. They also

simplified the TCA cycle because not all reactions included in earlier models [49,66] were necessary to fit their experimental data. It is worth mentioning that, as any model evolves, prior decisions may become obsolete and be replaced. It is necessary to dispel that the parsimonious principle does not favor oversimplifications as doing so risks omitting important but subtle mechanistic details. To borrow the words of Albert Einstein, “Everything should be made as simple as possible, but not simpler.”

Model Training

A rigorous model training process is necessary to ensure the quality of model predictions. Model training consists of model calibration and model validation. Model *calibration*, also known as model fitting, involves simulating experiments on a coding platform, comparing simulated outputs to experimental data and modifying the preliminary model until it can reproduce experimental data. Simulated data are interchangeable to model outputs although some modelers favor the latter terminology to avoid confusing simulated and experimental data. Model *validation* requires the calibrated model to simulate novel data sets – those that are not used in model calibration – without altering the model structure or the parameter set identified in model calibration. If the model outputs are significantly inconsistent with new data, the model needs recalibration. In practice, model training is a highly dynamic process which consists of a series of model calibration and validation attempts. Model training involves careful data mining and model parameterization, two aspects that are often overlooked in modeling publications. The following sections aim to fill in this gap. Each section will help to explain the what, why, and how aspects related to data and parameters. Despite being a technical topic, the concepts underlying model parameterization are intuitive. To aid

with the intuitive understanding, we will focus on the concepts rather than the technicality in this review.

Data mining is one of the most challenging aspects in modeling work because data define the parameter space in which the model operates. Although it is impossible to fit all the data sets available, the more data sets are used to “train” the model, the better the model can perform when challenged to reproduce novel data sets. Not only the quantity but also the quality of data is important. Surprisingly, there exists no gold standard for model-data consistency or the minimal number of data sets a model must be able to fit. Many published mitochondrial models only fit data qualitatively or semi-quantitatively, i.e., the model is able to produce only the trend or converting to a relative scale is necessary to fit the data [46,64].

Curating literature data benefits from the breadth and depth of knowledge of the curator to reconcile different experimental results. Assuming that the experiments were carefully planned and executed, these differences are likely to result from varying experimental conditions. For instance, data used in mitochondrial models are generated using isolated mitochondria, submitochondrial particles or purified proteins reconstituted into lipid vesicles. The buffers are likely different in pH and ionic strengths. Certain protocols require cooling of the sample. Even when all these factors are held constant, biological variations and tissue heterogeneity also introduce hidden variables into the data. Together, they can and have led to contrastingly different conclusions, as illustrated in the following paragraph.

Both using bovine heart submitochondrial particles, Grivennikova and colleagues show that the peak ROS production of complex II occurs around 50 μM succinate [82] while Siebels and Drose estimated this concentration to be 150 μM [59]. The difference is likely due to the

use of different inhibitors, which inevitably affects the electron distribution along the ETC. As a complex III inhibitor, myxothiazol causes the ETC segment upstream of the Q_o site to be further reduced. Atpenin A5 is a specific inhibitor of the quinone reductase site of complex II, so only those redox centers upstream of the II_Q site are further reduced. It is not possible, at least not at the time of this review, to experimentally quantify the electronic distribution along the ETC. By choosing to include both data set, Manhas and colleagues were able to reconcile this and other experimental discrepancies using a single kinetic model of complex II [50].

Generating data in-house permits more precise control over experimental conditions. Several groups have, in fact, generated their own data to supplement literature data [50]. It is important to note that in-house data should not be solely used because doing so will bias the model to a specific parameter space, i.e., the model will be able to reproduce only the in-house data and nothing else. Regardless, experimental data and model outputs should be displayed together to demonstrate the ability of the model to reproduce data. As simulating an experiment *in silico* enables the generation of more data points than what can be accomplished experimentally, model outputs are often presented as lines on figures. Accompanying experimental data are represented as symbols with margin of errors. Occasionally, the model outputs and data are tabulated. Unfortunately, even when models are claimed to fit experimental data, model outputs and data are often not shown together. It becomes the task of the reader to mine the cited references to be able to evaluate the fit between model outputs and data.

Constitutive equations, including how they are related, make up the model scaffold. Parameters are numerical values that lends specificity to the set of mathematical expressions.

Fixed parameters are treated as constants in the model as they are associated with low uncertainty level. When the uncertainty associated with a parameter is high, it is necessary to evaluate the effects of varying this parameter on the model outputs. Hence, the parameters are treated as “*adjustable* parameters.” For example, temperature is almost always treated as a fixed parameter in mitochondrial models since it is often fixed. Most equilibrium constants are also treated as fixed parameters. Also, enzyme activities are frequently adjusted during model calibration to account for variable enzyme concentrations. In any case, sensitivity analyses should be performed on all model parameters to identify structural and uncertainty issues associated with the model.

Parameterization is the process of determining the best parameter set for the mode. It involves making the decision to treat a parameter as fixed or adjustable, estimating the values of adjustable parameters and evaluating their contributions to model outputs (sensitivity analysis) [83]. It is beyond the scope of this review to discuss in detail the technical aspects of parameterization and sensitivity analysis. Therefore, only key concepts are presented. Many excellent original articles and reviews cover this area of modeling [83–85]. The best parameter set contains the fewest number of parameters yet is able to best reproduce the largest number of data sets. The initial set of adjustable parameters is guided by experimental data and refined by the process of local sensitivity coefficient analysis. Local sensitivity analysis helps to identify the relative contributions of adjustable parameters to model outputs. The term local here represents the fact that these values are to be interpreted in the vicinity of the parameter values the analysis is run with. There is another type of sensitivity analysis, called global sensitivity analysis, which partitions model output uncertainty associated with individual model

parameters (or any number of parameter combinations). In other words, global sensitivity analyses identify which parameters (or combinations thereof) dominate the model output variability. Local sensitivity analyses give insight into which parameters control the model's ability to explain data. In this process, model outputs are determined as the adjustable parameters are perturbed. Perturbations to the most sensitive parameters result in significant changes to model outputs. Most sensitive parameters are associated with the largest sensitivity coefficients. The opposite is true for the least sensitive parameters. Impertinent to model outputs, these parameters can be "hard coded," or in some instances, removed entirely from the model. The model parameterization is streamlined, and computational cost is reduced. While sensitivity coefficient analysis is a common practice in many engineering fields, it is not routinely performed in building mitochondrial models. In fact, only some models are published with sensitivity analysis [49,50,66,72,73].

Important Considerations

A model always evolve as new data are constantly produced. Model evolution often increases the specificity and complexity of the model. Processes that were once elusive become explicit, making the model more specific. An existing model also gets integrated into a larger-scale model wherein the model being integrated becomes a module in the new platform. For instance, several mitochondrial models have been integrated into skeletal muscle or cardiomyocyte models [67,86]. Scaling up inevitably increases computational cost as simulations involve solving a larger number of equations that are often more complex. While it is beyond the scope of this review to discuss in detail how to reduce this computational cost, the most commonly used strategies are briefly mentioned. Algebraic expressions can be used

instead of systems of ordinary differential equations (ODEs) assuming steady-state conditions. Although integrating into a larger-scale model is often associated with increased complexity, not all of the system components (model modules) are relevant to the observed system behavior. These components can be “absorbed,” phenomenologically modeled or simply removed. Along a similar vein, applying the parsimonious principle can also be particularly useful. In essence, the simplest model that can fit the largest number of data sets is often the best candidate for integrating into large-scale models when several models can equally explain the data. In practice, a combination of strategies is often used instead of any single one, and it is a matter of both theory and practice-guided intuition to choose the optimal strategy set. It is worth mentioning that no decisions are ever final because new data will inform what changes are necessary for the next generation of models.

The intensive nature of modeling work makes it practical to build upon existing models that have been properly constructed, calibrated, and validated. Using previously published models is a common practice among modelers, as shown in the next section. This collaborative effort requires the model codes be made publicly available. It is important to distinguish model codes from the equations that are included in the primary texts and supporting materials. The coding process translates these equations onto the coding platform, a process which requires at least some coding proficiency. But the so-called model code contains not only these equations but also the final parameter set and the experiments simulated. Ideally, the code should also include the sensitivity coefficient analysis. As executing the code should produce all the figures shown in the published manuscript, the code can be considered as an encrypted version of the written texts and figures. Having the codes readily available helps to eliminate mistakes from

translating equations and experiments into codes, especially considering the availability of many coding platforms. Mistakes during the translation of equations to codes are not uncommon and have led to discrepancies in the “host” models. The enhanced convenience of publicly available codes has prompted several journals to require including the codes with the manuscript. In the past, it was more common that the codes were provided by requesting them directly from the authors.

EXISTING MATHEMATICAL MODELS OF MITOCHONDRIA

This section covers the mainstream kinetic models of mitochondria as it is impossible to include all models in this review. Despite our best efforts, we do not always have access to all the models we wish to include especially older models. The models selected are the best representatives of the modeling approach and focus employed by their creators. When multiple models are included, they are presented in the chronological order as this organization facilitates comparison of subsequent model generations to their predecessors.

Achs-Garfinkel-Kohn Models

Developed in the 1970s, the Achs-Garfinkel-Kohn models set the stage for a mathematical modeling approach that is consistent with biophysical laws [61,62]. The models are mass and charged balanced, as well as being thermodynamically consistent. Achs and Garfinkel emphasize the necessity that the model outputs are consistent with experimental data at both the constituent (module) and whole system levels. They also highlight the importance of a model to fit experimental data *quantitatively* since a model in essence is a hypothetical picture of the system being modeled and should be able to reproduce existing data. To paraphrase the famous physicist Richard P. Feynman, it does not matter how beautiful your theory is if it does not agree with data.

One of the first Achs-Garfinkel-Kohn models is the totally ischemic excised dog heart model [61]. We choose to present this model as it is an extension of several prior models – the normal-flow perfused rat heart models [87,88], the ischemic perfused rat heart models [80,89] and the acutely ischemic dog heart models [62,90]. The ischemic rat heart models were converted to the totally ischemic excised dog heart model by decreasing the enzyme levels in

the rat heart model to one third. The totally ischemic excised dog heart model includes glycolytic, glycogenolytic and fatty acid metabolism enzymes. In fact, none of the models developed by other groups accounts for fatty acid metabolism although all contain the TCA cycle at varying degree of specificity [46,47,49,61,63,66]. The TCA cycle enzymes except for citrate synthase, malate dehydrogenase and pyruvate dehydrogenase are excluded as they are not active under ischemia. Excluding most TCA cycle enzymes and the capacity of matrix proteins to buffer pH led to the decision to model matrix pH using a forcing function. The model evokes specific assumptions of 1) the total oxygen content, 2) pyruvate trafficking across the inner mitochondrial membrane, 3) tissue inorganic phosphate level and 4) mitochondrial adenine nucleotide content remaining constant. Experimental data are included in the figures together with simulated values. As shown, the model outputs are highly consistent with data. Model are used to predict the concentrations of metabolites not quantified experimentally. However, it is unclear if the model was validated before it was used to generate predictions. Sensitivity analysis is not mentioned, either.

Korzeniewski-Zoladz Models

Assimilating the contemporary interest of the field in oxidative phosphorylation, the first Korzeniewski-Zoladz models aimed to understand the regulatory mechanisms underlying this process [46]. Transporters included in the model are the adenine nucleotide transporter (ANT) and the phosphate carrier (PiC). Matrix processes are substrate metabolism and the activity of the respiratory chain. The model also includes adenylate kinase, internal and external ATP consumption. It accounts for the interactions of Mg^{2+} , AMP and ADP with other environmental ions, as well as proton buffering and the redox equivalent pools. Fixed model

parameters include the values of compartment volumes, protein concentrations and equilibrium constants, which are curated from extant literature. An important assumption is that the reactions catalyzed by matrix dehydrogenases are fully irreversible and are dependent on only $[NAD^+]$. The assumption enables expressing substrate metabolism using a simple first-order rate law. The model also assumes a near equilibrium condition for the PiC and the ETC between NADH and cytochrome c. As opposed to a competing model [48], the ANT activity is modeled after the mechanism proposed by Klingenberg wherein the binding of a nucleotide to ANT on one side (ADP on the intermembrane and ATP on the matrix side) induces a conformational change that causes the transporter to open on the other side and release that nucleotide [91]. The competing model adopted the ternary complex mechanism of ANT. This model illustrates the utility of mathematical modeling in testing competing theories although the lack of proper parameterization limits the model validity.

The mitochondrial model was integrated into the skeletal muscle model in 2001 [67]. The model was used to derive the regulatory mechanisms underlying the transition from resting to active state in skeletal muscles. The overarching conclusion is that activating multiple steps of oxidative phosphorylation in parallel is necessary to explain the behaviors of skeletal muscles under high intensity workload. Increasing $[ADP]$ in the model does not adequately explain these changes. The model also suggests that only ATP synthesis flux is accounted for by the second-order dependence of oxidative phosphorylation on $[ADP]$. The skeletal muscle model includes the phosphocreatine kinase system, the cytosolic component that helps regulate the ATP concentration in skeletal muscle. The proton efflux from the cytosol to blood and the cytosolic proton buffering are also included. Finally, the total adenine nucleotide pool is increased to 6.7

mM to match the whole-cell concentration. The assumptions from the mitochondrial model are applied to the skeletal muscle model. Additional assumptions are made in the larger-scale model. The first assumption is that phosphocreatine kinase operates near equilibrium, which means the system is sensitive to changes in substrate and product concentrations. The second set of assumptions include the total concentrations of 1) the creatine pool, 2) the adenine nucleotide pool and 3) the phosphate pool. Lastly, ATP production by glycolysis is assumed to be negligible and omitted from the model. The authors acknowledged that glycolysis is important in maintaining ATP during a burst of high intensity workload but that condition is outside the scope of their model.

These models lean towards a more general approach as many processes are combined into a single rate law. Assumptions are explicitly stated in the models, a practice that is important yet often neglected. However, key mechanisms are likely missing from both models as only some model outputs are consistent with data. In the mitochondrial model, all simulated enzyme reactions except for external ATP utilization are significantly different from experimental data [46]. Reasonable consistency is achieved only at the pathway level, which lack mechanistic details. The skeletal muscle model utilizes only three data points, which are all [ADP] at varying respiratory states [67]. Despite being bioenergetic models, they do not incorporate any other bioenergetic data during model development. The discrepancies between model outputs and data could have originated from lumping all matrix dehydrogenation reactions in a single rate law. Combining the proton concentration gradient and membrane potential components of the electromotive force also limits the models to certain conditions. In fact, the inability of the models to simulate a novel data set using isolated

cardiac mitochondria [92] prompted Beard and colleagues to take a more detailed approach in their first mitochondrial model [49]. Thus, the models were used to make predictions despite not being successfully validated. Since the model predictions require proper execution of model calibration and validation, the predictions made by the Korzeniewski-Zoladz models are likely limited to a small set of conditions.

Cortassa-Aon Models

The group led by Cortassa and Aon has published several models of mitochondrial bioenergetics. Their work is medically oriented as the models were developed partly to better understand molecular events occurring during cardiac IR injury. One of the group's first comprehensive models, published in 2003, focuses on how substrate availability and varying phosphorylation potential regulate oxygen consumption rates (V_{O_2} in the model) [47]. Another primary aim is to understand how calcium regulates oxygen consumption rates by altering the NADH pool and membrane potential. The TCA cycle and oxidative phosphorylation are aspects similar to other models. However, the model also includes calcium dynamics. Substrate availability is expressed in terms of NADH and $FADH_2$ pools by varying the acetyl coA concentrations and referred to as the "push" mechanism. Workload is manipulated by changing the activity of the adenine nucleotide translocator (ANT) and membrane potential and introduced as the "pull" mechanism.

The mitochondrial bioenergetic model was integrated into a cardiomyocyte model with a focus on free radical homeostasis in which cellular components accounting for ROS production and elimination are added to the original model [68]. Although superoxide is produced by both ETC complexes I and III, the Q cycle catalyzed by complex III is considered

most relevant to superoxide production. The authors defend the decision by citing the lack of experimental data supporting significant superoxide production by complex I under their experimental decisions although the decision could have contributed to the discrepancies between model outputs and data. Superoxide diffusing from the matrix is reduced to hydrogen peroxide by cytosolic superoxide dismutase (Cu,Zn SOD). Cytosolic hydrogen peroxide is further reduced to water by cytosolic catalase. Mitochondrial glutathione peroxidase (GPX) eliminates matrix hydrogen peroxide, and mitochondrial glutathione reductase (GR) resets GPX to the reduced state. This model is not primarily concerned with the origins of superoxide and hydrogen peroxide produced by mitochondrial enzymes. Its principal interest lies in the oscillatory nature of superoxide production by cardiomyocytes. The model suggests that ROS is released from mitochondria in consecutive slow and fast phases. Specifically, ROS accumulates in the matrix during the slow-release phase until a certain threshold at which the inner membrane ion channel (IMAC) opening is triggered and ROS is released rapidly. However, the existence of IMAC remains speculative. Additionally, the model suggests that the scavenging enzymes are important in maintaining a healthy ROS level under physiological conditions. Although this last suggestion is reasonable, this model does not provide mechanistic details into how the scavenging enzymes accomplish this task.

The original mitochondrial bioenergetic model was updated in 2011 to account for the effects of ionic species on bioenergetic processes [63]. It is referred to as the model of energy metabolism and ion dynamics by the authors and as the updated bioenergetic model in this review for the sake of brevity. Compared to its predecessor, the updated model is more granular and renders a more accurate *in-silico* description of mitochondrial physiology for

several reasons. First, the mitochondrial Na^+/H^+ exchanger (NHE) and the phosphate carrier (PiC) are included. Second, the updated model distinguishes electrons entering the ETC at complexes I and II. Third, the equilibrium constants associated with enzymatic processes are adjusted for pH, and the binding of protons and Mg^{2+} to nucleotides is explicitly modeled. Lastly, the activity of ANT is modified to account for the effect of cytoplasmic ADP concentration. All these modifications reflect reality more closely. Model calibration of the updated bioenergetic model appears more rigorous. In the *original* mitochondrial bioenergetic model, the only experimental data set explicitly shown is the dependence of J_{O_2} on membrane potential [47]. In the *updated* model [63], model simulations are compared to experimental data of membrane potential and NADH fluorescence generated in-house. The NHE flux, PiC flux and TCA cycle metabolite concentrations are calibrated using literature data. However, experimental oxygen consumption rates are not compared to model simulations whilst it is arguably one of the most important bioenergetic variables.

The integrated two-compartment ROS model is the second ROS model developed by the Cortassa-Aon group but the first to focus chiefly on mitochondrial ROS [64]. This model will be referred to as the original mitochondrial ROS model to distinguish itself from the updated version published later in the year. This model expands the updated bioenergetic models by including a detailed mitochondrial ROS scavenging system. Unlike the previous ROS model, matrix superoxide dismutase (Mn-SOD) and the thioredoxin (TRX) system are added to the matrix ROS scavenging system. Hydrogen peroxide transportation is modeled as the product of the diffusion constant associated with hydrogen peroxide and its gradient between intra- and extra-matrix compartments. The model also relates ROS production and scavenging via the

consumption of NADH by transhydrogenase (TDH). ROS production remains treated as a lump-sum process in which oxygen leaking from the ETC is reduced to superoxide. Later in the same year, details were added to the original integrated ROS model to hash out the contributions of complexes I and III to total mitochondrial ROS production [65]. The complex I module was derived from the ETC model originally developed by Magnus and Keizer [93]. The modules representing complexes II, III and IV were adapted from the work of Demin *et al.* [94,95]. This model was applied to understand the effects of ischemia-reperfusion (IR) injury on free radical homeostasis [52].

All the Cortassa-Aon models follow a bottom-up and modular approach. Individual modules and the integrated models are claimed to be calibrated until model outputs match experimental data. However, only in more recent models did this practice become more consistent, at least as shown in the published manuscripts. In the updated bioenergetic model [63], the NHE, PiC and TCA cycle intermediates are constrained by experimental data prior to membrane potential and NADH fluorescence simulations. In the original integrated mitochondrial ROS model [64], the oxygen consumption rates, net hydrogen peroxide emission rates, membrane potential and NADH reduction states are compared to experimental data under a variety of experimental conditions. The contributions of the GPX and TRX systems to matrix scavenging are also experimentally calibrated. The updated ROS model, however, includes most calibration data sets at the integrated model level [65]. It is unclear if the ROS-producing modules in the updated ROS model were calibrated despite the rich literature on ROS and enzyme kinetics of the ETC complexes.

A close examination shows that the fit between model outputs and experimental data remains qualitative or semi-quantitative, as acknowledged by the authors. For example, the original integrated mitochondrial ROS model significantly underestimates the oxygen consumption and net hydrogen peroxide emission rates while overestimating the membrane potential [64]. The model also underestimates the NADH concentration by more than 50% during leak state and about 50% during oxidative phosphorylation. A similar trend is again observed in the uncoupling simulation and scavenging inhibitor titration simulation. The simulated ROS production in mitochondria energized with succinate in state 4 (Suc bars) and glutamate/malate in state 3 (G/M + ADP bars) achieves a reasonable fit with experimental data. However, the simulation overestimates ROS production under succinate-supported respiration in state 3 (Suc + ADP bars) and glutamate/malate-supported respiration in state 4 (G/M bars) by approximately 50%. In the presence of inhibitors, the model underestimates ROS production.

A factor that compromises the fit between model outputs and experimental data is the inconsistency among the ETC complex modules. As they are from models developed by separate groups with different modeling styles [93–95], some of the modules are more specific than others. In the updated ROS model, a handful of scaling factors were necessary to fit complex I module to experimental data (Supporting materials) [65]. Scaling factors are numerical constants that account for differences between model outputs and data. However, applying them without mechanistic reasons imposes non-physiological constraints on the model and results in excellent fit between model outputs and data at the module level but potentially poor fit at the system level. Another factor that could have contributed to the discrepancies is the decision not to model ROS production by the ETC complexes at a deeper,

more detailed level. The authors contend that the decision balances mechanistic details and computational cost. However, the decision to stay on a more general ground has led obvious inconsistencies between model outputs and data. Even when dutifully addressing the inconsistencies cannot eliminate them completely, it improves the quality of model predictions.

Markevich-Hoek Models

The first Markevich-Hoek model, published in 2015, is a partial model of mitochondrial ROS homeostasis [69]. In this kinetic model, superoxide production by the electron transport chain (ETC) complexes is quantitatively analyzed by a set of ODE equations. Hydrogen peroxide production is not considered since the model is focused on superoxide, which potentially underestimates total ROS production. The model includes but does not treat complexes II and IV as sources of superoxide. While the model treatment of complex II is consistent with contemporary experimental literature, evidence supporting significant ROS production by complex II emerged after the model was published [25,59,82].

Recently, the authors developed a kinetic model of ROS production by complex II in which ROS production is considered when the enzyme complex is fully assembled and disintegrated into SDHA/SDHB and SDHC/SDHD subunits [70]. The SDHA/SDHB subunit catalyzes the succinate oxidation reaction and relays electron from the flavin moiety to the [3Fe-4S] cluster. The SDHC/SDHD subunit catalyzes the reduction of quinone. As such, the decision to separate the enzyme complex into subunits seems to be strategically exposing all the redox centers that are putative sites of ROS production for analysis. However, since this separation is unlikely under physiological conditions, additional fitting to data under pathological conditions may be warranted to explore ROS production from complex II fragments in diseased states.

Following the kinetic model on ROS production by complex II, another model was developed to analyze the effects of succinate concentrations on succinate oxidation, quinol reduction and ROS production [71]. The sequel model extends the previous model on complex II and involves parametric analysis under different conditions.

The authors state that model simulations are fitted to experimental data in the ETC superoxide model [69]. While the corresponding experimental studies are cited, the readers are tasked with determining which data sets were selected for model fitting as experimental data are not included alongside model simulations. In the more recent work on complex II, only succinate titration and time-dependent data are included [70]. Thus, it is unclear from reading the published texts the consistency between model simulations and experimental data. It seems that the sequel model of complex II is a purely theoretical exploration as the model outputs are not compared to experimental data on succinate oxidation and quinol reduction rates [71]. The data, however, are available. None of the presented models lists the adjustable parameters and their relative contributions to the model outputs.

Several aspects require consideration given that a kinetic model of complex II ROS was recently developed. First, since ROS production by complex II is tightly coupled to succinate oxidation and the redox state of the quinol pool, uniting these two aspects into a single is indispensable to ensure the complex II model can perform normal catalytic function in addition to producing ROS. Second, integrating the united complex II model into the original ETC superoxide model is necessary to investigate the contribution of complex II to total mitochondrial ROS production. The assumption remains that the ETC complexes are the main ROS producers. Third, including hydrogen peroxide in the model is essential because two-

electron redox reactions are feasible between oxygen and the fully reduced flavin moieties of complexes I and II (FMNH₂ and FADH₂, respectively). Lastly, ROS production and scavenging by other matrix enzymes need to be considered as experimental data relevant to model fitting and validation become available.

Beard-Bazil-Vinnakota Models

The Beard-Bazil-Vinnakota models are based on the biophysical model of the respiratory chain and oxidative phosphorylation published by Beard in 2005 [49]. All the Beard-Bazil-Vinnakota models follow strictly the iterative process of model construction, calibration and validation. More importantly, sensitivity analysis is consistently performed to identify adjustable parameters and their relative contributions to model outputs. Adjustable parameters, together with their estimated values, are explicitly stated in all published models. In more recently published works, ranks associated with identified parameters are also included for the sake of the reader's convenience [50,72,73].

The original model was developed to address the inability of the widely used Korzeniewski-Zoladz model [46] to explain the data observed in Bose *et al.* [92]. The original Beard model accounts for 1) the biochemical reactions catalyzed by the ETC complexes I, III and IV that are associated with high electron flux regime, 2) substrate transport via the adenine nucleotide translocase (ANT) and the phosphate-hydrogen (P_i/H⁺) co-transporter, and 3) cation flux via the K⁺/H⁺ antiporter and passive permeation of K⁺ and H⁺. In contrast to prior models [46,93], this model treats the proton gradient and membrane potential components of the protonmotive force as separate state variables. Doing so and including the phosphate activation on the ETC complex III enable the model to fit previously unexplained data sets. While

incomplete, the model demonstrates the importance of modeling biophysical processes with respect to biophysical laws. The modeling approach used here becomes faithfully practiced in all future models developed by the Beard group.

The group took a natural step towards a comprehensive mitochondrial model which ideally accounts for all experimentally observed behaviors of *in vivo* and *in vitro* systems by explicitly modeling the TCA cycle and related reactions in their 2007 model [66]. In addition to the ANT and Pi/H⁺ co-transporter, eight other transporters are added to account for the movement of TCA cycle intermediates across the inner membrane. Additional co-transporters are the pyruvate/H⁺ and glutamate/H⁺ cotransporters. Antiporters include citrate/malate, α -ketoglutarate/malate, succinate/malate, malate/phosphate and aspartate/glutamate antiporters. Reactions catalyzed by pyruvate dehydrogenase (PDH), nucleoside diphosphokinase and glutamate oxaloacetate transaminase are also included as they are relevant to the TCA cycle. More importantly, the model accounts for substrate regulatory feedback on citrate synthase (CS), isocitrate dehydrogenase (IDH) and α -ketoglutarate dehydrogenase (α KDH). Including succinate dehydrogenase (SDH) completes the ETC. Because the TCA cycle reactions are modeled explicitly, parameters associated with the ETC complexes from the original model were updated. The Beard group has successfully used this model and its derivatives to develop insight into the molecular mechanisms associated with heart failure [96–98].

The Beard-Bazil-Vinnakota group chose to model ROS production from the ETC complexes separately before integrating these models into a single framework. The first ROS model, published in 2015, identifies the origins of superoxide and hydrogen peroxide

production by complex I [72]. The complex III ROS model was published two years later [73]. The most recent ROS model analyzes succinate oxidation and ROS production kinetics by complex II [50]. All the ETC complex models unite the primary substrate/product redox reactions (NADH by complex I, succinate by complex II and quinol by complex III) with ROS production. The model calibration process is rigorous and objective as each ROS-producing model is tasked with reproducing larger and more complicated data sets obtained under a variety of conditions. Some of the data sets also appear contradictory. For example, complex II model calibration includes succinate oxidation rates under different pH, in the presence and absence of the inhibitor atpenin A5 and other TCA cycle dicarboxylate intermediates [50]. Data sets curated for the ROS producing aspect include succinate titration in the presence of different inhibitors, TCA cycle dicarboxylate intermediates, a combination of both, and in the presence of inhibitors at different pH. At the time of this review, these modules have not been integrated with TCA cycle, oxidative phosphorylation and scavenging yet although that is a natural step to be taken next.

CONCLUSION

In this mini review, we survey the mainstream kinetic models of mitochondria. Other models exist, but they are not as widely used to our knowledge [60,99,100]. The models chosen include more than one aspect of mitochondrial physiology – namely, substrate metabolism, oxidative phosphorylation, calcium buffering and free radical homeostasis. Nevertheless, the models presented are only representative as it is impossible to include all of the models developed by each group in this mini review. All of the models reviewed account for the TCA cycle reactions and oxidative phosphorylation although they differ in the level of granularity. Many groups have attempted to model mitochondrial free radical homeostasis or at least a part of it. The group led by Cortassa and Aon combined free radical homeostasis, substrate metabolism and calcium dynamics into a single model [64,65]. The model outputs, however, only fit data qualitatively or semi-quantitatively. The Markevich-Hoek model excludes hydrogen peroxide and treats complex II as a non-ROS producing module [69]. The Beard-Bazil-Vinnakota group developed models of ETC complexes that can produce both the enzyme kinetics and ROS data [50,72,73]. But these modules are yet integrated into a single mitochondrial model. None of the models except for the Achs-Garfinkel model of the ischemic excised dog heart includes beta oxidation [61]. Calcium buffering is another aspect awaiting experimental data to inform model details.

In addition, we devote a section to key aspects in mathematical modeling. Some of these aspects deserve the space that is beyond the scope of this review, so we did our best to distill and present only the conceptual essence. We hope that this section will aid the reader in their exploration into the world of mathematical modeling. Briefly, we want to highlight that

model building is guided by data as much as by biophysical laws. Models that respect biophysical laws and are properly constrained by data operate in a physiologically feasible parameter space. Only these models are able to generate valuable mechanistic insights. This appealing utility necessitates careful data mining and parameterization, which is guided by the parsimonious principle. Finally, we want to communicate the iterative nature of building mathematical models to the reader because each model is constrained by current knowledge and data. In this respect, newly generated data are “real-life” validation challenges to existing models. At some point, even the best model will fail to explain a novel data set. But it is the model-data mismatch that perfect the existing model, an inevitable part of model evolution.

REFERENCES

REFERENCES

- 1 Virani, S.S. *et al.* (2021) Heart Disease and Stroke Statistics—2021 Update: A Report From the American Heart Association. *Circulation* 143
- 2 Hausenloy, D.J. and Yellon, D.M. (2015) Targeting Myocardial Reperfusion Injury — The Search Continues. *N Engl J Med* 373, 1073–1075
- 3 Ibáñez, B. *et al.* (2015) Evolving Therapies for Myocardial Ischemia/Reperfusion Injury. *Journal of the American College of Cardiology* 65, 1454–1471
- 4 Heusch, G. and Gersh, B.J. (2017) The pathophysiology of acute myocardial infarction and strategies of protection beyond reperfusion: a continual challenge. *European Heart Journal* 38, 774–784
- 5 Hausenloy, D.J. and Yellon, D.M. (2007) The evolving story of “conditioning” to protect against acute myocardial ischaemia-reperfusion injury. *Heart* 93, 649–651
- 6 Fröhlich, G.M. *et al.* (2013) Myocardial reperfusion injury: looking beyond primary PCI. *European Heart Journal* 34, 1714–1722
- 7 Braunwald, E. and Kloner, R.A. (1985) Myocardial reperfusion: a double-edged sword? *J. Clin. Invest.* 76, 1713–1719
- 8 Morciano, G. *et al.* (2017) Mechanistic Role of mPTP in Ischemia-Reperfusion Injury. In *Mitochondrial Dynamics in Cardiovascular Medicine* (Santulli, G., ed), pp. 169–189, Springer International Publishing
- 9 El Kazzi, M. *et al.* (2020) Neutrophil-Mediated Cardiac Damage After Acute Myocardial Infarction: Significance of Defining a New Target Cell Type for Developing Cardioprotective Drugs. *Antioxidants & Redox Signaling* 33, 689–712
- 10 Hansen Peter Riis (1995) Role of Neutrophils in Myocardial Ischemia and Reperfusion. *Circulation* 91, 1872–1885
- 11 Eltzschig, H.K. and Eckle, T. (2011) Ischemia and reperfusion—from mechanism to translation. *Nat Med* 17, 1391–1401
- 12 Kalogeris, T. *et al.* (2012) Chapter Six - Cell Biology of Ischemia/Reperfusion Injury. In *International Review of Cell and Molecular Biology* 298 (Jeon, K. W., ed), pp. 229–317, Academic Press
- 13 Murphy, E. and Steenbergen, C. (2008) Mechanisms Underlying Acute Protection From Cardiac Ischemia-Reperfusion Injury. *Physiological Reviews* 88, 581–609

- 14 Tani, M. and Neely, J.R. (1990) Na⁺ accumulation increases Ca²⁺ overload and impairs function in anoxic rat heart. *Journal of Molecular and Cellular Cardiology* 22, 57–72
- 15 Garlick, P.B. *et al.* (1987) Direct detection of free radicals in the reperfused rat heart using electron spin resonance spectroscopy. *Circ Res* 61, 757–760
- 16 Hausenloy, D.J. and Yellon, D.M. (2003) The mitochondrial permeability transition pore: its fundamental role in mediating cell death during ischaemia and reperfusion. *Journal of Molecular and Cellular Cardiology* 35, 339–341
- 17 Halestrap, A.P. (2010) A pore way to die: the role of mitochondria in reperfusion injury and cardioprotection. *Biochemical Society Transactions* 38, 841–860
- 18 Gardner, T.J. *et al.* (1983) Reduction of myocardial ischemic injury with oxygen-derived free radical scavengers. *Surgery* 94, 423–427
- 19 Ambrosio, G. *et al.* (1987) Evidence for a reversible oxygen radical-mediated component of reperfusion injury: reduction by recombinant human superoxide dismutase administered at the time of reflow. *Circulation* 75, 282–291
- 20 Stewart, J.R. *et al.* (1985) Prevention of free radical-induced myocardial reperfusion injury with allopurinol. *The Journal of Thoracic and Cardiovascular Surgery* 90, 68–72
- 21 Bulluck, H. *et al.* (2016) Reducing myocardial infarct size: challenges and future opportunities. *Heart* 102, 341–348
- 22 Kussmaul, L. and Hirst, J. (2006) The mechanism of superoxide production by NADH:ubiquinone oxidoreductase (complex I) from bovine heart mitochondria. *Proceedings of the National Academy of Sciences* 103, 7607–7612
- 23 Galkin, A. and Brandt, U. (2005) Superoxide Radical Formation by Pure Complex I (NADH:Ubiquinone Oxidoreductase) from *Yarrowia lipolytica*. *Journal of Biological Chemistry* 280, 30129–30135
- 24 Brand, M.D. (2010) The sites and topology of mitochondrial superoxide production. *Experimental Gerontology* 45, 466–472
- 25 Quinlan, C.L. *et al.* (2012) Mitochondrial Complex II Can Generate Reactive Oxygen Species at High Rates in Both the Forward and Reverse Reactions. *Journal of Biological Chemistry* 287, 27255–27264
- 26 Muller, F.L. *et al.* (2007) High rates of superoxide production in skeletal-muscle mitochondria respiring on both complex I- and complex II-linked substrates. *Biochemical Journal* 409, 491–499

- 27 Denton, R.M. *et al.* (1978) Calcium ions and the regulation of NAD⁺-linked isocitrate dehydrogenase from the mitochondria of rat heart and other tissues. *Biochemical Journal* 176, 899–906
- 28 Denton, R.M. and McCormack, J.G. (1980) On the role of the calcium transport cycle in heart and other mammalian mitochondria. *FEBS Letters* 119, 1–8
- 29 Johnson, K.A. and Goody, R.S. (2011) The Original Michaelis Constant: Translation of the 1913 Michaelis–Menten Paper. *Biochemistry* 50, 8264–8269
- 30 Karr, J.R. *et al.* (2012) A Whole-Cell Computational Model Predicts Phenotype from Genotype. *Cell* 150, 389–401
- 31 Jumbe, N. *et al.* (2003) Application of a mathematical model to prevent in vivo amplification of antibiotic-resistant bacterial populations during therapy. *J Clin Invest* 112, 275–285
- 32 Kremling, A. *et al.* (2015) Understanding carbon catabolite repression in *Escherichia coli* using quantitative models. *Trends in Microbiology* 23, 99–109
- 33 Hodgkin, A.L. and Huxley, A.F. (1952) A quantitative description of membrane current and its application to conduction and excitation in nerve. *The Journal of Physiology* 117, 500–544
- 34 Huxley, A.F. (2000) Mechanics and models of the myosin motor. *Phil. Trans. R. Soc. Lond. B* 355, 433–440
- 35 Onsager, L. and Machlup, S. (1953) Fluctuations and Irreversible Processes. *Phys. Rev.* 91, 1505–1512
- 36 Smith, E. and Morowitz, H.J. (2004) Universality in intermediary metabolism. *Proceedings of the National Academy of Sciences* 101, 13168–13173
- 37 Qian, H. *et al.* (2003) Stoichiometric network theory for nonequilibrium biochemical systems. *European Journal of Biochemistry* 270, 415–421
- 38 Williams, G.S.B. *et al.* (2007) A Probability Density Approach to Modeling Local Control of Calcium-Induced Calcium Release in Cardiac Myocytes. *Biophysical Journal* 92, 2311–2328
- 39 Greenstein, J.L. and Winslow, R.L. (2002) An Integrative Model of the Cardiac Ventricular Myocyte Incorporating Local Control of Ca²⁺ Release. *Biophysical Journal* 83, 2918–2945
- 40 Williams, G.S.B. *et al.* (2010) Models of cardiac excitation–contraction coupling in ventricular myocytes. *Mathematical Biosciences* 226, 1–15

- 41 Rudy, Y. (1993) Model Simulations of the Action-Potential and Electrical-Activity of the Mammalian Ventricular Cell. *J. Electrocardiol.* 25, 68–68
- 42 Matsuoka, S. *et al.* (2004) An In Silico Study of Energy Metabolism in Cardiac Excitation–Contraction Coupling. 54, 6
- 43 Gattoni, S. *et al.* (2017) Compensatory and decompensatory alterations in cardiomyocyte Ca²⁺ dynamics in hearts with diastolic dysfunction following aortic banding. *The Journal of Physiology* 595, 3867–3889
- 44 ten Tusscher, K.H.W.J. and Panfilov, A.V. (2006) Alternans and spiral breakup in a human ventricular tissue model. *American Journal of Physiology-Heart and Circulatory Physiology* 291, H1088–H1100
- 45 Kacser, H. (1986) On Parts and Wholes in Metabolism, in *The Organization of Cell Metabolism*, Boston, MA, pp. 327–337
- 46 Korzeniewski, B. and Froncisz, W. (1991) An extended dynamic model of oxidative phosphorylation. *Biochimica et Biophysica Acta (BBA) - Bioenergetics* 1060, 210–223
- 47 Cortassa, S. *et al.* (2003) An Integrated Model of Cardiac Mitochondrial Energy Metabolism and Calcium Dynamics. *Biophysical Journal* 84, 2734–2755
- 48 Holzhütter, H.-G. *et al.* (1985) A mathematical model to study short-term regulation of mitochondrial energy transduction. *Biochimica et Biophysica Acta (BBA) - Bioenergetics* 810, 252–268
- 49 Beard, D.A. (2005) A Biophysical Model of the Mitochondrial Respiratory System and Oxidative Phosphorylation. *PLOS Computational Biology* 1, e36
- 50 Manhas, N. *et al.* (2020) Computationally modeling mammalian succinate dehydrogenase kinetics identifies the origins and primary determinants of ROS production. *Journal of Biological Chemistry* 295, 15262–15279
- 51 Jafri, M.S. and Kumar, R. (2014) Chapter Five - Modeling Mitochondrial Function and Its Role in Disease. In *Progress in Molecular Biology and Translational Science* 123 (Blackwell, K. T., ed), pp. 103–125, Academic Press
- 52 Gauthier, L.D. *et al.* (2013) An Integrated Mitochondrial ROS Production and Scavenging Model: Implications for Heart Failure. *Biophysical Journal* 105, 2832–2842
- 53 Zhou, L. *et al.* (2009) Modeling Cardiac Action Potential Shortening Driven by Oxidative Stress-Induced Mitochondrial Oscillations in Guinea Pig Cardiomyocytes. *Biophysical Journal* 97, 1843–1852

- 54 Saleet Jafri, M. and Kotulska, M. (2006) Modeling the mechanism of metabolic oscillations in ischemic cardiac myocytes. *Journal of Theoretical Biology* 242, 801–817
- 55 Gutierrez, G. *et al.* (2004) Clinical review: Hemorrhagic shock. *Critical Care* 8, 373
- 56 Yellon, D.M. and Hausenloy, D.J. (2007) Myocardial Reperfusion Injury. *New England Journal of Medicine* 357, 1121–1135
- 57 Grivennikova, V.G. and Vinogradov, A.D. (2006) Generation of superoxide by the mitochondrial Complex I. *Biochimica et Biophysica Acta (BBA) - Bioenergetics* 1757, 553–561
- 58 St-Pierre, J. *et al.* (2002) Topology of Superoxide Production from Different Sites in the Mitochondrial Electron Transport Chain. *Journal of Biological Chemistry* 277, 44784–44790
- 59 Siebels, I. and Dröse, S. (2013) Q-site inhibitor induced ROS production of mitochondrial complex II is attenuated by TCA cycle dicarboxylates. *Biochimica et Biophysica Acta (BBA) - Bioenergetics* 1827, 1156–1164
- 60 Selivanov, V.A. *et al.* (2009) Bistability of Mitochondrial Respiration Underlies Paradoxical Reactive Oxygen Species Generation Induced by Anoxia. *PLoS Computational Biology* 5, e1000619
- 61 Achs, M.J. and Garfinkel, D. (1979) Metabolism of totally ischemic excised dog heart I. Construction of a computer model. *American Journal of Physiology* 237, 318–326
- 62 Garfinkel, D. and Achs, M.J. (1979) Metabolism of the acutely ischemic dog heart. II. Interpretation of a model. *American Journal of Physiology* 236, 21–30
- 63 Wei, A.-C. *et al.* (2011) Mitochondrial Energetics, pH Regulation, and Ion Dynamics: A Computational-Experimental Approach. *Biophysical Journal* 100, 2894–2903
- 64 Kembro, J.M. *et al.* (2013) Integrating mitochondrial energetics, redox and ROS metabolic networks: a two-compartment model. *Biophys J* 104, 332–343
- 65 Gauthier, L.D. *et al.* (2013) A Computational Model of Reactive Oxygen Species and Redox Balance in Cardiac Mitochondria. *Biophysical Journal* 105, 1045–1056
- 66 Wu, F. *et al.* (2007) Computer Modeling of Mitochondrial Tricarboxylic Acid Cycle, Oxidative Phosphorylation, Metabolite Transport, and Electrophysiology. *Journal of Biological Chemistry* 282, 24525–24537
- 67 Korzeniewski, B. and Zoladz, J.A. (2001) A model of oxidative phosphorylation in mammalian skeletal muscle. *Biophysical Chemistry* 92, 17–34

- 68 Cortassa, S. *et al.* (2004) A Mitochondrial Oscillator Dependent on Reactive Oxygen Species. *Biophysical Journal* 87, 2060–2073
- 69 Markevich, N.I. and Hoek, J.B. (2015) Computational modeling analysis of mitochondrial superoxide production under varying substrate conditions and upon inhibition of different segments of the electron transport chain. *Biochimica et Biophysica Acta (BBA) - Bioenergetics* 1847, 656–679
- 70 Markevich, N.I. *et al.* (2020) Computational Modeling Analysis of Generation of Reactive Oxygen Species by Mitochondrial Assembled and Disintegrated Complex II. *Front Physiol* 11,
- 71 Markevich, N.I. *et al.* (2020) Hysteresis and bistability in the succinate-CoQ reductase activity and reactive oxygen species production in the mitochondrial respiratory complex II. *Redox Biology* 37, 101630
- 72 Bazil, J.N. *et al.* (2014) Determining the origins of superoxide and hydrogen peroxide in the mammalian NADH:ubiquinone oxidoreductase. *Free Radical Biology and Medicine* 77, 121–129
- 73 Bazil, J.N. (2017) Analysis of a Functional Dimer Model of Ubiquinol Cytochrome c Oxidoreductase. *Biophysical Journal* 113, 1599–1612
- 74 Alberty, R.A. (2005) *Thermodynamics of Biochemical Reactions*, John Wiley & Sons.
- 75 Garlid, A.O. *et al.* (2013) Mitochondrial reactive oxygen species: which ROS signals cardioprotection? *American Journal of Physiology-Heart and Circulatory Physiology* 305, H960–H968
- 76 Zhang, Y. *et al.* (2013) ROS play a critical role in the differentiation of alternatively activated macrophages and the occurrence of tumor-associated macrophages. *Cell Research* 23, 898–914
- 77 Sena, L.A. *et al.* (2013) Mitochondria Are Required for Antigen-Specific T Cell Activation through Reactive Oxygen Species Signaling. *Immunity* 38, 225–236
- 78 Brown, G.C. *et al.* (1990) Control of respiration and oxidative phosphorylation in isolated rat liver cells. *European Journal of Biochemistry* 192, 355–362
- 79 Hafner, R.P. *et al.* (1990) Analysis of the control of respiration rate, phosphorylation rate, proton leak rate and protonmotive force in isolated mitochondria using the ‘top-down’ approach of metabolic control theory. *European Journal of Biochemistry* 188, 313–319
- 80 Kohn, M.C. and Garfinkel, D. (1977) Computer simulation of ischemic rat heart purine metabolism. I. Model construction. *American Journal of Physiology-Heart and Circulatory Physiology* 232, H386–H393

- 81 Malyala, S. *et al.* (2019) Calcium phosphate precipitation inhibits mitochondrial energy metabolism. *PLoS Comput Biol* 15, e1006719
- 82 Grivennikova, V.G. *et al.* (2017) Respiratory complex II: ROS production and the kinetics of ubiquinone reduction. *Biochimica et Biophysica Acta (BBA) - Bioenergetics* 1858, 109–117
- 83 Marino, S. *et al.* (2008) A methodology for performing global uncertainty and sensitivity analysis in systems biology. *Journal of Theoretical Biology* 254, 178–196
- 84 Leis, J.R. and Kramer, M.A. (1988) The simultaneous solution and sensitivity analysis of systems described by ordinary differential equations. *ACM Trans. Math. Softw.* 14, 45–60
- 85 IM, S. (1993) Sensitivity estimates for nonlinear mathematical models. *Math. Model. Comput. Exp* 1, 407–414
- 86 Beard, D.A. (2006) Modeling of Oxygen Transport and Cellular Energetics Explains Observations on In Vivo Cardiac Energy Metabolism. *PLOS Computational Biology* 2, e107
- 87 Achs, M.J. and Garfinkel, D. (1977) Computer simulation of energy metabolism in anoxic perfused rat heart. *American Journal of Physiology-Regulatory, Integrative and Comparative Physiology* 232, R164–R174
- 88 Achs, M.J. and Garfinkel, D. (1977) Computer simulation of rat heart metabolism after adding glucose to the perfusate. *American Journal of Physiology* 232, 175–184
- 89 Kohn, M.C. *et al.* (1977) Distribution of adenine nucleotides in the perfused rat heart. *American Journal of Physiology-Regulatory, Integrative and Comparative Physiology* 232, R158–R163
- 90 Achs, M. and Garfinkel, D. (1979) Metabolism of the Acutely Ischemic Dog Heart .1. Construction of a Computer-Model. *Am. J. Physiol.* 236, R21–R30
- 91 Klingenberg, M. (1985) The ADP/ATP Carrier in Mitochondrial Membranes. In *The Enzymes of Biological Membranes: Volume 4 Bioenergetics of Electron and Proton Transport* (Martonosi, A. N., ed), pp. 511–553, Springer US
- 92 Bose, S. *et al.* (2003) Metabolic Network Control of Oxidative Phosphorylation: Multiple Roles Of Inorganic Phosphate. *Journal of Biological Chemistry* 278, 39155–39165
- 93 Magnus, G. and Keizer, J. (1997) Minimal model of beta-cell mitochondrial Ca²⁺ handling. *American Journal of Physiology - Cell Physiology* 273, 717–733
- 94 Demin, O.V. *et al.* (1998) A model of O₂-generation in the complex III of the electron transport chain. *Mol Cell Biochem* 184, 21–33

- 95 Ov, D. *et al.* (2001) Kinetic modeling of energy metabolism and generation of active forms of oxygen in hepatocyte mitochondria. *Mol Biol (Mosk)* 35, 1095–1104
- 96 Wu, F. *et al.* (2009) Experimentally observed phenomena on cardiac energetics in heart failure emerge from simulations of cardiac metabolism. *Proceedings of the National Academy of Sciences* 106, 7143-7148
- 97 Gao, X. *et al.* (2019) Cardiac Metabolic Limitations Contribute to Diminished Performance of the Heart in Aging. *Biophysical Journal* 117, 2295–2302
- 98 Lopez, R. *et al.* (2020) Impaired Myocardial Energetics Causes Mechanical Dysfunction in Decompensated Failing Hearts. *Function* 1,
- 99 Selivanov, V.A. *et al.* (2011) Reactive Oxygen Species Production by Forward and Reverse Electron Fluxes in the Mitochondrial Respiratory Chain. *PLOS Computational Biology* 7, e1001115
- 100 Selivanov, V.A. *et al.* (2012) Multistationary and Oscillatory Modes of Free Radicals Generation by the Mitochondrial Respiratory Chain Revealed by a Bifurcation Analysis. *PLOS Computational Biology* 8, e1002700

CHAPTER 2 – CALCIUM OVERLOAD DECREASES NET FREE RADICAL EMISSION IN CARDIAC
MITOCHONDRIA

This chapter was adapted from the following previously published manuscript:

Duong, Q.V., Hoffman, A., Zhong, K., Dessinger, M.J., Zhang, Y., and Bazil, J.N. (2020) Calcium overload decreases net free radical emission in cardiac mitochondria. *Mitochondrion* 51, 126-139.

INTRODUCTION

Ischemia-reperfusion (IR) injuries underlie a variety of pathological settings that are associated with high mortality rates and long-term decreases in organ function. These injuries occur in common clinical settings such as acute coronary artery events, cerebrovascular accidents, and acute kidney injury [1]. While the pathophysiological events underlying IR injury have been reviewed extensively elsewhere [2,3], they are briefly summarized here. During ischemia, partial or complete cessation of oxygen delivery impedes electron transport system (ETS) activity. As a result, metabolites accumulate, and ETS redox centers become highly reduced. During this ischemic period, the cytoplasm acidifies and is flooded with calcium. Altogether, these factors create an environment conducive to free radical production. Although reperfusion is necessary for tissue salvage, paradoxically, most tissue damage occurs during this period. During reperfusion, exacerbation of calcium overload and a sudden increase in free radical levels trigger a phenomenon known as mitochondrial permeability transition [3–6]. After this transition, mitochondria switch from ATP producers to ATP consumers [7]. When the injury is most severe, such as that caused by prolonged or complete ischemia, this transition is irreversible and leads to ATP depletion and cell death. As the main triggers for this phenomenon are attributed to calcium overload and oxidative stress, many studies have suggested a causative relationship between calcium overload and the burst of reactive oxygen species (ROS) occurring in the reperfusion phase. But others have implied a vicious cycle between calcium and ROS production [8–11]. Nevertheless, the relationship between calcium and mitochondrial ROS production remains an important topic of investigation.

Oxidative stress during IR is primarily caused by the mitochondrial derived superoxide, a type of ROS. While the formation of superoxide is thermodynamically favorable [12,13], its production is under kinetic control [13]. Kinetic control is set by the mitochondrial membrane potential, the primary regulator of superoxide formation. This bioenergetic variable controls the degree of ETS redox center reduction and thus kinetically limits superoxide production. Under physiological conditions, free radical production is balanced by elimination to maintain free radical homeostasis and prevent oxidative stress. Recent evidence points to complexes I and III as the major ETS sources of ROS [13–15]; however, other mitochondrial enzymes also contribute to ROS production [16–19]. For example, the dihydrolipoamide dehydrogenase subunit (E3 component) of the matrix enzyme complexes α -ketoglutarate dehydrogenase, pyruvate dehydrogenase and branched-chain alpha-keto acid dehydrogenase has been shown to be a major source of ROS under conditions where NADH/NAD⁺ is maintained at a high level [16,20,21]. While many studies have linked calcium overload to excessive ROS formation during reperfusion [8,9,22], the precise mechanism linking these two factors remains unknown.

Metabolic alterations and calcium overload during IR are the major components of IR injury. As such, we tested the metabolite- and calcium-dependence of mitochondrial free radical homeostasis by quantitatively assessing net free radical generation from isolated cardiac mitochondria. The experiments were performed under various calcium challenges designed to reflect mitochondrial calcium loads that occur during IR injury. In addition, the effect of calcium on the metabolism of different substrates that are utilized by different metabolic pathways important for cardiac function were investigated. The respiratory and net free radical production rates were simultaneously measured. In parallel experiments, the membrane

potential, high amplitude swelling, and buffer calcium were quantified. We found a modest calcium-dependent stimulation of respiration in the absence of ADP but a profound inhibition of ADP-stimulated respiration with NADH-linked metabolites. Most importantly, we find that there is no explicit calcium-dependent stimulation of net free radical generation. In fact, our data reveal that calcium overload decreases free radical production in mitochondria as opposed to increasing it. These findings have important implications for the role of calcium in IR injury and ROS production.

MATERIALS AND METHODS

Mitochondria Isolation

Animal care and handling conformed to the National Institutes of Health's Guild for the Care and Use of Laboratory Animals and was approved by Michigan State University's Institutional Animal Care and Use Committee. Ventricular mitochondria from Hartley guinea pigs were isolated based on a previously described protocol [23,24] and will be briefly summarized here. Animals (4-6 weeks, 350-450 grams) were euthanized after being anesthetized with 5% isoflurane and tested to be unresponsive to noxious stimuli. The heart was perfused in chest with ice-cold cardioplegic solution until no blood was observed in the coronary arteries and cardiac veins. The cardioplegic solution (CS) consisted of 25 mM KCl, 100 mM NaCl, 10 mM dextrose, 25 mM MOPS and 1 mM EGTA at pH = 7.15. The heart was then excised and washed with ice-cold isolation buffer (IB). IB consisted of 200 mM mannitol, 50 mM sucrose, 5 mM K₂HPO₄ and 0.1% w/v BSA at pH = 7.15. Connective tissues, thymus and the great vessels were removed. Ventricular tissues were minced in ice-cold IB until small pieces on the order of 1 mm³ were left. The homogenate was then transferred to a 50-mL conical tube containing 0.5 U/mL protease (*Bacillus licheniformis*) in 25 mL IB. Tissue homogenization was done using an Omni handheld homogenizer at 18,000 rpm for 20 sec. Mitochondria were then recovered by gradient centrifugation in IB at 4 °C. Mitochondrial protein was quantified using the BCA assay and an Olis DM-245 spectrofluorometer with dual-beam absorbance module. The mitochondrial stock solution was diluted to a working concentration of 40 mg/mL. All reagents were from Sigma unless otherwise noted.

Experimental Set-up

For all experiments, mitochondria were suspended in a respiratory buffer containing 130 mM KCl, 5 mM K₂HPO₄, 20 mM MOPS, 1 mM MgCl₂ and 0.1% w/v BSA at pH of 7.1 at 37 °C. In the absence of EGTA, the free calcium concentration is approximately 4 μM due to chemical impurities [23]. Buffer sodium concentration in all experiments at 20 mM was achieved by adding the appropriate amount of NaCl to the standard respiratory buffer. Under physiological conditions, mitochondrial matrix sodium concentration is in the range of 5-10 mM. During ischemia, this value can increase to the 20 mM range. Performing the experiments at this level of sodium yields results that can more accurately delineate the capacity of mitochondria to handle calcium overload and oxidative stress during conditions like ischemia. However, experiments were also performed at lower sodium concentrations to explicitly investigate potential effects of exogenous sodium on mitochondrial bioenergetics. In experiments where a lower oxygen concentration ([O₂]) was needed, N₂ gas was bubbled into respiratory buffer. Oxygen-depleted buffer was added to the respiratory chamber, and the oxygen concentration was allowed to increase to a desired level by diffusion.

To investigate the effects of electron donors from various metabolic pathways on oxygen consumption and hydrogen peroxide emission rates, four combinations of substrates and inhibitors were used: pyruvate/L-malate (P/M), palmitoylcarnitine/L-malate (PC/M), succinate/rotenone (S/R) and succinate (S). Malate is added to pyruvate and palmitoylcarnitine to prevent the depletion of oxaloacetate during the experiments. Pyruvate is primarily an NADH-linked and a complex I substrate. Under the experimental conditions we used in this study, TCA cycle intermediates produced from pyruvate metabolism leak out of mitochondria.

Therefore, pyruvate is incompletely oxidized [25,26]. Electrons derived from palmitoylcarnitine enter the ETS via QH₂ and NADH. And with succinate, electrons enter the ETS via QH₂ at complex II. Rotenone inhibits complex I and prevents excess free radical production from its quinone-reductase site [15]. The appropriate volumes of substrates and/or inhibitor stock solutions were added to each 2-mL respiratory chamber in separate experiments to achieve the desired total concentrations of 5 mM pyruvate/1 mM L-malate, 25 μM palmitoylcarnitine/2 mM L-malate, 10 mM succinate/1 μM rotenone or 10 mM succinate. In the experiments where the total free calcium was set to zero, 1 mM EGTA was added to chelate calcium contamination from reagents and the isolation process.

Mitochondrial respiration, membrane potential and volume dynamics were all quantified using the same experimental protocol timeline. Specifically, substrates were added to the buffer at the beginning of each experiment. Instrumental background signal was allowed to stabilize prior to mitochondria addition. Mitochondria were then added to the final concentration of 0.1 mg/mL. After respiration reached a steady state and achieved leak state (leak), a bolus of CaCl₂ was injected to achieve sodium/calcium (Na⁺/Ca²⁺) cycling state. After respiration stabilized, 1 mM ADP was added to achieve the oxidative phosphorylation respiratory state (oxphos). In classic nomenclature, leak and oxphos states are also known as states 2 and 3, respectively. In some instances, state 4 is used to describe the leak state; however, state 4 is leak state respiration in the presence of high ATP and low ADP concentrations. There is not an equivalence in the classic nomenclature for Na⁺/Ca²⁺ cycling state. Therefore, the descriptive nomenclature will be used in the remainder of this study for

consistency and clarity. In high amplitude swelling and membrane potential experiments, 0.5 mM ADP used.

Oxygen Consumption Rates and Hydrogen Peroxide Emission Rates

Oxygen consumption rates (J_{O_2} , $\text{nmol mg}^{-1} \text{min}^{-1}$) and hydrogen peroxide emission rates ($J_{H_2O_2}$, $\text{pmol mg}^{-1} \text{min}^{-1}$) were simultaneously measured using an Oroboros Oxygraph (O2k) system. $J_{H_2O_2}$ was monitored using the Amplex UltraRed assay. Amplex UltraRed (AmpUR) was dissolved to a stock concentration of 10 mM according to the manufacturer's instructions. Type II horseradish peroxidase (HrP) and superoxide dismutase (SOD) were individually dissolved to the stock concentration of 500 U/mL and stored at the appropriate temperatures. Hydrogen peroxide calibration curves were made using a working solution of 200 μM H_2O_2 prepared fresh on the day of every experiment. An enzyme mixture was added containing HrP/SOD to the final concentrations of 1 U/mL and 0.5 U/mL, respectively, followed by the addition of 10 μM Amplex Ultra Red. After the amperimetric signal reached a steady state, mitochondria, metabolites, and calcium were added as detailed below.

High Amplitude Swelling Assay

Mitochondrial high amplitude swelling was determined by a decrease in absorbance at 540 nm using the Olis DM-245 spectrofluorometer with dual-beam absorbance module. However, in the presence of sufficient calcium, calcium phosphate granules cause an increase in apparent absorbance caused by light scattering. Mitochondria were challenged with calcium boluses at concentrations designed to elicit moderate calcium overload or at supraphysiological concentrations high enough to trigger permeability transition. The maximum concentrations that achieve the upper limits of moderate calcium overload in the J_{O_2} and $J_{H_2O_2}$ experiments are

20 μM for PC/M; 50 μM for P/M, S/R and S. They are referred to from here on as maximal experimental concentrations. Higher concentrations led to mitochondrial respiratory dysfunction. Permeability transition inducing concentrations are 100 μM for PC/M; 150 μM for P/M; 500 μM for S/R and S. These concentrations were sufficient to cause large amplitude swelling, a classic indicator for mitochondrial permeability transition.

Membrane Potential Measurement

Membrane potential was monitored by measuring the fluorescence of TMRM using the Olis DM-245 spectrofluorometer. Specifically, TMRM was diluted in 100% EtOH and added to a 2 mL buffer containing cuvette to the final concentration of 0.1 μM . TMRM accumulation into the mitochondrial matrix is a membrane potential driven process. At the concentration used in this study, matrix TMRM accumulation decreases fluorescence due to self-quenching. In these studies, the maximal experimental calcium concentrations were tested, as well as calcium concentrations that trigger permeability transition. In addition, buffer with 1 mM EGTA was also included as a control. For calibration, nigericin (30 ng/mg mitochondria) was added for maximal membrane potential and alamethicin (50 $\mu\text{g}/\text{mg}$ mitochondria) was added to completely depolarize the mitochondria.

Buffer Calcium Measurement

Buffer calcium was monitored by measuring the fluorescence of CaGreen-5N using the Olis DM-245 Spectrophotometer (excitation wavelength = 506 nm, emission wavelength = 531 nm). The final concentration of CaGreen-5N was 1 μM . After calcium addition, the calcium concentration in the buffer was measured in the steady-state. Then the maximal signal was achieved by adding 300 μM CaCl_2 . The minimal signal was achieved by adding 1 mM EGTA. The

steady-state buffer calcium was calculated using Eq. 2.1, assuming a K_d value of 30 μM previously determined by our lab [24]. The matrix calcium was then determined by subtracting the steady-state buffer calcium from the total calcium delivered by the boluses.

$$[Ca^{2+}]_{buffer} = K_d \frac{F - F_{min}}{F_{max}} \quad \text{Eq. 2.1}$$

Data Analysis and Statistical Testing

Data are presented as mean +/- standard deviation with individual data points included. Data were checked and confirmed for normality using the Shapiro-Wilk test. The effects of calcium on J_{O_2} , $J_{H_2O_2}$, membrane potential and volume were tested using the `anova1` function in Matlab. The effects of calcium boluses and substrates on calcium uptake were tested using the `anovan` function. A posthoc Tukey's range test was used to confirm any statistical significance among groups. At least 3 biological replicates were performed for each condition. A post-hoc power analysis was performed on the G*Power software [27,28] using the most conservative parameters of sample size, effect size, alpha = 0.05 and power = 0.80. The power analysis confirmed that the study (sample size, alpha value, effect size) is well-designed to detect statistical significance.

The p values associated with statistical significance indicated in the figures are reported either in the figure legend or in separate tables when there are more than a few values to report.

RESULTS

As shown in Fig. 2.1, the respiratory dynamic profile for each substrate tested is unique. After the addition of calcium, the respiratory rate generally increased above the leak state rate. This increase in respiration is more pronounced when S/R or S were the substrates. Moreover, when the substrates are P/M or S/R, ADP addition caused the oxygen consumption rate (J_{O_2}) to rapidly rise and reach a plateau regardless of calcium levels. This plateau is not observed when the substrate is PC/M in the presence of calcium or succinate alone with or without calcium. With P/M, the oxphos J_{O_2} monotonically decreased as a function of calcium bolus; however, calcium had little effect on oxphos J_{O_2} with S/R. Mitochondria respiring on PC/M displayed the most significant decrease in oxphos J_{O_2} by calcium. Oxygen consumption rates are essentially zero in experiments where 25 μM or 50 μM CaCl_2 were added to mitochondria respiring on PC/M. Therefore, calcium treatments were lowered to 10 μM and 20 μM in place of 25 μM and 50 μM total CaCl_2 for the PC/M group, respectively. When succinate was the sole substrate, the addition of ADP resulted in a jump in respiration followed by a decrease to a new steady-state respiratory rate. This steady-state respiratory rate is highest when there is no calcium and decreases as a function of calcium.

Calcium uptake has variable effects on respiration depending on the fuel source and respiratory states (Fig. 2.2). During leak state (blue bars), the presence of 4 μM CaCl_2 resulted in higher J_{O_2} averages. Statistical significance was reached with all substrate combinations between 0 and 4 μM CaCl_2 condition in the leak state. This is simply due to the sufficiently high contaminating calcium levels capable of stimulating respiration when this measurement was taken. The addition of calcium ($\text{Na}^+/\text{Ca}^{2+}$ cycling, red bars) further increased calcium-stimulated

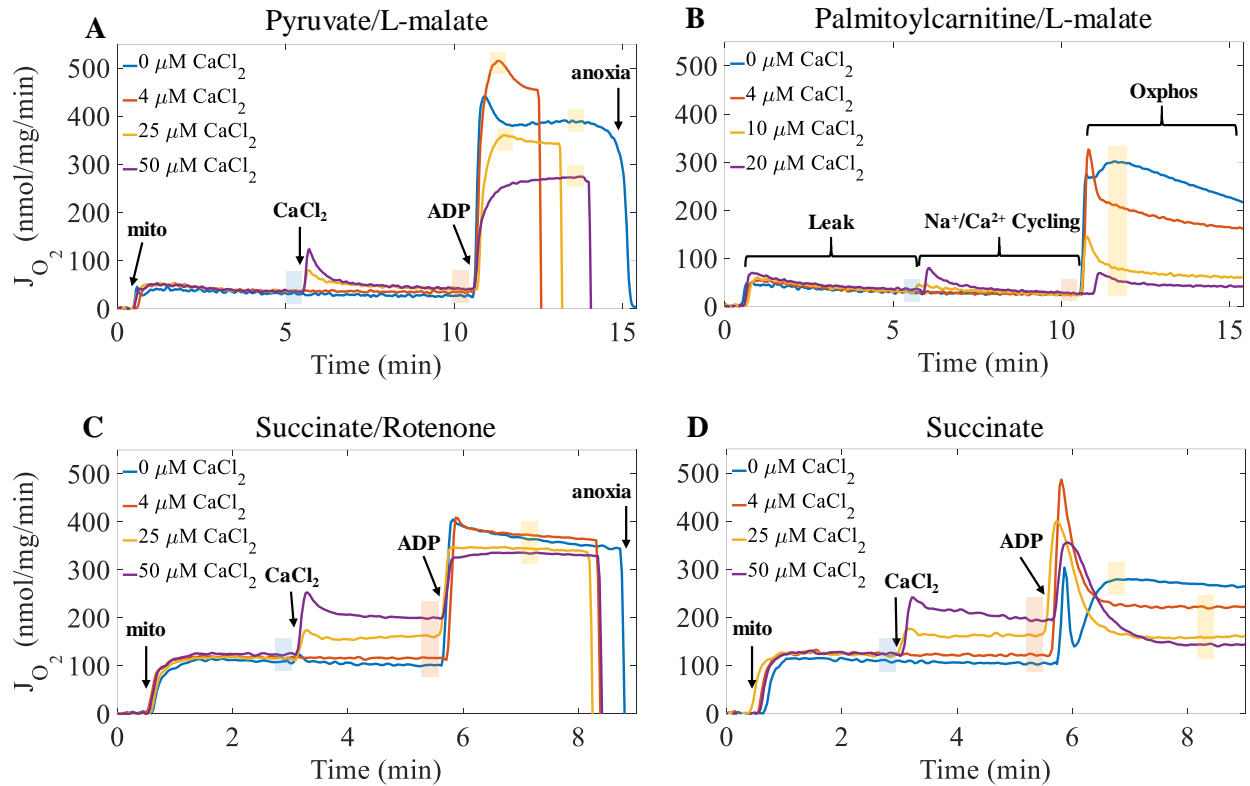


Figure 2.1 Calcium inhibits respiration for P/M, PC/M, and S but not S/R fueled mitochondria.

Mitochondria (0.1mg/mL) respiring on different substrates show distinct respiratory profile dynamics. Following mitochondria addition, J_{O_2} was allowed to stabilize. Then, a bolus of calcium was added to calcium-challenged groups (P/M, S/R and S: 25 μ M and 50 μ M $CaCl_2$; PC/M: 10 μ M and 20 μ M $CaCl_2$). In experiments where the total buffer Ca^{2+} was zero, 1 mM EGTA was added to remove trace amount of Ca^{2+} in the buffers. After stabilization, 1 mM ADP was added to stimulate maximal respiration. Leak state respiration is defined as the period between mitochondria addition and calcium bolus. Sodium/Calcium cycling state is between calcium bolus and ADP addition. Oxphos occurs after ADP addition. The sudden drop in J_{O_2} indicates anoxia. J_{O_2} of each respiratory state was averaged over 30 seconds, shown as the rectangular boxes on the figure. Boxes are color-matched with the respiratory states in subsequent figures.

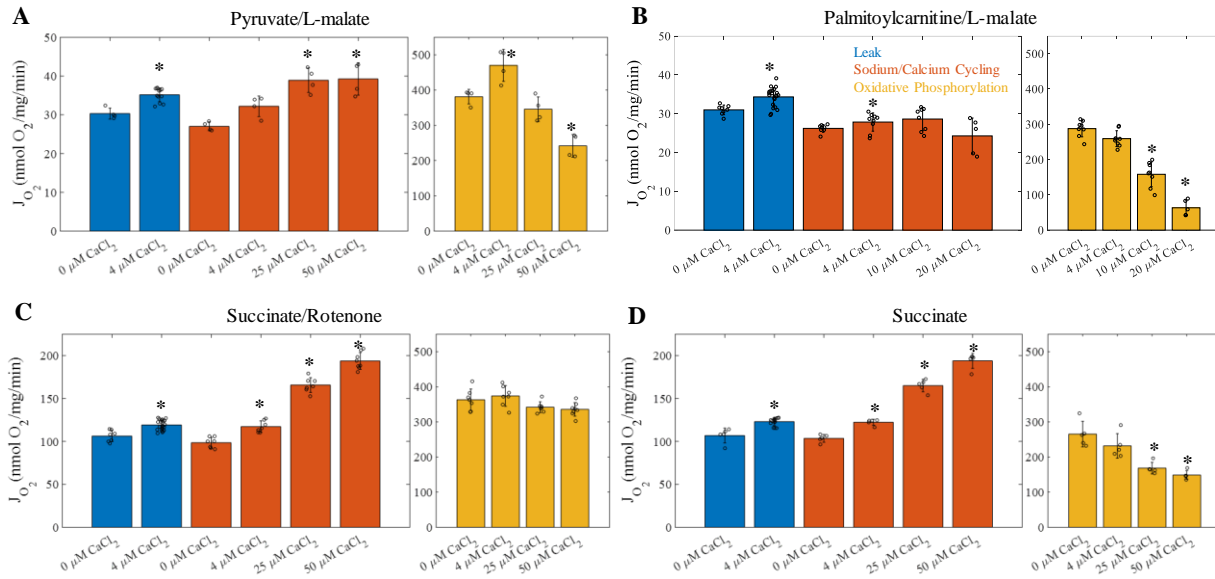


Figure 2.2 Calcium affects both leak and oxphos state respiration rates. Effects of calcium on respiration are substrate specific. Leak state (blue) respiration is enhanced in the presence of trace amount of buffer calcium (~ 4 μM) across all substrates. Mitochondria respiring on succinate with or without rotenone (C and D, respectively) had highest leak-state J_{O_2} . Sodium/Calcium cycling state (red) respiration is enhanced in the presence of increasing concentrations of calcium boluses up to 50 μM. The exception is PC/M. Mitochondria respiring on PC/M showed depressed J_{O_2} as the calcium concentration in the bolus exceeds 10 μM. For oxphos (yellow) respiration rates, buffer calcium above 4 μM depresses J_{O_2} across all substrates. In the absence of calcium, P/M respiring mitochondria have a lower J_{O_2} compared to when calcium was ~ 4 μM. However, mitochondria respired on PC/M or S had maximal oxphos when trace amount of calcium was removed. With S/R, respiration was nearly identical between the 0 and 4 μM groups, and the inhibitory effect of calcium on oxphos respiration is negligible. Statistical significance ($p < 0.05$) relative to 0 μM CaCl₂ is indicated by *.

respiration with primarily NADH-linked and Q-linked substrates (P/M, S/R or S). Respiration was either not affected or slightly inhibited by calcium in mitochondria respiring on mixed substrate (PC/M). These effects of calcium on $\text{Na}^+/\text{Ca}^{2+}$ cycling respiration were statistically significant when the substrates were P/M, S/R or S and statistically insignificant when PC/M was the substrate. During oxphos, a plateau was observed with the exception of PC/M and S. The maximal oxphos J_{O_2} in P/M containing buffer is achieved at $\sim 450 \text{ nmol mg}^{-1} \text{ min}^{-1}$ when the total buffer calcium is approximately $4 \mu\text{M}$. When the substrates are S/R, maximal oxphos J_{O_2} is achieved at $\sim 350 \text{ nmol mg}^{-1} \text{ min}^{-1}$ at the total buffer calcium of essentially zero or $4 \mu\text{M}$. In the absence of rotenone, the maximal succinate-supported J_{O_2} due to oxphos was $\sim 270 \text{ nmol mg}^{-1} \text{ min}^{-1}$ at the buffer calcium of $0 \mu\text{M}$. When the substrate was PC/M, maximal J_{O_2} was $\sim 290 \text{ nmol mg}^{-1} \text{ min}^{-1}$. Therefore, mitochondrial respiratory capacity was maximal with primarily NADH-linked substrates. Oxphos J_{O_2} was generally inhibited with increasing CaCl_2 . While the inhibitory effect was observed only after calcium exceeded $4 \mu\text{M}$ in P/M group, no statistical significance exists when calcium concentrations were 0 and $25 \mu\text{M}$. The inhibitory effect due to calcium was negligible for Q-linked substrate in the presence of rotenone. Mitochondria respiring on PC/M were exquisitely sensitive to calcium and showed a marked inhibition of oxphos J_{O_2} as the calcium concentration increased. Even at lower calcium boluses of 10 and $20 \mu\text{M}$, the inhibitory effect of calcium on respiration was significant. At lower buffer sodium concentrations, similar effects of calcium on respiration are observed across all respiratory states (Fig. S2.1). Statistical significance was not achieved between different buffer sodium groups. Selected statistical results are reported in Table 2.1, and a comprehensive list of statistical results is given in Table S2.1.

Table 2.1 Statistical significance between respiratory rates.

Respiratory States	Leak		Sodium/Calcium Cycling		Oxphos	
	calcium	p values	calcium	p values	calcium	p values
P/M	0 μ M	2.00E-04	0 μ M	---	0 μ M	1.52E-02
	25 μ M	---	25 μ M	3.39E-02	25 μ M	1.26E-03
	50 μ M	---	50 μ M	2.60E-02	50 μ M	3.69E-06
PC/M	0 μ M	9.00E-04	0 μ M	---	0 μ M	---
	10 μ M	---	10 μ M	---	10 μ M	1.61E-07
	20 μ M	---	20 μ M	---	20 μ M	3.78E-09
S/R	0 μ M	4.02E-05	0 μ M	1.03E-03	0 μ M	---
	25 μ M	---	25 μ M	3.95E-09	25 μ M	---
	50 μ M	---	50 μ M	3.78E-09	50 μ M	2.64E-02
Succinate	0 μ M	2.04E-05	0 μ M	1.31E-03	0 μ M	---
	25 μ M	---	25 μ M	6.84E-08	25 μ M	9.99E-03
	50 μ M	---	50 μ M	4.02E-09	50 μ M	9.78E-04

All values are compared to the 4 μ M CaCl₂ group within each substrate. The p values not associated with statistical significance are indicated by ---. A complete list can be found in the Appendix, Table S2.1.

To investigate the respiratory dynamics when succinate was the sole substrate, follow up experiments with combinations of succinate, rotenone, and glutamate were performed. In the presence of rotenone, glutamate addition to mitochondria respiring on succinate neither increases nor decreases oxphos J_{O_2} regardless of calcium concentrations (Fig. 2.3A, C). This is expected since rotenone inhibits complex I, and glutamate can be used to supply complex I with NADH. When rotenone is absent, the addition of glutamate leads to a significant increase in oxphos J_{O_2} (Fig. 2.3B, D). This glutamate-stimulatory effect is consistent across all calcium groups and statistically significant for all calcium groups when compared to the respiratory rate in the absence of rotenone (Fig. 2.3 and Table S2.2). While glutamate leads to an increase in respiration regardless of calcium group, there is a moderate inhibitory effect of calcium.

The effect of calcium on the ETS downstream of Complex I was tested by measuring FCCP-stimulated respiration in the presence of increased calcium concentrations (Fig 2.4). Mitochondria respiring on P/M reached maximal J_{O_2} of $\sim 785 \pm 100 \text{ nmol mg}^{-1} \text{ min}^{-1}$ in the absence of calcium. Even at the lower calcium bolus of $25 \mu\text{M}$, FCCP addition caused a significant drop P/M-supported respiration. This is due to mitochondrial permeability transition as shown below in Fig. 2.5A and also previously determined by Petronilli et al. [29]. While the maximal succinate-supported J_{O_2} is also reached in the absence of calcium ($\sim 755 \pm 21 \text{ nmol mg}^{-1} \text{ min}^{-1}$), calcium addition at both 25 and $50 \mu\text{M}$ minimally inhibited respiration. Results are reported with p values in Table S2.3. There are no significant differences between the low and high calcium treatment groups within the P/M or S/R group, respectively.

High amplitude swelling results in a rapid decrease in absorbance and is used as a gold-standard to monitor mitochondrial permeability transition. Representative absorbance

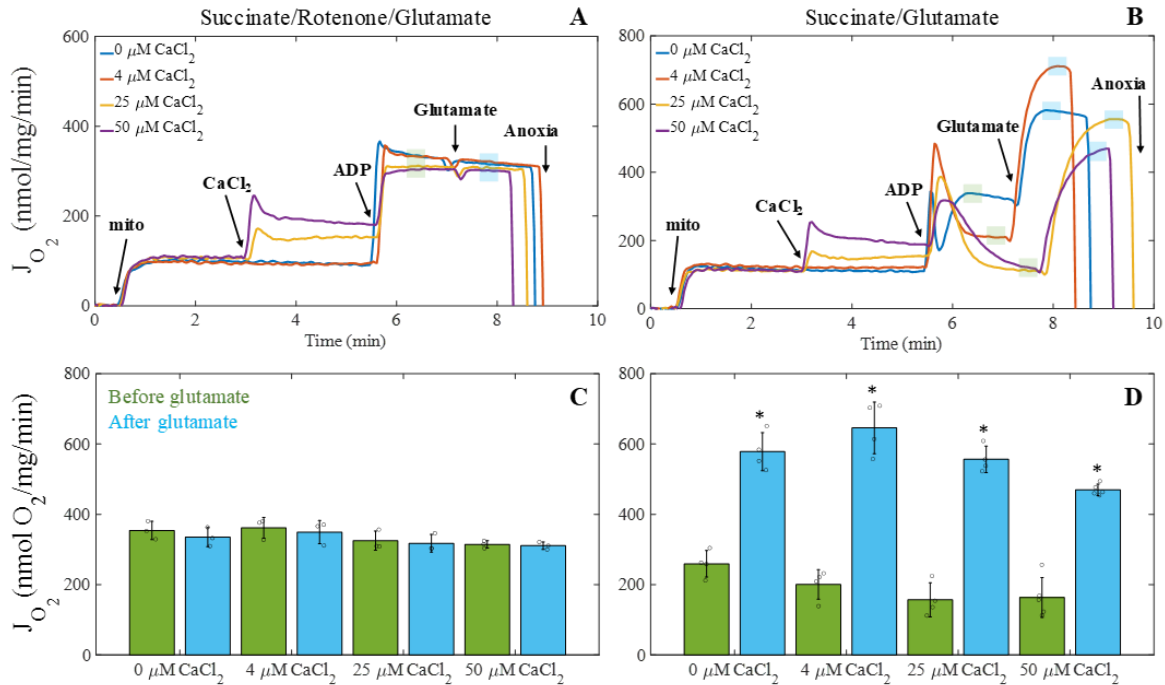


Figure 2.3 Effects of glutamate addition on oxphos J_{O_2} during succinate-fueled respiration. A- B) Representative respiratory dynamics of mitochondria respiring on succinate/rotenone/glutamate (A) and succinate/glutamate (B). The experiments were done in the same fashion as in Fig. 2.1. Approximately 1.5 minutes after ADP addition, glutamate was added to the final concentration of 5 mM in the respiratory chamber. C-D) Oxphos J_{O_2} was quantified before and after glutamate addition. Glutamate addition results in a significant increase in oxphos J_{O_2} when rotenone is absent. The increase in respiration caused by glutamate is consistent across all calcium concentrations. When rotenone is present, glutamate did not affect respiration as expected. Experiments were performed using at least 3 biological replicates. Asterisks (*) indicate statistical significance ($p < 0.01$) due to glutamate addition within the same calcium treatment group: $3E-3$ for 0 μM $CaCl_2$, $2E-3$ for 4 μM $CaCl_2$, $7E-3$ for 25 μM $CaCl_2$ and $6E-3$ for 50 μM $CaCl_2$.

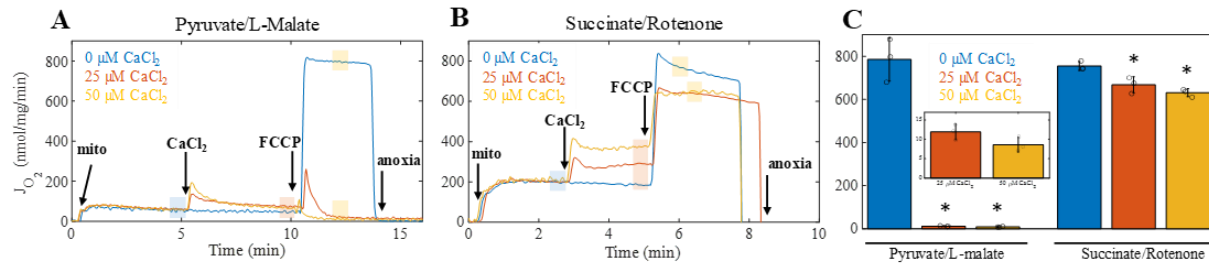


Figure 2.4 Calcium does not significantly affect the electron transport system downstream of Complex I. Oxygen consumption rates were measured in a similar experimental course as described in Fig. 2.1 except that ADP was replaced with FCCP (1 μM). A-B) Representative oxygen consumption dynamics of P/M-supported respiration (A) and S/R-supported respiration (B). C) Quantified oxygen consumption rates. In the presence of 25 and 50 μM $CaCl_2$, P/M-supported respiration was abolished upon FCCP addition. However, S/R-supported respiration showed no such decrease in respiration after FCCP addition. Experiments were performed using at least 3 biological replicates. Error bars are standard deviations. Asterisks (*) indicate statistical significance ($p < 0.01$) between calcium treatments compared to 0 μM $CaCl_2$. P/M 8.16E-6 for 25 μM $CaCl_2$ and 7.96E-6 for 50 μM $CaCl_2$. S/R: 1.66E-2 for 25 μM $CaCl_2$ and 3E-3 for 50 μM $CaCl_2$.

dynamics at 540 nm show that absorbance either increased or did not change upon adding the highest calcium concentrations tested (20 μM CaCl_2 for PC/M group; 50 μM CaCl_2 for P/M, S/R and succinate groups) (Fig. 2.5A-D). Therefore, high amplitude swelling due to mitochondrial permeability transition does not occur under our highest experimental calcium concentrations. At significantly higher calcium concentrations, high amplitude swelling results in a rapid decrease in absorbance to the level that is unchanged upon FCCP addition (Fig. 2.4A-D). Interestingly, different calcium concentrations are necessary to induce high amplitude swelling in a substrate-dependent manner. The addition of 150 μM and 100 μM CaCl_2 induced high amplitude swelling in P/M and PC/M groups, respectively. A significantly higher calcium bolus of 500 μM was necessary to induce high amplitude swelling in S/R and S groups. The precise threshold for each substrate required to elicit mitochondrial permeability transition was not further investigated in this study. The relative absorbance (%) confirms that high amplitude swelling did not occur upon adding the maximal calcium boluses in our experiments (Fig. 2.6). A complete table of averaged values, standard deviations and p values are reported in the Appendix (Table S2.4).

The substrate-specific trends in free radical emission ($J_{\text{H}_2\text{O}_2}$) are consistent with respiratory profiles (Fig. 2.7). The greatest spread among data points is associated with succinate. This is attributed to the variable nature of reverse electron transport. Hydrogen peroxide emission rates are highest during leak (blue) and lowest during oxphos (yellow). The $\text{Na}^+/\text{Ca}^{2+}$ cycling hydrogen peroxide emission rates (red) are in the middle range. Leak state $J_{\text{H}_2\text{O}_2}$ was highest in the S group, followed by the S/R group, and the leak state $J_{\text{H}_2\text{O}_2}$ was comparable among P/M and PC/M groups. While the presence of $\sim 4 \mu\text{M}$ free calcium resulted

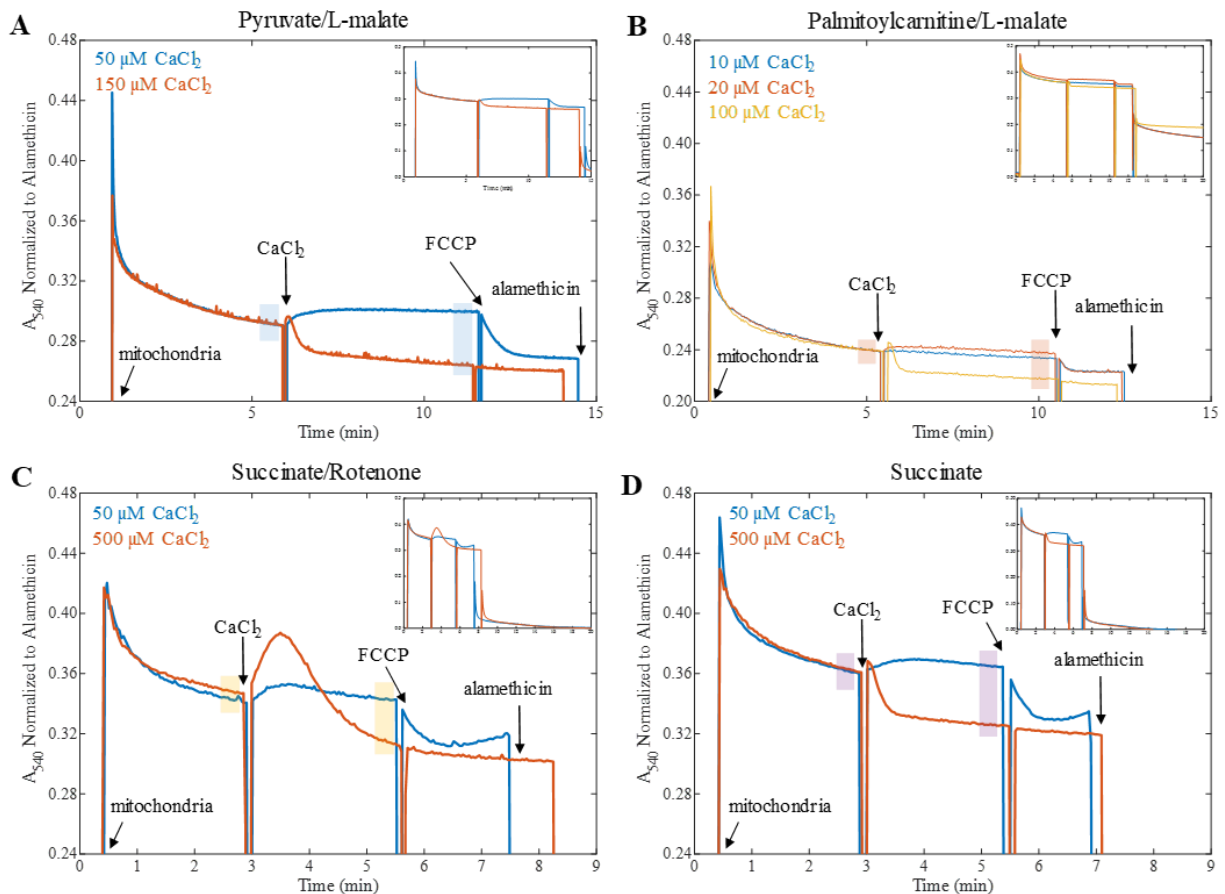


Figure 2.5 Moderate calcium overload does not trigger mitochondrial permeability transition. Representative absorbance dynamics at 540 nm was normalized to the signal following alamethicin addition (A-D). After an initial signal stabilization, mitochondria were added, and the signal was allowed to stabilize for 5 minutes (leak state absorbance). At this point, calcium was added at the maximal experimental bolus concentrations or at the concentrations that would induce high amplitude swelling. Absorbance was monitored for 5 minutes, followed by FCCP addition. Finally, alamethicin was added to completely permeabilize mitochondria (minimal absorbance). The maximal experimental boluses contain 20 μM Ca^{2+} for PC/M and 50 μM for P/M, S/R and S. The calcium bolus containing 10 μM Ca^{2+} was included for PC/M. The amounts of calcium necessary to induce high amplitude swelling depend on the substrates: 100 μM Ca^{2+} for PC/M, 150 μM for P/M and 50 μM for S/R and S.

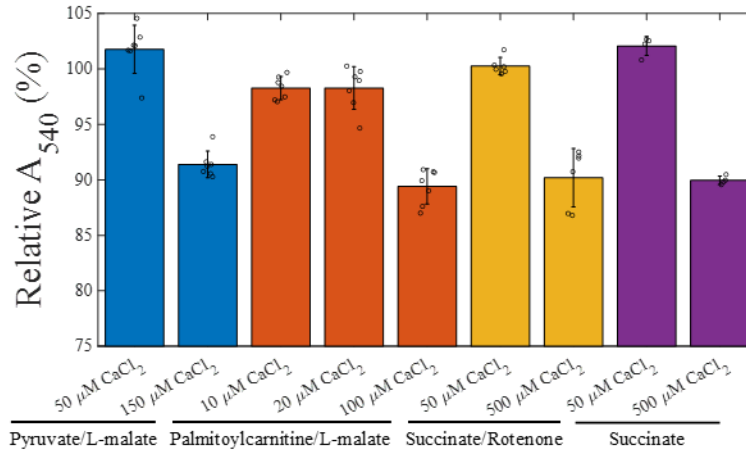


Figure 2.6 Relative absorbance (%) following calcium addition. The experimental course is as described in Fig. 2.4. The absorbance at 540 nm show that high amplitude swelling did not occur at the maximal experimental boluses. Statistical significance ($p < 0.01$) relative to maximal experimental calcium concentrations is indicated by *. The p values are 1.22E-7 for P/M, 1.14E-8 for PC/M, 4.19E-6 for S/R and 3.58E-8 for S.

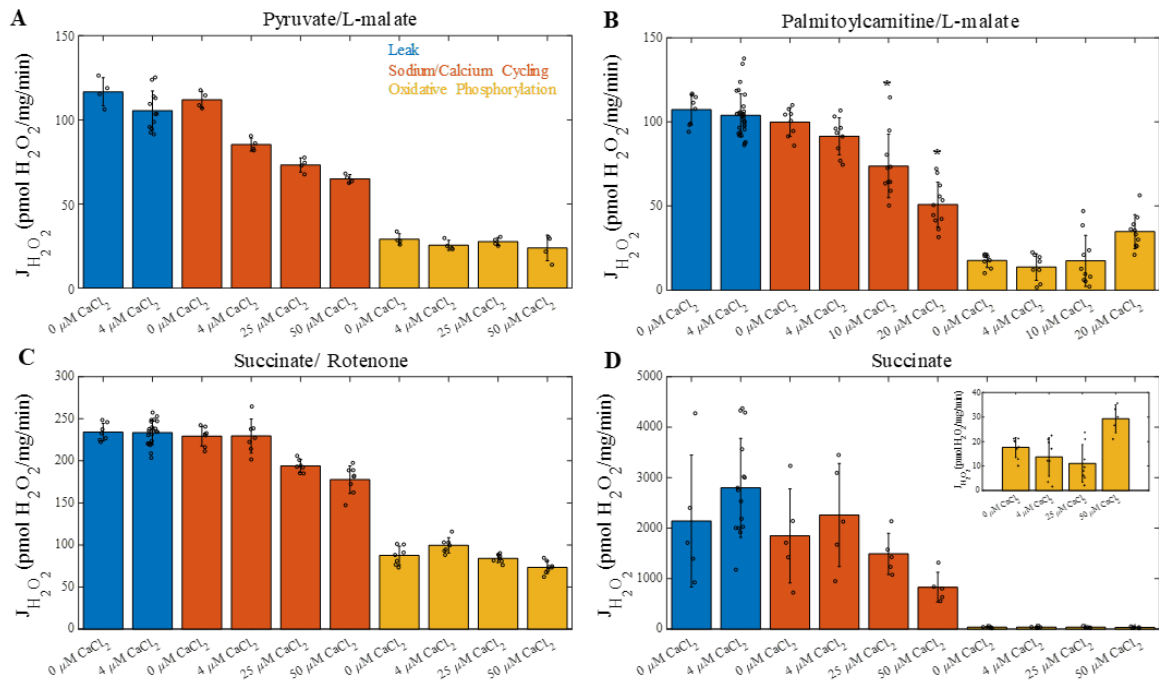


Figure 2.7 Net hydrogen peroxide emission rates are inhibited by calcium. The reported $J_{H_2O_2}$ measurements were obtained simultaneously as J_{O_2} reported in Figs. 2.1 and 2.2. Overall, the S group is associated with the greatest variation among data points. Leak state (blue) $J_{H_2O_2}$ was highest across respiratory states, regardless of the substrates. Of these rates, group S had the highest $J_{H_2O_2}$. The presence of rotenone decreased $J_{H_2O_2}$ by an order of magnitude. P/M and PC/M respiring mitochondria had similar and the lowest leak state $J_{H_2O_2}$ levels. The presence of free calcium at $\sim 4 \mu\text{M}$ did not affect $J_{H_2O_2}$ to a statistically significant level. Sodium/Calcium cycling state (red) $J_{H_2O_2}$ is depressed in the presence of increasing calcium concentrations although the amount of calcium to achieve statistical significance depends on the substrates. Oxphos (yellow) $J_{H_2O_2}$ was lowest across respiratory states, regardless of the substrates. Calcium does not alter oxphos $J_{H_2O_2}$ with the exception of PC/M where 20 μM calcium bolus resulted in a $J_{H_2O_2}$ that is highest in this group. Statistical significance ($p < 0.05$) relative to 4 μM CaCl_2 is indicated by *. Leak state: $2.00\text{E-}4$ (S). $\text{Na}^+/\text{Ca}^{2+}$ cycling state: $3.44\text{E-}6$ (PM, 0 μM CaCl_2), $4.74\text{E-}3$ (P/M, 25 μM CaCl_2), $5.35\text{E-}5$ (P/M, 50 μM CaCl_2), $5.63\text{E-}4$ (PC/M, 20 μM CaCl_2), $7.29\text{E-}4$ (S/R, 25 μM CaCl_2), $2.40\text{E-}6$ (50 μM CaCl_2). Oxphos state. $3.8\text{E-}2$ (S/R, 0 μM CaCl_2), $6.34\text{E-}3$ (S/R, 25 μM CaCl_2), $1.34\text{E-}5$ (S/R, 50 μM CaCl_2).

in a slight decrease in $J_{H_2O_2}$ in these two groups, the differences were not statistically significant. The Na^+/Ca^{2+} cycling $J_{H_2O_2}$ decreased as calcium concentrations were increased regardless of the substrates. During Na^+/Ca^{2+} cycling state, the order of decreasing $J_{H_2O_2}$ is $S > S/R > P/M \approx PC/M$. Note that the comparison between P/M and PC/M groups is based only on the order of magnitude in $J_{H_2O_2}$ since calcium treatments were lowered in PC/M group. Although the differences in $J_{H_2O_2}$ between S and other substrate groups were significant during leak and Na^+/Ca^{2+} cycling, oxphos $J_{H_2O_2}$ values were on the same order of magnitude across substrate groups. Overall, oxphos resulted in further decreases in $J_{H_2O_2}$ with overall no appreciable differences due to calcium across substrates except for S/R group. A complete list of averaged values, standard deviations and p values are reported in Table S2.5.

In addition to the swelling data (Figs. 2.5 and 2.6), representative membrane potential dynamics (Fig. 2.8) and relative membrane potential (Fig. 2.9) exclude the hypothesis that irreversible mitochondrial permeability transition causes calcium-induced mitochondrial dysfunction in this study. Compared to leak state membrane potential, mitochondria were able to maintain a membrane potential after calcium had been added at the maximal calcium concentrations tested. These concentrations are 20 μM for PC/M and 50 μM for P/M, S/R and S. In contrast, the calcium concentrations that resulted in high amplitude swelling (Figs. 2.5 and 2.6) caused a complete loss of membrane potential as shown in Fig. 2.8. At the highest experimental calcium concentrations (20 μM for PC/M and 50 μM for P/M, S/R and S), ADP addition caused a further decrease in membrane potential. These results are further evidence that mitochondria loaded with these levels of calcium remained well-coupled and were able to utilize the proton motive force to synthesize ATP. When ADP was added after excessive calcium

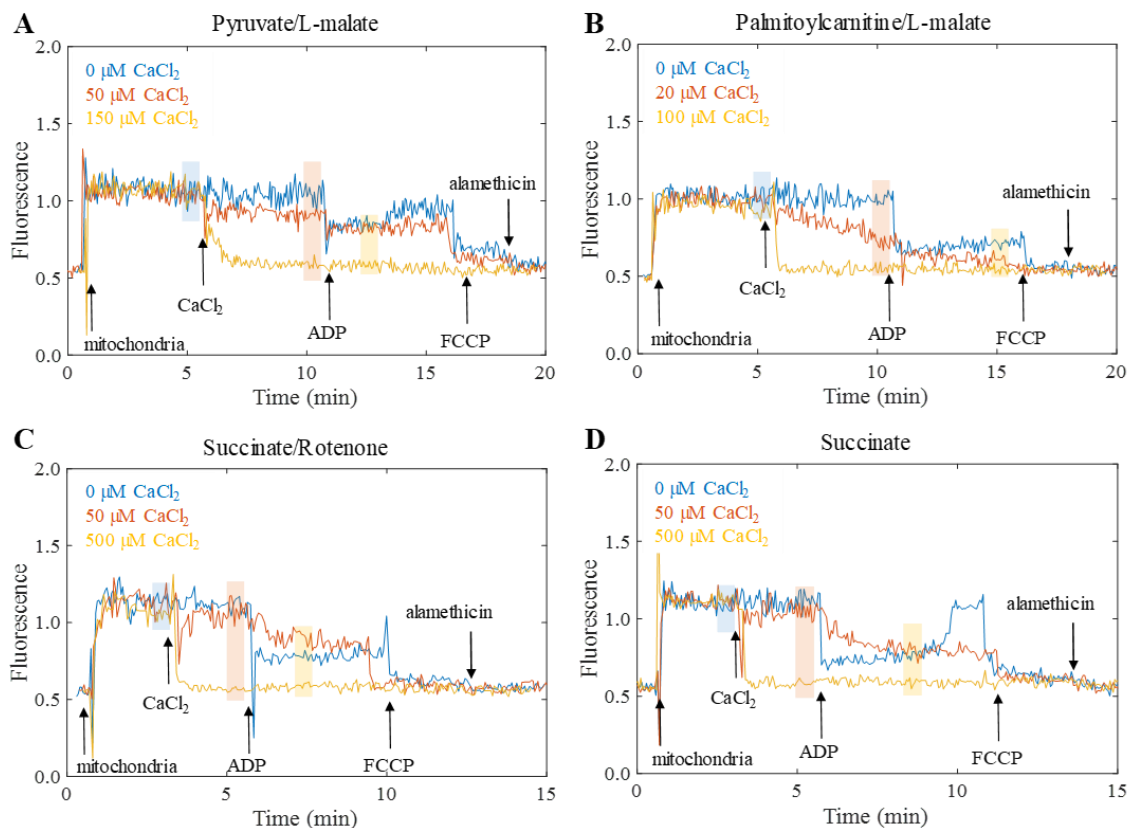


Figure 2.8 Mitochondria remain energized during moderate calcium overload. Representative membrane potential dynamics monitored using TMRM. The presence of trace amount of calcium caused a slight depression in leak state membrane potential when P/M or PC/M were the substrates (A and B, respectively). The slight depression due to trace amount of calcium was not observed when the substrate was succinate with or without rotenone (C and D, respectively). In all cases, the maximal calcium boluses used to test the effect of calcium on respiration and hydrogen peroxide emission rates did not result in complete depolarization. Specifically, mitochondria were able to maintain a membrane potential following 50 μM CaCl₂ bolus when they respired on P/M (A). In the presence of succinate with or without rotenone, the membrane potential was much higher compared to P/M and PC/M (C and D, respectively). Mitochondria respiring on PC/M appeared to be able to maintain a membrane potential following a 20 μM CaCl₂ bolus although the decrease in membrane potential did not reach a steady state (B). Depolarizing calcium concentrations are significantly higher than the maximal experimental calcium concentrations and are substrate specific: P/M + 150 μM CaCl₂, PC/M + 100 μM CaCl₂, S/R + 500 μM CaCl₂, Succinate + 500 μM CaCl₂. The maximal experimental calcium concentrations for J_{O₂} and J_{H₂O₂} measurements do not inhibit oxphos as membrane potential is further decreased upon ADP addition. However, the extent of decrease depends on the substrates. No further decrease in membrane potential upon ADP addition was observed at depolarizing calcium concentrations, confirming that mitochondria have been depolarized prior to ADP addition.

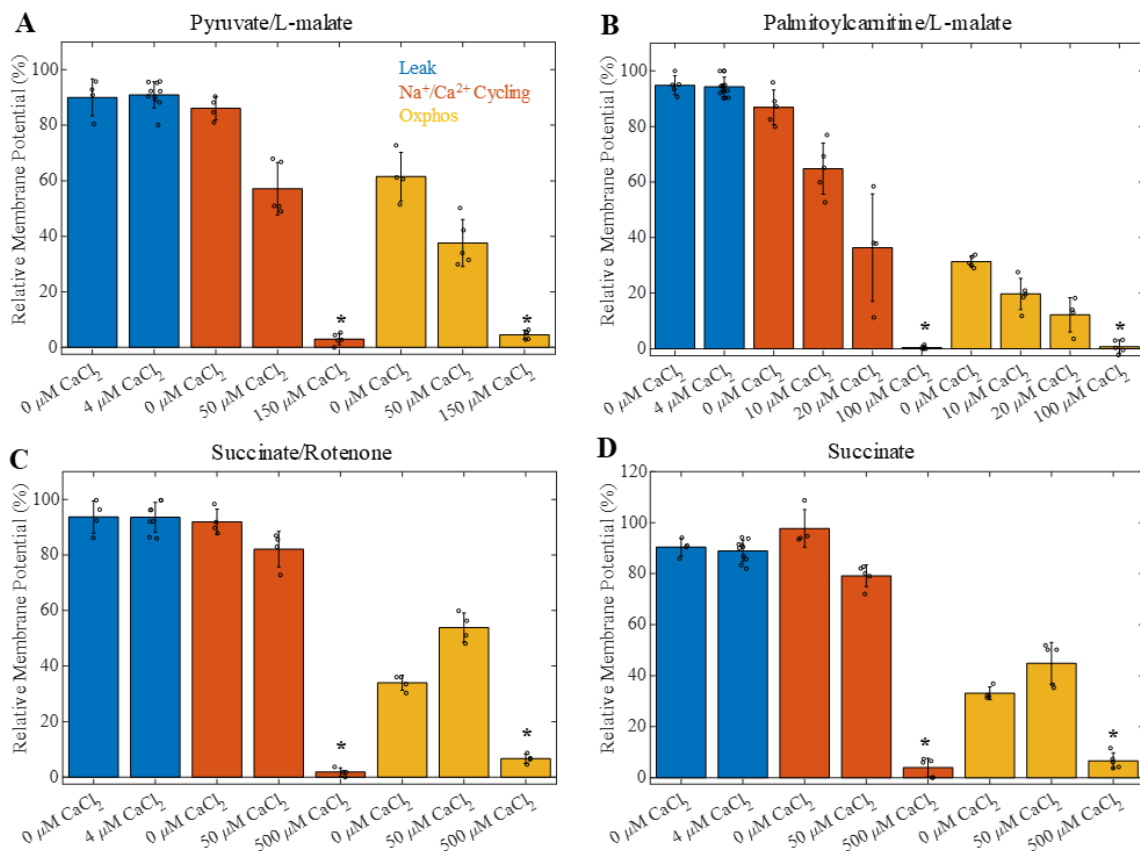


Figure 2.9 Mitochondrial membrane potential is affected by calcium loading. Relative membrane potential (%) obtained by dividing the averaged fluorescence over the fluorescence range. Mitochondria respired on succinate in the presence and absence of rotenone (G and H, respectively) were able to maintain a higher partial membrane potential compared to those respire on pyruvate/L-malate (E) after a 50 μM CaCl₂ bolus had been added. The ability of mitochondria respiring on palmitoylcarnitine/L-malate to maintain a membrane potential was compromised by calcium in a concentration-dependent manner (B). In all cases, the maximal experimental calcium boluses did not cause complete loss of membrane potential. The depolarizing calcium concentrations were significantly higher and resulted in a membrane potential that could not be further decreased by ADP. * indicates statistical significance between relative membrane potential due to maximal experimental calcium and depolarizing calcium concentrations. Sodium/Calcium cycling: 1.45E-7 for P/M, 5.94E-4 for PC/M, 1.61E-8 for S/R, and 7.26E-9 for S. Oxphos: 5.82E-5 for P/M, 6.16E-3 for PC/M, 5.37E-8 for S/R, and 1.37E-6 for S.

boluses (150 μM for P/M, 100 μM for PC/M, and 500 μM for S/R and S), no further drop in membrane potential was observed. This shows that these calcium concentrations caused complete membrane depolarization. The relative membrane potential values due to respiratory state and calcium are summarized in Fig. 2.9. Complete list of averages and p values are reported in Table S2.6. Together, results from the high-amplitude swelling and membrane potential assays exclude that irreversible mitochondrial permeability transition occurred at the concentrations of calcium used to test the effect of calcium on respiration and hydrogen peroxide emission rates.

Buffer calcium dynamics was monitored using CaGreen-5N. The representative calcium dynamics resemble the representative oxygen consumption dynamics (Fig. 2.10A-D). Steady-state buffer calcium levels after calcium injection for both low and high calcium treated groups are the same as when no additional calcium was added (low calcium: 10 μM for PC/M, 25 μM for P/M, S and S/R; high calcium: 20 μM for PC/M, 50 μM for P/M, S and S/R). Regardless of substrate or calcium bolus addition, mitochondria set the buffer calcium concentration to approximately 3-4 μM . This set point is a direct result of the calcium-dependence on the rate of calcium uptake by the calcium uniporter and the relative constant calcium efflux rate as described in detail by Nicholls and Chalmers [30] and further quantitatively characterized by Bazil et al. [24,31]. These data confirm that isolated mitochondria can sequester large amounts of exogenous calcium without triggering mitochondrial permeability transition. The steady-state buffer calcium concentrations are quantified using the relationship between buffer calcium and fluorescence intensity, as given in Eq. 2.1 (Fig. 2.10E). Matrix calcium content was then obtained by subtracting the steady-state buffer calcium from the total calcium taken up by

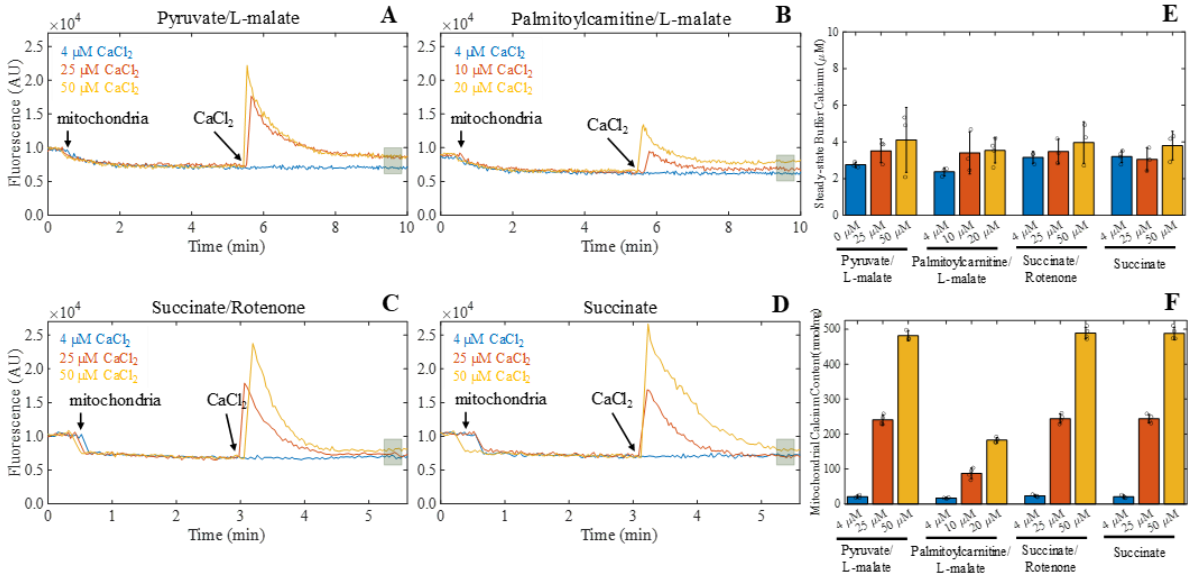


Figure 2.10 Buffer and steady-state matrix calcium. A-D) Representative fluorescence dynamics using CaGreen-5N. A) Pyruvate/L-malate (P/M). B) Palmitoylcarnitine/L-malate (PC/M). C) Succinate/Rotenone (S/R). D) Succinate (S). The steady-state buffer calcium levels in the low calcium bolus are similar to those delivered by the maximal calcium bolus. Mitochondria take up calcium from the maximal bolus without being permeabilized. The steady-state concentration of buffer calcium was quantified from the fluorescence signal averaged over shaded region where indicated. E) Steady-state buffer calcium 5 minutes (2.5 minutes for S and S/R) following calcium bolus injection was determined using Eq. 2.1. Regardless of the calcium bolus, the averaged steady-state buffer calcium concentration was approximately the same within a substrate and across substrate groups. F) Mitochondrial calcium content at the corresponding 5-minute mark (2.5 minutes for S and S/R) was determined by subtracting the remaining steady-state calcium concentration in the buffer from the initial calcium concentration plus the bolus addition. The total mitochondrial calcium content was calculated based on a mitochondrial concentration of 0.1 mg/ml. No statistical difference exists between P/M, S/R and S group. Comparisons cannot be made with the PC/M group since the calcium boluses deliver much lower calcium at 10 and 20 μM CaCl₂.

mitochondria and quantified with respect to the mitochondrial concentration in the assay conditions (Fig. 2.10F).

The effects of calcium on $J_{H_2O_2}$ over a range of $[O_2]$ were monitored at 5 minutes and 10 minutes (Fig. 2.11). There is a monotonic relationship between $J_{H_2O_2}$ and $[O_2]$, and calcium decreased the $J_{H_2O_2}$ at all $[O_2]$. At 5 minutes, no differences in $J_{H_2O_2}$ were observed whether the initial buffer calcium was 0 or 4 μM regardless of the substrates (Fig. 2.11A-C). At 10 minutes, the presence of as much as 4 μM Ca^{2+} resulted in a downward shift of the curves when P/M and PC/M were the substrates (Fig. 2.11D, E). The relationship between $J_{H_2O_2}$ and $[O_2]$ was preserved at 10 minutes when the substrates were S/R (Fig. 2.11F).

We next assessed the effects of electron turn-over on free radical homeostasis with P/M, PC/M and S/R. It has been argued that increased electron turn-over can increase the rate of superoxide formation. If true, there should be a non-zero correlation between $J_{H_2O_2}$ and J_{O_2} . However, we found that $J_{H_2O_2}$ and J_{O_2} are essentially independent as shown on Fig. 2.12. Data from Fig. 2.2 and 2.7 for the 0 and 4 μM calcium conditions were combined and plotted together as shown.

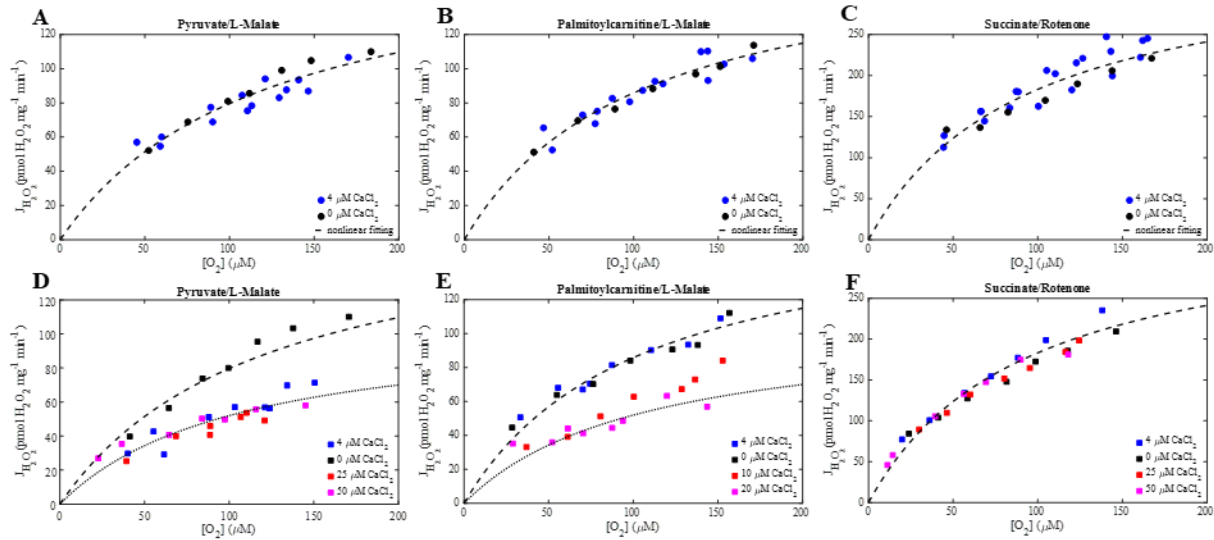


Figure 2.11 Hydrogen peroxide emission rates are dependent on oxygen concentration. A-C) Measurements taken at 5 minutes showed no differences in $J_{H_2O_2}$ between 0 and 4 μM CaCl_2 . The best-fit lines were produced using nonlinear coefficients assuming the empirical model of steady-state $J_{H_2O_2}$ where $J_{H_2O_2} = V_{\max} [O_2] / (K_m + [O_2])$. D-F) Measurements taken at 10 minutes showed substrate-dependent effects of calcium on $J_{H_2O_2}$ over a range of $[O_2]$. The presence of $\text{CaCl}_2 \geq 4 \mu\text{M}$ (for P/M) or $\text{CaCl}_2 \geq 10 \mu\text{M}$ (PC/M) depresses $J_{H_2O_2}$; however, calcium does not affect $J_{H_2O_2}$ for S/R. The same values of V_{\max} and K_m from the fitting procedure at 5 minutes were used to construct the best-fit line at 10 minutes when calcium does not affect the curves. The V_{\max} values are 175.7 (P/M), 174.1 (PC/M) and 353.1 (S/R). The K_m values are 120.7 (P/M), 102.8 (PC/M) and 92.8 (S/R). When present, the effect of calcium on the nonlinearity relationship was accounted for by redetermining V_{\max} and K_m . The V_{\max} values are 107.1 (P/M), 137 (PC/M) and 353.1 (S/R). K_m values are 106 (P/M), 102.5 (PC/M) and 92.8 (S/R).

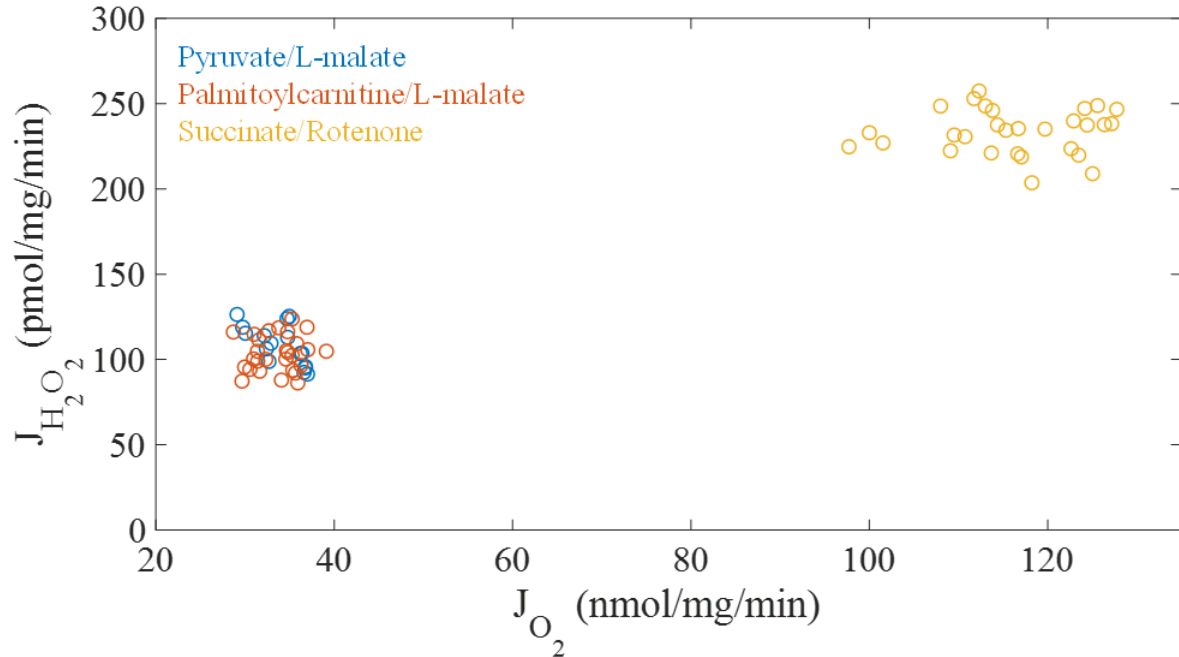


Figure 2.12 Hydrogen peroxide emission rate is independent of oxygen consumption rate. The slopes of $J_{H_2O_2}$ versus J_{O_2} are -2.8227 (-4.715, -0.9299) for P/M, 0.3428 (-1.276, 1.962) for PC/M and 0.0736 (-0.5598, 0.707) for S/R. The y-intercepts are 204.1453 (139.7, 268.6) for P/M, 92.0105 (37.45, 146.6) for PC/M and 69.6132 (151.4, 298.9) for S/R. Values in parenthesis represent 95 % confidence intervals. These slopes indicate negligible dependency, if any, between $J_{H_2O_2}$ and J_{O_2} . Filled circles represent individual data points. Colors are for different substrates: blue for P/M, red for PC/M and yellow for S/R.

DISCUSSION

Mitochondrial respiration depends on the fuel source

Overall, these data confirm that the absolute J_{O_2} rates are dependent on the fuel sources. Succinate in the presence or absence of rotenone results in the greatest J_{O_2} for leak and Na^+/Ca^{2+} cycling states. As a Q-linked substrate, succinate donates electrons to the ETS at complex II and bypass complex I. Electrons from pyruvate enter the ETS at complex I via NADH. Under our experimental conditions, pyruvate is not fully metabolized, so the number of electrons entering complex II is low [25,26]. Those from palmitoylcarnitine enter the ETS at both complex I and II. Since complex I is an energy-conserving site by the virtue of its proton pumping activity, a loss of protons per pair of electrons is inevitable when electrons enter the ETS downstream of complex I. Therefore, the maintenance of the membrane potential when mitochondria respiring on Q-linked substrates (succinate \pm rotenone in this study) results in an increased electron turn-over (reflected as J_{O_2}) to maintain the membrane potential. Moreover, since complex II does not pump protons and complexes III and IV are capable of supporting a higher membrane potential than complex I, higher membrane potentials and thus leak rates are maintained with substrates that bypass complex I.

While the primary Q-linked substrates yield the highest leak- and Na^+/Ca^{2+} cycling J_{O_2} , they had the lowest oxphos J_{O_2} rates compared to the primary NADH-linked substrate P/M. This is most likely due to the accumulation of inhibitory levels of oxaloacetate (OAA) and succinate transport limitations. OAA is a potent inhibitor of complex II [32]. It has a high binding affinity for complex II ($K_d \sim 10^{-8}$ M), and the OAA-CII complex has a slow rate of dissociation ($k_{off} \sim 10^{-2}$ min⁻¹) [33]. Under physiological TCA cycle turnover conditions, OAA is converted to either

citrate or aspartate. The former reaction requires acetyl-coA from pyruvate or fatty acids, and the latter requires glutamate. Because neither acetyl-coA nor glutamate is added in the succinate-supported groups, inhibitory levels of OAA accumulate in the matrix. The relatively low activity of the dicarboxylate carrier has also been demonstrated as another limiting factor on the maximum respiratory capacity of succinate fueled mitochondria [1]. Therefore, succinate cannot support high oxphos-state respiration rates compared to P/M.

Leak-state J_{O_2} is essentially identical whether the substrate is PC/M or P/M. During Na^+/Ca^{2+} cycling state, J_{O_2} is smaller when PC/M is the substrate. Respiration was essentially not affected by calcium up to 10 μM $CaCl_2$ bolus. Beyond this level respiration was compromised (Figs. 2.1B and 2.2B). From a bioenergetic perspective, palmitoylcarnitine yields significantly more reducing equivalents per molecule compared to pyruvate. Each pyruvate completely going through the TCA cycle as acetyl-coA yields 3 NADH and 1 QH_2 . A palmitoylcarnitine molecule is completely oxidized after 8 cycles of β -oxidation, each of which yields 4 NADH and 2 QH_2 per acetyl-CoA. Therefore, the complete turn-over of a palmitoylcarnitine yields a total of 32 NADH and 16 QH_2 molecules. Three consequences result from this higher yield of reducing equivalents by PC. First, a slower oxidation rate of PC is sufficient to maintain the membrane potential. Second, excess reducing equivalents not utilized by the ETS can inhibit β -oxidation enzymes [34]. Third, substrate competition among β -oxidation enzymes leads to accumulation of acyl-CoA intermediates [35]. These culminate in a plausible mechanism explaining the data shown in Figs. 2.1 and 2.2 that calcium above 4 μM inhibits complex I-supported respiration, leading to higher levels of NADH and lower PC/M-dependent respiration. It is also possible that uncoupling by fatty acid contributes to the lower PC/M dependent respiration. As uncoupling

enables more fatty acids to enter the matrix, it leads to greater amounts of acyl-CoA intermediates that impedes β -oxidation enzymes. The uncoupling nature of fatty acids is distinct from uncoupling mediated by the ATP/ADP nucleotide translocase and has been extensively studied [36–44]. On the other hand, whether calcium directly regulates β -oxidation enzymes remains unknown. Thus, it is a potential mechanism that can also explain our data.

While calcium addition dissipates membrane potential and results in enhanced respiration, increasing calcium concentrations inhibits respiration during oxphos (Fig. 2.2). The inhibition by calcium is also substrate-dependent. When the substrate was P/M, respiratory depression was observed at calcium levels above 4 μ M. With PC/M and S, respiration during oxphos was depressed in the presence of as much as 4 μ M CaCl_2 . Interestingly, when respiration was supported by S/R, the depressive effect of calcium on respiration was not seen. To validate the potential inhibitory effect of calcium on the ETS downstream of complex I, we measured J_{O_2} in the presence of 1 μ M FCCP. We found that FCCP slightly depressed the maximum succinate-supported J_{O_2} in the presence of 25 and 50 μ M CaCl_2 compared to control (0 μ M CaCl_2). However, when mitochondria respired on P/M, adding FCCP to the calcium-loaded mitochondria completely abolished oxygen consumption rates. These results support a prior study which found that high calcium primarily inhibits complex I-dependent respiration and minimally affects downstream ETS components [24].

Oxaloacetate accumulation depresses maximal succinate-supported respiration

Current evidence suggests that OAA accumulation is responsible for the discrepancies in oxphos J_{O_2} between S and S/R groups after ADP addition. In the absence of rotenone, a higher level of OAA accumulates and inhibits complex II [32]. This causes a decrease in respiration as

shown in Figs. 2.1D and 2.2D. In this condition, complex I maintains a low NADH/NAD⁺ ratio and facilitates even more OAA accumulation with the assumption that malate dehydrogenase is near equilibrium. Lowering OAA levels, therefore, by adding acetyl-CoA or glutamate will relieve this inhibitory effect of OAA on oxphos J_{O2} of the S group. In a similar fashion, with rotenone present, complex I is inhibited and higher NADH levels necessarily decrease OAA levels via malate dehydrogenase reaction near equilibrium. The key reactions leading to these results are given in a pathway diagram in the Appendix (Fig. S2.8). This effect of rotenone on NADH levels in mitochondria respiring on succinate has been previously shown by Aldakkak et al. [45] Our data show that glutamate addition led to a significant respiratory increase at each calcium concentration (Fig. 2.3). A similar result has also been recently reported by Fink et al. [46] For the lower calcium boluses, the increase in respiration can be explained by a combination of NADH production by glutamate metabolism in addition to a decrease in the OAA concentration. However, at the highest calcium bolus, the contribution to respiration by glutamate metabolism is essential zero as shown in Fig. S2.7. Specifically, there is an approximately 96% drop in respiration on glutamate between the 0 and 50 μM calcium bolus. In absolute terms, this is a change from ~ 362 to ~ 15 nmol mg⁻¹ min⁻¹. However, there is only a 11 % drop in respiration in the S/G group between the 0 and 50 μM calcium bolus, or in absolute terms, a change from ~ 578 to ~ 470 nmol mg⁻¹ min⁻¹. Therefore, glutamate does not contribute to complex I activity in this calcium condition. This leaves only the decrease OAA concentration as the viable mechanism that can explain the significant increase respiration rates after glutamate addition.

Respiratory changes are driven by membrane potential

While the calcium concentrations in this study are in the ischemic range, they are above the range that stimulates maximal metabolism and below those triggering mitochondrial permeability transition (Figs. 2.1, 2.2, 2.5 and 2.6). At low mitochondrial micromolar concentrations, calcium is a known activator of FAD-glycerolphosphate dehydrogenase, pyruvate dehydrogenase phosphatase, isocitrate dehydrogenase and α -ketoglutarate dehydrogenase [47]. Given the mitochondrial concentration of 0.1 mg/mL in the respiratory chambers, the calcium per mitochondria in this study was well above the saturating levels [48]. In addition, after bulk calcium uptake by the mitochondria, the steady-state buffer free calcium is in the 3-4 μ M range when the calcium added is less than or equal to 50 μ M (Fig. 2.10). Therefore, the respiratory increase in the presence of calcium above 4 μ M is not due to the stimulatory effect of calcium on matrix dehydrogenases. The increase in respiration induced by calcium addition is rather a membrane potential driven process. As calcium entering and leaving the matrix in a steady-state fashion dissipates membrane potential, mitochondria turn over more oxygen to re-establish the membrane potential. This results in an increase of the respiratory rates following calcium addition. The addition of ADP further drops the membrane potential and stimulates respiration. These results are consistent with classic bioenergetic principles.

Increased calcium concentrations do not increase ROS emission rates

Our results using isolated cardiac mitochondria show that increasing calcium concentrations either does not affect or has an inhibitory effect on $J_{H_2O_2}$. Our observation is consistent with those reported by several other groups [49,50]. However, there are studies

suggesting that calcium enhances ROS generation [9,22,51]. Therefore, it is important to be aware that the effects of calcium on ROS homeostasis are still highly debatable as many lines of opposing evidence exist. Discrepancies are likely to arise from differences in experimental designs including tissue choice, developmental stage, treatment and detection system. For example, the calcium concentrations employed in our study are in a similar range to those in Starkov et al. and Komary et al. [49,50]. Our results are consistent with these studies. However, in one study where calcium is suggested to enhanced ROS, the calcium concentrations used are much higher ranging between 300 and 500 μM CaCl_2 [51]. As our study demonstrate that these calcium levels permeabilize mitochondria, the net ROS increase in these studies is likely due to the scavenging system being compromised and/or the release of non-neutralized matrix ROS. Another difference is that mitochondria in the calcium-enhanced ROS experiment are de-energized while ours, as well as those in Starkov et al. and Komary et al. are energized with different substrates [49,50]. That experimental design can influence results; therefore, interpretations must be made within the context of the experiment. It is also necessary to be mindful of what can and cannot be generalized from the results. Our study does not perturb the mitochondrial metabolic network with inhibitors or supraphysiological concentrations of calcium. Thus, it serves a solid foundation from which to build from regarding the complex relationship between calcium and mitochondrial ROS homeostasis.

Net hydrogen peroxide emission rates are driven by membrane potential

During leak state, membrane potentials and net hydrogen peroxide emission rates are maximal across substrates (Figs. 2.7-9). Calcium addition partially depolarizes membrane potential and slightly decreases $J_{\text{H}_2\text{O}_2}$. During oxidative phosphorylation, the membrane

potential was further decreased, followed by a corresponding decrease in $J_{H_2O_2}$. Data from the S and S/R groups clearly demonstrate the causal effect of membrane potential on $J_{H_2O_2}$. When succinate was the substrate, calcium overload dissipates membrane potential by a smaller degree compared to P/M and PC/M groups. Therefore, the $J_{H_2O_2}$ levels are higher and consistent with this observation. During oxidative phosphorylation, all substrate groups have similar membrane potential. As a result, the $J_{H_2O_2}$ are similar.

A definitive conclusion cannot be reached that calcium decreases ROS production since the AmpUR assay detects the net ROS emission. However, it is very likely that calcium lowers ROS production by decreasing membrane potential. The membrane potential dependence of net ROS production was first appreciated by Skulachev [52] and subsequently demonstrated by independent works by Liu [53] and Korshunov et al. [54]. Liu showed this relationship in state 4 respiration by titrating malonate (0-5 mM) to succinate-respiring mitochondria from rat heart. In addition to malonate titration, Korshunov and colleagues manipulated membrane potential by adding ADP + P_i or SF6847 to rat heart mitochondria pre-treated with H_2O_2 to deplete antioxidants. Several independent studies performed in later years also yield results that support this concept [55–58]. Our group has reached the same conclusion by titrating different calcium boluses and triggering oxidative phosphorylation to alter membrane potential. We found that the membrane potential dependence of ROS homeostasis is also true in mitochondria not depleted of antioxidants and irrespective of the substrate sources. Therefore, our study serves as another independent line of evidence that supports the monotonic relationship between net ROS homeostasis and the membrane potential component of the protonmotive force.

Electron flux does not appreciably influence hydrogen peroxide emission rates

As electrons derived from succinate bypass complex I, increased electron turn-over downstream of complex I is necessary to maintain the membrane potential. Because H_2O_2 is formed by a redox reaction between O_2 and a redox center, increased electron turnover has been linked to proportional increase in $J_{\text{H}_2\text{O}_2}$. However, when $J_{\text{H}_2\text{O}_2}$ is plotted against J_{O_2} , the slopes are essentially zero (Fig. 2.12). Therefore, our results suggest that $[\text{O}_2]$ is a more influential determinant in the net hydrogen peroxide formation in healthy mitochondria.

Hydrogen peroxide emission rates are non-linearly dependent on oxygen concentration

The hydrogen peroxide emission rate is a non-linear function of $[\text{O}_2]$ regardless of the substrates (Fig. 2.10). The nonlinear relationship between $J_{\text{H}_2\text{O}_2}$ and $[\text{O}_2]$ has been previously reported [59,60]. However, $J_{\text{H}_2\text{O}_2}$ reaches the maximum values at higher O_2 concentrations in our study. The contribution of our study is that we also determined how calcium affects this relationship. We further proposed an empirical model to relate the effects of oxygen, substrate and calcium on free radical homeostasis. Specifically, our empirical model relates the fluorescence of resorufin to the steady-state matrix hydrogen peroxide (Fig. 2.13).

Mathematical derivation of steady-state matrix hydrogen peroxide further relates the free radical production, elimination and transportation processes together. This derivation is described below.

Because AmpUR and HrP/SOD are used in excess amounts, hydrogen peroxide emitted by mitochondria is immediately converted to resorufin. Therefore, the change in resorufin concentration detected fluorometrically corresponds directly to rate of hydrogen peroxide emission (Eq. 2.2).

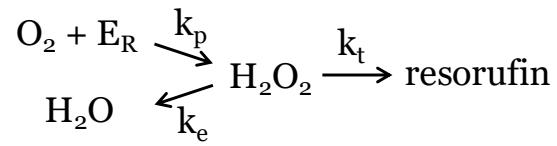


Figure 2.13 Schematic of resorufin formation. The schematic relates the resorufin formation to hydrogen peroxide production, elimination, and transportation. The term E_R represents mitochondrial sites available for oxygen reduction. The terms k_p , k_e , and k_t are described in the text.

$$\frac{d[\text{resorufin}]}{dt} = - \left(\frac{d[\text{H}_2\text{O}_2]}{dt} \right) \text{buffer} \quad \text{Eq. 2.2}$$

Buffer hydrogen peroxide is proportional to the level of matrix hydrogen peroxide ($[\text{H}_2\text{O}_2]_m$) and the rate of hydrogen peroxide transport (k_t) across the mitochondrial membranes (Eq. 2.3).

$$\left(\frac{d[\text{H}_2\text{O}_2]}{dt} \right) \text{buffer} = k_t [\text{H}_2\text{O}_2]_{\text{matrix}} \quad \text{Eq. 2.3}$$

In turn, the steady-state matrix hydrogen peroxide concentration is dependent on the total capacity of electron donors (E_R) and three primary processes including hydrogen peroxide production, elimination and transport across the mitochondrial membranes (Eq. 2.4). The rates of these individual factors are denoted k_p , k_e and k_t , respectively.

$$[\text{H}_2\text{O}_2]_{\text{matrix}} = \frac{E_R [\text{O}_2]}{\frac{k_e + k_t}{k_p} + [\text{O}_2]} \quad \text{Eq. 2.4}$$

The scavenging system comprises of the Mn-SOD, peroxiredoxin (Prx) and glutathione peroxidase (GPX). However, because hydrogen peroxide is the ROS species detected using the HrP assay (as opposed to superoxide), the Mn-SOD reaction becomes part of the production rather than elimination processes. The rate of hydrogen peroxide production (k_p) is dependent on the superoxide concentration (substrate), which in turn is dependent on the $[\text{O}_2]$ and the redox state of an electron donor. Although not explicitly described by Eq. 2.4, the redox state of an electron donor is dependent on respiratory states and therefore the membrane potential. For the sake of clarity, the reduction potential of the electron donor refers to its tendency to be reduced. Given this definition, a donor's reduction potential is most positive during oxphos, most negative during leak state and somewhere in between during $\text{Na}^+/\text{Ca}^{2+}$ cycling state. Therefore, the hydrogen peroxide production rates are expected to be lowest during oxphos,

highest during leak state and somewhere in between during $\text{Na}^+/\text{Ca}^{2+}$ cycling state. And this is exactly what our data show.

The empirical model resembles the Michaelis-Menten relationship. Here, the apparent V_{max} is the product of total enzyme reducing capacity (E_R) and the rate of H_2O_2 transportation across the mitochondrial membranes (k_t). The term K_m is the ratio of the sum of hydrogen peroxide elimination and transport over the production rates (k_e , k_t and k_p , respectively). The rate of hydrogen peroxide transport across the mitochondrial membranes has been determined to approximate that of water [61,62], so it is likely that different V_{max} values are determined by E_R . As different substrates produce different number of reducing equivalents that donate electrons to the ETS at various points, the total capacity reducing sites is substrate dependent. Our experimental data suggest that E_R is highest with Q-linked substrate (succinate \pm rotenone) and comparable between NADH-linked and mixed substrates. Assuming that k_t is independent of substrates and calcium, K_m relates k_p to k_e terms. Our data suggest that free radical elimination (k_e) is unable to balance free radical production (k_p) when the substrate is Q-linked, which results in a smaller K_m for this substrate. However, an additional equation is necessary to quantitatively determine k_p and k_e . It is known that ROS production and elimination are both modulated by the mitochondrial matrix NADH/NAD^+ poise although they appear as opposing factors in determining net ROS [63,64]. This concept is recapitulated as Redox Optimized ROS Balance wherein mitochondria ROS emission is minimized when the organelles operate somewhere between the extremities of complete oxidation and reduction [63]. The unique aspect of the measurements shown in Fig. 2.11 is that they lead to an empirical model enabling insight into processes upstream of the final fluorescence measurements using the AmpUR

assay. To our best knowledge, we are also the first to comprehensively investigate the effect of calcium on this Michaelis-Menten like relationship between $J_{H_2O_2}$ and $[O_2]$.

Strengths and Limitations of Study

Our primary goal of this study was to comprehensively determine how substrates and calcium affect mitochondrial respiration and net ROS production rates in healthy mitochondria. As such, we performed experiments using mitochondria isolated from the ventricular cardiomyocytes of guinea pigs in the absence of injury or disease. Among rodents, guinea pigs are the animals to use in studies related to human cardiovascular diseases. The cardiomyocyte of guinea pigs shares many similarities with that of humans compared to rats and mice. Some of the most important features are the plateau phase of action potential [65], calcium handling [66–70], purine nucleotide metabolism [71], complement IF1 [72,73] and expression of the β -myosin heavy chain isoform [69,74]. Therefore, our results will be particularly useful as a reference for future studies of cardiovascular diseases in human that use guinea pigs as the animal model.

To delineate the capacity of mitochondrial calcium handling, we utilized calcium boluses in the ischemic range but do not trigger irreversible mitochondrial permeability transition. Using a healthy model, various substrates and sub-permeability transition calcium levels enables us to define the full capacity of mitochondria in neutralizing ROS. We demonstrate that mitochondria not only are capable of taking up a large amount of calcium but do so in a substrate-dependent manner. Specifically, mitochondria respiring on PC/M have a significantly lower ability to take up calcium. We also provide evidence to support that high calcium inhibits the ETS primarily at complex I. In addition to characterizing how ROS homeostasis and

respiratory dynamics response to calcium, our study serves as an additional, independent line of evidence that net ROS production depends on membrane potential. In this study, membrane potential is altered as calcium enters the mitochondrial matrix and ADP stimulates oxidative phosphorylation. In the other studies, membrane potential was manipulated by adding different amounts of inhibitors or malonate. That we used a different system and approach to alter the membrane potential yet arrive at the same conclusion irrefutably supports this relationship.

Finally, we contribute an empirical model that relates oxygen, substrates, and calcium to the fluorescence measurement. To our best knowledge, previous studies attempting to link upstream processes to the net hydrogen peroxide measurement did not cover the range of calcium. However, in developing the empirical model, we realized that a more detailed, sophisticated model is necessary to further determine not only the relative contribution of individual ROS producers and scavengers but also how they operate under these conditions. In fact, the precise mechanism responsible for mitochondrial free radical homeostasis in the healthy state remains an important standing scientific question. In studies that utilize the AmpUR assay such as ours, H_2O_2 is used as a surrogate for $\text{O}_2^{\bullet-}$. While the longer half-life of H_2O_2 improves reproducibility for quantitative measurements, it is important to note that the fluorescence obtained is a net measurement. Thus, the measurement itself is not informative of H_2O_2 formation or H_2O_2 elimination, only the net production of H_2O_2 . As such, the contributions of individual mitochondrial enzyme that produce or consume ROS cannot be determined using this approach. Traditionally, site-specific inhibitors are used to quantify site-specific ROS production with the underlying assumption that the use of inhibitors does not alter the redox

state of mitochondria (at least not to an appreciable degree). However, it is well-known that inhibiting electron flow causes the upstream sites to be more reduced and the downstream to be more oxidized. Therefore, when the mitochondrial redox state is perturbed, interpretation of data calls for certain degree of precaution. And while it is tempting to speculate on the origins of free radicals from these data, a computational model that is comprehensive and biophysically detailed is needed to pinpoint the specific sites and their relative contribution to total ROS emission rates.

SUMMARY

The data show that mitochondrial respiration and hydrogen peroxide emission rates are dependent on substrates and calcium treatments which can be readily understood from the bioenergetic perspective. Seemingly contradictory data such as the maximal J_{O_2} of mitochondria respiring on S/R and S being lower than that of P/M are consistent with OAA inhibition and substrate transport limitations. We also demonstrated that calcium does not enhance net ROS emission in healthy cardiac mitochondria. We further showed that net ROS emission is strongly dependent on membrane potential, which is consistent with results from several previously reported studies. In addition, our data on the calcium sensitivity of PC/M supported metabolism helps explain the heart is more susceptible to IR injury when fatty acids are the sole substrate [75].

One theme we consistently encountered during our analysis is how to study individual variables that affect mitochondrial respiration and ROS emission without disturbing the mitochondrial redox landscape. In studying free radical production, using inhibitors to block certain sites of the ETS is a common approach aimed to dissect site-specific contributions to the net pool of free radical produced. While a wealth of invaluable information has been accumulated using this approach, using inhibitors inevitably induces systemic alterations to the mitochondrial redox landscape. The extent of deviation cannot be quantified since the native state is unknown. Moreover, data interpretation from many site-specific inhibitor experiments assumes a linear relationship among variables, but this relationship cannot be verified. To our knowledge, site-specific contributions to free radical production and elimination in the absence of inhibitors remain elusive. Thus, the quest for the native redox state of a system cannot be

experimentally accomplished with available technologies. With the results of this study, our goal is to use the insights of the empirical model to develop a more detailed computational model that can explain data from this study and other studies.

APPENDIX

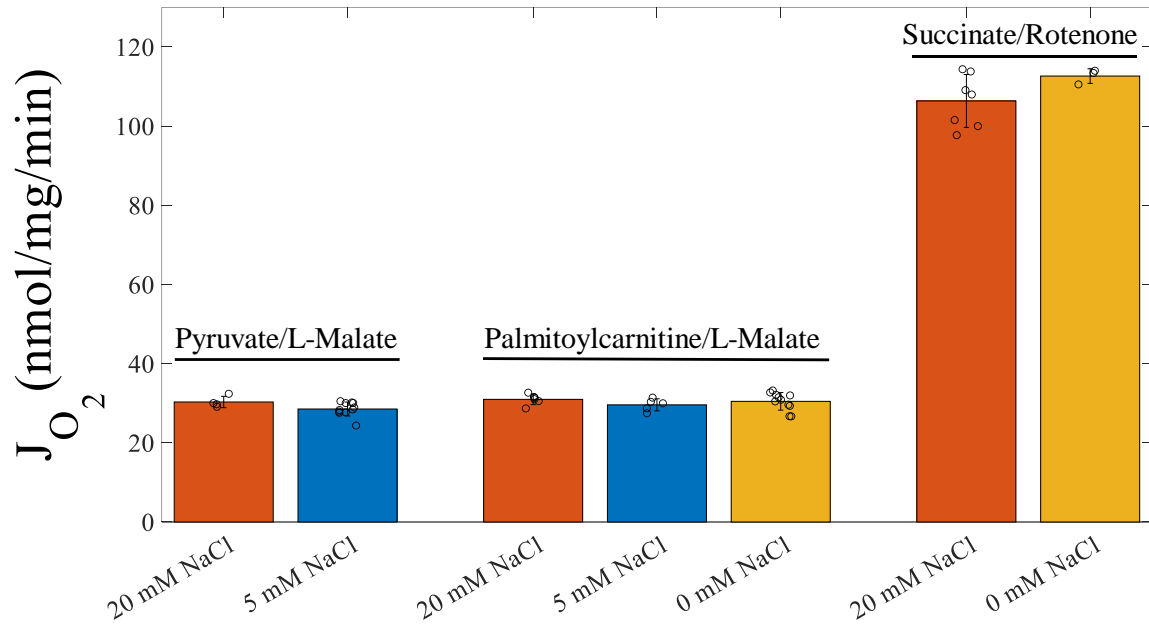


Figure S2.1 Effects of buffer sodium on leak-state oxygen consumption rates (J_{O_2}). At a given total buffer calcium, buffer sodium does not affect leak-state J_{O_2} irrespective of the substrate. The experiments were performed in similar fashion to that outlined under the experimental section. Bar colors represent sodium concentrations: yellow, 0 mM; blue 5 mM; red, 20 mM.

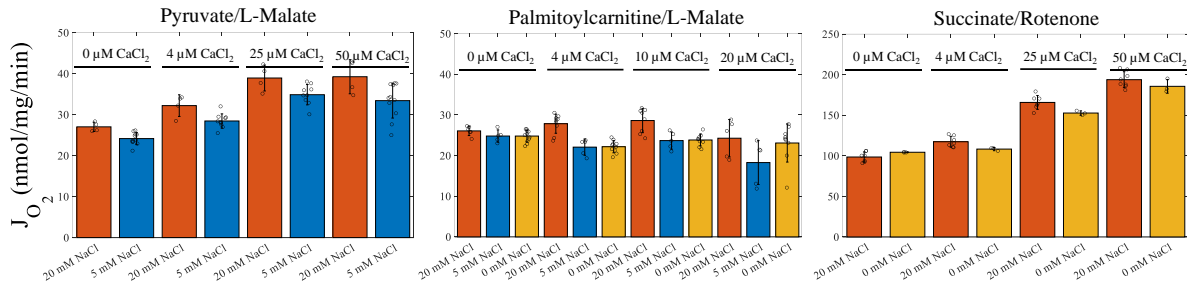


Figure S2.2 Effects of buffer sodium on sodium/calcium cycling oxygen consumption rates (J_{O_2}). At a given total buffer calcium, buffer sodium does not affect sodium/calcium cycling J_{O_2} irrespective of the substrate. The stimulatory effect of calcium is consistent at different buffer sodium concentrations. The experiments were performed in similar fashion to that outlined under the experimental section. Bar colors represent sodium concentrations: yellow, 0 mM; blue 5 mM; red, 20 mM.

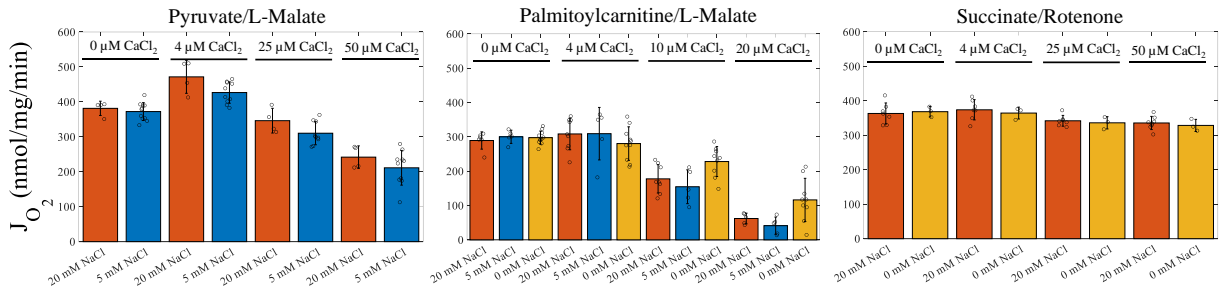


Figure S2.3 Effects of buffer sodium on oxphos-state net oxygen consumption rates (J_{O_2}). At a given total buffer calcium, buffer sodium does not affect oxphos-state J_{O_2} irrespective of the substrate. The inhibitory effect of calcium on respiration is consistent at different buffer sodium concentrations. The experiments were performed in similar fashion to that outlined under the experimental section. Bar colors represent sodium concentrations: yellow, 0 mM; blue 5 mM; red, 20 mM.

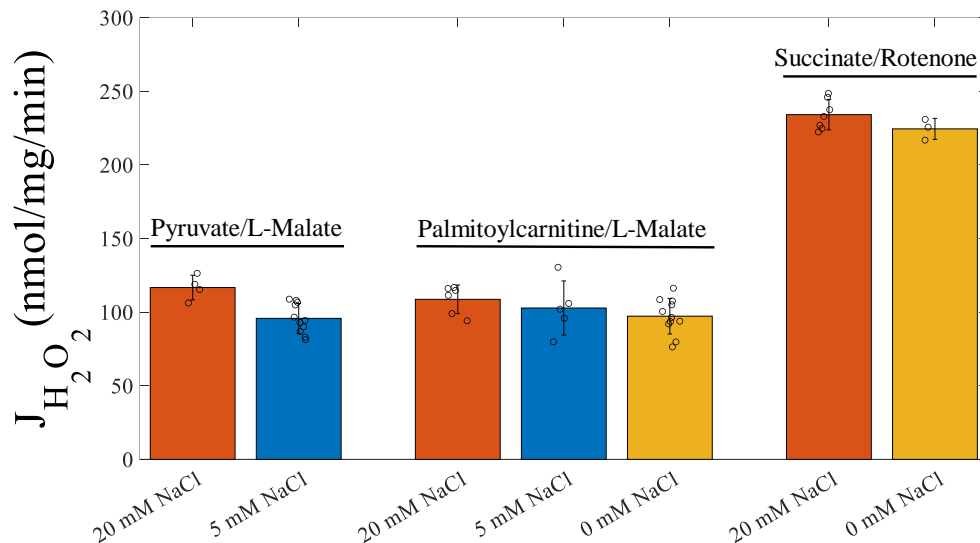


Figure S2.4 Effects of buffer sodium on leak-state net hydrogen peroxide emission rates ($J_{H_2O_2}$). At a given total buffer calcium, buffer sodium does not affect leak-state $J_{H_2O_2}$ irrespective of the substrate. The calcium dependence of ROS is consistent at different buffer sodium concentrations. The experiments were performed in similar fashion to that outlined under the experimental section. Bar colors represent sodium concentrations: yellow, 0 mM; blue 5 mM; red, 20 mM.

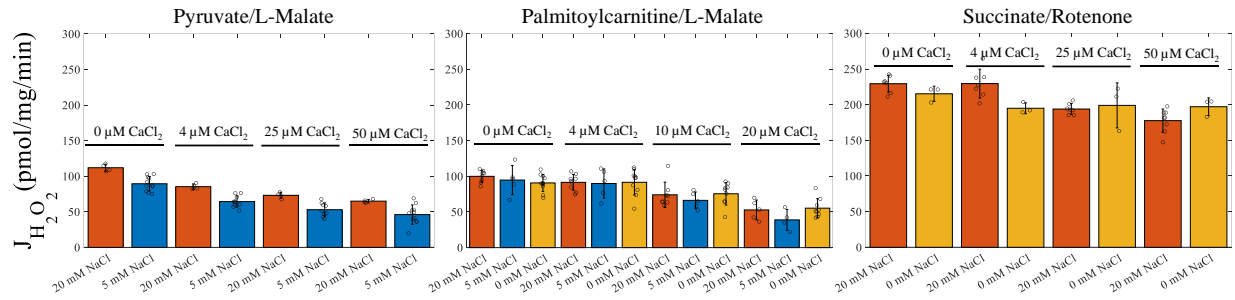


Figure S2.5 Effects of buffer sodium on sodium/calcium cycling net hydrogen peroxide emission rates ($J_{H_2O_2}$). At a given total buffer calcium, buffer sodium does not affect sodium/calcium cycling $J_{H_2O_2}$ irrespective of the substrate. The calcium dependence of ROS is consistent at different buffer sodium concentrations. The experiments were performed in similar fashion to that outlined under the experimental section. Bar colors represent sodium concentrations: yellow, 0 mM; blue 5 mM; red, 20 mM.

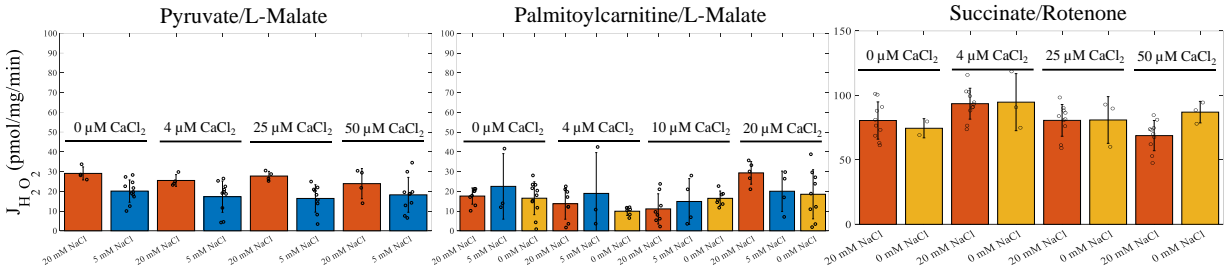


Figure S2.6 Effects of buffer sodium on oxphos-state net hydrogen peroxide emission rates ($J_{H_2O_2}$). At a given total buffer calcium, buffer sodium does not affect oxphos-state $J_{H_2O_2}$ irrespective of the substrate. The calcium dependence of ROS is consistent at different buffer sodium concentrations. The experiments were performed in similar fashion to that outlined under the experimental section. Bar colors represent sodium concentrations: yellow, 0 mM; blue 5 mM; red, 20 mM.

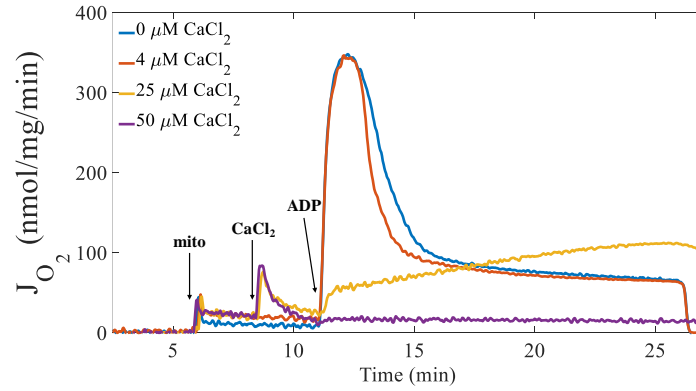


Figure S2.7 Glutamate-dependent respiration is significantly inhibited by calcium. Glutamate-supported oxygen consumption rates (J_{O_2}) were measured in a similar experimental course as described in Fig. 2.1. The glutamate concentration used was 5 mM. The oxphos-state oxygen consumption rate in the presence of 50 μM CaCl_2 was negligible.

Table S2.1 Comprehensive table of statistical results from Table 2.1. Highlighted values are statistically significant for oxygen consumption rates.

Substrates	Group A	Group B	p values		
			Leak	Sodium/Calcium Cycling	Oxidative Phosphorylation
Pyruvate/ L-malate	25 μ M CaCl ₂	50 CaCl ₂	N/A	9.99E-01	5.14E-03
	25 μ M CaCl ₂	0 μ M CaCl ₂	N/A	5.38E-04	4.88E-01
	25 μ M CaCl ₂	4 μ M CaCl ₂	N/A	3.39E-02	1.26E-03
	50 μ M CaCl ₂	0 μ M CaCl ₂	N/A	4.26E-04	4.69E-04
	50 μ M CaCl ₂	4 μ M CaCl ₂	N/A	2.60E-02	3.69E-06
	0 μ M CaCl ₂	4 μ M CaCl ₂	2.00E-04	1.19E-01	1.52E-02
Palmitoyl carnitine/L- malate	10 μ M CaCl ₂	20 CaCl ₂	N/A	4.82E-02	7.18E-06
	10 μ M CaCl ₂	0 μ M CaCl ₂	N/A	3.21E-01	5.96E-09
	10 μ M CaCl ₂	4 μ M CaCl ₂	N/A	9.37E-01	1.61E-07
	20 μ M CaCl ₂	0 μ M CaCl ₂	N/A	6.14E-01	3.77E-09
	20 μ M CaCl ₂	4 μ M CaCl ₂	N/A	1.20E-01	3.78E-09
	0 μ M CaCl ₂	4 μ M CaCl ₂	9.00E-04	6.22E-01	1.52E-01
Succinate/ Rotenone	25 μ M CaCl ₂	50 CaCl ₂	N/A	2.77E-06	9.57E-01
	25 μ M CaCl ₂	0 μ M CaCl ₂	N/A	3.78E-09	3.80E-01
	25 μ M CaCl ₂	4 μ M CaCl ₂	N/A	3.95E-09	9.31E-02
	50 μ M CaCl ₂	0 μ M CaCl ₂	N/A	3.78E-09	1.53E-01
	50 μ M CaCl ₂	4 μ M CaCl ₂	N/A	3.78E-09	2.64E-02
	0 μ M CaCl ₂	4 μ M CaCl ₂	4.02E-05	1.03E-03	8.45E-01
Succinate	25 μ M CaCl ₂	50 CaCl ₂	N/A	1.20E-05	6.67E-01
	25 μ M CaCl ₂	0 μ M CaCl ₂	N/A	4.29E-09	2.02E-04
	25 μ M CaCl ₂	4 μ M CaCl ₂	N/A	6.84E-08	9.99E-03
	50 μ M CaCl ₂	0 μ M CaCl ₂	N/A	3.99E-09	2.44E-05
	50 μ M CaCl ₂	4 μ M CaCl ₂	N/A	4.02E-09	9.78E-04
	0 μ M CaCl ₂	4 μ M CaCl ₂	2.04E-05	1.31E-03	2.47E-01

Table S2.2 The inhibitory effect of oxaloacetate on complex II can be relieved by adding glutamate. Values are oxygen consumption rates (nmol/mg/min) of mitochondria (0.1 mg/ mL) respiring on a QH₂-linked substrate in FET (S/R) and RET (S) at varied calcium levels.

Succinate/ Rotenone	0 μM CaCl₂		4 μM CaCl₂		25 μM CaCl₂		50 μM CaCl₂	
Calcium	0 mM Glu	5 mM Glu	0 mM Glu	5 mM Glu	0 mM Glu	5 mM Glu	0 mM Glu	5 mM Glu
Mean	354.1	335.1	361.4	349.3	324.9	317.5	314.3	310.6
STD	26.0	26.9	29.7	33.0	27.4	25.0	10.6	10.7
Succinate	Leak		4 μM CaCl₂		25 μM CaCl₂		50 μM CaCl₂	
Calcium	0 mM Glu	5 mM Glu	0 mM Glu	5 mM Glu	0 mM Glu	5 mM Glu	0 mM Glu	5 mM Glu
Mean	259.1	578.3	200.4	646.0	156.5	556.4	163.4	469.7
STD	37.8	54.2	42.2	73.4	48.5	37.6	56.9	16.1

Table S2.3 Calcium affects the ETC at complex I. The oxygen consumption rates of mitochondria (0.1 mg/mL) respiring on NADH- or QH₂-linked substrate in FET (P/M and S/R, respectively) following FCCP addition (1 μM) at varied calcium levels.

Pyruvate/L-malate	J_{o2} (nmol/mg/min)		
Calcium	0 μM CaCl ₂	25 μM CaCl ₂	50 μM CaCl ₂
Mean	784.9415	11.9066	8.616
STD	99.9191	2.0211	1.8943
Succinate/Rotenone	J_{o2} (nmol/mg/min)		
Calcium	0 μM CaCl ₂	25 μM CaCl ₂	50 μM CaCl ₂
Mean	754.7921	667.3908	630.9106
STD	20.5412	37.1524	18.4627

Table S2.4 Irreversible mPT does not occur in our experimental conditions. Values are absorbance at 540 nm, a standard way to assess mitochondria swelling.

Substrates	Pyruvate/L-malate		Palmitoylcarnitine/ L-malate			Succinate/ Rotenone		Succinate	
Calcium (μM)	50	150	10	20	100	50	500	50	500
Mean	101.8	91.4	98.3	98.3	89.4	100.3	90.2	102.1	90.0
STD	2.2	1.2	1.0	1.9	1.6	0.8	2.6	0.9	0.4

Table S2.5 Comprehensive table of statistical values for net hydrogen peroxide emission rates. Highlighted values are statistically significant.

Substrates	Group A [CaCl ₂]	Group B [CaCl ₂]	p values		
			Leak	Sodium/Calcium Cycling	Oxidative Phosphorylation
Pyruvate/ L-malate	25	50	N/A	5.55E-02	9.43E-01
	25	0	N/A	5.93E-08	9.75E-01
	25	4	N/A	4.74E-03	6.42E-01
	50	0	N/A	1.13E-08	7.68E-01
	50	4	N/A	5.36E-05	9.17E-01
	0	4	1.01E-01	3.44E-06	4.09E-01
Palmitoylcarnitine / L-malate	10	20	N/A	2.56E-02	5.08E-02
	10	0	N/A	8.83E-03	9.44E-01
	10	4	N/A	2.25E-01	8.41E-01
	20	0	N/A	1.74E-05	1.47E-01
	20	4	N/A	5.63E-04	1.66E-02
	0	4	2.29E-01	5.29E-01	5.68E-01
Succinate/ Rotenone	25	50	N/A	1.72E-01	1.21E-01
	25	0	N/A	7.65E-04	8.70E-01
	25	4	N/A	7.29E-04	6.34E-03
	50	0	N/A	2.52E-06	2.26E-02
	50	4	N/A	2.40E-06	1.34E-05
	0	4	9.20E-01	1.00E+00	3.79E-02
Succinate	25	50	N/A	5.07E-01	9.84E-01
	25	0	N/A	8.69E-01	1.00E+00
	25	4	N/A	3.80E-01	9.93E-01
	50	0	N/A	1.70E-01	9.72E-01
	50	4	N/A	3.34E-02	9.22E-01
	0	4	2.00E-04	8.12E-01	9.97E-01

Table S2.6 Mitochondria were able to maintain membrane potential at the maximal experimental calcium conditions. Relative membrane potential (%) were obtained using the fluorescent dye TMRM.

Pyruvate/L-malate	Leak		Sodium/Calcium Cycling			Oxphos		
CaCl ₂ (μM)	EGTA	No EGTA	0	50	150	0	50	150
Mean	90.0	90.9	86.1	57.1	3.0	61.5	37.6	4.6
STD	6.7	4.7	4.1	9.4	2.1	8.7	8.5	1.6
Palmitoylcarnitine/L-malate	Leak		Sodium/Calcium Cycling			Oxphos		
CaCl ₂ (μM)	EGTA	No EGTA	0	20	100	0	20	100
Mean	94.8	94.3	86.9	36.4	0.4	31.4	12.2	0.7
STD	3.4	3.5	6.2	19.3	0.6	2.0	6.2	2.3
Succinate/Rotenone	Leak		Sodium/Calcium Cycling			Oxphos		
CaCl ₂ (μM)	EGTA	No EGTA	0	50	500	0	50	500
Mean	93.7	93.5	91.9	82.1	1.8	34.0	53.8	6.6
STD	5.8	5.4	4.6	6.4	1.5	2.7	5.3	1.7
Succinate	Leak		Sodium/Calcium Cycling			Oxphos		
CaCl ₂ (μM)	EGTA	No EGTA	0	50	500	0	50	500
Mean	90.4	88.9	97.7	79.2	4.0	33.1	44.8	6.6
STD	3.4	4.2	7.4	4.2	3.6	2.5	8.2	3.1

REFERENCES

REFERENCES

- 1 Martin, J.L. *et al.* (2019) Mitochondrial mechanisms and therapeutics in ischaemia reperfusion injury. *Pediatr Nephrol* 34, 1167–1174
- 2 Kalogeris, T. *et al.* (2012) Chapter Six - Cell Biology of Ischemia/Reperfusion Injury. In *International Review of Cell and Molecular Biology* 298 (Jeon, K. W., ed), pp. 229–317, Academic Press
- 3 Kalogeris, T. *et al.* (2016) Ischemia/Reperfusion. In *Comprehensive Physiology* pp. 113–170, American Cancer Society
- 4 Griffiths, E.J. and Halestrap, A.P. (1995) Mitochondrial non-specific pores remain closed during cardiac ischaemia, but open upon reperfusion. *Biochemical Journal* 307, 93–98
- 5 Baines, C.P. (2009) The mitochondrial permeability transition pore and ischemia-reperfusion injury. *Basic Res Cardiol* 104, 181–188
- 6 Bernardi, P. *et al.* (2015) The Mitochondrial Permeability Transition Pore: Channel Formation by F-ATP Synthase, Integration in Signal Transduction, and Role in Pathophysiology. *Physiological Reviews* 95, 1111–1155
- 7 Steenbergen, C. *et al.* (2009) Cardioprotection and altered mitochondrial adenine nucleotide transport. *Basic Res Cardiol* 104, 149–156
- 8 Brookes, P.S. *et al.* (2004) Calcium, ATP, and ROS: A mitochondrial love-hate triangle. *American Journal of Physiology - Cell Physiology* 287, C817–C833
- 9 Görlach, A. *et al.* (2015) Calcium and ROS: A mutual interplay. *Redox Biology* 6, 260–271
- 10 Hansson, M.J. *et al.* (2008) Calcium-induced generation of reactive oxygen species in brain mitochondria is mediated by permeability transition. *Free Radical Biology and Medicine* 45, 284–294
- 11 Tretter, L. and Adam-Vizi, V. (2012) High Ca²⁺ load promotes Hydrogen peroxide generation via activation of α -glycerophosphate dehydrogenase in brain mitochondria. *Free Radical Biology and Medicine* 53, 2119–2130
- 12 Cadenas, E. and Davies, K.J.A. (2000) Mitochondrial free radical generation, oxidative stress, and aging
This article is dedicated to the memory of our dear friend, colleague, and mentor Lars Ernster (1920–1998), in gratitude for all he gave to us. *Free Radical Biology and Medicine* 29, 222–230

- 13 Murphy, M.P. (2008) How mitochondria produce reactive oxygen species. *Biochemical Journal* 417, 1–13
- 14 Chen, Q. *et al.* (2003) Production of Reactive Oxygen Species by Mitochondria: CENTRAL ROLE OF COMPLEX III*. *Journal of Biological Chemistry* 278, 36027–36031
- 15 Lambert, A.J. and Brand, M.D. (2004) Inhibitors of the Quinone-binding Site Allow Rapid Superoxide Production from Mitochondrial NADH:Ubiquinone Oxidoreductase (Complex I)*. *Journal of Biological Chemistry* 279, 39414–39420
- 16 Starkov, A.A. *et al.* (2004) Mitochondrial α -ketoglutarate dehydrogenase complex generates reactive oxygen species. *Journal of Neuroscience* 24, 7779–7788
- 17 Quinlan, C.L. *et al.* (2012) Mitochondrial Complex II Can Generate Reactive Oxygen Species at High Rates in Both the Forward and Reverse Reactions*. *Journal of Biological Chemistry* 287, 27255–27264
- 18 Goncalves, R.L.S. *et al.* (2015) Sites of Superoxide and Hydrogen Peroxide Production by Muscle Mitochondria Assessed ex Vivo under Conditions Mimicking Rest and Exercise*. *Journal of Biological Chemistry* 290, 209–227
- 19 Starkov, A.A. and Fiskum, G. (2001) Myxothiazol Induces H₂O₂ Production from Mitochondrial Respiratory Chain. *Biochemical and Biophysical Research Communications* 281, 645–650
- 20 Andreyev, A.Y. *et al.* (2015) Mitochondrial ROS metabolism: 10 Years later. *Biochemistry (Moscow)* 80, 517–531
- 21 Tretter, L. and Adam-Vizi, V. (2004) Generation of reactive oxygen species in the reaction catalyzed by α -ketoglutarate dehydrogenase. *Journal of Neuroscience* 24, 7771–7778
- 22 Feissner, R.F. *et al.* (2009) Crosstalk signaling between mitochondrial Ca²⁺ and ROS. *Front Biosci* 14, 1197–1218
- 23 Wollenman, L.C. *et al.* (2017) The effect of respiration buffer composition on mitochondrial metabolism and function. *PLOS ONE* 12, e0187523
- 24 Malyala, S. *et al.* (2019) Calcium phosphate precipitation inhibits mitochondrial energy metabolism. *PLoS Comput Biol* 15, e1006719
- 25 LaNoue, K.F. *et al.* (1972) Feedback Interactions in the Control of Citric Acid Cycle Activity in Rat Heart Mitochondria. *Journal of Biological Chemistry* 247, 667–679
- 26 LaNoue, K. *et al.* (1970) Control of Citric Acid Cycle Activity in Rat Heart Mitochondria. *Journal of Biological Chemistry* 245, 102–111

- 27 Faul, F. *et al.* (2007) G*Power 3: A flexible statistical power analysis program for the social, behavioral, and biomedical sciences. *Behavior Research Methods* 39, 175–191
- 28 Faul, F. *et al.* (2009) Statistical power analyses using G*Power 3.1: Tests for correlation and regression analyses. *Behavior Research Methods* 41, 1149–1160
- 29 Petronilli, V. *et al.* (1993) Physiological effectors modify voltage sensing by the cyclosporin A-sensitive permeability transition pore of mitochondria. *Journal of Biological Chemistry* 268, 21939–21945
- 30 Nicholls, D.G. and Chalmers, S. (2004) The Integration of Mitochondrial Calcium Transport and Storage. *J Bioenerg Biomembr* 36, 277–281
- 31 Bazil, J.N. *et al.* (2013) Modeling the calcium sequestration system in isolated guinea pig cardiac mitochondria. *J Bioenerg Biomembr* 45, 177–188
- 32 Siebels, I. and Dröse, S. (2013) Q-site inhibitor induced ROS production of mitochondrial complex II is attenuated by TCA cycle dicarboxylates. *Biochimica et Biophysica Acta (BBA) - Bioenergetics* 1827, 1156–1164
- 33 Vinogradov, A.D. *et al.* (1989) Regulation of succinate dehydrogenase and tautomerization of oxaloacetate. *Advances in Enzyme Regulation* 28, 271–280
- 34 Lopaschuk, G.D. *et al.* (2010) Myocardial Fatty Acid Metabolism in Health and Disease. *Physiological Reviews* 90, 207–258
- 35 Martines, A.-C.M.F. *et al.* (2017) The promiscuous enzyme medium-chain 3-keto-acyl-CoA thiolase triggers a vicious cycle in fatty-acid beta-oxidation. *PLoS Comput Biol* 13, e1005461
- 36 Bertholet, A.M. and Kirichok, Y. (2018) The Mechanism FA-Dependent H⁺ Transport by UCP1. In *Brown Adipose Tissue* 251 (Pfeifer, A. *et al.*, eds), pp. 143–159, Springer International Publishing
- 37 Busiello, R.A. *et al.* (2015) Mitochondrial uncoupling proteins and energy metabolism. *Front. Physiol.* 6,
- 38 Andreyev, A.Y. *et al.* (1989) The ATP/ADP-antiporter is involved in the uncoupling effect of fatty acids on mitochondria. *European Journal of Biochemistry* 182, 585–592
- 39 Dedukhova, V.I. *et al.* (1991) Uncoupling effect of fatty acids on heart muscle mitochondria and submitochondrial particles. *FEBS Letters* 295, 51–54
- 40 Simonyan, R.A. and Skulachev, V.P. (1998) Thermoregulatory uncoupling in heart muscle mitochondria: involvement of the ATP/ADP antiporter and uncoupling protein. *FEBS Letters* 436, 81–84

- 41 Skulachev, V.P. (1991) Fatty acid circuit as a physiological mechanism of uncoupling of oxidative phosphorylation. *FEBS Letters* 294, 158–162
- 42 Cortassa, S. *et al.* (2017) Mitochondrial respiration and ROS emission during β -oxidation in the heart: An experimental-computational study. *PLoS Comput Biol* 13, e1005588
- 43 Borst, P. *et al.* (1962) Uncoupling activity of long-chain fatty acids. *Biochimica et Biophysica Acta* 62, 509–518
- 44 Brand, M.D. *et al.* (2005) The basal proton conductance of mitochondria depends on adenine nucleotide translocase content. *Biochemical Journal* 392, 353–362
- 45 Aldakkak, M. *et al.* (2013) Mitochondrial handling of excess Ca^{2+} is substrate-dependent with implications for reactive oxygen species generation. *Free Radical Biology and Medicine* 56, 193–203
- 46 Fink, B.D. *et al.* (2018) Oxaloacetic acid mediates ADP-dependent inhibition of mitochondrial complex II-driven respiration. *Journal of Biological Chemistry* 293, 19932–19941
- 47 Denton, R.M. (2009) Regulation of mitochondrial dehydrogenases by calcium ions. *Biochimica et Biophysica Acta (BBA) - Bioenergetics* 1787, 1309–1316
- 48 Wan, B. *et al.* (1989) Regulation of Citric Acid Cycle by Calcium. *Journal of Biological Chemistry* 264, 13430–13439
- 49 Komary, Z. *et al.* (2008) H_2O_2 generation is decreased by calcium in isolated brain mitochondria. *Biochimica et Biophysica Acta (BBA) - Bioenergetics* 1777, 800–807
- 50 Starkov, A.A. *et al.* (2002) Regulation of hydrogen peroxide production by brain mitochondria by calcium and Ba^{2+} . *Journal of Neurochemistry* 83, 220–228
- 51 Castilho, R.F. *et al.* (1995) Permeabilization of the inner mitochondrial membrane by Ca^{2+} ions is stimulated by t-butyl hydroperoxide and mediated by reactive oxygen species generated by mitochondria. *Free Radical Biology and Medicine* 18, 479–486
- 52 Skulachev, V.P. (1996) Role of uncoupled and non-coupled oxidations in maintenance of safely low levels of oxygen and its one-electron reductants. *Quarterly Reviews of Biophysics* 29, 169–202
- 53 Liu, S. (1997) Generating, Partitioning, Targeting and Functioning of Superoxide in Mitochondria. *Bioscience Reports* 17, 259–272
- 54 Korshunov, S.S. *et al.* (1997) High protonic potential actuates a mechanism of production of reactive oxygen species in mitochondria. *FEBS Letters* 416, 15–18

- 55 Panov, A. *et al.* (2007) Species- and tissue-specific relationships between mitochondrial permeability transition and generation of ROS in brain and liver mitochondria of rats and mice. *American Journal of Physiology-Cell Physiology* 292, C708–C718
- 56 Votyakova, T.V. and Reynolds, I.J. (2001) $\Delta\Psi_m$ -Dependent and -independent production of reactive oxygen species by rat brain mitochondria. *Journal of Neurochemistry* 79, 266–277
- 57 Rottenberg, H. *et al.* (2009) Membrane Potential Greatly Enhances Superoxide Generation by the Cytochrome bc₁ Complex Reconstituted into Phospholipid Vesicles*. *Journal of Biological Chemistry* 284, 19203–19210
- 58 Korshunov, S.S. *et al.* (1998) Fatty acids as natural uncouplers preventing generation of O[•]-₂ and H₂O₂ by mitochondria in the resting state. *FEBS Letters* 435, 215–218
- 59 Hoffman, D.L. and Brookes, P.S. (2009) Oxygen Sensitivity of Mitochondrial Reactive Oxygen Species Generation Depends on Metabolic Conditions. *Journal of Biological Chemistry* 284, 16236–16245
- 60 Robb, E.L. *et al.* (2018) Control of mitochondrial superoxide production by reverse electron transport at complex I. *Journal of Biological Chemistry* 293, 9869–9879
- 61 Bienert, G.P. *et al.* (2006) Membrane transport of hydrogen peroxide. *Biochimica et Biophysica Acta (BBA) - Biomembranes* 1758, 994–1003
- 62 Bienert, G.P. and Chaumont, F. (2014) Aquaporin-facilitated transmembrane diffusion of hydrogen peroxide. *Biochimica et Biophysica Acta (BBA) - General Subjects* 1840, 1596–1604
- 63 Aon, M.A. *et al.* (2010) Redox-optimized ROS balance: A unifying hypothesis. *Biochimica et Biophysica Acta (BBA) - Bioenergetics* 1797, 865–877
- 64 Nickel, A. *et al.* (2014) Mitochondrial reactive oxygen species production and elimination. *Journal of Molecular and Cellular Cardiology* 73, 26–33
- 65 Watanabe, T. *et al.* (1985) Ventricular action potentials, ventricular extracellular potentials, and the ECG of guinea pig. *Circ Res* 57, 362–373
- 66 Bers, D.M. (2002) Cardiac excitation–contraction coupling. 415, 8
- 67 Pieske, B. *et al.* (1999) Ca²⁺ Handling and Sarcoplasmic Reticulum Ca²⁺ Content in Isolated Failing and Nonfailing Human Myocardium. *Circulation Research* 85, 38–46
- 68 Kiss, E. *et al.* (1995) Differential Changes in Cardiac Phospholamban and Sarcoplasmic Reticular Ca²⁺-ATPase Protein Levels. *Circulation Research* 77, 759–764

- 69 Malhotra, A. *et al.* (1992) Cardiac contractile proteins in hypertrophied and failing guinea pig heart. *Cardiovascular Research* 26, 153–161
- 70 Siri, F.M. *et al.* (1989) Compensatory hypertrophy and failure in gradual pressure-overloaded guinea pig heart. *American Journal of Physiology-Heart and Circulatory Physiology* 257, H1016–H1024
- 71 De Jong, J.W. *et al.* (1991) Does xanthine oxidase cause damage during myocardial ischemia? *Bratisl Lek Listy* 92, 41–47
- 72 Rouslin, W. *et al.* (1995) Content and binding characteristics of the mitochondrial ATPase inhibitor, IF1 in the tissues of several slow and fast heart-rate homeothermic species and in two poikilotherms. *J Bioenerg Biomembr* 27, 117–125
- 73 Rouslin, W. and Broge, C.W. (1993) Factors Affecting the Species-Homologous and Species-Heterologous Binding of Mitochondrial ATPase Inhibitor, IF1, to the Mitochondrial ATPase of Slow and Fast Heart-Rate Hearts. *Archives of Biochemistry and Biophysics* 303, 443–450
- 74 Clark, W.A. *et al.* (1982) Species correlations between cardiac isomyosins. A comparison of electrophoretic and immunological properties. *Journal of Biological Chemistry* 257, 5449–5454
- 75 Ferrari, R. *et al.*, eds. (1984) *Myocardial Ischemia and Lipid Metabolism*, Springer US.

**CHAPTER 3 – COMPUTATIONALLY MODELING MAMMALIAN SUCCINATE DEHYDROGENASE
KINETICS IDENTIFIES THE ORIGINS AND PRIMARY DETERMINANTS OF ROS PRODUCTION**

This chapter was adapted from the following previously published manuscript (* denotes equal contribution):

Manhas, N. *, Duong, Q.V. *, Lee, P., Richardson, J.D., Robertson, J.D., Moxley, M.A., and Bazil,

J.N. (2020) Analysis of mammalian succinate dehydrogenase kinetics and reactive oxygen species production. *J Biol Chem* 295, 15262-15279.

INTRODUCTION

Succinate dehydrogenase (SDH) is a heterotetrametric protein attached to the mitochondrial inner membrane of eukaryotes and many bacteria. It is both a Krebs cycle enzyme and a member of the mitochondrial electron transport system (ETS) [1,2]. Similar to other ETS members, SDH houses several major redox centers. The flavoprotein subunit SDHA contains a flavin adenine dinucleotide (FAD) covalently bound to one of the active sites. The SDHB subunit contains three iron-sulfur clusters: [2Fe-2S], [4Fe-4S], [3Fe-4S] (ISCs). In mammals, subunits C and D (SDHC and SDHD) contain a single transmembrane cytochrome *b heme* [3,4]. These subunits along with the interface of SDHB form the ubiquinone (Q) binding site (Q site) [4,5]. SDH couples the oxidation of succinate to fumarate with the reduction of Q to ubiquinol (QH₂). The oxidation of each succinate molecule provides two electrons that fully reduce the flavin (FAD to FADH₂). Electrons are subsequently shuttled through the ISCs one at a time. The first electron is transferred to the [2Fe-2S] iron-sulfur center from FADH₂, producing a flavin radical (FADH[•]). When the [2Fe-2S] ISC becomes oxidized by downstream redox centers, the flavin radical passes the second electron to this ISC and becomes fully oxidized (FAD). Similarly, consecutive one-electron transfers from the ISCs to the Q reductase site reduce Q to QH₂. As a part of this process, a stable semiquinone (SQ) is formed [4,6,7]. The overall catalytic reaction is given by Eq. 3.1.



In mammalian mitochondria, 11 sites including SDH are known to produce reactive oxygen species (ROS) [8,9]. In this paper, ROS refers to superoxide (O₂^{•-}) or hydrogen peroxide

(H₂O₂) and will be explicitly defined where needed for clarity. ROS were historically considered toxic and inevitable byproducts of aerobic respiration [10]. However, it is now appreciated that in the physiological setting, ROS act as important and beneficial signaling molecules [11–13]. That said, toxic levels of ROS do contribute to a milieu of pathological processes [14–19]. Complex III is commonly argued as the dominant source of ROS under resting conditions, while complex I is attributed as the primary source of ROS under many pathological conditions including ischemia/reperfusion (I/R) injury. However, the role of complex II is less certain [20].

The most common implication of SDH in disease is its role in creating the environment favorable for excessive ROS production in I/R injury. Specifically, SDH reverses during ischemia due to excess fumarate produced by purine nucleotide breakdown [15]. Succinate accumulation occurs because complex I continues forward electron transport, regenerating QH₂ needed to sustain the reverse reaction of complex II [21]. In this setting, succinate replaces oxygen as the final electron acceptor. Succinate accumulates in the surrounding tissue until either fumarate is exhausted or reperfusion begins. During reperfusion, SDH metabolizes the available succinate to produce QH₂, leading to hyper-reduction of the Q pool and hyperpolarization of the inner mitochondrial membrane [21]. The combination of a highly reduced Q pool and a hyperpolarized membrane potential drives complex I to enter the so-called reverse electron transport (RET) state. In the RET state, complex I produces ROS at extremely high rates [21,22]. Note that it is more accurate to describe complex I during RET as entering a near equilibrium state [14,21,23]. In this state, the redox centers on complex I are maintained in a highly reduced state which can lead to the generation of significant amounts of free radicals. As late reperfusion transitions to normoxia, fluxes through the ETS and TCA return

to normal and ROS levels subside [15,16]. Therefore, in the current paradigm, the primary role of SDH in I/R injury induced oxidative stress is by creating environmental factors that favor ROS production.

Recent studies have shown that SDH may significantly contribute to total mitochondrial ROS production under a variety of physiological and pathological settings [13,17,24–28]. For instance, when complexes I and III are inhibited and the succinate concentration is low (~100 μ M), SDH produces ROS at high rates relative to complexes I and III [24,29]. In addition, skeletal muscle mitochondria respiring on succinate have been shown to produce high rates of ROS [30]. Moreover, ROS from SDH has been recently shown to play key roles in promoting the pro-inflammatory phenotype in macrophages [27] and differentiation of helper T cells [28]. Mutations that alter ROS production by SDH have also been implicated in some cancers [31–33]. These new lines of evidence inevitably raise the question that SDH plays a more deterministic role in health and disease than previously thought. They also suggest the enzyme is an overlooked target in developing therapies that target mitochondrial oxidative stress.

The renewed interest in SDH as a therapeutic target in mitigating mitochondrial oxidative stress necessitates a precise mechanistic understanding of how ROS is produced by the enzyme. Unfortunately, experimental studies on the origin of ROS production by SDH are inconclusive. In one study, the flavin site of SDH was reported to produce comparable amounts of ROS as the quinone binding site of complex I in mitochondria respiring on fatty acid substrates [34]. In a different study, Quinlan et al. demonstrated that, in mitochondria isolated from rat skeletal muscle respiring on succinate, the flavin site of SDH produces the most ROS at low levels of succinate or when QH₂ oxidation is inhibited [8,24]. In a corroborating study using

bovine sub-mitochondrial particles (SMP), Siebels and Drose showed that SDH generates ROS from the flavin site when its Q site is inhibited by atpenin [35]. However, Paraganama et al. argues that the Q site can produce comparable amount of ROS as the flavin site [36]. Evidence of an additional ROS production site, the ISC near the Q site, was recently put forth in a study by Grivennikova et al. [37]. While these studies all agree that the flavin site can generate a significant amount of ROS, they differ on the contribution by the Q site. Each study measured ROS production using the Amplex UltraRed assay in combination with site-specific inhibitors. [8,13,24,34–36,38]; however, this approach does not uniquely identify the mechanisms or precise conditions for ROS production by SDH. As such, the mechanisms of ROS production by SDH are an ongoing topic of debate.

Nevertheless, a unified mechanism may underlie the results from these different studies. To explore this possibility, computational modeling is an essential tool. With computational modeling, it is possible to parse the intricate interactions among the various components of a complex biological systems such as an enzyme. It also enables further insight into how these components work together and respond to environmental factors. Motivated to elucidate the precise mechanisms of ROS production by SDH under physiological [11] and pathological conditions [15], we herein developed a comprehensive computational model of SDH kinetics and ROS production. Adopting a similar approach to our previous studies [14,21,23], the model framework is based on fundamental laws of thermodynamics and involves a rigorous model calibration process. Specifically, the model parameters are adjusted until the model outputs, such as succinate oxidation rates or total ROS production, are

consistent with the experimental data. This iterative process results in a model that is not only thermodynamically consistent but also capable of reproducing the experimental data.

Our analysis of the model presented herein reveals that while the FAD site does produce ROS, the primary source is the [3Fe-4S] ISC under normal physiological conditions. However, the FAD site is the dominant site and produces significant levels of H₂O₂ when the Q reductase site of SDH is inhibited by atpenin or the respiratory chain downstream of SDH is blocked. Moreover, the model shows that the inhibitory effects of atpenin are not simply attributed to competitive binding at the Q site but also include allosteric effects that modulate the enzyme catalytic turnover. Lastly, the model can be integrated into large-scale models of metabolism and used to explore the role of SDH in bioenergetics and free radical homeostasis at the organelle, cell, and tissue levels.

MATERIALS AND METHODS

Model Construction

The modeling approach for this study is based on our prior work [14,23]. In brief, structural, thermodynamic, and kinetic data are used to constrain the model, and enzyme state-transitions are governed by the law of mass action. The model includes the redox biochemistry reactions that occur at the FAD, ISCs and Q sites. The FAD site contains the binding site for succinate and other dicarboxylates. While ubiquinone and its analogues can hypothetically bind to both the proximal and distal Q sites, quinone reduction has been shown to occur at the proximal Q site, Q_p site. The function of the distal Q site, Q_d site, is still unknown [4,39]. Reactions at these sites are assumed to be independent from each other (i.e., there are no long-distance conformational changes required for enzyme catalysis between the Q_p and the FAD sites). However, the Q_d site is assumed to exert some control over turnover at the FAD and proximal Q sites when atpenin or other molecules are bound to this site.

The enzyme kinetic model consists of five oxidation states which constitute the oxidation state of the entire enzyme. For example, all redox centers are oxidized in the E_0 state, at least one redox center is one-electron reduced in the E_1 state, and so on and so forth. A minimum of five oxidation states were necessary to fit the experimental data. Including more did not improve fits to the data. Transitions between oxidation states are governed by the Gibbs' free energies of the redox reactions involved. Two-electron reactions involve the succinate/fumarate (SUC/FUM), Q/QH₂ and O₂/H₂O₂ couples. One-electron reactions involve the O₂/O₂^{•-} couple. Binding of substrates, products and inhibitors at the FAD and Q sites is assumed to be faster than state transition rates. Forward state-transition rate constants are

estimated from experimental data while the reverse rate constants are calculated from the forward rates and equilibrium constants for the respective reaction. The equilibrium constants are computed from the midpoint potentials taken from the literature (Table S3.1) and adjusted to account for the effects of pH and temperature. The rates corresponding to these reactions are shown in the Appendix from Eqs. S3.78-S3.91. The transitions between each oxidation state is fully reversible and governed by the law of mass action.

Within each oxidation state, the enzyme complex can exist in various substates characterized by the combination of redox centers reduced or oxidized. Since electrons on the complex reorganize on very fast time scales ($< \mu\text{s}$) relative to turnover, we compute these substates using the Boltzmann distribution as shown in Eq. 3.2.

$$S_r^k = \frac{e^{-\Delta G_r^k / RT}}{\sum_r e^{-\Delta G_r^k / RT}} \quad \text{Eq. 3.2}$$

In Eq. 3.2, S_r^k is the fraction of redox centers r existing in the oxidation state k that is reduced, and ΔG_r^k are the free energy change for each redox center r calculated from the linear superposition of the midpoint potentials. The redox centers r can consist of a single redox center or any other combination of redox centers in the complex. To calculate the free energy change for the combination of redox center, the individual free energies for the redox center reactions are summed (i.e., they are independent from each other). The number of combinations of reduced redox centers for each state is given by the binomial coefficient where n is the number of redox centers and k is the number of electrons on the complex. For details on calculating substates, see Eqs. S3.45-S3.77 in the Appendix.

As mentioned above, substrates and products are assumed to bind/unbind much faster than transitions among oxidation states of the enzyme. It is assumed that binding events are independent of substates and that binding at the Q and FAD sites are independent of each other. When the enzyme is in the appropriate enzyme-substrate complex configuration, the appropriate redox reaction proceeds. Binding polynomials (BP) are used to give the fraction of the enzyme in a certain enzyme-substrate configuration. The BP for the Q_p-site (P_{Qp}) partitions this binding site into the unbound, Q-, QH₂- and atpenin-bound fractions. The expressions $1/P_{Qp}$, $[Q]/K_Q/P_{Qp}$, $[QH_2]/K_Q/P_{Qp}$ and $[atpenin]/K_A/P_{Qp}$, indicates the fractions of the total Q sites unbound or bound to ubiquinone, ubiquinol or atpenin, respectively. In a similar manner, the Q_d-site can be partitioned into free and bound states as well. The BP for the FAD site (P_{FAD}) partitions this binding site into the unbound, succinate-, fumarate-, malate-, malonate- and oxaloacetate-bound fractions. Similarly, the expressions $1/P_{FAD}$, $[succinate]/K_{SUC}/P_{FAD}$, $[fumarate]/K_{FUM}/P_{FAD}$, $[malate]/K_{MAL}/P_{FAD}$, $[malonate]/K_{MALO}/P_{FAD}$ and $[oxaloacetate]/K_{OAA}/P_{FAD}$ give the fractions of the total FAD sites bound to succinate, fumarate, malate, malonate and oxaloacetate, respectively. The BPs for the FAD- and Q-sites are given below.

Steady-state turnover of succinate oxidation and ROS production rates are calculated using the solution of the linear equations governing the oxidation state transitions as shown in Eq. S3.92 in the Appendix. The first five rows correspond to the permissible oxidation state transitions. The last row is used to set the steady-state solution to fractions of one (i.e., $\sum_i E_i = 1$; see the Appendix for further details). The Moore-Penrose pseudo inverse is then used to calculate the unique solution to the linear system of equations [40]. The edges connecting to the oxidation states shown in Fig. 3.1 (Results) represents the partial reactions that govern how

state i is connected to state j . These reactions rates, k_{ij} , represent molecular processes such as the reduction of FAD to FADH₂ by succinate, oxidation of FADH^{*} or FADH₂ by oxygen, and Q reduction at the Q site. The equations for the partial reactions are given in the Eqs. S3.78-S3.91 in the Appendix. Before the enzyme can transition between oxidation states, it must be in the appropriate enzyme-substrate complex configuration. For example, succinate oxidation can only occur when the FAD binding site is available for succinate to bind, and the FAD is fully oxidized. Binding polynomials (Eqs. 3.3-5) are used to calculate the fraction of succinate bound to the complex, and the Boltzmann distribution (Eq. 3.2) is used to calculate the fraction of the protein complex with a fully oxidized FAD within a given oxidation state. The net steady-state rate of succinate oxidation is then computed by summing over the oxidation state transition rates as shown in Eq. 3.6. Next, the net steady-state O₂^{*} production rate is computed by summing the net O₂^{*} production when the FADH^{*} or [3Fe-4S] react with oxygen as shown in Eq. 3.7. The steady-state H₂O₂ production rate is computed when the fully reduced flavin reacts with oxygen as given in Eq. 3.8. Lastly, the steady-state QH₂ production rate is given by Eq. 3.9. Because mass and energy conservation are strictly obeyed, phenazine and TMPD reduction rates are also computed using Eq. 3.9. For simplicity, we assume reduction of these exogenous electron acceptors occurs in rapid, sequential one-electron steps and lump them together as a two-electron reduction reaction.

$$P_{FAD} = 1 + \frac{[succinate]}{K_{SUC}} + \frac{[fumarate]}{K_{FUM}} + \frac{[malate]}{K_{MAL}} + \frac{[malonate]}{K_{MALO}} + \frac{[oxaloacetate]}{K_{OAA}} \quad \text{Eq. 3.3}$$

$$P_{Qp} = 1 + \frac{[QH_2]}{K_{QH_2}} + \frac{[Q]}{K_Q} + \frac{[atpenin]}{K_{Ap}} \quad \text{Eq. 3.4}$$

$$P_{Qd} = 1 + \frac{[atpenin]}{K_{Ad}} \quad \text{Eq. 3.5}$$

$$J_{SUC} = E_{tot} \left(k_{02}^{SUC/FAD} E_0 + k_{13}^{SUC/FAD} E_1 + k_{24}^{SUC/FAD} E_2 - k_{20}^{FUM/FADH_2} E_2 - k_{31}^{FUM/FADH_2} E_3 - k_{42}^{FUM/FADH_2} E_4 \right) \quad \text{Eq. 3.6}$$

$$J_{O_2^-} = E_{tot} \left(\begin{array}{l} k_{10}^{O_2/FADH} E_1 + k_{21}^{O_2/FADH} E_2 + k_{32}^{O_2/FADH} E_3 + k_{43}^{O_2/FADH} E_4 - k_{01}^{O_2^*/FAD} E_0 - k_{12}^{O_2^*/FAD} E_1 - k_{23}^{O_2^*/FAD} E_2 - k_{34}^{O_2^*/FAD} E_3 \\ + k_{10}^{O_2/3Fe-4S_{red}} E_1 + k_{21}^{O_2/3Fe-4S_{red}} E_2 + k_{32}^{O_2/3Fe-4S_{red}} E_3 + k_{43}^{O_2/3Fe-4S_{red}} E_4 - k_{01}^{O_2^*/3Fe-4S_{ox}} E_0 - k_{12}^{O_2^*/3Fe-4S_{ox}} E_1 \\ - k_{23}^{O_2^*/3Fe-4S_{ox}} E_2 - k_{34}^{O_2^*/3Fe-4S_{ox}} E_3 \end{array} \right) \quad \text{Eq. 3.7}$$

$$J_{H_2O_2} = E_{tot} \left(k_{20}^{O_2/FADH_2} E_2 + k_{31}^{O_2/FADH_2} E_3 + k_{42}^{O_2/FADH_2} E_4 - k_{02}^{FADH_2/FAD} E_0 - k_{13}^{FADH_2/FAD} E_1 - k_{24}^{FADH_2/FAD} E_2 \right) \quad \text{Eq. 3.8}$$

$$J_{QH_2} = J_{SUC} - J_{O_2^-} / 2 - J_{H_2O_2}, \quad \text{Eq. 3.9}$$

Experimental Data

The model was calibrated using a variety of literature data listed in Table 3.1. These data include succinate oxidation, Q reduction, $O_2^{\bullet-}$ and H_2O_2 production rates under different experimental conditions. The data set contains information about the kinetics and ROS production by SDH necessary to identify model parameters. Most of the kinetic data on succinate oxidation is from bovine heart mitochondria [41,42], and some are from pig heart mitochondria [43]. The ROS data set is from bovine heart mitochondria and includes both $O_2^{\bullet-}$ and H_2O_2 production rates [35,37]. We did not use data from Quinlan et al. as the reported data include an unknown contribution of the ROS scavenging system [24]. Both succinate oxidation and ROS data sets are obtained under a variety of experimental conditions including variations in enzyme concentrations, temperatures, pH, substrates concentrations and inhibitors concentrations. Experimental conditions are explicitly stated to simulate the experiments as faithfully as possible. However, the use of scaling factors is still necessary to account for experimental differences among the data sets such as species-dependent differences in enzyme

kinetics. Even so, the values are in the acceptable range of 0.5 to 5 showing only minor adjustments were needed to fit the data. Also, in some experiments, endogenous quinone was used as the electron acceptor without any information on the redox state of Q pool [35,37,42]. In order to simulate these data, we relied on monotonic functions of succinate and inhibitors to predict the Q pool redox state. These equations are given in the Appendix (Eqs. S3.1-S3.3).

Experimental Details

Animal care and handling conformed to the National Institutes of Health's Guide for the Care and Use of Laboratory Animals and was approved by Michigan State University's Institutional Animal Care and Use Committee. Mitochondria from Hartley guinea pig ventricular myocytes were isolated based on protocol previously described [22,44,45] and will be briefly summarized here. Animals (4-6 weeks, 350-450 grams) were decapitated after being anesthetized with 5% isoflurane and tested to be unresponsive to noxious stimuli. The heart was then immediately perfused with ice-cold cardioplegic solution until no blood was seen in the coronary arteries and cardiac veins. The cardioplegic solution consisted of 25 mM KCl, 100 mM NaCl, 10 mM dextrose, 25 mM MOPS and 1 mM EGTA at pH = 7.15. The heart was then excised and washed with ice-cold isolation buffer (IB). IB consisted of 200 mM mannitol, 50 mM sucrose, 5 mM K₂HPO₄ and 0.1% w/v BSA at pH = 7.15. Connective tissues, thymus and the great vessels were removed, and the ventricles were minced in ice-cold IB until small pieces of about 1 mm³ remained. The homogenate was then transferred to a 50-mL conical tube containing 0.5 U/mL protease (*Bacillus licheniformis*) in 25 mL IB. Tissue homogenization was done using an Omni handheld homogenizer at 18,000 rpm for 20 sec. Mitochondria were obtained using gradient centrifugation in IB at 4 °C. Mitochondrial protein was quantified using

the BCA assay and an Olis DM-245 spectrofluorometer with dual-beam absorbance module. The mitochondria were then subjected to three freeze-thaw cycles at -80 °C and stored at -80 °C until use. The net H₂O₂ production rate was monitored using the Amplex UltraRed assay on the Olis DM-245 spectrofluorometer with dual-beam absorbance module. Amplex UltraRed (AmpUR) (excitation 560 nm, emission 590 nm) was dissolved to a stock concentration of 10 mM and stored according to the manufacturer's instructions. Type II horseradish peroxidase (HrP) and superoxide dismutase (SOD) were individually dissolved to the stock concentrations of 500 U/mL and stored at the appropriate temperatures. Myxothiazol and rotenone stock concentrations are 2 mM and 1 mM, respectively. The buffer (pH 7.2) contained 120 mM KCl, 5 mM HEPES, 1 mM EGTA and 0.3% w/v bovine serum albumin. Hydrogen peroxide calibration curves were made using a working solution of 200 μM H₂O₂ prepared fresh on the day of every experiment.

Fluorescence was monitored after mitochondria and inhibitors had been added to the buffer. After 2 minutes, succinate was added to the desired final concentrations. In the succinate titration experiments, the final concentrations are 50, 100, 200, 300, 500, 1000, 3000 and 5000 μM succinate. The rate of ROS production was measured after SDH was fully activated and the rate became linear as previously shown [37]. In the DQ titration experiments, succinate concentrations were either 200 μM or 5 mM. After 10 minutes, DQ was added to the final concentrations of 12.5, 25, 50, 75, 100, 150 and 200 μM. The final concentrations are 10 μM Amplex UltraRed, 1 unit/mL HrP, 10 units/ mL SOD, 4 μM rotenone, 2 μM myxothiazol and 0.1 mg/mL mitochondria. Following DQ additions, signal was monitored for at least 10 minutes. At

least 3 replicates were performed at each condition, and all experiments were performed at 37 °C.

Model Simulations

The model was numerically simulated using MATLAB (R2019a). The parameter optimization was performed on a Dell desktop PC (64-bit operating system and x64-based processor Intel® core™ i7-7700 CPU @3.60GHz and 16 GB RAM) using the Parallel Computing Toolbox. A parallelized simulated annealing algorithm was first used to globally search for feasible parameters which were then refined using a local, gradient-based optimization algorithm. The analytic solutions for the state-steady oxidation states were obtained with the MATLAB symbolic toolbox. When the standard deviation for data were not given, a standard deviation of 10% of the max value in a given data set was used during parameter estimation.

RESULTS

Details on model construction are given in the Methods section and briefly summarized here. A brief overview of the model development, fitting, and corroboration procedure is given in Fig. S3.1. The model is constructed based on structural, thermodynamic and kinetic data relevant to the enzyme (Fig. 3.1A). Each partial reaction used for model construction is shown in Fig. 3.1B. Succinate oxidation presents a major route of entry for electrons in the SDH complex. Electrons entering the FAD site, however, can be blocked by other non-SDH dicarboxylate substrates that are present in the mitochondrial matrix including malonate, malate and oxaloacetate. In addition, oxaloacetate causes the enzyme to enter an inactive state [46]. Quinol oxidation at the Q_p site is another way by which SDH is reduced. This manner of reduction can be inhibited by atpenins, potent competitive inhibitors of quinone binding at the Q_p site. Of the atpenins, atpenin A5 is the most specific and referred to in this study as atpenin for simplicity. Other inhibitors acting upstream or downstream of SDH can also influence the enzyme's oxidation state. Some of the most common inhibitors used in experimental settings include myxothiazol, stigmatellin and rotenone. Myxothiazol and stigmatellin inhibit electron flow downstream while rotenone inhibits electron flow upstream of the enzyme complex.

Under normal conditions, succinate oxidation is coupled to quinone reduction and mediated by one- or two-electron reactions (Fig. 3.1B). As these reactions occur, the enzyme transitions among different oxidation states (E_i) at specific rates (k_{ij}) determined by substrate/product concentrations and environmental conditions. Once electrons enter the complex, they rapidly equilibrate to the lowest energy state determined by the redox center midpoint potentials (Fig. 3.1C). However, when redox centers on SDH capable of interacting

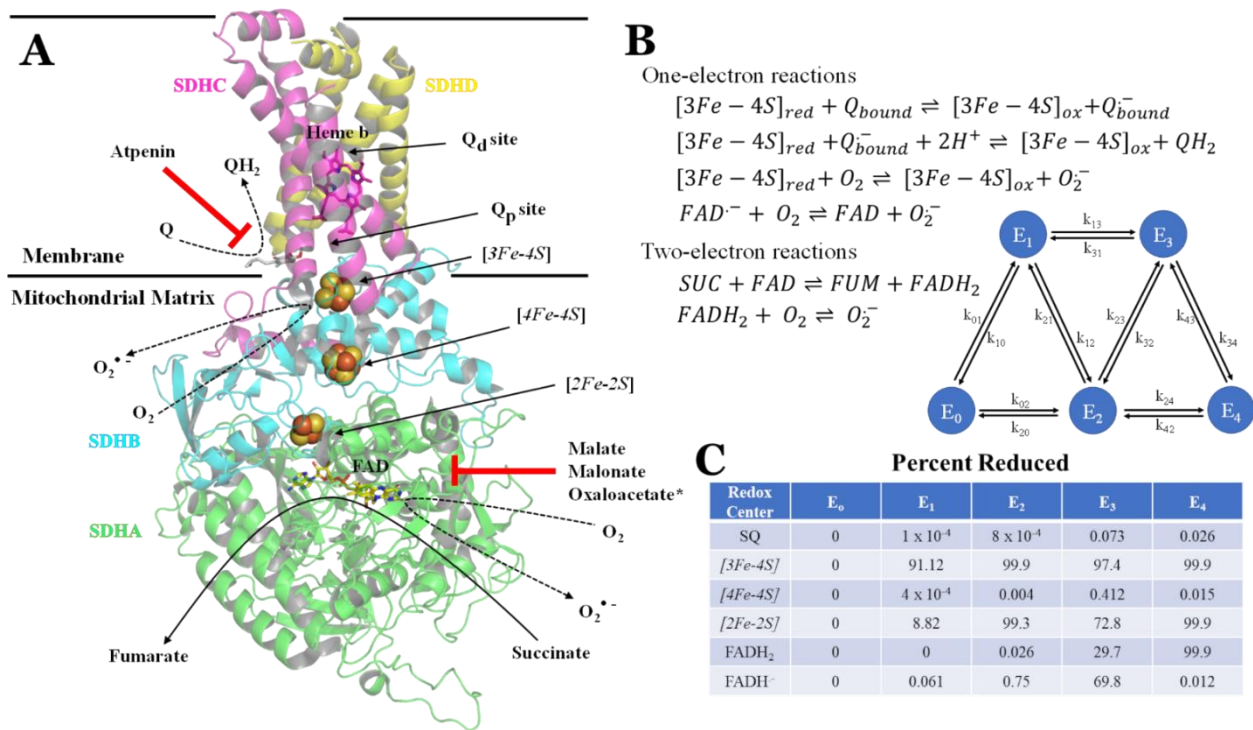


Figure 3.1 Overview of the SDH model. A) The ribbon diagram shows the four subunits along with the major redox centers of SDH. The SDHA subunit constitutes a covalently bound FAD in the dicarboxylate binding site where succinate is oxidized to fumarate to generate the fully reduced flavin. The SDHB subunit contains three iron-sulfur clusters ([2Fe-2S], [4Fe-4S], and [3Fe-4S]) that shuttle electrons one at a time from to produce QH₂ at the proximal Q site (Q_p) and the heme group at the interface between the SDHC and SDHD subunits. A distal quinone binding site has been proposed (Q_d). B) The redox state transition diagram depicts the possible redox states (E_i) of the enzyme in which i^{th} is the redox state that corresponds to the total number of electrons residing on the enzyme. The transition rates among these redox states are denoted k_{ij} (details in the Appendix). Relevant redox reactions that underly redox state transitions are either one or two-electron mediated. C) At each enzyme oxidation state, the percent of each redox center that is in a reduced state is determined. A fully oxidized Q pool and pH 7 were used to calculate the percentages. The SDH ribbon diagram was generated from the crystal structure by Sun et al. [3]. *In addition to competing with succinate at the dicarboxylate binding site, oxaloacetate also causes the enzyme to resume an inactive conformation.

with oxygen become reduced, ROS are formed as side reactions. To gain insight into how these reactions govern SDH kinetics and ROS production, a mathematical model encompassing all the relevant components of the enzyme was constructed, calibrated, and corroborated.

The data used in model fitting and validation are summarized in Table 3.1 [35,37,41–43]. A dot plot of data collected in-house is presented in Fig. S3.2. In selecting experimental data to calibrate the model, several key factors were considered. First, the data come from only mammalian sources. This criterion allows for a more consistent data set to construct a model that can be integrated into large-scale metabolic network simulations relevant to mammals. Second, a wide range of experimental conditions are necessary to eliminate biases inherent to experimental conditions so that the model can account for different experimental results. As such, we chose data sets derived from purified enzyme, sub-mitochondrial particles and permeabilized mitochondria. Third, the experimental protocols must contain sufficient information for model simulations in order to minimize the number of adjustable parameters otherwise needed to simulate different environmental conditions. For example, we did not choose data obtained from intact mitochondria to avoid confounding issues such as the activity of ROS scavenging pathways and metabolite transport. Fourth, the data must comprehensively address the distinct kinetic and ROS production behaviors of SDH. Considering all these criteria, data on both succinate oxidation and ROS production rates are included. Altogether, the studies listed in Table 3.1 yield a comprehensive and detailed data set capable of supporting the parameterization of a biophysically detailed SDH kinetic model. The fixed model parameters consist of many thermodynamic parameters obtained from the literature. They include midpoint potentials and pKa values and are given in Table S3.2. The adjustable model

Table 3.1 Experimental data used for model fitting.

Species and Enzyme Origin	Electron acceptor	Kinetic Data	ROS Data	pH	Temp	Scaling Factors	Reference
pig heart enzyme	PMS	yes	no	7.8	25 °C	1.0	Zeijlemaker <i>et al.</i> [43]
bovine heart enzyme	TMPD	yes	no	6.5 - 9	22 °C	0.82	Vinogradov <i>et al.</i> [41]
bovine heart SMP	DQ, Q ₁₀	yes	no	7.4	32 °C	4.0	Jones and Hirst [42]
bovine heart SMP	Q ₁₀ , PMS	yes	yes	7.5	30 °C	0.56	Grivennikova <i>et al.</i> [37]
bovine heart SMP	Q ₁₀	yes	yes	7.2 - 8	37 °C	3.7	Siebels and Drose [35]
guinea pig heart isolated mitochondria	DQ, Q ₁₀	yes	yes	7.2	37 °C	3.0	this study

Q₁₀, ubiquinone; DQ, decylubiquinone, PMS, phenazine methosulfate; TMPD, N,N,N',N' tetramethyl-P-phenylenediamine

parameters consist of forward rate constants of product formation and ROS production rates; the dissociation constants for substrates, products and inhibitors; and other factors necessary to properly simulate the environmental conditions (Table 3.2).

All the adjustable parameters are in a physiologically suitable range and nearly all are identifiable. Identifiable parameters are highly sensitive and independent of other parameters. A small change in the value of a sensitive parameter causes a large change in a model output. The opposite is true for an insensitive parameter. The normalized sensitivity coefficients in Table 3.2 give information about the contribution of each parameter to the model output. The normalized sensitivity coefficients are computed using Eq. S3.98. Correlation coefficients are presented in a Fig. S3.3 of the Appendix as a heat map. The correlation coefficients provide information on the degree the model parameters are linearly dependent with each other in a local region of parameter space. The residual analysis given in Fig. S3.4 shows that the residuals follow a normal distribution which indicates that there are no systematic biases in the model simulations.

While the model consists of 19 adjustable parameters to simulate the data, they are the minimum number required to simulate all the data in a thermodynamically consistent manner. Each parameter governs the model's biochemical and biophysical behavior under a large range of experimental conditions. That said, some parameter correlation is unavoidable due to the limited amount of data available for each simulated reaction. For example, the rate constant for QH_2 production, the quinone/semiquinone midpoint potential, and the atpenin dissociation constant at the proximal binding site are the only parameters strongly correlated with each other (> 0.8). To decorrelate these parameters, additional measurements on quinone binding

Table 3.2 Model adjustable parameters.

Parameters	Definition	Values	Sensitivity	Rank
$k_{f_0}^{SUC}$	rate constant for succinate oxidation	52.9 s ⁻¹	0.532	6
$k_{f_0}^{QH_2}$	rate constant for QH ₂ production	2.48 x 10 ⁷ s ⁻¹	0.162	13
K_{SUC}	succinate dissociation constant	355 μM	0.336	9
K_{FUM}	fumarate dissociation constant	1.0 mM	0.105	14
K_Q	quinone dissociation constant	0.29 nM	0.039	19
K_{QH_2}	quinol dissociation constant	0.19 nM	0.079	17
k_f^P	rate constant for phenazine reduction	7.47 x 10 ⁹ M ⁻¹ s ⁻¹	0.470	7
k_f^{TMPD}	rate constant for TMPD reduction	8.29 x 10 ⁹ M ⁻¹ s ⁻¹	0.560	4
K_H	H ⁺ dissociation constant at Q _p -site	170 nM	0.098	15
K_{MALO}	malonate dissociation constant	14.8 μM	0.559	5
K_{MAL}	malate dissociation constant	294 μM	0.724	2
K_{OAA}	oxaloacetate dissociation constant	0.822 μM	0.620	3
K_{Ap}	atpenin dissociation constant at Q _p site	1.67 x 10 ⁻⁴ pM	0.377	8
K_{Ad}	atpenin dissociation constant at Q _d site	68.3 nM	0.066	18
$\beta_{atpenin}$	atpenin inhibitory factor	14.6	0.170	12
$E_m^{Q/Q^{\bullet-}}$	Q/Q ^{•-} midpoint potential	284 mV	1.72	1
$k_{f_0}^{FADH^{\bullet}}$	rate constant for O ₂ ^{•-} production by FADH [•]	8.15 x 10 ⁵ M ⁻¹ s ⁻¹	0.281	11
$k_{f_0}^{3Fe-4S}$	rate constant for O ₂ ^{•-} production by [3Fe-4S]	6.68 x 10 ⁹ M ⁻¹ s ⁻¹	0.300	10
$k_{f_0}^{FADH_2}$	rate constant for H ₂ O ₂ production by FADH ₂	2.61 x 10 ³ M ⁻¹ s ⁻¹	0.075	17

affinities and their modulation by Q-site inhibitors are required. The top five most sensitive parameters are associated with the semiquinone reduction potential, dicarboxylate inhibition constants (malonate, malate and oxaloacetate), and TMPD reduction rate constant. Not surprisingly, some parameters associated with the quinone binding site are among the least sensitive. We designed and ran additional experiments to perturb the Q pool described below to improve the identifiability of these parameters, but they only led to a marginal increase in identifiability. This is because quantitative measurements of the quinone and quinol concentrations using kinetic assays are required to significantly improve their identifiability. A novel mass spectrometry-based method to collect end-point measurements of the Q pool was recently developed [47], but it is extremely resource intensive and cannot capture dynamic changes. Unfortunately, there does not exist a simple and straightforward approach to accurately measure the dynamic changes of these metabolites.

Model Simulations of Succinate Oxidation Rates Under Different Conditions Are Faithful to Experimental Data

Model simulations and experimental data of succinate oxidation kinetics using PMS and TMPD as electron acceptors are shown in Fig. 3.2 [37,41,43]. Overall, the model is able to simulate experimental data very well. For simplicity, the reduction of PMS and TMPD is assumed to obey second-order kinetics (i.e., there is no stable ES complex formed). For details concerning the reduction kinetics, see Eqs. S3.75-S3.88 in the Appendix. As seen in Fig 3.2, the succinate oxidation rates when either PMS or TPMD is the electron acceptor are similar for a given concentration. Thus, the fitted second-order rate constants given in Table 3.2 are similar in magnitude. The model is also able to reproduce pH-dependent succinate oxidation rates.

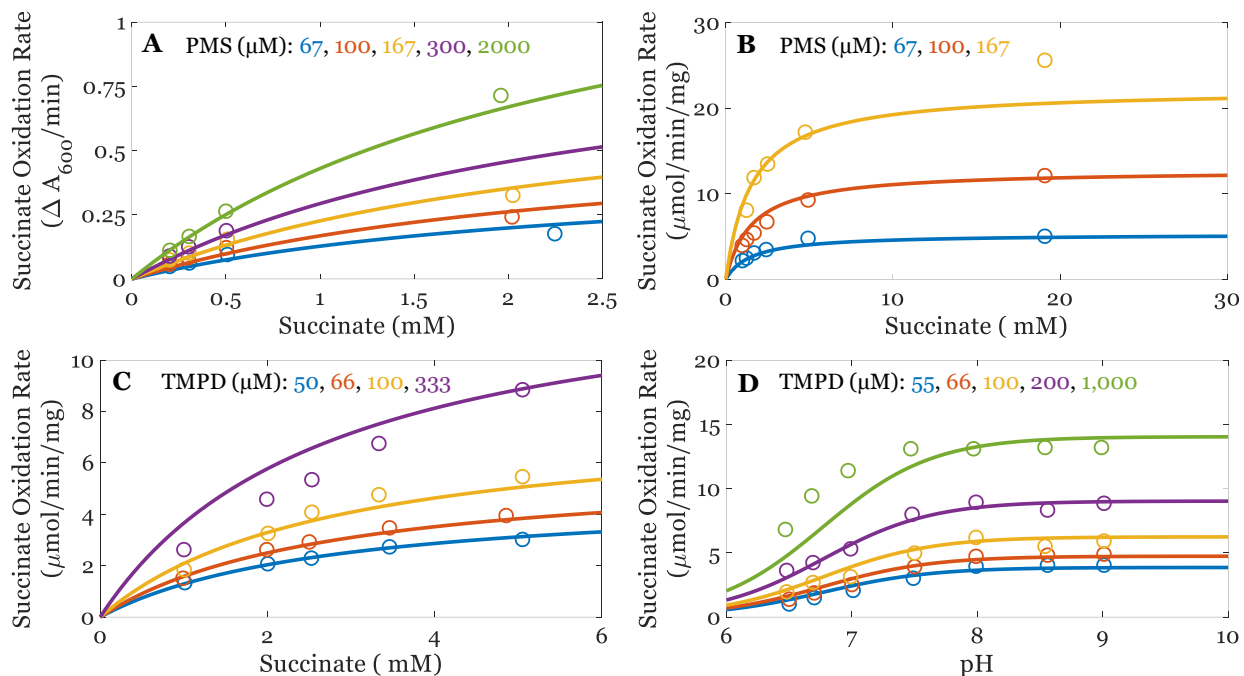


Figure 3.2 Succinate oxidation rates at varied concentrations of different electron acceptors. Model simulations (lines) are compared to experimental data (open circles) [38,41]. A-B) The effect of varying succinate and phenazine methylsulfate (PMS) concentrations on succinate oxidation rates. The PMS concentrations are (in μM) 67 (blue), 100 (red), 167 (yellow), 300 (purple) and 2000 (green) in panel A and 50 (blue), 200 (red) and 2000 (yellow) in panel B. For panel B, the malonate concentration was $50 \mu\text{M}$. C) Model simulations of the effect of varying succinate and tetramethyl-p-phenylenediamine (TMPD) concentrations compared to the data from Jones and Hirst [42]. The TMPD concentrations (in μM) are 50 (blue), 66 (red), 100 (yellow) and 333 (purple). Malonate was present at $100 \mu\text{M}$. D) Model simulations of the effect of varying pH and TMPD concentrations on succinate oxidation rates compared to the data from Jones and Hirst [42]. The concentrations of WB (in μM) are 50 (blue), 66 (red), 100 (yellow), 200 (purple) and 1000 (green). The succinate concentration was fixed at $100 \mu\text{M}$.

Specifically, at pH above 8, the reaction becomes independent of pH and precipitously drops in a manner dependent on both pH and electron acceptor concentration. When the acceptor concentration is high, the rate does not drop until the pH falls below 7.5; however, when the acceptor concentration is low, the rate begins to drop near pH 8. This is because higher concentrations of electron acceptors compensate for lower concentrations of the enzyme in the right protonation state. This pH effect is ascribed to an active-site sulfhydryl group with a pKa around 7 near the flavoprotein which is believed to be required for succinate oxidation [48,49]. In the model, these results are obtained using an explicit pH-dependence for succinate oxidation at the flavin site as shown in Eq. S3.13.

In a series of titration experiments, the effects of substrates and inhibitors at the FAD and Q sites on succinate oxidation are shown in Fig. 3.3. Data from Jones and Hirst are shown in panels A-C (top row), and data from Siebels and Drose are shown in panels D-F (bottom row). Both data sets are obtained using bovine heart SMP but differ in the enzyme and substrate concentrations. The data from Jones and Hirst were performed using 0.30 $\mu\text{g}/\text{mL}$ complex II, 5 mM succinate and 100 μM decylubiquinone [42]. In Siebels and Drose, SMPs were present at 0.12 mg/mL with 100 μM succinate [35]. Atpenin A5 titration leads to a significant drop in succinate oxidation rates in both data set. However, the atpenin-titration results are quantitatively different. This is likely due to the different enzyme concentrations and experimental conditions used. For example, at an atpenin concentration of 25 nM, succinate oxidation is 93% inhibited in the Jones and Hirst data set (Fig. 3.3B), but at 30 nM it is only inhibited by 65% in the Siebels and Drose dataset (Fig. 3.3D). To fit these disparities, the model fitting results in a compromise where it underestimates the atpenin-dependent inhibition for

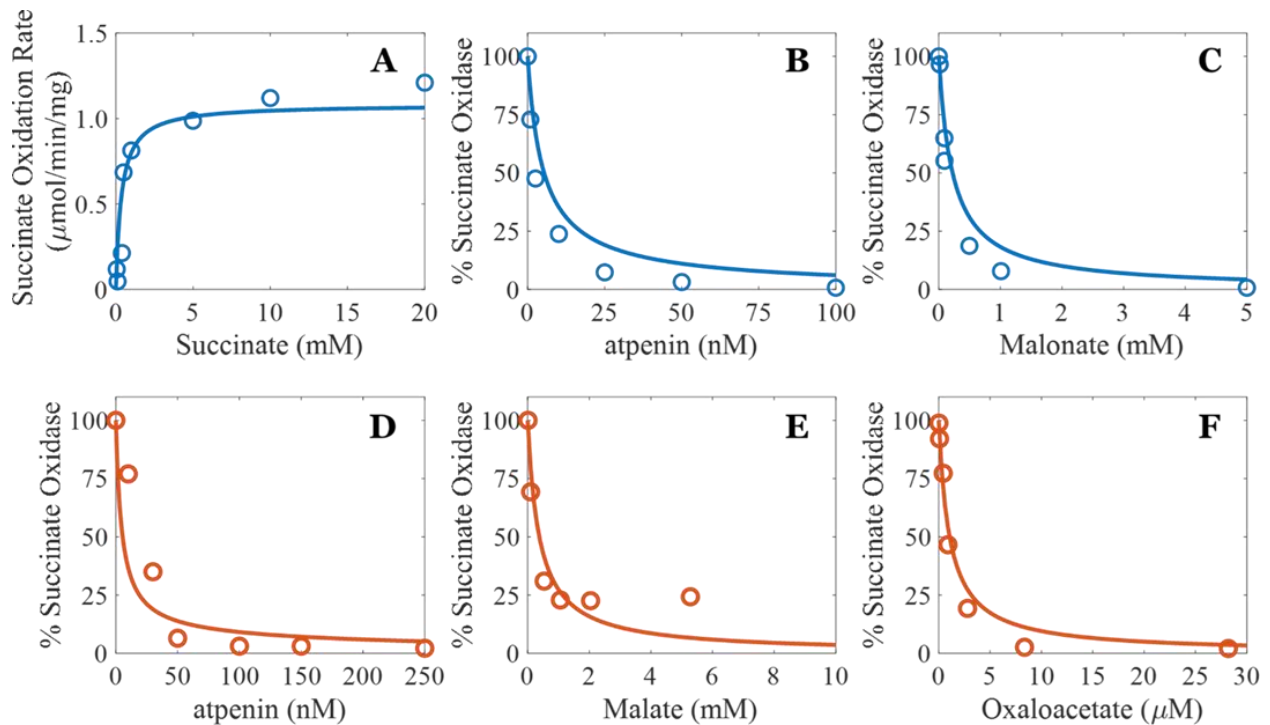


Figure 3.3 Succinate oxidation kinetics in the presence of SDH inhibitors using bovine heart SMP. Model simulations (lines) are compared to experimental data (open circles). Experimental data are from Jones and Hirst [42] (A-C) and Siebels and Drose [35] (D-F). Data from Jones and Hirst are obtained using 30 μg/mL solubilized membranes, 5 mM succinate and 100 μM decylubiquinone. A) Succinate oxidation rate saturates near 5 mM succinate with an apparent K_M of 2 mM. B-C) Relative succinate oxidation rates are significantly inhibited with increasing concentrations of atpenin (0-100 nM) and malonate (0-5 mM). E-F) Data from Siebels and Drose are obtained using 0.12 mg/mL SMP and 100 μM succinate. Relative succinate oxidation rates are significantly inhibited with increasing concentrations of atpenin (0-250 nM), malate (0-10 mM) and oxaloacetate (0-30 μM).

the Jones and Hirst dataset and overestimates it for the Siebels and Droese dataset. Without any additional information, these experimental discrepancies cannot be reconciled. The atpenin inhibition data was modeled by assuming atpenin binds to the Q_p site and prevents Q or QH_2 binding. In addition to the Q_p site, atpenin at high concentrations has been shown to occupy the Q_d site, also known as the non-canonical Q site [5,50]. Atpenin binding to the Q_d site has been speculated to affect succinate oxidation. This mechanism was found necessary to include in the model in order to obtain the best fits to the data.

Titration of the succinate competitive inhibitors malonate, malate and oxaloacetate also decreases succinate oxidation rates (Fig. 3.3C, E, and F). The concentration required to inhibit succinate oxidase is different for each inhibitor. Oxaloacetate is the most potent SDH inhibitor, followed by malonate and malate. These results coincide with the fitted dissociation constants shown in Table 3.1. In the presence of these dicarboxylates, fewer FAD sites are available for succinate binding and thus decreases enzyme turnover.

Model Simulations Are Consistent with Experimental ROS Production Rates

ROS production by SDH displays a biphasic succinate-dependence, as shown in Fig. 3.4. At low concentrations, ROS production is stimulated; however, ROS production is suppressed at higher concentrations. The model was calibrated using data sets from two independent studies. In the experiments by Grivennikova et al. [37], peak ROS production occurs at around 50 μ M succinate (Fig. 3.4A). In Siebels and Droese [35], the peak is shifted to approximately 150 μ M (Fig. 3.4B). The primary difference between these two studies is the presence of myxothiazol in Grivennikova et al. and atpenin in Siebels and Droese. Whereas atpenin competitively inhibits QH_2 binding at the Q_p site of SDH, myxothiazol competitively inhibits QH_2 binding to complex III

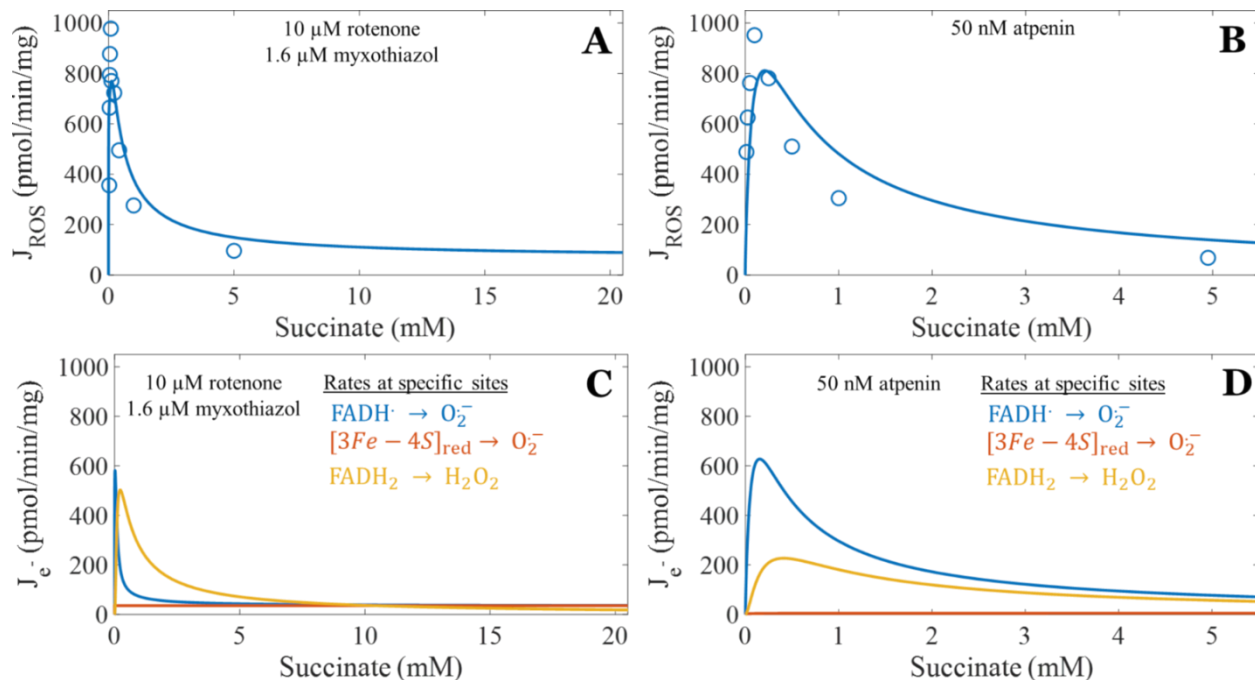


Figure 3.4 Maximum ROS produced by SDH occurs at sub-millimolar concentrations of succinate. Model simulations (lines) are compared to experimental data (open circles) from bovine heart SMP. A) Experimental $J_{H_2O_2}$ are obtained in the presence of 10 μ M rotenone, 1.6 μ M myxothiazol, 2 units/mL horseradish peroxidase (HrP) and 6 units/mL bovine superoxide dismutase (SOD) [37]. B) Experimental $J_{H_2O_2}$ are obtained in the presence of 50 nM atpenin [35]. C) Model simulations of site-specific ROS production rates for the conditions shown in panel A). D) Model simulations of site-specific ROS production rates for the conditions shown in panel B). In both panels C) and D), rates are given with respect to the same electron equivalents as in A) and B).

at the heme b_L site. The model simulates ROS production rates reported in both studies using the same model framework by exploring the distinct effects of myxothiazol and atpenin. The model predicts that the FAD site is the primary site of ROS under the conditions used in both studies. However, the major ROS species is different between studies. In the Grivennikova et al. simulation, H_2O_2 originated from the fully reduced flavin, $FADH_2$, is the primary ROS species (Fig. 3.4). When myxothiazol is present, the Q pool is nearly fully reduced and capable of reducing SDH via QH_2 oxidation at the Q_p site. The result is that a higher proportion of the enzyme is reduced and capable of producing ROS. In contrast, in the Siebels and Drose simulation, $O_2^{\bullet-}$ derived from the flavin radical is the primary ROS species, followed by H_2O_2 from the fully reduced flavin (Fig. 3.4D). Model simulations reveal this is primarily because the FAD site is not as reduced as compared to when atpenin is absent. The predominant form of the flavin under this condition is the flavin radical, which only produces $O_2^{\bullet-}$. The shift of the peak succinate concentration for maximal ROS production is also explained by the different effects by these inhibitors on the enzyme oxidation state. When atpenin is present, the only reductant for SDH is succinate. Therefore, it takes a higher concentration of succinate to reduce enough of the enzyme to reach peak ROS production rates, which shifts the succinate titration curve to the right in Siebels and Drose. In addition, as stated above, succinate also blocks ROS production from the FAD site, so the ability of succinate to drive ROS production is limited.

The difference in total and site-specific ROS production rates in the presence of stigmatellin or atpenin as the succinate concentration is increased is shown in Fig. 3.5. Stigmatellin competitively inhibits QH_2 binding to complex III near the Rieske ISP site. Similar to when myxothiazol is present, the Q pool is fully reduced with stigmatellin, and quinol oxidation

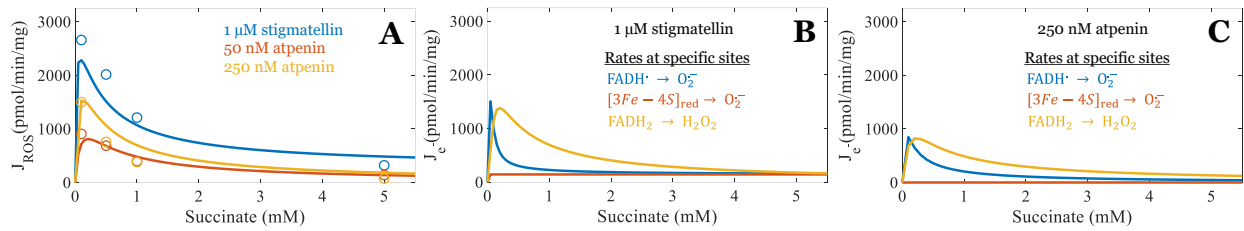


Figure 3.5 Succinate-dependent ROS production of SMPs in the presence of stigmatellin or atpenin. A) Model simulations (lines) are compared to experimental data (open circles) from Siebels and Drose [35]. B) Site-specific ROS production rates when 1 μ M stigmatellin is present. C) Site-specific ROS production rates when 250 nM atpenin is present. Site-specific rates are given with respect to the same electron equivalents as in A).

at the Q_p site serves as an additional source of electrons for free radical production. So turnover at both electron input and output (reverse) of the enzyme complex results in the highest ROS production rates. In the presence of either inhibitor, the FAD is the major source of ROS, and $O_2^{\bullet-}$ from the FAD site at low succinate concentrations is highest among ROS species. As the succinate concentration increases, H_2O_2 production from the FAD site exceeds the $O_2^{\bullet-}$ rate from this site. But as the succinate concentration further increases, the ROS production rate from the FAD site decreases due to succinate binding to the FAD, making it unavailable to interact with oxygen. However, when atpenin is present, electron transfer from the ISC to quinone or oxygen is blocked [50,51]. Therefore, $O_2^{\bullet-}$ production from the FAD remains the dominant source of ROS, and the ISC produces no ROS when atpenin is present (Fig. 3.5C). In addition, the enzyme is more oxidized compared to when stigmatellin is present, so the amount of enzyme with a fully reduced flavin is lower. Thus, the rate of H_2O_2 production is lower.

The effects of titrating atpenin and non-SDH dicarboxylate substrates on ROS production rates are presented in Fig. 3.6. Increasing atpenin concentrations lead to an increase in ROS production rates which reaches a maximum at 250 nM. In the presence of 250 nM atpenin, increasing malate or oxaloacetate concentration causes the ROS production rate to significantly decrease. Malate concentrations in the mM range lead to a significant drop in ROS production rates (Fig. 3.6B). Oxaloacetate is much more potent and completely inhibits ROS production after 20 μ M (Fig. 3.6C). These data further corroborate that the availability of the FAD site for oxygen binding is necessary for ROS formation by complex II. As more FAD sites are occupied by non-SDH dicarboxylate substrates, less ROS is produced despite the optimal atpenin concentration. These results are supported by prior work demonstrating that ROS are

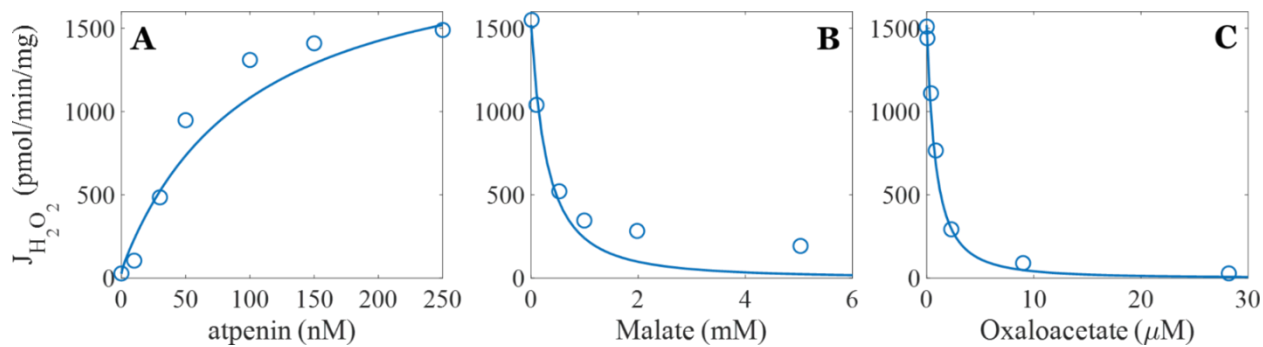


Figure 3.6 Effects of titrating atpenin and non-SDH dicarboxylate substrates on ROS production by complex II. Model simulations (lines) are compared to experimental data (open circles) for each panel [35]. Experimental data are obtained from bovine heart SMP. A) Rate of H_2O_2 production is increased at increasing concentrations of atpenin (0-250 nM), a potent and specific inhibitor of quinone reductase activity. B-C) In the presence of 250 nM atpenin, ROS production rates are decreased as the concentrations of malate and oxaloacetate is increased. Malate and oxaloacetate compete with succinate at the FAD binding site.

produced from the FAD site when the dicarboxylate site is unoccupied and the enzyme is reduced [13,34]. As these TCA cycle dicarboxylates regulate SDH turnover, it is fortunate that they also do not lead to excess ROS production like the Q site inhibitor atpenin. This would necessarily lead to oxidative stress when these dicarboxylates accumulate under conditions such as I/R injury. However, if electron exit is blocked at the FAD site while the enzyme is maintained in a highly reduced state from a reduced Q pool, ROS from the [3Fe-4S] ISC can produce significant amounts of ROS as shown by Quinlan et al. [24].

Titration of fumarate in the presence of varying succinate concentrations results in a drop in $O_2^{\bullet-}$ and total ROS production rates as shown in Fig. 3.7. When atpenin was absent from the experiments, it was assumed that the quinone/quinol redox couple was in equilibrium with the fumarate/succinate couple. Therefore, the equilibrium relationship between the free energies associated with the fumarate/succinate and quinone/quinol couples were used to calculate the quinone and quinol concentrations. When atpenin was present, the Q pool redox state predictor functions (Eq. S3.1) were used to calculate the quinone and quinol concentrations. At a given fumarate to succinate ratio, the ROS production rate is higher in the presence of complex III inhibitors alone compared to when atpenin is included. Without atpenin present, significant turnover at the Q_p site of complex II, in addition to turnover at the FAD site, leads to a more reduced FAD fraction and hence more ROS production. While atpenin stimulates ROS production from the FAD site, the rate is one third to one half of that with stigmatellin alone. This difference highlights the importance of the Q_p site as a source of electrons via quinol oxidation for the ROS production at the FAD site. While the [3Fe-4S] ISC and FAD sites can all produce ROS, both experimental data and model simulations suggest that most of ROS comes

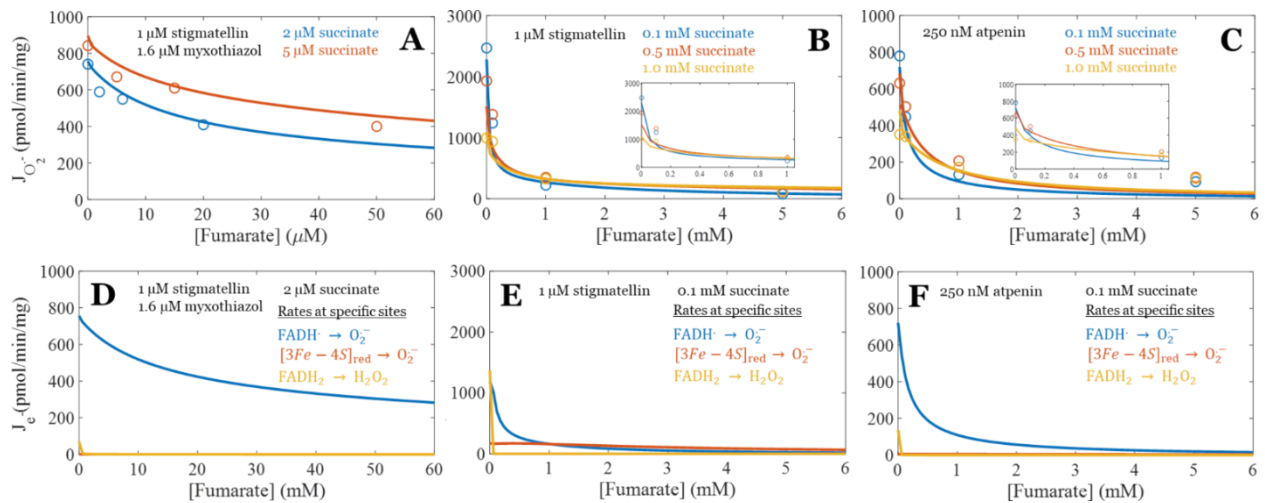


Figure 3.7 Effects of varying fumarate/succinate ratios on atpenin and complex III inhibitor induced ROS production. Model simulations (lines) are compared with experimental data (open circles). A) Data are obtained from Grivennikova et al. [37]. Bovine heart SMP (0.1 mg/mL) are prepared in the presence of 1.6 μ M myxothiazol and 10 μ M rotenone. Atpenin is added to the final concentration of 1 μ M. B-C) Data are from Siebels and Drose [35]. Bovine heart SMP (0.12 mg/mL) are prepared without myxothiazol or rotenone. B) Stigmatellin is added to the final concentration of 1 μ M C). Atpenin is added to the final concentration of 50 nM. In all conditions, the increasing the fumarate concentration leads to a decrease in ROS production rates. D-F) Site-specific ROS production rates corresponding to their respective panels above. Site-specific rates are given with respect to the same electron equivalents as in above panels.

from the reduced flavin under these conditions. In addition, the model simulations show that H_2O_2 production rates are significantly suppressed in the presence of fumarate. These findings further corroborate that a reduced flavin unobstructed by metabolites and other molecules is required to produce significant amounts of ROS.

The model simulations show distinct pH-dependent ROS profiles for stigmatellin and atpenin as shown in Fig. 3.8. ROS production from the FAD site was best fit when the FAD radical or fully reduced FAD cofactor was deprotonated as shown in Eqs. S3.15 and S3.17. In the presence of stigmatellin, both ROS species increase as pH is increased (Figs. 3.8A & C). This is due to the pH-dependent partial reactions occurring at FAD and Q_p sites of the complex. As pH becomes more alkaline, both succinate and quinol oxidation become more favorable from a mass action perspective. As a result, the enzyme oxidation status becomes more reduced, and the fraction of reduced FAD is significantly elevated. In contrast, this rise in ROS production as the conditions become more alkaline are not observed when atpenin is present (Figs. 3.8B & D). With atpenin, quinol oxidation at the Q_p site is inhibited. FAD reduction arises only from succinate oxidation, which does not reduce the FAD as much as when quinol oxidation was also allowed to contribute. Therefore, ROS production is overall lower under this condition despite the thermodynamic favorability of ROS production from the FAD site in alkaline conditions.

Model Testing and Corroboration

The experimental data used above to constrain the SDH model lacked sufficient perturbations to the endogenous Q pool to adequately identify some of the Q site related parameters. Therefore, we designed some experiments using uninhibited guinea pig cardiac SDH and the quinone analogue decylubiquinone (DQ) as shown in Fig. 3.9. Decylubiquinone was

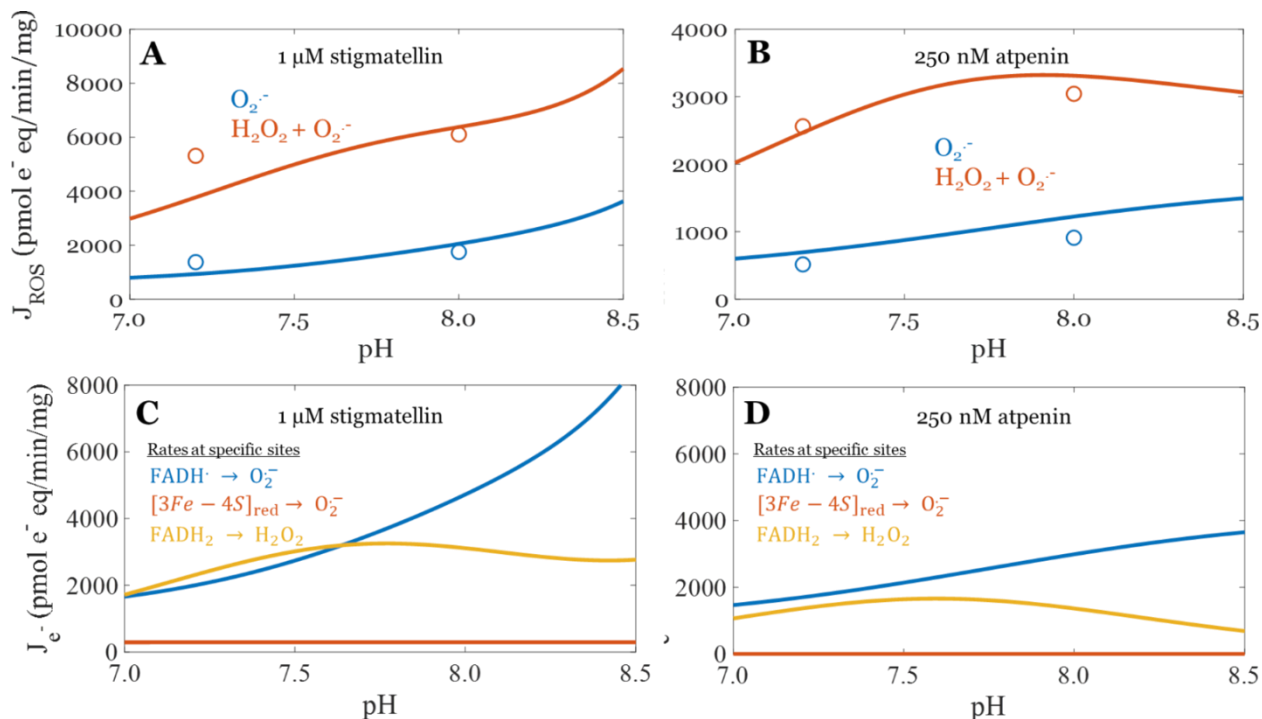


Figure 3.8 The effects of pH on ROS production rates in the presence of inhibitors. In A), the stigmatellin concentration was 1 μ M. In B), the atpenin concentration was 250 nM. Model simulations (lines) are compared to experimental data (open circles) from Siebels and Drose [35]. Experimental data show $O_2^{\cdot-}$ in blue and total ROS ($H_2O_2 + O_2^{\cdot-}$) in orange using bovine heart SMP. Malonate of 1.5 mM is added in both experiments. As discussed in Grivennikova et al. [37], we assumed the presence of a small but significant amount of contaminating superoxide dismutase in these experiments. Based on model analysis, this amounts to an approximate 65% underestimation of the superoxide production rate in the Siebels and Drose experiments. This factor was explicitly included when simulating these data. C-D) Site-specific ROS production rates corresponding to their respective panels above. Site-specific rates are given with respect to the same electron equivalents as in above panels.

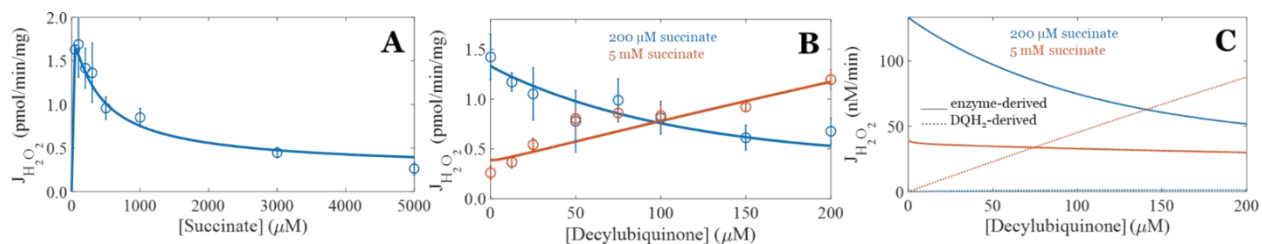


Figure 3.9 Decylubiquinone can directly reduce oxygen and amplify resorufin fluorescence. A)

Succinate-dependent SDH ROS production kinetics from freeze-thawed guinea pig cardiac mitochondria show the same trend as rat SDH. In these experiments, the guinea pig cardiac mitochondria were inhibited with 4 μ M rotenone and 2 μ M myxothiazol. For more details, see the experimental details given in the methods. B) Net hydrogen peroxide emission rates in DQ titration experiments reveal that DQ decreases ROS at low succinate concentrations (200 μ M) and increases ROS at high succinate concentrations (5 mM). The model quantitatively predicted this drop in ROS; however, an additional parameter, k_{O_2, DQH_2} , was required to fit the increase in ROS at high succinate concentrations. The value of this parameter in these simulations was $0.0022 \text{ M}^{-1}\text{s}^{-1}$. C) Model analysis reveals that for the low succinate condition, DQH₂ derived ROS is negligible but becomes significant when the concentration of succinate is high. Open circles represent the experimental means, and the error bars are standard deviations from at least 3 biological replicates. Model simulations are represented by the solid lines. The ODE system used to simulate the concentration dynamics is given in Eqs. S3.97-105 in the Appendix.

used to manipulate the endogenous Q pool redox levels. In these experiments, we first quantified ROS production by SDH at different succinate concentrations as done in prior studies (Fig. 3.9A). Our results show that ROS production from cardiac guinea pig SDH possesses the same succinate-dependence as SDH from other rodents. We then chose two succinate concentrations, 200 μM and 5 mM, to use in the DQ titration experiments to perturb the endogenous Q pool (Fig. 3.9B). At the lower succinate concentration, adding DQ resulted in a dramatic drop in ROS production by SDH. This is due to a decrease in both the succinate and QH_2 concentrations and an increase in fumarate and Q concentrations catalyzed by SDH. The result was predicted by the model. The decreased ROS in the DQ titration experiment at 200 μM succinate led to the prediction of a similar trend at 5 mM succinate. In contrast, the addition of DQ when the succinate concentration is higher (5 mM) leads to a surprising increase in ROS production. In the absence of SDH, the addition of DQ leads to zero ROS as expected. Therefore, the increase in ROS when SDH is present is due to SDH-catalyzed production of DQH_2 and the near instantaneous reaction of DQH_2 with oxygen in the buffer. This rapid reaction was confirmed by adding DQH_2 to the assay buffer in the absence of SDH. When this was done, all Amplex UltraRed was immediately converted to resorufin as indicated by the rapid color change of the ROS reporter. Thus, the increase in ROS at high succinate concentrations when DQ is titrated is enzyme mediated. This rapid reduction of DQ by succinate is facilitated by SDH. This result underscores the importance in considering the impact of environmental changes when interpreting ROS data with DQ present.

These experiments were then modeled using the SDH model presented above and a small ODE model given in the Appendix (see Eqs. S3.97-103). Results from this simulation are

shown in Fig. 3.9C. The ODE model was necessary to simulate the dynamics of DQ, O₂ and ROS species. The model was able to reproduce both the succinate titration and DQ titration data at the 200 μM succinate concentration without any additional parameters other than a scaling factor to account for differences in SDH activity across species. However, a new parameter, k_{O_2, DQH_2} , was required to simulate the DQ titration experiments at the 5 mM succinate concentration. This parameter is a lumped rate constant which incorporates the rapid SDH-mediated reaction between succinate and DQ to form DQH₂ and the subsequent diffusion-limited reaction between DQH₂ and O₂. The model simulations of this process reveal that the impact of DQH₂-mediated ROS production is negligible at the lower succinate concentration. However, at the higher succinate level, the majority of ROS detected by the reporter assay is from DQH₂. For example, at 5 mM succinate concentration, DQH₂-derived ROS when DQ is 200 μM accounts for over half of the total experimentally measured ROS. Therefore, our model analysis reveals the importance of accounting for DQ-mediated side reactions when a quinone analog is employed.

The model was also corroborated using the experimental data from Grivennikova et al. [52]. In this study, ROS production rates from SMPs were measured with a variety of substrates, inhibitors and oxygen concentrations. From these data, the SDH specific data were selected and used to test model validity. As shown in Fig. 3.10, the model reproduces the experimental data with high fidelity without tuning the adjustable parameter set. It reproduces the linear relationship between ROS production and oxygen concentration in Fig. 3.10A. In addition, the model matches the kinetic rate of succinate oxidase under the conditions described in

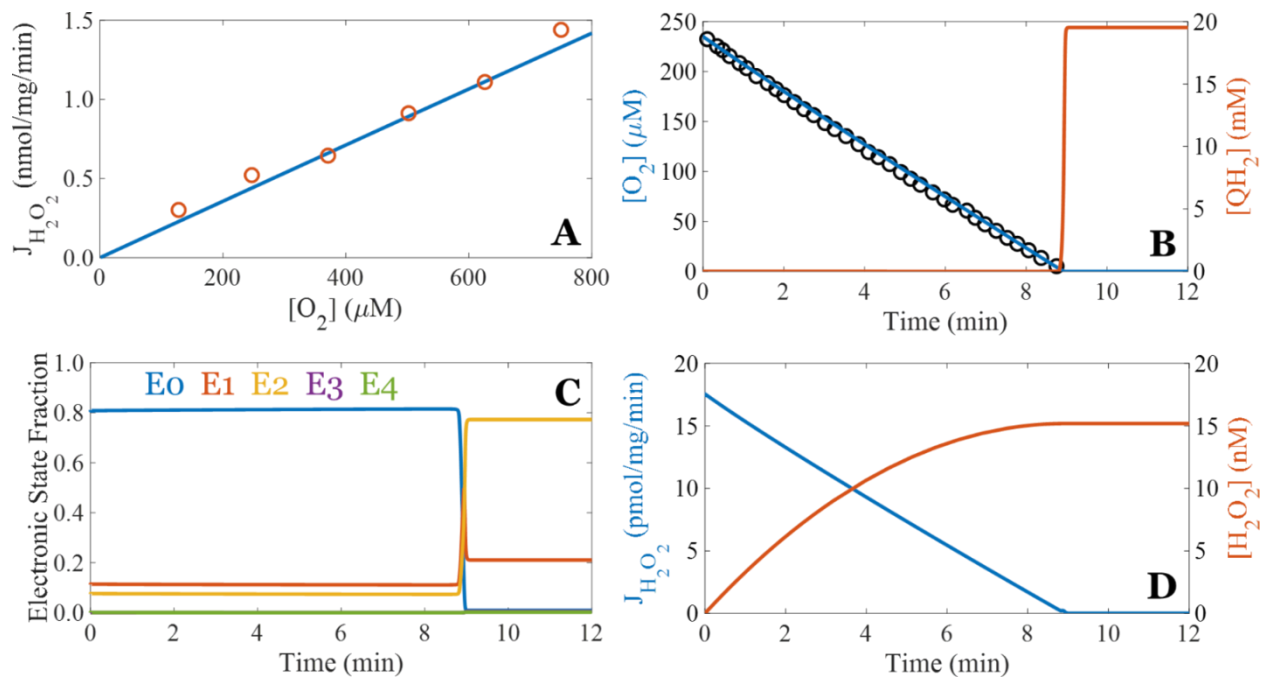


Figure 3.10 Model corroboration of ROS production and SDH kinetics. The data are from Grivennikova et al. [52]. The enzyme concentration for these simulations was 2 nM in A) and 22 nM in B-D). The ODE system used to simulate oxygen concentration dynamics is given in Eqs. S3.97-105 in the Appendix.

Grivennikova et al. [52]. The quinol concentration and SDH oxidation state fractions are shown as predictions during the conditions in Fig. 3.10B and 3.10C, respectively. Furthermore, the contribution of SDH to the total ROS detected during this experiment is shown in Fig. 3.10D. Comparing this value to the total value Grivennikova et al. measured during this experiment reveals that SDH contributes approximately 1% to the total ROS produced by SMPs during their experimental protocol.

Together, model analysis demonstrates that ROS production by SDH occurs in both the “forward” and “reverse” modes. It does not matter where the electrons come from: either succinate in the forward mode or QH₂ in the reverse mode. To quantify the amounts of ROS produced by the major redox centers when SDH works in the reverse direction, a simulation was performed in which the Q pool redox status determines the enzyme oxidation state distribution (Fig. 3.11). The model predicts that, despite acting on SDH at different sites, atpenin (1 μM) and malonate (0.5 mM) lead to nearly identical ROS production rates by the enzyme (Fig. 3.11A). This result is corroborated by a prior study from the Brand group [24]. However, site-specific ROS production rates are distinct. When the Q_p site is inhibited, O₂^{•-} derived from the flavin radical is the primary source of ROS (Fig. 3.11B). Superoxide derived from the [3Fe-4S] ISC and H₂O₂ originated from the fully reduced flavin are negligible. When the flavin site is inhibited, most of the total ROS originates from the [3Fe-4S] ISC (Fig. 3.11C). The predictions are consistent with the inhibitory mechanisms associated with atpenin and malonate. Since malonate occupies the flavin, it prevents electrons from leaving the enzyme by which the [3Fe-4S] ISC becomes reduced and primed to participate in a one-electron redox reaction with oxygen. Therefore, the model suggests that both the flavin and [3Fe-4S] ISC can

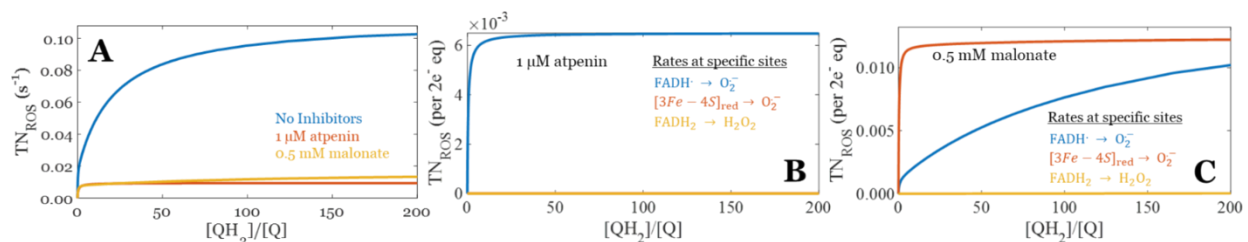


Figure 3.11 Model prediction of site-specific ROS production when the enzyme oxidation state is determined by the Q pool redox state. A) Inhibiting SDH at either the flavin or Q_p site results in an approximately 90% reduction in total ROS production. B) The primary enzyme produced ROS is superoxide originating from the flavin radical when SDH is inhibited at the Q_p site. C) In the presence of 0.5 mM malonate, most of the enzyme ROS is from the $[3Fe-4S]$ ISC with a significant fraction originating from the FAD site when the Q pool is highly reduced. Under both conditions, hydrogen peroxide originating from the fully reduced flavin is negligible.

be a significant source of ROS and that environmental factors dictate which one is the primary ROS contributor.

To test the model's ability to simulate ROS production from intact mitochondria, it was integrated into a recent model of oxidative phosphorylation [44]. The integrated model was then used to simulate succinate-dependent leak-state and ADP-stimulated respiration and ROS emission reported in an earlier study [22]. These results are given in Table 3.3 and demonstrate that the model simulations quantitatively match the experimental measurements. The consistency between the model simulations and experimental results upon integration highlights the importance of constructing biophysically accurate and thermodynamically consistent enzyme models when attempting to simulate metabolic phenomena at a systems level.

Model Predicts the [3Fe-4S] ISC is the Primary Source of ROS

Lastly, the model was used to predict succinate oxidation and ROS production rates as a function of the succinate/fumarate and quinol/quinone ratios in the absence of inhibitors, as shown in Fig. 3.12. The succinate oxidation rate is maximum when the succinate/fumarate ratio is high and the quinol/quinone ratio is low. The turnover in the forward direction predicted by the model is in the range previously determined by other groups [46,53,54]. The model also predicts that enzyme's turnover in the reverse direction is approximately equal to the forward direction. This has a profound effect on the enzyme behavior during pathological conditions such as ischemia whereby this enzyme is speculated to be responsible for the significant accumulation of succinate during ischemia [15,16]. In contrast to the inhibitor-based

Table 3.3 Integrated model simulation results.

Respiration and ROS Production	Experiment	Model
Leak-state J_{O_2} (nmol mg ⁻¹ min ⁻¹)	106 ± 7	113
Leak-state $J_{H_2O_2}$ (pmol mg ⁻¹ min ⁻¹)	234 ± 10	225
Oxphos-state J_{O_2} (nmol mg ⁻¹ min ⁻¹)	363 ± 31	341
Oxphos-state $J_{H_2O_2}$ (pmol mg ⁻¹ min ⁻¹)	87 ± 10	79

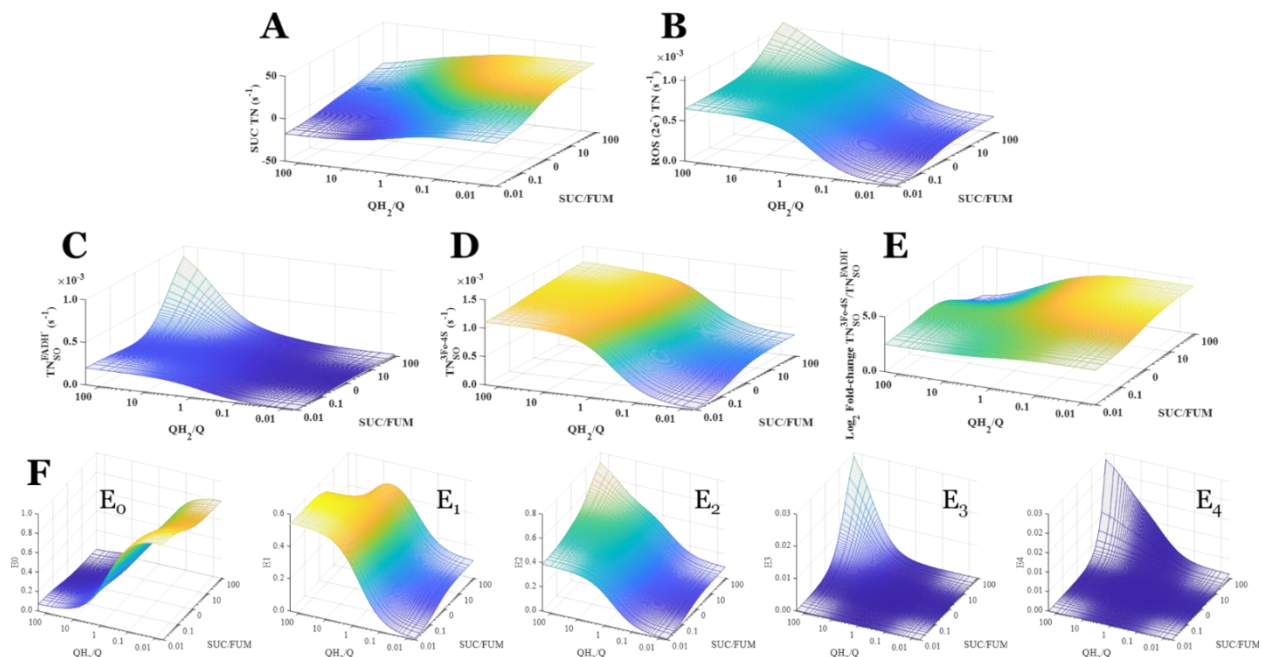


Figure 3.12 Model simulations of succinate and ROS turnover of SDH as a function of succinate/fumarate and QH_2/Q ratios. A) Steady-state turnover rates of succinate oxidation. B) Steady-state production of total ROS. C) Steady-state ROS production from the FAD site. D) Steady-state ROS production from the $[3Fe-4S]$ ISC site. E) The \log_2 fold-change of steady-state ROS production rates from the $[3Fe-4S]$ ISC site relative to the FAD site. F) Steady-state enzyme oxidation states for these conditions. The simulations were conducted at 37 °C with a total Q pool of 20 mM, with succinate + fumarate = 20 mM, $[O_2] = 20\ \mu M$, and at pH 7. The $O_2^{\bullet-}$ and H_2O_2 concentrations were set to zero.

experiments described above, the model predicts that ROS production from the [3Fe-4S] ISC is the primary source of free radicals when no inhibitors are present (Fig. 3.12E). This is not surprising considering that, under inhibitor free conditions, the enzyme is mostly in the E₀, E₁, and E₂ oxidation states (Fig. 3.12F). In these states, electrons on the complex have a higher probability residing on the ISCs instead of the FAD. Therefore, ROS production from the FAD contributes by a lesser extent to the total ROS production in an uninhibited, fully functional mitochondrion. Under these conditions, H₂O₂ production by SDH is negligible and occurs only when the oxidation state E₄ is elevated. Under conditions that favor the oxidation state E₄, the probability of a fully reduced FAD is high (Fig. 3.1C). These include when fumarate is absent or present in the low micromolar range, and inhibitors at or downstream of the Q_p site are present.

DISCUSSION

In SDH, the two major sites for ROS production are proposed to be the covalently bound FAD and the Q site [13,24,29,34,55]. The [3Fe-4S] ISC site has recently been suggested to produce ROS [37]. However, which site is the dominant source, what ROS species is formed, and what conditions are conducive for ROS production at each site have not been quantitatively addressed. Using *S. cerevisiae* as an experimental model, several groups determined that the Q site is a strong contender for most ROS production [38,56]. Additional studies on *E. coli* support the Q site origin hypothesis [55,57]. However, studies using *A. suum* argued that both the FAD and the Q sites can produce ROS [36]. In contrast, other studies reported that only the FAD site produces ROS [13,55]. In mammalian SDH, studies have shown ROS is produced when the enzyme is supplied with succinate only after the Q site was inhibited [24,34]. But no study demonstrably showed whether $O_2^{\bullet-}$ [37] or H_2O_2 [35] is the dominant ROS species formed. In contrast, it has been argued that SDH from *E. coli* mainly produces $O_2^{\bullet-}$ from the FAD site [55]. This and other studies concluded that quinol fumarate oxidoreductases generate $O_2^{\bullet-}$ from the fully reduced FAD [4,55]. However, the mechanism underlying the ROS production was not elucidated. To answer these questions, we developed, analyzed and corroborated a computational model of SDH that quantitatively describes the necessary conditions for ROS production, the contribution of each site responsible for ROS production, and the factors that control how much ROS is produced by SDH.

The kinetics of succinate oxidation by reconstituted SDH has been thoroughly investigated [41,43,46]. Despite the different experimental conditions across studies, succinate oxidation is dependent on succinate concentrations, the concentrations of electron acceptors,

pH, the presence of non-SDH dicarboxylate substrates and quinone reductase inhibitors (Figs 3.2 & 3.3). The model simulates these data sets as faithfully as possible and uses a single framework to reproduce both succinate oxidation kinetics and ROS production rates. Based on model analysis, key differences reported across different studies are due to experimental conditions. More importantly, the model supports the notion that the non-canonical Q binding (Q_d) site modulates succinate oxidation. Specifically, including this site and its effects on succinate oxidation was necessary to simultaneously fit the data from Jones and Hirst and Siebels and Droese (Fig. 3.3). The model result is supported by crystal structures that show occupancy of the Q_d site at high atpenin concentrations [5,50].

The model is capable of simulating ROS production rates under a variety of experimental conditions. In two succinate titration experiments, Grivennikova et al. [37] and Siebels and Droese [35] reported different succinate concentrations that correspond to peak ROS production rates, depending on the inhibitors present (Figs. 3.4 & 3.5). To fit these data sets, the Q pool redox poise is simulated using equations that account for either complex III or SDH inhibitors. Model analysis reveals that a key determinant of SDH-derived ROS is the Q pool redox poise, which is set by a specific inhibitor. In the presence of atpenin, QH_2 oxidation by complex III results in an oxidized Q pool. As a result, ROS production from SDH is decreased. When complex III inhibitors are present, electron turnover downstream of SDH is inhibited, which leads to a more reduced Q pool. This results in QH_2 oxidation at the Q_p site of SDH and increases the number of reduced redox centers on the complex. Thus, ROS production rates are higher in the presence of stigmatellin and myxothiazol than atpenin (Fig. 3.7). The distinct pH dependency of ROS production also reflects the unique effects of SDH and complex III inhibitors on the Q pool

redox poise (Fig. 3.8). Quinol oxidation, which liberates a proton, is favorable as pH increases. However, this reaction is minimized when atpenin occupies the Q_p site. Thus, total ROS production reaches a plateau at alkaline pH in the presence of atpenin but continues to increase in the presence of complex III inhibitors (Fig. 3.8).

Prior studies have argued that the FAD site is able to produce both O₂^{•-} and H₂O₂ [13,24,29,34,55]. However, which is the dominant species and under which conditions is still an open question. In the study by Siebels and Drose [35], it was determined that H₂O₂ was the primary ROS species produced from the FAD site. We suspect their prep contained low, yet significant amounts, of superoxide dismutase contamination as described by Grivennikova et al. [37]. In support of this, the simulations shown in Fig. 3.8 reveal that, under both stigmatellin- and atpenin-induced ROS production, SDH mainly produces ROS as O₂^{•-} from the FAD site. The results from these simulations are supported by several studies which used rat skeletal muscle mitochondria to show that most ROS originating from the FAD site is O₂^{•-} [8,24]. In addition, a different study found that the vast majority of total ROS produced by *E. coli* SDH is also O₂^{•-} [55]. These findings and the model simulation results strongly point to O₂^{•-} as the major free radical species originating from the FAD site.

In addition to the FAD site, the Q_p site is another candidate for major ROS production by SDH. Recently, the ISCs have been also suggested to produce significant amounts of ROS. Model analysis reveals that ROS originate mostly from the FAD site or the [3Fe-4S] ISC. We initially included ROS production from the bound semiquinone but found its inclusion superfluous when fitting the data. The production of ROS at the FAD site and [3Fe-4S] ISC requires that they are in a reduced state and unoccupied. These prerequisites explain the decreased ROS

production rates in the presence of malonate, malate and oxaloacetate (Figs. 3.6 & 3.7). The non-SDH dicarboxylate substrates can bind to the FAD site, preventing succinate from reducing the enzyme and oxygen accessing the reduced flavin. Likewise, binding of molecules such as atpenin to the Q_p site can also physically block the ISC from reacting with oxygen. However, since the ISC does not interact with the non-SDH dicarboxylate substrates, ISC-derived ROS is sensitive to only atpenin or other Q_p site inhibitors.

To address the uncertainty associated with the kinetics of quinone binding and oxidation/reduction at the Q sites, we designed an experiment using isolated mitochondria from guinea pig cardiomyocytes and DQ to perturb the endogenous Q pool (Fig. 3.9). Our experimental data show that succinate oxidation kinetics in guinea pig exhibits a similar trend observed in other mammals. In addition, ROS production profile is uniquely dependent on succinate concentration. At 200 μ M succinate, ROS production decreases as DQ level rises. At 5 mM succinate, the opposite is true. Our model analysis demonstrates that this is due to DQH_2 -derived ROS at high succinate concentrations. The model analysis highlights the importance of careful consideration of the SDH-mediated DQH_2 production and its subsequent reaction with oxygen in the buffer. Failure to account for this side reaction leads to overestimation of SDH-derived ROS.

Following model calibration, we validated the model using the SDH-specific data set from Grivennikova et al. [52]. The validation step is necessary to ensure that key aspects of the model are tested against experimental data not used during parameter fitting. That said, as additional data become available, model improvements should be made. The model as presented herein is able to reproduce the oxygen dependence of ROS production without tuning

the adjustable parameters. The validation process further shows that, under the prevailing conditions, ROS production obeys second-order kinetics. In these conditions, oxygen availability and the Q pool redox poise are the key determinants of ROS production (Fig. 3.10). When either of these factors becomes limited, ROS production drops. In this context, the Q pool redox poise is important for ROS formation because it dictates the enzyme oxidation state. Therefore, any environmental factors that affect the Q pool redox poise – such as the use of Q_p site complex III inhibitors - will affect the enzyme oxidation state and ROS production. Our simulation in Fig. 3.11 again highlights this notion.

Finally, we used the model to deconstruct the kinetics underlying ROS production in uninhibited, fully functional mitochondria (Fig. 3.12). As discussed, ROS production is dependent on electrons supplied by succinate (forward mode) or QH₂ (reverse mode). In the absence of inhibitors, most of the enzyme population is in the E₀, E₁ and E₂ oxidation states. In these states, electrons are most likely to occupy the [3Fe-4S] ISC and give rise to O₂^{•-}. The FAD site is also a significant source of O₂^{•-} but contributes less to total ROS than the [3Fe-4S] ISC in the absence of inhibitors. Thus, by using experimental data from studies that employ inhibitors, our modeling approach results in a model that allows us to understand ROS production in the absence of inhibitors.

The SDH model is the ideal choice to include in metabolic simulations when scaling up the cell or tissue level, because the model simulates both the primary biochemical reaction and the side reactions that produce ROS using an algebraic expression. Large-scale metabolic models can be used to understand both normal and pathological metabolic scenarios involving mitochondrial succinate metabolism as in I/R injury [15,16] mitochondrial ROS production as in

skeletal muscle bioenergetics [58], and immune responses [27,59,60]. However, simulating these types of models is computationally expensive. Nearly all large-scale models of metabolism are systems of nonlinear ordinary (one independent variable, e.g. time) or partial (multiple independent variables, e.g. time and space) differential equations. As a result, any enzymatic or transport process that is also modeled as a system of differential equations adds to the complexity and computational cost. Thus, a model that can simulate multiple reactions using algebraic expressions significantly reduces the simulation cost and is very advantageous to use in the large-scale models of metabolism. There are several models similar to our SDH model that simulate the kinetics of the main reaction along with side reactions such as ROS production [61–64], but these models are systems of differential equations themselves. Integrating them into large-scale models of metabolism dramatically increases the computational cost. Therefore, our approach provides a unique way to model these primary reactions along with their associated side reactions in large-scale models without significantly adding to the computational complexity and associated cost.

In summary, our study resolves the critical issue pertaining to the identity, origin and conducive conditions of ROS production by SDH. The model suggests that the primary species formed is $O_2^{\bullet-}$. During physiological conditions, the [3Fe-4S] ISC is the primary source; however, the FAD can become a major source during pathological conditions. Hydrogen peroxide is produced in appreciable quantities only when SDH is inhibited and fumarate is absent. In the physiological setting, the fumarate concentration will never be zero; therefore, H_2O_2 production by SDH is an experimental phenomenon. In developing our model, we included succinate oxidation and linked it to ROS production as succinate is an important source of electron for

SDH. The model presented herein is the only comprehensive SDH model that can simulate both the enzyme kinetics and ROS production rates for a wide range of conditions. As a result, this model is ideal for integrating into large-scale models of mitochondrial metabolism to study ROS production from the ETS during physiological and pathophysiological conditions.

APPENDIX

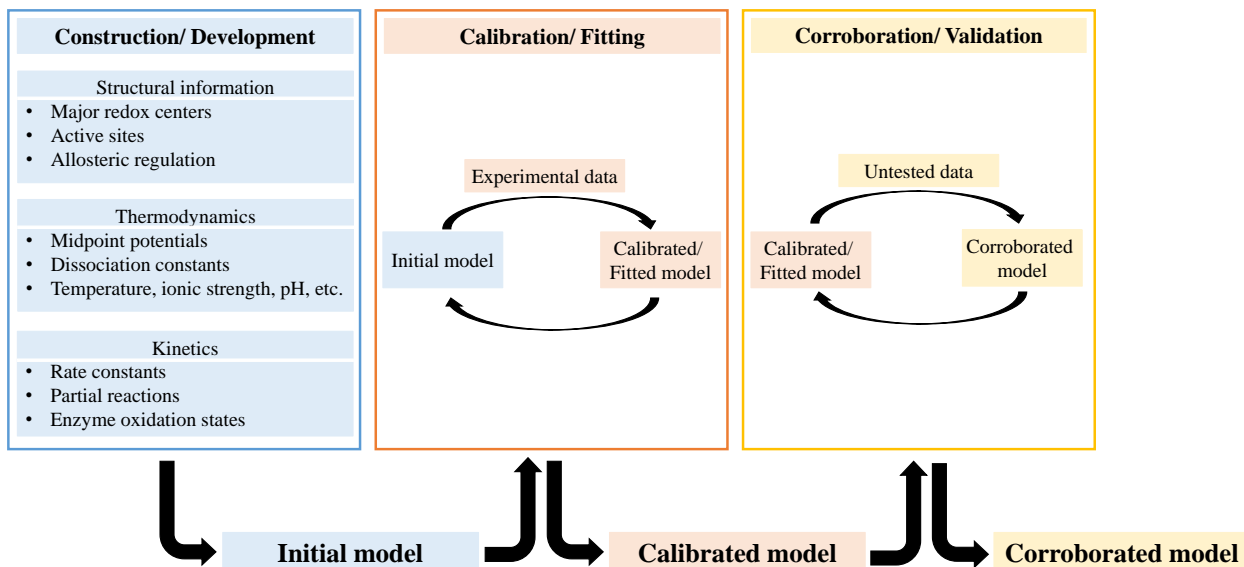


Figure S3.1 Methodology overview. The general modeling approach involves a three-stage process of model construction, calibration, and corroboration. In the initial construction stage (blue), a base model emerges from structural, thermodynamic, and kinetic data. In the calibration stage (orange), outputs of the base model are compared to experimental data. The adjustable model parameters are tuned until the model outputs match the experimental data. At this point, the adjustable model parameters are optimized. During the final stage of model corroboration (yellow), the model outputs are compared to experimental data that were not used in the calibration stage. The revised model is validated if outputs are consistent with experimental data. Otherwise, the model is sent back to the calibration stage.

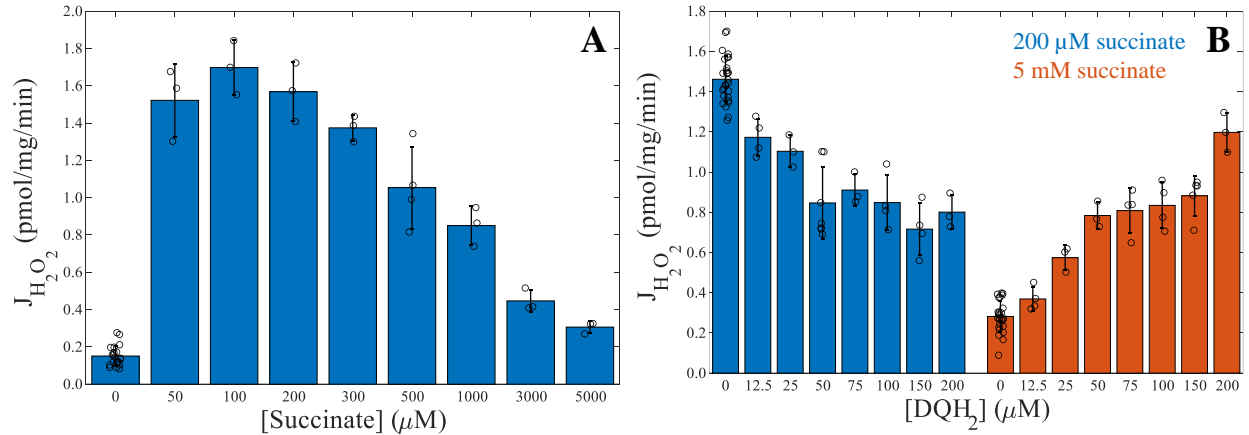


Figure S3.2 Net hydrogen peroxide emission rates were measured in-house using mitochondria isolated from guinea pig cardiomyocytes. The net hydrogen peroxide emission rate was monitored using the Amplex UltraRed assay (excitation 560 nm, emission 590 nm). A) Succinate titration. Mitochondria were added to the reaction mixture containing myxothiazol and rotenone. After 2 minutes of stabilization, succinate was added to the final concentrations of 50, 100, 200, 300, 500, 1000, 3000 or 5000 μM . B) Decylubiquinol (DQH₂) titration was obtained at 200 μM and 5 mM succinate concentrations. The initial stage of the experiment is similar to the succinate titration. After 10 minutes following succinate addition, DQH₂ was added to the final concentrations of 12.5, 25, 50, 75, 100, 150 or 200 μM . In all experiments, the final concentrations are 10 μM Amplex UltraRed, 1 U/mL HrP, 10 U/mL SOD, 4 μM rotenone, 2 μM myxothiazol and 0.1 mg/mL mitochondria. At least 3 replicates were performed at each succinate or DQH₂ concentration.

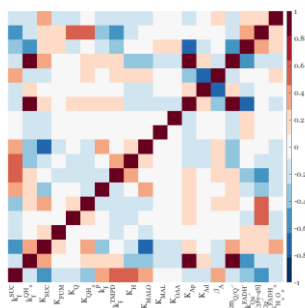


Figure S3.3 Correlation heat map for adjustable parameters given in Table 3.2. Matrix of correlation coefficient between the adjustable parameters. The normalized parameter sensitivity matrix is computed using Eq. S3.98. The sensitivity coefficients were computed from the parameter sensitivity matrix given in Eq. S3.99. Correlation coefficients range between -1 (negative correlation) to $+1$ (positive correlation). A coefficient value of 0 means the two parameters are uncorrelated. Substrates: succinate (SUC), quinone (Q), oxygen (O_2); products: fumarate (FUM), quinol (QH_2), superoxide, (O_2^*), and hydrogen peroxide (H_2O_2); inhibitors: atpenin (A5), malonate (MALO), oxaloacetate (OAA), malate (MAL); other notations: $[2Fe-2S] = ISC_1$, $[4Fe-4S] = ISC_2$, $[4Fe-3S] = ISC_3$.

Table S3.1 Fixed model parameters.

Parameters	Definition	Values	Units	References
R	Ideal gas constant	8.314	J/mol/K	-
F	Faraday's constant	96.5	J/mV/mol	-
K_{FADH}	pKa for flavin free radical	8	-	[65]
K_{FADH_2}	pKa for fully reduce flavin	7.7	-	[65]
$E_m^0_{FAD/FADH}$	FAD/FADH midpoint potential	385	mV	[65]
$E_m^0_{FADH/FADH_2}$	FADH/FADH ₂ midpoint potential	284	mV	[65]
$E_m^0_{FAD/FADH_2}$	FADH/FADH ₂ midpoint potential	333.8	mV	[65]
$E_m^{ISC_1}$	Midpoint potential of $[2Fe-2S]_{ox,,red}$	0	mV	[37]
$E_m^{ISC_2}$	Midpoint potential of $[4Fe-4S]_{ox,,red}$	-260	mV	[37]
$E_m^{ISC_3}$	Midpoint potential of $[3Fe-4S]_{ox,,red}$	60	mV	[37]
$E_m^{O_2/O_2^{\cdot-}}$	O ₂ /O ₂ ^{•-} midpoint potential	-160	mV	[66]
$E_m^{O_2/H_2O_2}$	O ₂ /H ₂ O ₂ midpoint potential	940	mV	[66]
$E_m^0_{FUM/SUC}$	FUM/SUC midpoint potential	445	mV	[67]
$E_m^0_{Q/QH_2}$	Q/QH ₂ midpoint potential	464	mV	[68]
$E_m^0_P$	Phenazine midpoint potential	358	mV	[69]
$E_m^0_{TMPD}$	TMPD midpoint potential	270	mV	[70]
$[Q]_{tot}$	Total mitochondrial quinone concentration	20	mM	[14]

Midpoint potentials are given at 273 K and pH 0 except for the ISCs, oxygen/superoxide, and oxygen/hydrogen peroxide couples. Those are given with respect to 273 K and pH 7. All potentials are given as reduction potentials.

Table S3.2 Environmental parameters.

Parameters	Description	Value	Sensitivity	Rank
Q	succinate/QH ₂ constant	1 M	0.022	4
Q _{bc1}	succinate/QH ₂ constant in the presence of complex III inhibitors	211 nM	0.052	3
Q _{A5}	atpenin inhibitory constant	604 nM	0.017	5
Q _{MAL}	malate inhibitory constant	31.6 mM	2.73x10 ⁻⁶	6
Q _{OAA}	oxaloacetate inhibitory constant	70.6 μM	6.87x10 ⁻⁶	7
Q _{FUM}	fumarate inhibitory constant	5.99 μM	0.133	2
Q _{MALO}	malonate inhibitory constant	188 μM	0.167	1

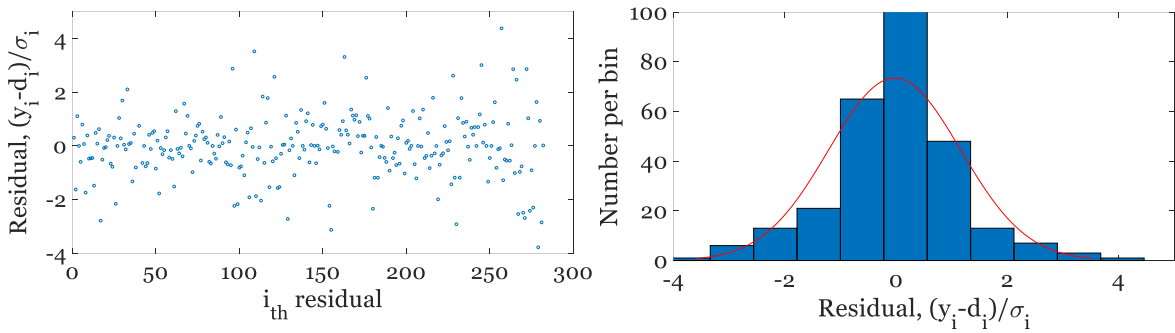


Figure S3.4 Model Residual Analysis. Left) Model residuals are randomly permuted and plotted as shown. Right) Model residuals are binned and plotted as a histogram indicating they follow a normal distribution. The normal distribution function is plotted with a mean of 0, standard deviation of 1.18, and a pre-exponential term equal to 74. These results show the model fits are unbiased and there are no systematic errors present.

$$[QH_2] = Q_{tot} / (1 + Q/[SUC]) \cdot (1 + [A5]/Q_{A5}) \cdot (1 + [MALO]/Q_{MALO}) \cdot (1 + [MAL]/Q_{MAL}) \cdot (1 + [FUM]/Q_{FUM}) \cdot (1 + [OAA]/Q_{OAA}) \quad \text{Eq. S3.1}$$

If complex III inhibitors are present, the following equation is used:

$$[QH_2] = Q_{tot} / (1 + Q_{bc1}/[SUC]) \cdot (1 + [A5]/Q_{A5}) \cdot (1 + [MALO]/Q_{MALO}) \cdot (1 + [MAL]/Q_{MAL}) \cdot (1 + [FUM]/Q_{FUM}) \cdot (1 + [OAA]/Q_{OAA}) \quad \text{Eq. S3.2}$$

$$[Q] = [Q]_{tot} - [QH_2] \quad \text{Eq. S3.3}$$



$$P_{Qp} = 1 + \frac{[QH_2]}{K_{QH_2}} + \frac{[Q]}{K_Q} + \frac{[A5]}{K_{Ap}} \quad \text{Eq. S3.13}$$

$$P_{Qd} = 1 + \frac{[A5]}{K_{Ad}} \quad \text{Eq. S3.14}$$

$$P_{FAD} = 1 + \frac{[SUC]}{K_{SUC}} + \frac{[FUM]}{K_{FUM}} + \frac{[MAL]}{K_{MAL}} + \frac{[MALO]}{K_{MALO}} + \frac{[OAA]}{K_{OAA}} \quad \text{Eq. S3.15}$$

$$k_f^{SUC} = k_{f_0}^{SUC} \cdot (1 + [A5] / K_{A_2}) / (1 + \beta_A [A5] / K_{A_2}) / (1 + [H^+] / K_H) \quad \text{Eq. S3.16}$$

$$k_f^{QH_2} = k_{f_0}^{QH_2} \cdot (1 + [A5] / K_{A_2}) / (1 + \beta_A [A5] / K_{A_2}) \quad \text{Eq. S3.17}$$

$$k_f^{FADH^*} = k_{f_0}^{FADH^*} / P_{FAD} / (1 + [H^+] / K_{FADH}) \quad \text{Eq. S3.18}$$

$$k_f^{3Fe-4S} = k_{f_0}^{3Fe-4S} / P_Q \quad \text{Eq. S3.19}$$

$$k_f^{FADH_2} = k_{f_0}^{FADH_2} / P_{FAD} / (1 + [H^+] / K_{FADH_2}) \quad \text{Eq. S3.20}$$

$$E_m^{FAD/FADH} = E_m^0{}^{FAD/FADH} + (RT/F) \cdot \log([H^+] \cdot (1 + K_{FADH} / [H^+])) \quad \text{Eq. S3.21}$$

$$E_m^{FADH/FADH_2} = E_m^0{}^{FADH/FADH_2} + (RT/F) \log([H^+] \cdot (1 + [H^+] / K_{FADH_2}) / (1 + [H^+] / K_{FADH})) \quad \text{Eq. S3.22}$$

$$E_m^{FAD/FADH_2} = E_m^0{}^{FAD/FADH_2} + (RT/2F) \log \left(\frac{[H^+]^2 \cdot (1 + [H^+] / K_{FADH_2})}{(1 + K_{FADH} / [H^+]) / (1 + [H^+] / K_{FADH})} \right) \quad \text{Eq. S3.23}$$

$$E_m^{SQ/QH_2} = 2E_m^0{}^{SQ/QH_2} + 2(RT/F) \log([H^+]) - E_m^0{}^{Q/SQ} \quad \text{Eq. S3.24}$$

$$E_m^{Q/QH_2} = E_m^0{}^{Q/QH_2} + (RT/F) \log([H^+]) \quad \text{Eq. S3.25}$$

$$E_m^{FUM/SUC} = E_m^0{}^{FUM/SUC} + (RT/F) \log([H^+]) \quad \text{Eq. S3.26}$$

$$E_m^P = E_m^0{}^P + (RT/2F) \log([H^+]) \quad \text{Eq. S3.27}$$

$$E_m^{TMPD} = E_m^0{}^{TMPD} + (RT/2F) \log([H^+]) \quad \text{Eq. S3.28}$$

$$E_{mb}^{Q/SQ} = E_m^0{}^{Q/SQ} + (RT/F) \log(K_Q) \quad \text{Eq. S3.29}$$

$$E_{mb}^{SQ/QH_2} = E_m^0{}^{SQ/QH_2} - (RT/F) \log(K_{QH_2}) \quad \text{Eq. S3.30}$$

$$E_{mb}^{FUM/SUC} = E_m^0{}^{FUM/SUC} - (RT/2F) \log(K_{SUC}) + (RT/2F) \log(K_{FUM}) \quad \text{Eq. S3.31}$$

$$K_{eq}^{FUM/FADH_2} = e^{2F/RT(E_{mb}^{FUM/SUC} - E_m^0{}^{FAD/FADH_2})} \quad \text{Eq. S3.32}$$

$$K_{eq}^{QH_2/ISC_3} = e^{F/RT(E_m^{SQ/OH_2} - E_m^{ISC_3})} \quad \text{Eq. S3.33}$$

$$K_{eq}^{GEA/ISC_1ISC_3} = e^{2F/RT(E_m^{GEA} - E_m^{ISC_3} - E_m^{ISC_1})} \quad \text{Eq. S3.34}$$

$$K_{eq}^{O_2^-/ISC_3} = e^{F/RT(E_m^{O_2/O_2^-} - E_m^{ISC_3})} \quad \text{Eq. S3.35}$$

$$K_{eq}^{O_2^-/FADH} = e^{F/RT(E_m^{O_2/O_2^-} - E_m^{FAD/FADH})} \quad \text{Eq. S3.36}$$

$$K_{eq}^{H_2O_2/FADH_2} = e^{2F/RT(E_m^{O_2/H_2O_2} - E_m^{FAD/FADH_2})} \quad \text{Eq. S3.37}$$

$$E_h^{FAD/FADH} = E_m^{FAD/FADH} \quad \text{Eq. S3.38}$$

$$E_h^{FADH/FADH_2} = E_m^{FADH/FADH_2} \quad \text{Eq. S3.39}$$

$$E_h^{ISC_1} = E_m^{ISC_1} \quad \text{Eq. S3.40}$$

$$E_h^{ISC_2} = E_m^{ISC_2} \quad \text{Eq. S3.41}$$

$$E_h^{ISC_3} = E_m^{ISC_3} \quad \text{Eq. S3.42}$$

$$E_h^{Q/SQ} = E_{mb}^{Q/SQ} + (RT/F) \log(Q/K_Q/P_Q) \quad \text{Eq. S3.43}$$

$$\Delta G = -nF\Delta E \quad \text{Eq. S3.44}$$

$$S_r^k = \frac{e^{-\Delta G_r^k/RT}}{\sum_r e^{-\Delta G_r^k/RT}} \quad \text{Eq. S3.45}$$

$$D_1 = e^{-\Delta G_{FADH}/RT} + e^{-\Delta G_{ISC_1}/RT} + e^{-\Delta G_{ISC_2}/RT} + e^{-\Delta G_{ISC_3}/RT} + e^{-\Delta G_{SQ}/RT} \quad \text{Eq. S3.46}$$

$$\begin{aligned} D_2 = & \left(e^{-\Delta G_{FADH}/RT} e^{-\Delta G_{FADH_2}/RT} \right) + \left(e^{-\Delta G_{FADH}/RT} e^{-\Delta G_{ISC_1}/RT} \right) + \left(e^{-\Delta G_{FADH}/RT} e^{-\Delta G_{ISC_2}/RT} \right) \\ & + \left(e^{-\Delta G_{FADH}/RT} e^{-\Delta G_{ISC_3}/RT} \right) + \left(e^{-\Delta G_{FADH}/RT} e^{-\Delta G_{SQ}/RT} \right) + \left(e^{-\Delta G_{ISC_1}/RT} e^{-\Delta G_{ISC_2}/RT} \right) + \left(e^{-\Delta G_{ISC_1}/RT} e^{-\Delta G_{ISC_3}/RT} \right) \\ & + \left(e^{-\Delta G_{ISC_1}/RT} e^{-\Delta G_{SQ}/RT} \right) + \left(e^{-\Delta G_{ISC_2}/RT} e^{-\Delta G_{ISC_3}/RT} \right) + \left(e^{-\Delta G_{ISC_2}/RT} e^{-\Delta G_{SQ}/RT} \right) + \left(e^{-\Delta G_{ISC_3}/RT} e^{-\Delta G_{SQ}/RT} \right) \end{aligned} \quad \text{Eq. S3.47}$$

$$\begin{aligned}
D_3 = & \left(e^{-\Delta G_{FADH}/RT} e^{-\Delta G_{FADH_2}/RT} e^{-\Delta G_{ISC_1}/RT} \right) + \left(e^{-\Delta G_{FADH}/RT} e^{-\Delta G_{FADH_2}/RT} e^{-\Delta G_{ISC_2}/RT} \right) \\
& + \left(e^{-\Delta G_{FADH}/RT} e^{-\Delta G_{FADH_2}/RT} e^{-\Delta G_{ISC_3}/RT} \right) + \left(e^{-\Delta G_{FADH}/RT} e^{-\Delta G_{FADH_2}/RT} e^{-\Delta G_{SQ}/RT} \right) \\
& + \left(e^{-\Delta G_{FADH}/RT} e^{-\Delta G_{ISC_1}/RT} e^{-\Delta G_{ISC_2}/RT} \right) + \left(e^{-\Delta G_{FADH}/RT} e^{-\Delta G_{ISC_1}/RT} e^{-\Delta G_{ISC_3}/RT} \right) \\
& + \left(e^{-\Delta G_{FADH}/RT} e^{-\Delta G_{ISC_1}/RT} e^{-\Delta G_{SQ}/RT} \right) + \left(e^{-\Delta G_{FADH}/RT} e^{-\Delta G_{ISC_2}/RT} e^{-\Delta G_{ISC_3}/RT} \right) \\
& + \left(e^{-\Delta G_{FADH}/RT} e^{-\Delta G_{ISC_2}/RT} e^{-\Delta G_{SQ}/RT} \right) + \left(e^{-\Delta G_{FADH}/RT} e^{-\Delta G_{ISC_3}/RT} e^{-\Delta G_{SQ}/RT} \right) \\
& + \left(e^{-\Delta G_{ISC_1}/RT} e^{-\Delta G_{ISC_2}/RT} e^{-\Delta G_{ISC_3}/RT} \right) + \left(e^{-\Delta G_{ISC_1}/RT} e^{-\Delta G_{ISC_2}/RT} e^{-\Delta G_{SQ}/RT} \right) \\
& + \left(e^{-\Delta G_{ISC_1}/RT} e^{-\Delta G_{ISC_3}/RT} e^{-\Delta G_{SQ}/RT} \right) + \left(e^{-\Delta G_{ISC_2}/RT} e^{-\Delta G_{ISC_3}/RT} e^{-\Delta G_{SQ}/RT} \right)
\end{aligned} \tag{Eq. S3.48}$$

$$\begin{aligned}
D_4 = & \left(e^{-\Delta G_{FADH}/RT} e^{-\Delta G_{FADH_2}/RT} e^{-\Delta G_{ISC_1}/RT} e^{-\Delta G_{ISC_2}/RT} \right) + \left(e^{-\Delta G_{FADH}/RT} e^{-\Delta G_{FADH_2}/RT} e^{-\Delta G_{ISC_1}/RT} e^{-\Delta G_{ISC_3}/RT} \right) \\
& + \left(e^{-\Delta G_{FADH}/RT} e^{-\Delta G_{FADH_2}/RT} e^{-\Delta G_{ISC_1}/RT} e^{-\Delta G_{SQ}/RT} \right) + \left(e^{-\Delta G_{FADH}/RT} e^{-\Delta G_{FADH_2}/RT} e^{-\Delta G_{ISC_2}/RT} e^{-\Delta G_{ISC_3}/RT} \right) + \\
& + \left(e^{-\Delta G_{FADH}/RT} e^{-\Delta G_{FADH_2}/RT} e^{-\Delta G_{ISC_2}/RT} e^{-\Delta G_{SQ}/RT} \right) + \left(e^{-\Delta G_{FADH}/RT} e^{-\Delta G_{FADH_2}/RT} e^{-\Delta G_{ISC_3}/RT} e^{-\Delta G_{SQ}/RT} \right) + \\
& + \left(e^{-\Delta G_{FADH}/RT} e^{-\Delta G_{ISC_1}/RT} e^{-\Delta G_{ISC_2}/RT} e^{-\Delta G_{ISC_3}/RT} \right) + \left(e^{-\Delta G_{FADH}/RT} e^{-\Delta G_{ISC_1}/RT} e^{-\Delta G_{ISC_2}/RT} e^{-\Delta G_{SQ}/RT} \right) + \\
& + \left(e^{-\Delta G_{FADH}/RT} e^{-\Delta G_{ISC_1}/RT} e^{-\Delta G_{ISC_3}/RT} e^{-\Delta G_{SQ}/RT} \right) + \left(e^{-\Delta G_{FADH}/RT} e^{-\Delta G_{ISC_2}/RT} e^{-\Delta G_{ISC_3}/RT} e^{-\Delta G_{SQ}/RT} \right) + \\
& + \left(e^{-\Delta G_{ISC_1}/RT} e^{-\Delta G_{ISC_2}/RT} e^{-\Delta G_{ISC_3}/RT} e^{-\Delta G_{SQ}/RT} \right)
\end{aligned} \tag{Eq. S3.49}$$

$$S_X^0 = 1 \tag{Eq. S3.50}$$

$$S_{FADH}^1 = \frac{\left(e^{-\Delta G_{FADH}/RT} \right)}{D_1} \tag{Eq. S3.51}$$

$$S_{FAD}^1 = 1 - S_{FADH}^1 \tag{Eq. S3.52}$$

$$S_{ISC_{3,red}}^1 = \frac{\left(e^{-\Delta G_{ISC_3}/RT} \right)}{D_1} \tag{Eq. S3.53}$$

$$S_{ISC_{3,ox}}^1 = 1 - S_{ISC_3}^1 \tag{Eq. S3.54}$$

$$S_{\notin SQ, ISC_{3,ox}}^1 = 1 - S_{ISC_3}^1 - S_{SQ}^1 \tag{Eq. S3.55}$$

$$S_{ISC_{1,ox},ISC_{3,ox}}^1 = \frac{\left(e^{-\Delta G_{FADH}/RT} + e^{-\Delta G_{ISC_2}/RT} + e^{-\Delta G_{SQ}/RT} \right)}{D_1} \quad \text{Eq. S3.56}$$

$$S_{FADH}^2 = \frac{\left(e^{-\Delta G_{FADH}/RT} \right) \left(e^{-\Delta G_{ISC_1}/RT} + e^{-\Delta G_{ISC_2}/RT} + e^{-\Delta G_{ISC_3}/RT} + e^{-\Delta G_{SQ}/RT} \right)}{D_2} \quad \text{Eq. S3.57}$$

$$S_{FADH_2}^2 = \frac{\left(e^{-\Delta G_{FADH}/RT} e^{-\Delta G_{FADH_2}/RT} \right)}{D_2} \quad \text{Eq. S3.58}$$

$$S_{FAD}^2 = 1 - S_{FADH}^2 - S_{FADH_2}^2 \quad \text{Eq. S3.59}$$

$$S_{ISC_{3,red}}^2 = \frac{\left(e^{-\Delta G_{ISC_3}/RT} \right) \left(e^{-\Delta G_{FADH}/RT} + e^{-\Delta G_{ISC_1}/RT} + e^{-\Delta G_{ISC_2}/RT} + e^{-\Delta G_{SQ}/RT} \right)}{D_2} \quad \text{Eq. S3.60}$$

$$S_{ISC_{3,ox}}^2 = 1 - S_{ISC_{3,red}}^2 \quad \text{Eq. S3.61}$$

$$S_{ISC_{1,red},ISC_{3,red}}^2 = \frac{\left(e^{-\Delta G_{ISC_3}/RT} e^{-\Delta G_{ISC_1}/RT} \right)}{D_2} \quad \text{Eq. S3.62}$$

$$S_{ISC_{1,ox},ISC_{3,ox}}^2 = 1 - S_{ISC_{1,red},ISC_{3,red}}^2 \quad \text{Eq. S3.63}$$

$$S_{SQ \sim ISC_{3,red}}^2 = \frac{\left(e^{-\Delta G_{ISC_3}/RT} e^{-\Delta G_{SQ}/RT} \right)}{D_2} \quad \text{Eq. S3.64}$$

$$S_{\notin SQ,ISC_{3,ox}}^2 = 1 - S_{SQ \sim ISC_{3,red}}^2 \quad \text{Eq. S3.65}$$

$$S_{FADH}^3 = \frac{\left(e^{-\Delta G_{FADH}/RT} \right) \left(e^{-\Delta G_{ISC_1}/RT} e^{-\Delta G_{ISC_2}/RT} + e^{-\Delta G_{ISC_1}/RT} e^{-\Delta G_{ISC_3}/RT} + e^{-\Delta G_{ISC_1}/RT} e^{-\Delta G_{SQ}/RT} + e^{-\Delta G_{ISC_2}/RT} e^{-\Delta G_{ISC_3}/RT} + e^{-\Delta G_{ISC_2}/RT} e^{-\Delta G_{SQ}/RT} + e^{-\Delta G_{ISC_3}/RT} e^{-\Delta G_{SQ}/RT} \right)}{D_3} \quad \text{Eq. S3.66}$$

$$S_{FADH_2}^3 = \frac{\left(e^{-\Delta G_{FADH}/RT} e^{-\Delta G_{FADH_2}/RT} \right) \left(e^{-\Delta G_{ISC_1}/RT} + e^{-\Delta G_{ISC_2}/RT} + e^{-\Delta G_{ISC_3}/RT} + e^{-\Delta G_{SQ}/RT} \right)}{D_3} \quad \text{Eq. S3.67}$$

$$S_{FAD}^3 = 1 - S_{FADH}^3 - S_{FADH_2}^3 \quad \text{Eq. S3.68}$$

$$S_{ISC_{3,red}}^3 = \frac{\left(e^{-\Delta G_{ISC_3}/RT} \right) \left(e^{-\Delta G_{FADH}/RT} e^{-\Delta G_{FADH_2}/RT} + e^{-\Delta G_{FADH}/RT} e^{-\Delta G_{ISC_1}/RT} + e^{-\Delta G_{FADH}/RT} e^{-\Delta G_{ISC_2}/RT} + e^{-\Delta G_{FADH}/RT} e^{-\Delta G_{SQ}/RT} + e^{-\Delta G_{ISC_1}/RT} e^{-\Delta G_{ISC_2}/RT} + e^{-\Delta G_{ISC_1}/RT} e^{-\Delta G_{SQ}/RT} + e^{-\Delta G_{ISC_2}/RT} e^{-\Delta G_{SQ}/RT} \right)}{D_3} \quad \text{Eq. S3.69}$$

$$S_{ISC_{3,ox}}^3 = 1 - S_{ISC_{3,red}}^3 \quad \text{Eq. S3.70}$$

$$S_{ISC_{1,red}, ISC_{3,red}}^3 = \frac{\left(e^{-\Delta G_{ISC_1}/RT} e^{-\Delta G_{ISC_3}/RT} \right) \left(e^{-\Delta G_{FADH}/RT} + e^{-\Delta G_{ISC_2}/RT} + e^{-\Delta G_{SQ}/RT} \right)}{D_3} \quad \text{Eq. S3.71}$$

$$S_{SQ-ISC_{3,red}}^3 = \frac{\left(e^{-\Delta G_{ISC_3}/RT} e^{-\Delta G_{SQ}/RT} \right) \left(e^{-\Delta G_{FADH}/RT} + e^{-\Delta G_{ISC_1}/RT} + e^{-\Delta G_{ISC_2}/RT} \right)}{D_3} \quad \text{Eq. S3.72}$$

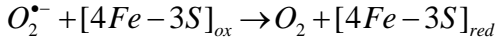
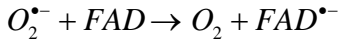
$$S_{FADH}^4 = \frac{\left(e^{-\Delta G_{FADH}/RT} \right) \left(e^{-\Delta G_{ISC_1}/RT} e^{-\Delta G_{ISC_2}/RT} e^{-\Delta G_{ISC_3}/RT} + e^{-\Delta G_{ISC_1}/RT} e^{-\Delta G_{ISC_2}/RT} e^{-\Delta G_{SQ}/RT} + e^{-\Delta G_{ISC_1}/RT} e^{-\Delta G_{ISC_3}/RT} e^{-\Delta G_{SQ}/RT} + e^{-\Delta G_{ISC_2}/RT} e^{-\Delta G_{ISC_3}/RT} e^{-\Delta G_{SQ}/RT} \right)}{D_4} \quad \text{Eq. S3.73}$$

$$S_{FADH_2}^4 = \frac{\left(e^{-\Delta G_{FADH}/RT} e^{-\Delta G_{FADH_2}/RT} \right) \left(e^{-\Delta G_{ISC_1}/RT} e^{-\Delta G_{ISC_2}/RT} + e^{-\Delta G_{ISC_1}/RT} e^{-\Delta G_{ISC_3}/RT} + e^{-\Delta G_{ISC_2}/RT} e^{-\Delta G_{ISC_3}/RT} + e^{-\Delta G_{ISC_1}/RT} e^{-\Delta G_{SQ}/RT} + e^{-\Delta G_{ISC_2}/RT} e^{-\Delta G_{SQ}/RT} + e^{-\Delta G_{ISC_3}/RT} e^{-\Delta G_{SQ}/RT} \right)}{D_4} \quad \text{Eq. S3.74}$$

$$S_{ISC_{3,red}}^4 = \frac{\left(e^{-\Delta G_{ISC_3}/RT} \right) \left(e^{-\Delta G_{FADH}/RT} e^{-\Delta G_{FADH_2}/RT} e^{-\Delta G_{ISC_1}/RT} + e^{-\Delta G_{FADH}/RT} e^{-\Delta G_{FADH_2}/RT} e^{-\Delta G_{ISC_2}/RT} + e^{-\Delta G_{FADH}/RT} e^{-\Delta G_{FADH_2}/RT} e^{-\Delta G_{ISC_3}/RT} + e^{-\Delta G_{FADH}/RT} e^{-\Delta G_{FADH_2}/RT} e^{-\Delta G_{SQ}/RT} + e^{-\Delta G_{FADH}/RT} e^{-\Delta G_{ISC_1}/RT} e^{-\Delta G_{ISC_2}/RT} + e^{-\Delta G_{FADH}/RT} e^{-\Delta G_{ISC_1}/RT} e^{-\Delta G_{ISC_3}/RT} + e^{-\Delta G_{FADH}/RT} e^{-\Delta G_{ISC_2}/RT} e^{-\Delta G_{ISC_3}/RT} + e^{-\Delta G_{FADH}/RT} e^{-\Delta G_{ISC_1}/RT} e^{-\Delta G_{SQ}/RT} + e^{-\Delta G_{FADH}/RT} e^{-\Delta G_{ISC_2}/RT} e^{-\Delta G_{SQ}/RT} + e^{-\Delta G_{FADH}/RT} e^{-\Delta G_{ISC_3}/RT} e^{-\Delta G_{SQ}/RT} + e^{-\Delta G_{FADH_2}/RT} e^{-\Delta G_{ISC_1}/RT} e^{-\Delta G_{ISC_2}/RT} + e^{-\Delta G_{FADH_2}/RT} e^{-\Delta G_{ISC_1}/RT} e^{-\Delta G_{ISC_3}/RT} + e^{-\Delta G_{FADH_2}/RT} e^{-\Delta G_{ISC_2}/RT} e^{-\Delta G_{ISC_3}/RT} + e^{-\Delta G_{FADH_2}/RT} e^{-\Delta G_{ISC_1}/RT} e^{-\Delta G_{SQ}/RT} + e^{-\Delta G_{FADH_2}/RT} e^{-\Delta G_{ISC_2}/RT} e^{-\Delta G_{SQ}/RT} + e^{-\Delta G_{FADH_2}/RT} e^{-\Delta G_{ISC_3}/RT} e^{-\Delta G_{SQ}/RT} \right)}{D_3} \quad \text{Eq. S3.75}$$

$$S_{ISC_{1,red}, ISC_{3,red}}^4 = \frac{\left(e^{-\Delta G_{ISC_1}/RT} e^{-\Delta G_{ISC_3}/RT} \right) \left(e^{-\Delta G_{FADH}/RT} e^{-\Delta G_{FADH_2}/RT} + e^{-\Delta G_{FADH}/RT} e^{-\Delta G_{ISC_2}/RT} + e^{-\Delta G_{FADH}/RT} e^{-\Delta G_{SQ}/RT} \right)}{D_3} \quad \text{Eq. S3.76}$$

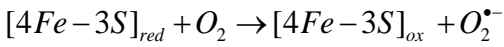
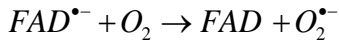
$$S_{SQ \sim ISC_{3,red}}^4 = \frac{\left(e^{-\Delta G_{SQ}/RT} e^{-\Delta G_{ISC_3}/RT} \right) \left(e^{-\Delta G_{FADH}/RT} e^{-\Delta G_{FADH_2}/RT} + e^{-\Delta G_{FADH}/RT} e^{-\Delta G_{ISC_1}/RT} + e^{-\Delta G_{FADH}/RT} e^{-\Delta G_{ISC_2}/RT} \right)}{D_4} \quad \text{Eq. S3.77}$$



$$k_{01}^{O_2^{\bullet-}/FAD} = \frac{k_f^{FADH^{\bullet-}}}{K_{eq}^{SO/FADH}} [O_2^{\bullet-}] S^0$$

$$k_{01}^{O_2^{\bullet-}/3Fe-4S} = \frac{k_f^{3Fe-4S}}{K_{eq}^{O_2^{\bullet-}/ISC_3}} [O_2^{\bullet-}] S^0$$

$$k_{01} = k_{01}^{O_2^{\bullet-}/FAD} + k_{01}^{O_2^{\bullet-}/3Fe-4S}$$



$$k_{10}^{O_2/FADH^{\bullet-}} = k_f^{FADH^{\bullet-}} [O_2] S_{FADH}^1$$

$$k_{10}^{O_2/ISC_3} = k_f^{3Fe-4S} [O_2] S_{ISC_{3,red}}^1$$

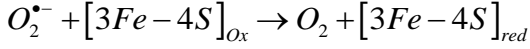
$$k_{10} = k_{10}^{O_2/FADH^{\bullet-}} + k_{10}^{O_2/ISC_3}$$

Eq. S3.80

$$\begin{aligned}
E_0 &\rightarrow E_2 \\
H_2O_2 + FAD &\rightarrow O_2 + FADH_2 \\
SUC + FAD &\rightarrow FUM + FADH_2 \\
QH_2 + [4Fe - 3S]_{ox} &\rightarrow Q^{\bullet-} \sim [4Fe - 3S]_{red} + 2H^+ \\
GEA_{red} + [4Fe - 3S]_{ox}, [2Fe - 2S]_{ox} &\rightarrow GEA_{ox} + [4Fe - 3S]_{red}, [2Fe - 2S]_{red} \\
k_{02}^{H_2O_2/FAD} &= \frac{k_f^{FADH_2}}{k_{eq}^{H_2O_2/FADH_2}} [H_2O_2] S^0 \\
k_{02}^{SUC/FAD} &= k_f^{SUC} \frac{[SUC]/K_{SUC}}{P_{FAD}} S^0 \\
k_{02}^{QH_2/\notin SQ, ISC_{3,ox}} &= \frac{k_f^{QH_2}}{K_{eq}^{QH_2/ISC_3}} \frac{[QH_2]/K_{QH_2}}{P_Q} S^0 \\
k_{02}^{GEA/ISC_{1,ox}, ISC_{3,ox}} &= \frac{k_f^{GEA}}{K_{eq}^{GEA/ISC_1, ISC_3}} [GEA] S^0 \\
k_{02} &= k_{02}^{H_2O_2/FAD} + k_{02}^{SUC/FAD} + k_{02}^{QH_2/\notin SQ, ISC_{3,ox}} + k_{02}^{GEA/ISC_{1,ox}, ISC_{3,ox}}
\end{aligned}$$

Eq. S3.81

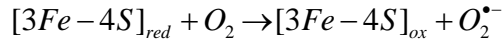
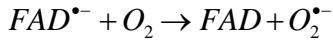
$$\begin{aligned}
E_2 &\rightarrow E_0 \\
O_2 + FADH_2 &\rightarrow H_2O_2 + FAD \\
FADH_2 + FUM &\rightarrow FAD + SUC \\
Q^{\bullet-} \sim [4Fe - 3S]_{red} + 2H^+ &\rightarrow QH_2 + [4Fe - 3S]_{ox} \\
GEA_{ox} + [4Fe - 3S]_{red}, [2Fe - 2S]_{red} &\rightarrow GEA_{red} + [4Fe - 3S]_{ox}, [2Fe - 2S]_{ox} \\
k_{20}^{O_2/FADH_2} &= k_f^{H_2O_2} [O_2] S_{FADH_2}^2 \\
k_{20}^{FUM/FADH_2} &= \frac{k_f^{SUC}}{k_{eq}^{FUM/FADH_2}} \frac{[FUM]/K_{FUM}}{P_{FAD}} S_{FADH_2}^2 \\
k_{20}^{SQ \sim ISC_3/QH_2} &= k_f^{QH_2} S_{SQ \sim ISC_{3,red}}^2 \\
k_{20}^{ISC_1, ISC_3/GAE} &= k_f^{GAE} S_{ISC_{1,red}, ISC_{3,red}}^2 \\
k_{20} &= k_{20}^{O_2/H_2O_2} + k_{20}^{FUM/FADH_2} + k_{20}^{SQ \sim ISC_3/QH_2} + k_{20}^{ISC_1, ISC_3/GAE}
\end{aligned}$$



$$k_{12}^{O_2^{\bullet-}/FAD} = \frac{k_f^{FADH}}{K_{eq}^{SO/FADH}} [O_2^{\bullet-}] S_{FAD}^1$$

$$k_{12}^{O_2^{\bullet-}/3Fe-4S} = \frac{k_f^{3Fe-4S}}{K_{eq}^{O_2^{\bullet-}/ISC_3}} [O_2^{\bullet-}] S_{ISC_3,ox}^1$$

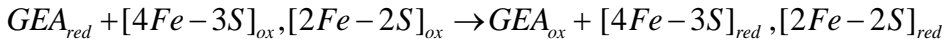
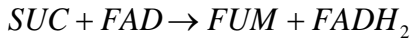
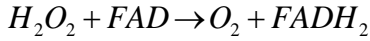
$$k_{12} = k_{12}^{O_2^{\bullet-}/FAD} + k_{12}^{O_2^{\bullet-}/3Fe-4S}$$



$$k_{21}^{O_2/FADH^{\bullet-}} = k_f^{FADH^{\bullet-}} [O_2] S_{FADH}^2$$

$$k_{21}^{O_2/3Fe-4S} = k_f^{3Fe-4S} [O_2] S_{ISC_3,red}^2$$

$$k_{21} = k_{21}^{O_2/FADH^{\bullet-}} + k_{21}^{O_2/3Fe-4S}$$



$$k_{13}^{H_2O_2/FAD} = \frac{k_f^{FADH_2}}{k_{eq}^{H_2O_2/FADH_2}} [H_2O_2] S_{FAD}^1$$

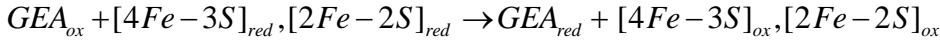
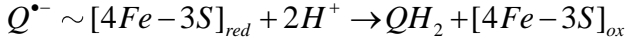
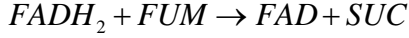
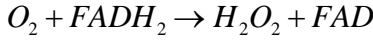
$$k_{13}^{SUC/FAD} = k_f^{SUC} \frac{[SUC]/K_{SUC}}{P_{FAD}} S_{FAD}^1$$

$$k_{13}^{QH_2/\notin SQ, ISC_3, ox} = \frac{k_f^{QH_2}}{K_{eq}^{QH_2/ISC_3}} \frac{[QH_2]/K_{QH_2}}{P_Q} S_{\notin SQ, ISC_3, ox}^1$$

$$k_{13}^{GEA/ISC_{1,ox}, ISC_{3,ox}} = \frac{k_f^{GEA}}{K_{eq}^{GEA/ISC_1, ISC_3}} [GEA] S_{ISC_{1,ox}, ISC_{3,ox}}^1$$

$$k_{13} = k_{13}^{H_2O_2/FAD} + k_{13}^{SUC/FAD} + k_{13}^{QH_2/\notin SQ, ISC_3, ox} + k_{13}^{GEA/ISC_{1,ox}, ISC_{3,ox}}$$

$$E_3 \rightarrow E_1 \quad \text{Eq. S3.85}$$



$$k_{31}^{O_2/FADH_2} = k_f^{H_2O_2} [O_2] S_{FADH_2}^3$$

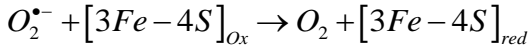
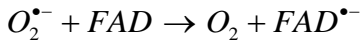
$$k_{31}^{FUM/FADH_2} = \frac{k_f^{SUC}}{k_{eq}^{FUM/FADH_2}} \frac{[FUM]/K_{FUM}}{P_{FAD}} S_{FADH_2}^3$$

$$k_{31}^{SQ \sim ISC_3/QH_2} = k_f^{QH_2} S_{SQ \sim [4Fe-3S]_{red}}^3$$

$$k_{31}^{ISC_1ISC_3/GAE} = k_f^{GAE} S_{ISC_1,red,ISC_3,red}^3$$

$$k_{31} = k_{31}^{O_2/H_2O_2} + k_{31}^{FUM/FADH_2} + k_{31}^{SQ \sim ISC_3/QH_2} + k_{31}^{ISC_1ISC_3/GAE}$$

$$E_2 \rightarrow E_3 \quad \text{Eq. S3.86}$$

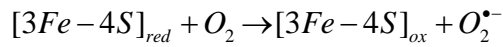
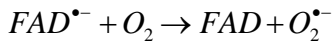


$$k_{23}^{O_2^{\bullet-}/FAD} = \frac{k_f^{FADH}}{K_{eq}^{SO/FADH}} [O_2^{\bullet-}] S_{FAD}^2$$

$$k_{23}^{O_2^{\bullet-}/3Fe-4S} = \frac{k_f^{3Fe-4S}}{K_{eq}^{O_2^{\bullet-}/ISC_3}} [O_2^{\bullet-}] S_{ISC_3,ox}^2$$

$$k_{23} = k_{23}^{O_2^{\bullet-}/FAD} + k_{23}^{O_2^{\bullet-}/3Fe-4S}$$

$$E_3 \rightarrow E_2 \quad \text{Eq. S3.87}$$

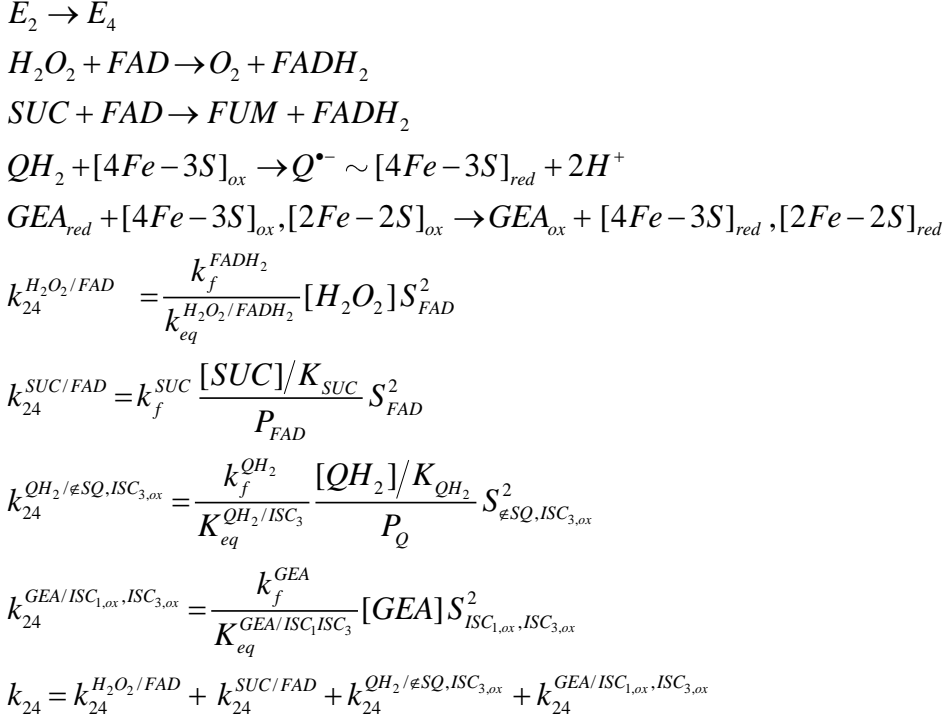


$$k_{32}^{O_2/FADH^{\bullet-}} = k_f^{FADH^{\bullet-}} [O_2] S_{FADH}^3$$

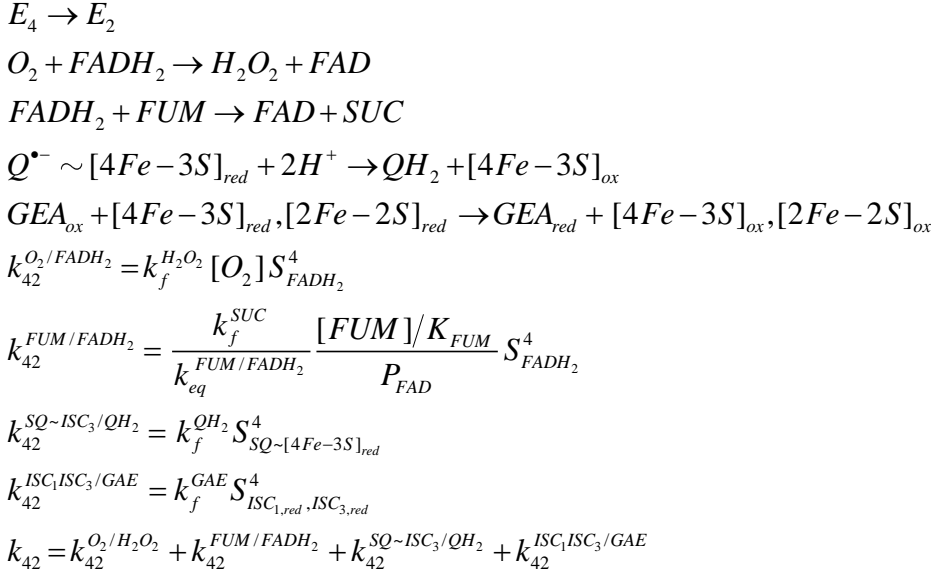
$$k_{32}^{O_2/3Fe-4S} = k_f^{3Fe-4S} [O_2] S_{ISC_3,red}^3$$

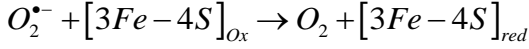
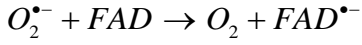
$$k_{32} = k_{32}^{O_2/FADH^{\bullet-}} + k_{32}^{O_2/3Fe-4S}$$

Eq. S3.88



Eq. S3.89

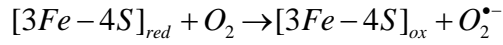
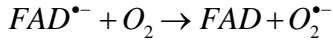




$$k_{34}^{O_2^{\bullet-}/FAD} = \frac{k_f^{FADH}}{K_{eq}^{SO/FADH}} [O_2^{\bullet-}] S_{FAD}^3$$

$$k_{34}^{O_2^{\bullet-}/3Fe-4S} = \frac{k_f^{3Fe-4S}}{K_{eq}^{O_2^{\bullet-}/ISC_3}} [O_2^{\bullet-}] S_{ISC_3,ox}^3$$

$$k_{34} = k_{34}^{O_2^{\bullet-}/FAD} + k_{34}^{O_2^{\bullet-}/3Fe-4S}$$



$$k_{43}^{O_2/FADH^{\bullet-}} = k_f^{FADH^{\bullet-}} [O_2] S_{FADH}^4$$

$$k_{43}^{O_2/3Fe-4S} = k_f^{3Fe-4S} [O_2] S_{ISC_3,red}^4$$

$$k_{43} = k_{43}^{O_2/FADH^{\bullet-}} + k_{43}^{O_2/3Fe-4S}$$

$$\begin{bmatrix} -(k_{01} + k_{02}) & k_{01} & k_{02} & 0 & 0 \\ k_{01} & -(k_{10} + k_{12} + k_{13}) & k_{21} & k_{31} & 0 \\ k_{02} & k_{12} & -(k_{20} + k_{21} + k_{23} + k_{24}) & k_{32} & k_{42} \\ 0 & k_{13} & k_{23} & -(k_{31} + k_{32} + k_{43}) & k_{34} \\ 0 & 0 & k_{24} & k_{34} & -(k_{42} + k_{43}) \\ 1 & 1 & 1 & 1 & 1 \end{bmatrix} \begin{bmatrix} E_0 \\ E_1 \\ E_2 \\ E_3 \\ E_4 \end{bmatrix} = \begin{bmatrix} 0 \\ 0 \\ 0 \\ 0 \\ 0 \\ 1 \end{bmatrix} \quad \text{Eq. S3.92}$$

$$J_{SUC} = E_{tot} \left(k_{02}^{SUC/FAD} E_0 + k_{13}^{SUC/FAD} E_1 + k_{24}^{SUC/FAD} E_2 - k_{20}^{FUM/FADH_2} E_2 - k_{31}^{FUM/FADH_2} E_3 - k_{42}^{FUM/FADH_2} E_4 \right) \quad \text{Eq. S3.93}$$

$$J_{O_2^{\bullet-}} = E_{tot} \left(k_{10}^{O_2/FADH} E_1 + k_{21}^{O_2/FADH} E_2 + k_{32}^{O_2/FADH} E_3 + k_{43}^{O_2/FADH} E_4 - k_{01}^{O_2^{\bullet-}/FAD} E_0 - k_{12}^{O_2^{\bullet-}/FAD} E_1 - k_{23}^{O_2^{\bullet-}/FAD} E_2 - k_{34}^{O_2^{\bullet-}/FAD} E_3 \right. \\ \left. + k_{10}^{O_2/3Fe-4S_{red}} E_1 + k_{21}^{O_2/3Fe-4S_{red}} E_2 + k_{32}^{O_2/3Fe-4S_{red}} E_3 + k_{43}^{O_2/3Fe-4S_{red}} E_4 - k_{01}^{O_2^{\bullet-}/3Fe-4S_{ox}} E_0 - k_{12}^{O_2^{\bullet-}/3Fe-4S_{ox}} E_1 \right. \\ \left. - k_{23}^{O_2^{\bullet-}/3Fe-4S_{ox}} E_2 - k_{34}^{O_2^{\bullet-}/3Fe-4S_{ox}} E_3 \right) \quad \text{Eq. S3.94}$$

$$J_{H_2O_2} = E_{tot} \left(k_{20}^{O_2/FADH_2} E_2 + k_{31}^{O_2/FADH_2} E_3 + k_{42}^{O_2/FADH_2} E_4 - k_{02}^{FADH_2/FAD} E_0 - k_{13}^{FADH_2/FAD} E_1 - k_{24}^{FADH_2/FAD} E_2 \right) \quad \text{Eq. S3.95}$$

$$J_{QH_2} = J_{SUC} - J_{O_2^{\bullet-}} / 2 - J_{H_2O_2} \quad \text{Eq. S3.96}$$

$$J_{GEA} = J_{SUC} - J_{O_2^*} / 2 - J_{H_2O_2} \quad \text{Eq. S3.97}$$

$$S_{i,j} = \frac{df_i}{dp_j} \frac{p_j}{f_i} \quad \text{Eq. S3.98}$$

$$\bar{S}_j = \frac{1}{N_i} \sum_{\forall i: \left| \frac{df_i}{dp_j} \right| > 0} |S_{i,j}| \quad \text{Eq. S3.99}$$

$$\frac{d[SUC]}{dt} = -J_{SUC} \quad \text{Eq. S3.100}$$

$$\frac{d[FUM]}{dt} = J_{SUC} \quad \text{Eq. S3.101}$$

$$J_{O_2} = 5 \times 10^{-7} \left[\frac{[QH_2]}{[QH_2] + 10^{-6}} \right] \cdot \left[\frac{[O_2]}{[O_2] + 5 \times 10^{-7}} \right] \quad \text{Eq. S3.102}$$

$$\frac{d[QH_2]}{dt} = (2 \cdot J_{O_2} - J_{QH_2}) / V_{lp} \quad \text{Eq. S3.103}$$

$$\frac{d[QH_2]}{dt} = -(2 \cdot J_{O_2} - J_{QH_2}) / V_{lp} \quad \text{Eq. S3.104}$$

$$\frac{d[O_2]}{dt} = -(J_{O_2^*} + J_{H_2O_2} + J_{O_2}) \quad \text{Eq. S3.105}$$

$$\frac{d[H_2O_2]}{dt} = J_{O_2^*} / 2 + J_{H_2O_2} \quad \text{Eq. S3.106}$$

REFERENCES

REFERENCES

- 1 Dhingra, R. and Kirshenbaum, L.A. (2015) Succinate dehydrogenase/complex II activity obligatorily links mitochondrial reserve respiratory capacity to cell survival in cardiac myocytes. *Cell Death Dis* 6, e1956–e1956
- 2 Hwang, M.-S. *et al.* (2014) Powerhouse down: Complex II dissociation in the respiratory chain. *Mitochondrion* 19, 20–28
- 3 Sun, F. *et al.* (2005) Crystal Structure of Mitochondrial Respiratory Membrane Protein Complex II. *Cell* 121, 1043–1057
- 4 Yankovskaya, V. (2003) Architecture of Succinate Dehydrogenase and Reactive Oxygen Species Generation. *Science* 299, 700–704
- 5 Maklashina, E. and Cecchini, G. (2010) The quinone-binding and catalytic site of complex II. *Biochimica et Biophysica Acta (BBA) - Bioenergetics* 1797, 1877–1882
- 6 Ruzicka, F.J. *et al.* (1975) Interaction of ubisemiquinone with a paramagnetic component in heart tissue. *Proceedings of the National Academy of Sciences* 72, 2886–2890
- 7 Salerno, J.C. and Ohnishi, T. (1980) Studies on the stabilized ubisemiquinone species in the succinate-cytochrome c reductase segment of the intact mitochondrial membrane system. *Biochemical Journal* 192, 769–781
- 8 Quinlan, C.L. *et al.* (2013) Sites of reactive oxygen species generation by mitochondria oxidizing different substrates. *Redox Biology* 1, 304–312
- 9 Brand, M.D. (2010) The sites and topology of mitochondrial superoxide production. *Experimental Gerontology* 45, 466–472
- 10 Boveris, A. *et al.* (1972) The cellular production of hydrogen peroxide. *Biochemical Journal* 128, 617–630
- 11 Sena, L.A. and Chandel, N.S. (2012) Physiological Roles of Mitochondrial Reactive Oxygen Species. *Molecular Cell* 48, 158–167
- 12 Finkel, T. (1998) Oxygen radicals and signaling. *Current Opinion in Cell Biology* 10, 248–253
- 13 Brand, M.D. (2016) Mitochondrial generation of superoxide and hydrogen peroxide as the source of mitochondrial redox signaling. *Free Radical Biology and Medicine* 100, 14–31
- 14 Bazil, J.N. (2017) Analysis of a Functional Dimer Model of Ubiquinol Cytochrome c Oxidoreductase. *Biophysical Journal* 113, 1599–1612

- 15 Chouchani, E.T. *et al.* (2014) Ischaemic accumulation of succinate controls reperfusion injury through mitochondrial ROS. *Nature* 515, 431–435
- 16 Chouchani, E.T. *et al.* (2016) A Unifying Mechanism for Mitochondrial Superoxide Production during Ischemia-Reperfusion Injury. *Cell Metabolism* 23, 254–263
- 17 Hausenloy, D.J. and Yellon, D.M. (2013) Myocardial ischemia-reperfusion injury: a neglected therapeutic target. *J. Clin. Invest.* 123, 92–100
- 18 Raha, S. and Robinson, B.H. (2001) Mitochondria, oxygen free radicals, and apoptosis. *American Journal of Medical Genetics* 106, 62–70
- 19 Raha, S. and Robinson, B.H. (2000) Mitochondria, oxygen free radicals, disease and ageing. *Trends in Biochemical Sciences* 25, 502–508
- 20 Zorov, D.B. *et al.* (2014) Mitochondrial Reactive Oxygen Species (ROS) and ROS-Induced ROS Release. *Physiological Reviews* 94, 909–950
- 21 Bazil, J.N. *et al.* (2016) Catalytic Coupling of Oxidative Phosphorylation, ATP Demand, and Reactive Oxygen Species Generation. *Biophysical Journal* 110, 962–971
- 22 Duong, Q.V. *et al.* (2020) Calcium overload decreases net free radical emission in cardiac mitochondria. *Mitochondrion* 51, 126–139
- 23 Bazil, J.N. *et al.* (2014) Determining the origins of superoxide and hydrogen peroxide in the mammalian NADH:ubiquinone oxidoreductase. *Free Radical Biology and Medicine* 77, 121–129
- 24 Quinlan, C.L. *et al.* (2012) Mitochondrial Complex II Can Generate Reactive Oxygen Species at High Rates in Both the Forward and Reverse Reactions*. *Journal of Biological Chemistry* 287, 27255–27264
- 25 Konstam, M.A. *et al.* (2018) Evaluation and Management of Right-Sided Heart Failure: A Scientific Statement From the American Heart Association. *Circulation* 137,
- 26 Harjola, V.-P. *et al.* (2016) Contemporary management of acute right ventricular failure: a statement from the Heart Failure Association and the Working Group on Pulmonary Circulation and Right Ventricular Function of the European Society of Cardiology. *European Journal of Heart Failure* 18, 226–241
- 27 Mills, E.L. *et al.* (2016) Succinate Dehydrogenase Supports Metabolic Repurposing of Mitochondria to Drive Inflammatory Macrophages. *Cell* 167, 457–470.e13
- 28 Bailis, W. *et al.* (2019) Distinct modes of mitochondrial metabolism uncouple T cell differentiation and function. *Nature* 571, 403–407

- 29 Orr, A.L. *et al.* (2012) A Refined Analysis of Superoxide Production by Mitochondrial sn-Glycerol 3-Phosphate Dehydrogenase*. *Journal of Biological Chemistry* 287, 42921–42935
- 30 Muller, F.L. *et al.* (2007) High rates of superoxide production in skeletal-muscle mitochondria respiring on both complex I- and complex II-linked substrates. *Biochemical Journal* 409, 491–499
- 31 Owens, K.M. *et al.* (2012) Genomic instability induced by mutant succinate dehydrogenase subunit D (SDHD) is mediated by O₂-• and H₂O₂. *Free Radical Biology and Medicine* 52, 160–166
- 32 Dong, L.-F. *et al.* (2011) Mitochondrial Targeting of Vitamin E Succinate Enhances Its Proapoptotic and Anti-cancer Activity via Mitochondrial Complex II*. *Journal of Biological Chemistry* 286, 3717–3728
- 33 Kluckova, K. *et al.* (2013) Mitochondrial complex II, a novel target for anti-cancer agents. *Biochimica et Biophysica Acta (BBA) - Bioenergetics* 1827, 552–564
- 34 Quinlan, C.L. *et al.* (2013) Chapter Twelve - The Determination and Analysis of Site-Specific Rates of Mitochondrial Reactive Oxygen Species Production. In *Methods in Enzymology* 526 (Cadenas, E. and Packer, L., eds), pp. 189–217, Academic Press
- 35 Siebels, I. and Dröse, S. (2013) Q-site inhibitor induced ROS production of mitochondrial complex II is attenuated by TCA cycle dicarboxylates. *Biochimica et Biophysica Acta (BBA) - Bioenergetics* 1827, 1156–1164
- 36 Paranagama, M.P. *et al.* (2010) Contribution of the FAD and quinone binding sites to the production of reactive oxygen species from *Ascaris suum* mitochondrial complex II. *Mitochondrion* 10, 158–165
- 37 Grivennikova, V.G. *et al.* (2017) Respiratory complex II: ROS production and the kinetics of ubiquinone reduction. *Biochimica et Biophysica Acta (BBA) - Bioenergetics* 1858, 109–117
- 38 Szeto, S.S.W. *et al.* (2007) Ubiquinone-binding Site Mutations in the *Saccharomyces cerevisiae* Succinate Dehydrogenase Generate Superoxide and Lead to the Accumulation of Succinate*. *Journal of Biological Chemistry* 282, 27518–27526
- 39 Cecchini, G. (2003) Function and structure of complex II of the respiratory chain. *Annu Rev Biochem* 72, 77–109
- 40 Penrose, R. (1955) A generalized inverse for matrices. *Mathematical Proceedings of the Cambridge Philosophical Society* 51, 406–413
- 41 Vinogradov, A.D. *et al.* (1979) Studies on the succinate dehydrogenating system. I. Kinetics of the succinate dehydrogenase interaction with a semiquinone radical of N,N,N',N'-

- tetramethyl-p-phenylenediamine. *Biochimica et Biophysica Acta (BBA) - Bioenergetics* 545, 141–154
- 42 Jones, A.J.Y. and Hirst, J. (2013) A spectrophotometric coupled enzyme assay to measure the activity of succinate dehydrogenase. *Analytical Biochemistry* 442, 19–23
- 43 Zeijlemaker, W.P. *et al.* (1969) Studies on succinate dehydrogenase: IV. Kinetics of the overall reaction catalysed by preparations of the purified enzyme. *Biochimica et Biophysica Acta (BBA) - Enzymology* 178, 213–224
- 44 Malyala, S. *et al.* (2019) Calcium phosphate precipitation inhibits mitochondrial energy metabolism. *PLoS Comput Biol* 15, e1006719
- 45 Vinnakota, K.C. *et al.* (2016) Feedback Regulation and Time Hierarchy of Oxidative Phosphorylation in Cardiac Mitochondria. *Biophys J* 110, 972–980
- 46 Vinogradov, A.D. *et al.* (1989) Regulation of succinate dehydrogenase and tautomerization of oxaloacetate. *Advances in Enzyme Regulation* 28, 271–280
- 47 Burger, N. *et al.* (2020) A sensitive mass spectrometric assay for mitochondrial CoQ pool redox state in vivo. *Free Radical Biology and Medicine* 147, 37–47
- 48 Vinogradov, A.D. *et al.* (1976) Reactivity of the Sulfhydryl Groups of Soluble Succinate Dehydrogenase. *European Journal of Biochemistry* 63, 365–371
- 49 Kenney, W. (1975) The reaction of N-ethylmaleimide at the active site of succinate dehydrogenase. *Journal of Biological Chemistry* 250, 3089–3094
- 50 Horsefield, R. *et al.* (2006) Structural and Computational Analysis of the Quinone-binding Site of Complex II (Succinate-Ubiquinone Oxidoreductase): A MECHANISM OF ELECTRON TRANSFER AND PROTON CONDUCTION DURING UBIQUINONE REDUCTION*. *Journal of Biological Chemistry* 281, 7309–7316
- 51 Miyadera, H. *et al.* (2003) Atpenins, potent and specific inhibitors of mitochondrial complex II (succinate-ubiquinone oxidoreductase). *Proceedings of the National Academy of Sciences* 100, 473–477
- 52 Grivennikova, V.G. *et al.* (2018) Oxygen-dependence of mitochondrial ROS production as detected by Amplex Red assay. *Redox Biology* 17, 192–199
- 53 Maklashina, E. *et al.* (2006) Differences in Protonation of Ubiquinone and Menaquinone in Fumarate Reductase from *Escherichia coli**. *Journal of Biological Chemistry* 281, 26655–26664
- 54 Hatefi, Y. *et al.* (1971) Succinate dehydrogenase. II. Enzymic properties. *Biochemistry* 10, 2517–2524

- 55 Messner, K.R. and Imlay, J.A. (2002) Mechanism of Superoxide and Hydrogen Peroxide Formation by Fumarate Reductase, Succinate Dehydrogenase, and Aspartate Oxidase*. *Journal of Biological Chemistry* 277, 42563–42571
- 56 Guo, J. and Lemire, B.D. (2003) The Ubiquinone-binding Site of the *Saccharomyces cerevisiae* Succinate-Ubiquinone Oxidoreductase Is a Source of Superoxide*. *Journal of Biological Chemistry* 278, 47629–47635
- 57 Imlay, J.A. and Fridovich, I. (1991) Assay of metabolic superoxide production in *Escherichia coli*. *Journal of Biological Chemistry* 266, 6957–6965
- 58 Goncalves, R.L.S. *et al.* (2015) Sites of Superoxide and Hydrogen Peroxide Production by Muscle Mitochondria Assessed *ex Vivo* under Conditions Mimicking Rest and Exercise*. *Journal of Biological Chemistry* 290, 209–227
- 59 Weinberg, S.E. *et al.* (2015) Mitochondria in the Regulation of Innate and Adaptive Immunity. *Immunity* 42, 406–417
- 60 West, A.P. *et al.* (2011) TLR signalling augments macrophage bactericidal activity through mitochondrial ROS. *Nature* 472, 476–480
- 61 Orii, Y. and Miki, T. (1997) Oxidation Process of Bovine Heart Ubiquinol-Cytochrome c Reductase as Studied by Stopped-flow Rapid-scan Spectrophotometry and Simulations Based on the Mechanistic Q Cycle Model*. *Journal of Biological Chemistry* 272, 17594–17604
- 62 Demin, O.V. *et al.* (1998) A model of O₂-generation in the complex III of the electron transport chain. *Mol Cell Biochem* 184, 21–33
- 63 Selivanov, V.A. *et al.* (2009) Bistability of Mitochondrial Respiration Underlies Paradoxical Reactive Oxygen Species Generation Induced by Anoxia. *PLOS Computational Biology* 5, e1000619
- 64 Guillaud, F. *et al.* (2014) Superoxide production by cytochrome bc₁ complex: A mathematical model. *Biochimica et Biophysica Acta (BBA) - Bioenergetics* 1837, 1643–1652
- 65 Ohnishi, T. *et al.* (1981) Thermodynamic and electron paramagnetic resonance characterization of flavin in succinate dehydrogenase. *J Biol Chem* 256, 5577–5582
- 66 Mailloux, R.J. (2015) Teaching the fundamentals of electron transfer reactions in mitochondria and the production and detection of reactive oxygen species. *Redox Biol* 4, 381–398
- 67 Tinoco, I. *et al.* (1995) *Physical chemistry: principles and applications in biological sciences*,
- 68 Alberty, R.A. (2005) *Thermodynamics of Biochemical Reactions*, John Wiley & Sons.

- 69 Ksenzhek, O.S. *et al.* (1977) Electrochemical properties of some redox indicators. *Bioelectrochemistry and Bioenergetics* 4, 346–357
- 70 Szentrimay, R. *et al.* (1977) Evaluation of Mediator-Titrants for the Indirect Coulometric Titration of Biocomponents. *Electrochemical Studies of Biological Systems* 38, 143–169

CHAPTER 4 – COMPUTATIONAL MODELING IDENTIFIES SITE-SPECIFIC SUPEROXIDE AND
HYDROGEN PEROXIDE PRODUCTION OF THE MITOCHONDRIAL ELECTRON TRANSPORT CHAIN

INTRODUCTION

Reactive oxygen species (ROS) were once considered by-products of cellular respiration but are now recognized as important signaling molecules [1–4]. Under pathological conditions like ischemia/reperfusion (I/R) injury, elevated ROS levels contribute to cell death [5]. This type of injury occurs after a period of partial or complete loss of tissue blood flow (ischemia) followed by the restoration of normal flow (reperfusion). Although reperfusion is necessary to salvage ischemic tissue, it can lead to significant tissue damage in a ROS-dependent manner [5]. This is an unfortunate common event associated with clinical situations such as organ transplantation [6] and hypovolemic shock [7]. Though I/R injury can affect any organ, metabolically active tissue such as brain and myocardium are most the sensitive to this injury. As a result, enormous efforts have been undertaken to ameliorate the detrimental effects of reperfusion-dependent oxidative stress. However, efforts to pharmacologically prevent oxidative stress to salvage ischemic tissue have not produced effective clinical treatment options [5,8,9].

In most mammalian cells, mitochondria are the primary source of ROS [10–12]. As such, mitochondrial ROS homeostasis is essential to maintaining mitochondrial and cellular physiology. In essence, ROS production and elimination act as countering forces which determine the mitochondrial net ROS emission. The mechanisms underlying ROS production have been reviewed extensively elsewhere [13,14], and only key details are provided here. The electron transport system (ETS) complexes I and III are accepted as the major mitochondrial ROS producers. Their respective contributions to total ROS emission varied according to the bioenergetic state of the organelle [10]. Matrix enzymes can likewise produce ROS, but their

contribution is often considered limited [15–17]. Under physiological conditions, forward electron transport (FET) occurs. Pyruvate (P) from glucose metabolism is oxidized through the Krebs cycle to generate NADH, which enters the ETS at complex I. Since electrons entering complex II from pyruvate metabolism is generally low [18,19], pyruvate is commonly considered as an NADH-linked substrate. Succinate (S) is oxidized by complex II or transported out of the matrix by the dicarboxylate carrier (DCC). Despite the different entry points, electrons converge at the quinone (Q) pool and are passed onto cytochrome c and ultimately molecular oxygen (O_2). Under metabolic states that favor increased membrane potential and a highly reduced Q pool, reverse electron transport (RET) occurs in which complex I enters the near equilibrium state and produces significant amounts of ROS. Thus, ROS production is enhanced under RET compared to FET.

The one- or two-electron reduction of O_2 by an ETS redox center upstream of complex IV produces superoxide or hydrogen peroxide, respectively. In complex I, the redox centers include a flavin mononucleotide at the NADH oxidase site (site I_F) [20], a semiquinone (SQ) at the Q reductase site (site I_Q) [21] and a chain of iron-sulfur (Fe-S) clusters that rapidly relay electrons between the two [22,23]. Likewise, complex II harbors a flavin adenine dinucleotide (FAD) at the succinate oxidase site (II_F), a Q reductase site (II_Q), and a chain of Fe-S clusters [24,25]. The mammalian complex III redox centers include cytochrome c_1 , a high- and low-potential b type heme, the Reiske iron-sulfur protein (ISP) and two quinone binding sites (Q_N and Q_P) [26]. Superoxide arising from complex III is generally accepted to originate from the semiquinone at the quinone binding site proximal to the intermembrane space (Q_P) [27].

The topic of site-specific ROS production has attracted experimental researchers for many years. Both pharmacological and genetic approaches have been utilized to dissect the contribution of redox centers to total mitochondrial ROS. While complexes I and III are the major ROS producers, the contribution of specific redox centers at physiologically relevant metabolic states remains elusive. For example, both site I_F [28–30] and I_Q [31] are proposed as major ROS-producing sites of complex I. Complex II was widely accepted as a negligible source of ETS ROS [32]. However, several more recent studies suggest that complex II produces significant amounts of ROS under appropriate conditions [33,34]. Such discrepancies in experimental data arise from the caveats inherent to experimental studies and have contributed to unsuccessful efforts to target oxidative stress in clinical settings. In particular, the use of chemical inhibitors and genetic models inevitably alter the native electron distribution in unpredictable patterns leading to epiphenomena and conflicting experimental results. Differences in experimental conditions including species, tissues, developmental stage, etc. introduce additional confounding factors that are often neglected and make comparing results from different studies difficult. Lastly, the pursuit is further impeded by the lack of a robust method to distinguish species-specific ROS without interfering with other mitochondrial and extra-mitochondrial processes.

Computational modeling is a useful platform to address these challenges. A computational model serves as a quantitative framework to analyze mitochondrial bioenergetic data from a single, unified perspective. Several models of mitochondria exist at varying levels of complexity, focus, and approach [35–42]. Some investigate the kinetics underlying ROS production by individual ETS complexes [38–40] while others integrate mitochondrial ROS

production and elimination in a substrate-specific context [41,42]. However, to our knowledge, none consistently reproduces a wide range of experimental data using a unified, coherent, and consistent framework. Thus, the origin of superoxide and hydrogen peroxide from the ETS remains elusive from a computational or experimental perspective.

We herein developed, analyzed, and corroborated a comprehensive model that simulates mitochondrial ROS homeostasis in the context of varied substrate utilization. This model is focused on ROS originated from the ETS and is referred to as the ETS-ROS model. Modules relevant to ROS originating from the ETS were individually developed, parametrized and corroborated against a variety of data sets [38–40]. These include complexes I, II and III. Biochemical reactions are thermodynamically consistent and mass-and-charge balanced. These modules are then incorporated into a single integrated framework, producing a model that is coherent and operates within biophysical constraints. The ETS-ROS model reproduces experimental data of not only net ROS production but also other mitochondrial bioenergetic variables. Using this approach, we have identified the regulation of ROS production by substrate metabolism via alterations to the NADH and Q pool redox states. The model also suggests that the scavenging system is saturable, allowing for cellular oxidative stress when ROS production overwhelms ROS elimination.

MATERIALS AND METHODS

General Approach to Modeling and Processes Included

Our modeling approach is modular and parsimonious, containing the models of complexes I [38], II [39] and III [40] previously published by our group. These models are biophysically detailed and thermodynamically consistent. They were individually calibrated and corroborated against a wide range of kinetic data sets. In this ETS-ROS model, the part of the Krebs cycle explicitly modeled are succinate oxidation and fumarate reduction. The remaining Krebs cycle reactions are not necessary to explain the experimental data and, thus, excluded to stay faithful to the parsimonious principle. Our in-house experimental data reveal a moderate level of malic enzyme (ME) activity in mitochondria isolated from guinea pig ventricular cardiomyocytes (Fig. S4.1), supporting its inclusion in the model. Several other studies also support the expression of ME in cardiac tissue of guinea pigs [43,44]. We found that including the ME reaction is necessary to fit the calibration data sets (Table 4.1). A summary of processes that are explicitly modeled are shown in Figure 4.1. Notations of the redox centers included in the text are described in Table 4.1.

Model Simulations

The model was numerically simulated using MATLAB (R2019a). The parameter optimization was performed on a Dell desktop PC (64-bit operating system and x64-based processor Intel® core™ i7-7700 CPU @3.60GHz and 16 GB RAM) using the Parallel Computing Toolbox. A parallelized simulated annealing algorithm was first used to globally search for feasible parameters which were then refined using a local, gradient-based optimization algorithm. The analytic solutions for the state-steady oxidation states were obtained with the

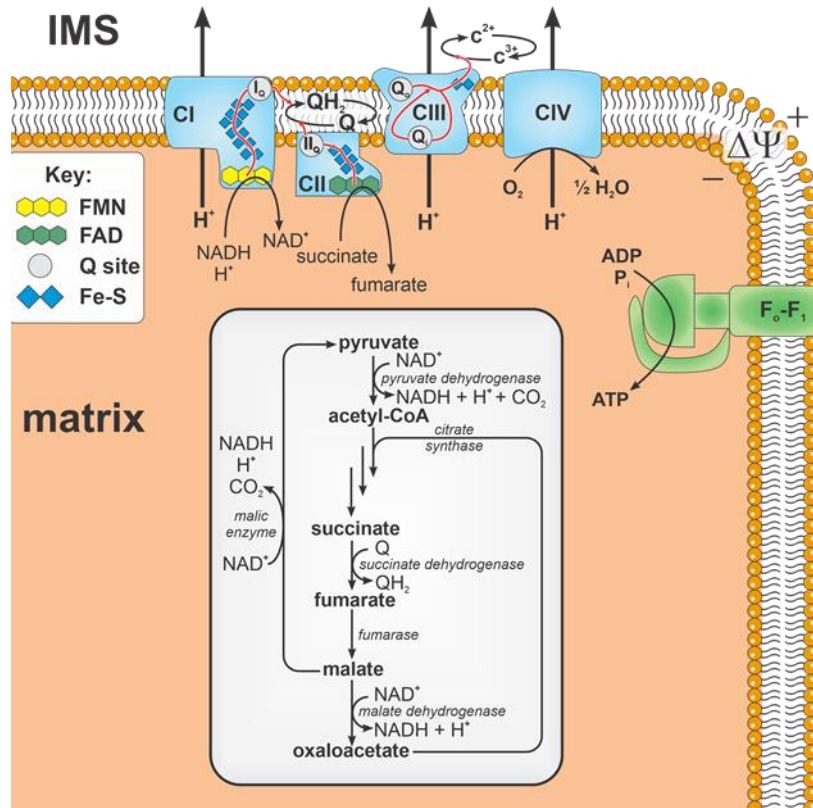


Figure 4.1 Schematic of explicitly modeled phenomena. The model consists of a partially lumped Krebs's cycle with non-lumped enzymatic reactions shown in the white box. Black arrows denote chemical reactions. Red arrows denote electron flux through redox centers. FMN = flavin mononucleotide, FAD = flavin adenine dinucleotide, Q = ubiquinone, QH₂ = ubiquinol, Fe-S = iron sulfur clusters, IMS = intermembrane space, CI – CIV = complexes I – IV, Q site = quinol/quinone binding site.

Table 4.1 Description of the ETS redox centers included in the model.

Notations	Description	Species formed
I _Q	Quinone reductase site of complex I (ubisemiquinone)	superoxide
I _{FMNH₂}	I _F , fully reduced form	superoxide, hydrogen peroxide
I _{FMNH•-}	I _F , radical form	superoxide
II _[3Fe-4S]	[3Fe-4S] cluster near the Q site in complex II	superoxide
II _{FADH₂}	II _F , fully reduced form	hydrogen peroxide
II _{FADH•-}	II _F , radical form	superoxide
III _{Q_p}	Q _p site in complex III	superoxide

MATLAB symbolic toolbox. When the standard deviation for data were not given, a standard deviation of 10% of the max value in a given data set was used during parameter estimation.

Data Sets

The intricate relationship between substrate utilization and ROS homeostasis necessitates that model calibration includes experimental data under both NADH- and QH₂-linked substrate supported respiration. The calibration data set includes the oxygen consumption rates (J_{O_2} , nmol/mg/min), net hydrogen peroxide emission rates ($J_{H_2O_2}$, pmol/mg/min) and NADH reduction (%) under NADH- and QH₂-linked supported respiration in both FET and RET modes. Forward electron transport occurs when respiration is supported by pyruvate/L-malate (P/M) and S in the presence of rotenone (S/R). Reverse electron transport occurs under QH₂-linked supported respiration when rotenone is absent (S). The calibrated model is subsequently challenged against a variety of data sets. The first validation data set includes the J_{O_2} and $J_{H_2O_2}$ data obtained when respiration is supported by both NADH- and QH₂-linked substrates (P/M/S). The second data set recapitulates the monotonic relationship of $J_{H_2O_2}$ on oxygen concentrations in FET mode. The list of all the data sets utilized in the construction, calibration and validation of the model is summarized in Table 4.2.

The majority of the experimental data used for calibrating the model were from a previous publication of ours [45]. In this study, we measured the oxygen consumption rate (J_{O_2} , nmol mg⁻¹ min⁻¹) and net hydrogen peroxide emission rate ($J_{H_2O_2}$, pmol mg⁻¹ min⁻¹) of mitochondria respiring on P/M, S and S/R. To avoid confounding factors due to different experimental conditions, we collected the L-M, NADH and P/M/S data sets under similar experimental conditions, following the same well-established protocol in our lab [46]. Briefly, all

Table 4.2 Summary of data used in this study.

Modelling Stage	Data Sets	References
Construction	$J_{O_2} - L-M$	This study
Calibration	$J_{O_2} - P/M, S/R$	Duong <i>et al.</i> [45]
	$J_{O_2} - S$	This study
	$J_{H_{2O_2}} - P/M, S/R$	Duong <i>et al.</i> [45]
	$J_{H_{2O_2}} - S$	This study
	$J_{H_{2O_2}}$ v.s. $[O_2]$	Duong <i>et al.</i> [45]
Validation	NADH – P/M, S/R, S	This study
	P/M/S – $J_{O_2}, J_{H_{2O_2}}$	This study

L-M: L-malate; P: pyruvate; S: succinate; R: rotenone

experiments were performed using a standard KCl-based mitochondrial suspension buffer containing 130 mM KCl, 5 mM K_2HPO_4 , 20 mM MOPS, 1 mM $MgCl_2$, 1 mM EGTA and 0.1% w/v BSA (pH of 7.1 at 37 °C). When used, the final concentrations of mitochondria, substrates, and inhibitors were 0.1 mg/mL mitochondria, 5 mM pyruvate (P), 1 mM L-malate (M), 10 mM succinate (S), 1 μ M rotenone (R), and 500 μ M ADP. The data were analyzed using the software MatLab. Experimental details that are unique to this study are presented below.

Model Parameters

The fixed model parameters are thermodynamic and kinetic data obtained from the literature including our prior work [38–40]. The adjustable parameters consist of parameters related to both ROS kinetics and substrate metabolism. Guided by the parsimonious principle, we chose the smallest set of adjustable parameters necessary to simulate the calibration data sets. The ROS kinetic parameters are concerned with the capacity of mitochondria to remove hydrogen peroxide and the transport of it from the matrix. The capacity of mitochondria to remove hydrogen peroxide is interchangeably referred to as the scavenging capacity in this paper. It is modelled in a Michaelis-Menten like fashion - saturable and dependent on the hydrogen peroxide concentration. The ETS parameters include the activity of complex I, the activity of complex III, the total enzyme amount of complex II and the inhibitory effect of oxaloacetate (OAA) on complex II. The remaining adjustable parameters are concerned with metabolite transport and substrate utilization (Table 4.3).

All adjustable parameters are identifiable; they are highly sensitive and uncorrelated. A parameter is considered highly sensitive if a small perturbation to the parameter results in a large perturbation in a model output. The opposite is true for an insensitive parameter. The

Table 4.3 Model adjustable parameters.

Parameter	Definition	Unit	Value	Sensitivity	Rank
$k_{f_{ME}}$	Rate constant of malic enzyme	$\text{nmol mg}^{-1} \text{min}^{-1} \text{M}^{-2}$	1.0762	0.0785	4
K_{DH}	ATPase feedback constant on dehydrogenase activity	M	1.1023	0.0071	10
N_{DH}	NADH/NAD ⁺ feedback constant on dehydrogenase activity	--	0.8790	0.0026	11
X_{DH}	Dehydrogenase activity	$\text{nmol mg}^{-1} \text{min}^{-1}$	1.0294	0.0309	8
$Et_{ot_{CIII}}$	$\text{nmol mg}^{-1} \text{min}^{-1}$	nmol mg^{-1}	1.0120	0.0952	2
$Et_{ot_{CI}}$	Complex I content	nmol mg^{-1}	1.0375	0.1119	1
$Et_{ot_{CII}}$	Complex II content	nmol mg^{-1}	0.9936	0.0219	9
V_{max_DCC}	Maximal capacity of the dicarboxylate carrier	$\text{nmol mg}^{-1} \text{min}^{-1}$	1.0666	0.0759	5
V_{max_FH}	Maximal capacity of fumarate hydratase	$\text{nmol mg}^{-1} \text{min}^{-1}$	1.0378	0.0013	12
$V_{max_scavenging}$	Maximal scavenging	$\text{nmol mg}^{-1} \text{min}^{-1}$	0.0400	0.0872	3
$K_{m_scavenging}$	[H ₂ O ₂] at half maximal scavenging capacity	nM	150	0.0715	7
$k_{f_{Emission_H2O2}}$	H ₂ O ₂ permeability rate constant	min^{-1}	13554	0.0715	6

normalized sensitivity coefficients are computed to inform the contribution of each adjustable parameter to the model output in similar manner done in our previous works [38–40].

Oxygen Consumption and Net Hydrogen Peroxide Emission Rates

The Oroboros Oxygraph (O2k) was used to simultaneously measure J_{O_2} ($\text{nmol mg}^{-1} \text{ min}^{-1}$) and $J_{H_2O_2}$ ($\text{pmol mg}^{-1} \text{ min}^{-1}$), described in detail in one of our previous publications [45]. Briefly, $J_{H_2O_2}$ values were measured using the Amplex UltraRed/Horseradish Peroxidase/Superoxide Dismutase assay. The reduction of hydrogen peroxide is coupled with the oxidation of Amplex UltraRed to resorufin. Resorufin fluorescence is converted to hydrogen peroxide concentration by using a hydrogen peroxide calibration curve obtained each experiment day from freshly prepared hydrogen peroxide standards. A post-hoc analysis of our previous $J_{H_2O_2}$ data sets using S as the substrate reveals that S-dependent $J_{H_2O_2}$ is highly sensitive to respiratory control ratio (RCR). Higher $J_{H_2O_2}$ values correspond to RCR greater than 18. Thus, we repeated $J_{H_2O_2}$ measurements using mitochondria with an RCR in this range. Mitochondria were energized with L-M, S or the P/M/S combination (leak state). An ADP bolus was added to stimulate oxidative phosphorylation (oxphos state) after 5 minutes under L-M supported respiration, 2.5 minutes under S- and 2 minutes under P/M/S-supported respiration. These time periods were chosen to allow measurement of steady-state J_{O_2} while maintaining adequate oxygen supply for oxidative phosphorylation turnover.

NADH Fluorescence Measurement

The fluorescence of NADH was monitored on an Olis DM-245 spectrofluorometer. Fluorescence was monitored with $\lambda_{\text{excitation}} = 355 \text{ nm}$ (8 nm bandpass filter) and $\lambda_{\text{emission}} = 450 \text{ nm}$ (13 nm bandpass filter). Baseline fluorescence was monitored for 1 minute followed by mitochondria addition. Substrates were added after 5 minutes of equilibration. A bolus of ADP stimulated oxidative phosphorylation. Fluorescence minima were obtained by uncoupling mitochondria with FCCP to produce maximally oxidized nicotinamide pools. Maximal fluorescence was obtained in the presence of rotenone to produce maximally reduced nicotinamide pools. Experimental data are shown in Fig. S4.2.

RESULTS

The experimental fidelity of the ETS-ROS model is critically related to its ability to predict the in vivo response of the ETS under a wide variety of physiological and pathophysiological scenarios. Including both FET and RET modes of ROS production data into model calibration was essential to pin down the parameters associated with site specific ROS fluxes under these diverse experimental conditions. The substrate combinations of P/M and S/R induce FET whereas the RET was favored with S as the sole substrate. We used the P/M/S data, which consist of both FET and RET processes, to corroborate the model. The model outputs are rounded up to the nearest digits.

Oxygen Consumption and Net Hydrogen Peroxide Emission Rates

As shown in Figure 4.2A-C, the calibrated model was compared to experimentally determined J_{O_2} (nmol/mg/min) and $J_{H_2O_2}$ (pmol/mg/min). With P/M as substrates, leak-state J_{O_2} (nmol/mg/min) are 30.3 ± 1.4 after 5 minutes and 27 ± 1.1 after 10 minutes. The corresponding J_{O_2} outputs from the model are 29 at 5 minutes and 7 at 10 minutes. The experimental oxphos-state J_{O_2} is 381.4 ± 20.6 (Fig. 4.2A) compared to the model output of 376. Similar consistency was obtained when mitochondria were energized with succinate in the presence of rotenone (S/R) (Fig. 4.2B), as well as succinate in the absence of rotenone (S) (Fig. 4.2C). The presence of rotenone did not affect leak-state J_{O_2} but resulted in a slightly elevated oxphos-state J_{O_2} . This is likely due to oxaloacetate accumulation, leading to complex II inhibition when rotenone is absent. The inhibitory effect of oxaloacetate on complex II has been thoroughly discussed in our previously published work and is supported by other studies. Experimental data and model outputs are summarized in Table 4.4.

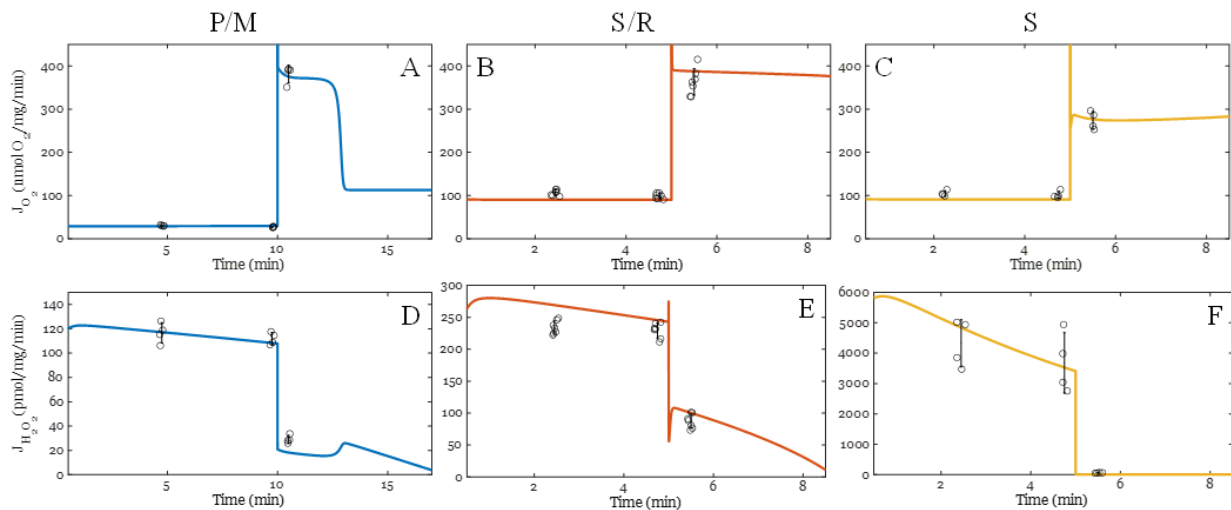


Figure 4.2 Model simulations of oxygen consumption and hydrogen peroxide emission rates. A-C: oxygen consumption rates (J_{O_2} , nmol/mg/min); D-F: net hydrogen peroxide emission rates ($J_{H_2O_2}$, pmol/mg/min) in forward electron transport (FET) and reverse electron transport (RET) modes. FET occurs when the substrates are P/M (A and D, blue) or S/R (B and E, orange). RET occurs when S is the substrate and rotenone is absent (C and F, yellow). The model outputs are represented by the solid lines. Individual data points are represented by the open black circles; error bars represent the standard deviations. Experimental data are obtained using mitochondria isolated from the ventricular cardiomyocytes of guinea pigs, as described in our previous work [45]. As shown, the model outputs are within the experimental ranges for both J_{O_2} and $J_{H_2O_2}$ in both FET and RET modes.

Table 4.4 Comparison of experimental and model J_{O_2} (pmol/mg/min).

Substrates	Respiratory state	Experimental data	Model outputs
Pyruvate/L-malate (P/M)	5-minute leak	30.3 ± 1.4	29
	10-minute leak	27 ± 1.1	27
	Oxphos	381.4 ± 20.6	376
Succinate/Rotenone (S/R)	2.5-minute leak	106.4 ± 6.7	90
	5.0-minute leak	98.5 ± 6.3	90
	Oxphos	363.3 ± 30.6	384
Succinate (S)	2.5-minute leak	106.9 ± 8.6	91
	5.0-minute leak	103.6 ± 4.5	91
	Oxphos	265.4 ± 36.3	275

The model is also able to capture the ROS emission kinetics by energized mitochondria operating in FET and RET modes during leak and oxphos states (Fig. 4.2D-E). Experimentally determined leak-state $J_{H_2O_2}$ values (pmol/mg/min) in mitochondria energized with P/M were 117 ± 8 at 5 minutes and 112 ± 5 at 10 minutes. The corresponding model outputs are 117 and 107, respectively. The oxphos-state $J_{H_2O_2}$ was experimentally determined to be 29 ± 4 in comparison to the model output of 18 pmol/mg/min (Fig. 4.2D). Under conditions favoring FET with succinate as substrate (S/R), the model outputs remain consistent with experimentally determined results (Fig. 4.2E). In the absence of rotenone, RET led to significantly higher $J_{H_2O_2}$ in vitro and in silico (Fig. 4.2F). Experimental data and model outputs are summarized in Table 4.4. Notably, changes in the model $J_{H_2O_2}$ are consistent with the dependence of ROS generation on membrane potential (Fig. S4.3). In all cases, the leak-state $J_{H_2O_2}$ values at the second time points (10 minutes for P/M and 5 minutes for S and S/R) are slightly decreased likely due to the decreased oxygen concentrations. Experimental data and model outputs are summarized in Table 4.5.

NADH Reduction States

Electrons from NADH are utilized to generate the protonmotive force. Thus, the redox state of the NADH pool is critical for mitochondrial ROS homeostasis. The model simulations of NADH reduction state must, therefore, be consistent with experimental data. As shown in Figure 4.3, succinate-supported respiration in the presence of rotenone yielded a more reduced NADH pool in both leak and oxphos states compared to the P/M substrates. With P/M as the substrates, turnover of NADH at complex I favors a more oxidized NADH pool in leak and oxphos states.

Table 4.5 Comparison of experimental and model $J_{H_2O_2}$.

Substrates	Respiratory state	Experimental data	Model outputs
Pyruvate/L-malate (P/M)	5-minute leak	117 ± 8	117
	10-minute leak	112 ± 5	108
	Oxphos	29 ± 4	18
Succinate/Rotenone (S/R)	2.5-minute leak	234 ± 10	269
	5.0-minute leak	229 ± 12	243
	Oxphos	87 ± 11	76
Succinate (S)	2.5-minute leak	$4,300 \pm 775$	4,946
	5.0-minute leak	$3,700 \pm 991$	3,465
	Oxphos	61 ± 7	80

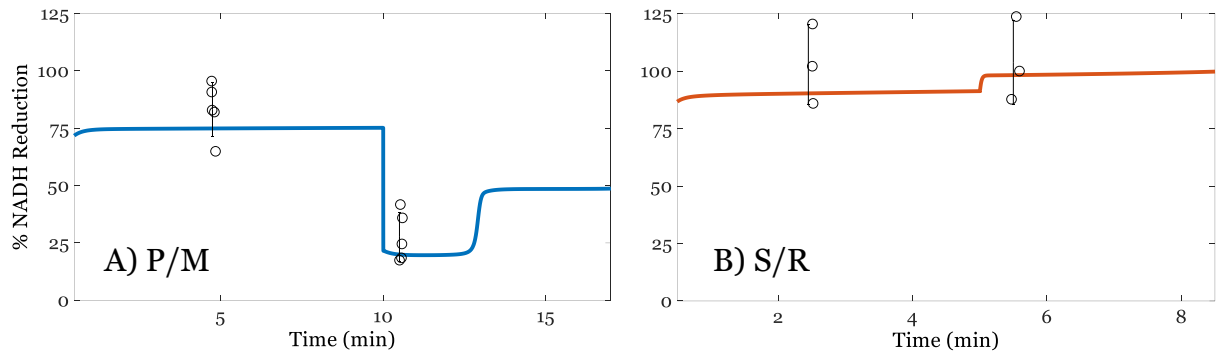


Figure 4.3 Model simulations of NADH reduction (%). A) Pyruvate/L-malate (P/M). B) Succinate with rotenone (S/R). The model outputs are represented by solid lines and within the experimental ranges. Individual data points are included; error bars represent the standard deviations. Experimental data are obtained using mitochondria isolated from the ventricular cardiomyocytes of guinea pigs. As shown, the model outputs are within the experimental ranges. Overall, succinate-supported respiration in the presence of rotenone maintains a more reduced NADH pool compared to P/M.

Oxygen Consumption, Net Hydrogen Peroxide Production Rates, and Oxygen Concentration Dynamics Under Both NADH- and QH₂-linked Substrate Metabolism

The final adjustable parameter set (Table 4.2) was used to predict the J_{O_2} , $J_{H_2O_2}$ and $[O_2]$ dynamics when mitochondria were energized with a combination of NADH- and QH₂-linked substrates (P/M/S). Under these conditions, electrons enter the ETS at complexes I and II then converge at the Q pool [47]. Such conditions favor the reduction of the Q pool and high membrane potential, resulting in ROS generation at complex I through RET. As shown in Figure 4.4, the ETS-ROS model outputs are consistent with experimental data using the final adjustable parameters. Experimentally determined leak-state J_{O_2} (nmol/mg/min) are 129 ± 5 at 2 minutes and 121 ± 12 at 4 minutes. The oxphos-state J_{O_2} is 729 ± 91 nmol/mg/min. The corresponding simulated J_{O_2} (nmol/mg/min) are 89 at 2-minute leak state, 89 at 4-minute leak state and 702 during oxphos (Fig. 4.4A). Experimentally measured $J_{H_2O_2}$ (pmol/mg/min) are $4,304 \pm 499$ at 2-minute leak state, $3,843 \pm 713$ at 4-minute leak state and 82 ± 7 during oxphos. The corresponding model predictions are 4,420, 3,461 and 33 pmol/mg/min (Fig. 4.4B). Importantly, both J_{O_2} and $J_{H_2O_2}$ were significantly elevated compared to substrate mixtures which favor electron entry at either complex I or II (Figs. 4.2A, B).

Monotonic Relationship Between $J_{H_2O_2}$ and $[O_2]$

Although $J_{H_2O_2}$ is essentially independent of $[O_2]$ until it drops below 10 μ M, the monotonic relationship between $J_{H_2O_2}$ and $[O_2]$ has been described by several groups [45,48,49]. To test whether the ETS-ROS model can adequately capture this dependence, we compared the simulated $J_{H_2O_2}$ to experimentally determined values at varying $[O_2]$. As shown,

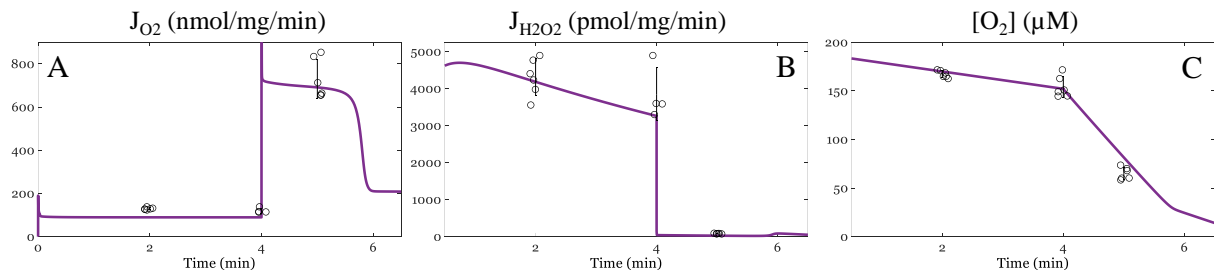


Figure 4.4 Model simulations of oxygen consumption, hydrogen peroxide emission, and oxygen concentration dynamics. Oxygen consumption rates (J_{O_2} , nmol/mg/min), hydrogen peroxide emission rates ($J_{H_2O_2}$, pmol/mg/min) and oxygen concentration dynamics when the substrates include both pyruvate/L-malate (P/M) and succinate (S). The model outputs are represented by the solid lines. Individual data points are shown by the open black circles; error bars represent the standard deviations. Experimental data are obtained using mitochondria isolated from the ventricular cardiomyocytes of guinea pigs, as described in our previous work [45]. Isolated mitochondria (0.1 mg/mL) were energized with P/M/S. The respiratory and net hydrogen peroxide emission rates were quantified simultaneously using the O2k oxygraph.

the model simulations (solid lines) are consistent with experimental data when mitochondria are energized with NADH-linked substrates and QH₂-linked substrates with RET inhibition. As shown, the monotonic relationship between J_{H₂O₂} and [O₂] is dependent on substrate utilization. When S/R are the substrates, the net J_{H₂O₂} is more sensitive to changes in [O₂], and a non-linearity is observed at low [O₂]. Model analysis reveals the non-linearity associated with hydrogen peroxide production at the lower [O₂] range results in the bent in total ROS production (Fig. 4.5A). Consequently, the net J_{H₂O₂} is non-linear. The scavenging activity in this [O₂] region also mirrors the hydrogen peroxide production, supporting the assumption that the scavenging system responds to changes in ROS production (Fig. 4.5B).

The high level of consistency between model simulations and experimental data demonstrate that our model is structurally sound and appropriately calibrated. We next used the ETS-ROS model to 1) investigate the monotonic relationship between J_{H₂O₂} and [O₂] and 2) predict the effects of substrate utilization on site-specific and species-specific contributions to mitochondrial ROS production during different respiratory states and ETS flux directions. These model predictions provide valuable mechanistic information about mitochondrial redox homeostasis that are experimentally infeasible.

Hydrogen Peroxide Production by Site I_F Underlies the Kinetics of Net ROS Emission Rates at Low [O₂]

Preliminary model analysis of the monotonic dependence between net J_{H₂O₂} and [O₂] reveals that, when mitochondria are energized by succinate and RET is inhibited, H₂O₂ production is sensitive to changes in [O₂] (Fig. 4.6). We previously proposed an empirical model

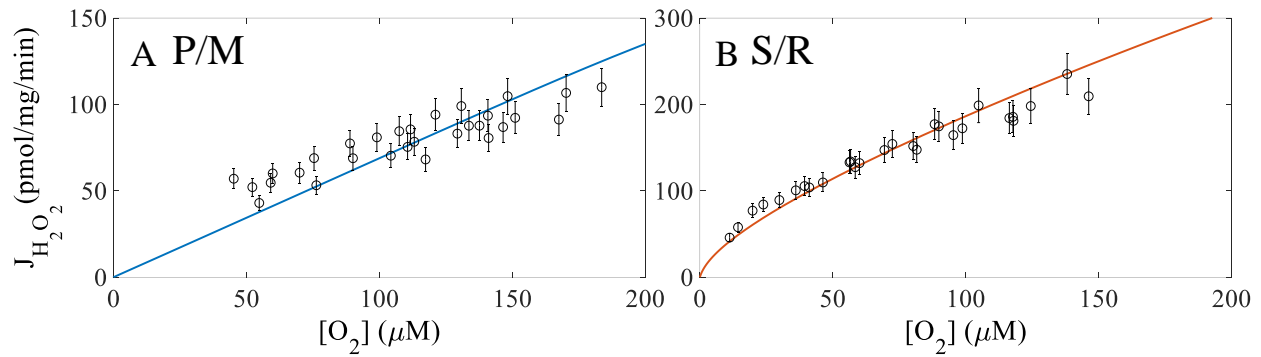


Figure 4.5 Model simulation of the monotonic relationship between net hydrogen peroxide emission rates and oxygen concentrations. Net hydrogen peroxide emission rates ($J_{H_2O_2}$, pmol/mg/min) and oxygen concentrations (μ M). Open, black circles represent experimental data; error bars represent the standard deviations. Model simulations are shown by the solid lines. Experimental data and simulated values were leak-state $J_{H_2O_2}$ values at varying oxygen concentrations. A) Mitochondria were energized with P/M. B) Mitochondria were energized with S and RET is inhibited (S/R). As shown, the model is able to capture the monotonic dependence between $J_{H_2O_2}$ and $[O_2]$ for both substrates. Importantly, the monotonicity appears linear with P/M and non-linear with S/R as the substrates.

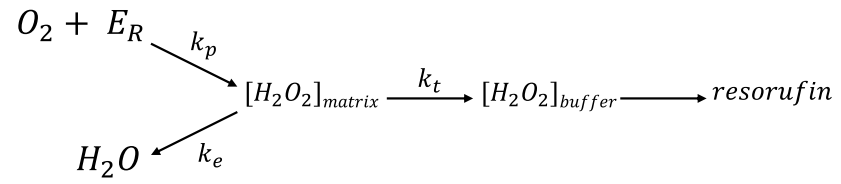


Figure 4.6. Schematic that relates the resorufin formation to steady-state net matrix H_2O_2 .
 The term E_R represents mitochondrial sites available for oxygen reduction.

to explain this phenomenon [45]. Briefly, the resorufin fluorescence corresponds directly to the net $J_{\text{H}_2\text{O}_2}$ emission ($[\text{H}_2\text{O}_2]_{\text{buffer}}$), which is proportional to the steady-state net matrix H_2O_2 ($[\text{H}_2\text{O}_2]_{\text{matrix}}$). A Michaelis-Menten like relationship was proposed to explain the $[\text{H}_2\text{O}_2]_{\text{matrix}}$ (Eq. 4.1). The $[\text{H}_2\text{O}_2]_{\text{matrix}}$ is positively related to the reduced electron donors (ER), oxygen concentration ($[\text{O}_2]$) and the rate constant of H_2O_2 production (k_p). It is negatively related to the rates at which $[\text{H}_2\text{O}_2]_{\text{matrix}}$ is removed by scavenging (k_e) and efflux from the matrix (k_t). While the empirical model was able to qualitatively describe the phenomenon, it is incapable of dissecting the contributions of individual redox centers to the net $J_{\text{H}_2\text{O}_2}$ measured. It also does not explain the different trends in the monotonic dependence between $J_{\text{H}_2\text{O}_2}$ and $[\text{O}_2]$ under P/M- and S/R-supported respiration, as communicated in our previous work.

$$[\text{H}_2\text{O}_2]_{\text{matrix}} = \frac{E_R [\text{O}_2]}{\frac{k_e + k_t}{k_p} + [\text{O}_2]} \quad \text{Eq. 4.1}$$

Using our computational ETS-ROS model, we dissected the individual processes underlying the net $J_{\text{H}_2\text{O}_2}$ measurements (Fig. 4.7). The total ROS (J_{ROS}) is the sum of hydrogen peroxide ($J_{\text{H}_2\text{O}_2}$) and half of the superoxide flux ($J_{\text{SO}}/2$). The active scavenging is the fraction of the maximal scavenging capacity curated from literature data (10). Mitochondria energized with S/R produce more total ROS compared to those energized with P/M. Expectedly, the scavenging system is enhanced under S/R-supported respiration, tracking with ROS production (Figs 4.7A, 4.7E). A linear dependence between total J_{ROS} and $[\text{O}_2]$ was observed, and H_2O_2 production is negligible when mitochondria were energized with P/M (Fig. 4.7A). However, J_{ROS} and scavenging activity both exhibit a nonlinear dependence on $[\text{O}_2]$ under SR-supported respiration (Fig. 4.7E). Additionally, the non-linearity associated with total J_{ROS} is due to $J_{\text{H}_2\text{O}_2}$ (dotted lines), which exceeds J_{SO} (dashed lines) until $[\text{O}_2]$ exceeds 150 μM .

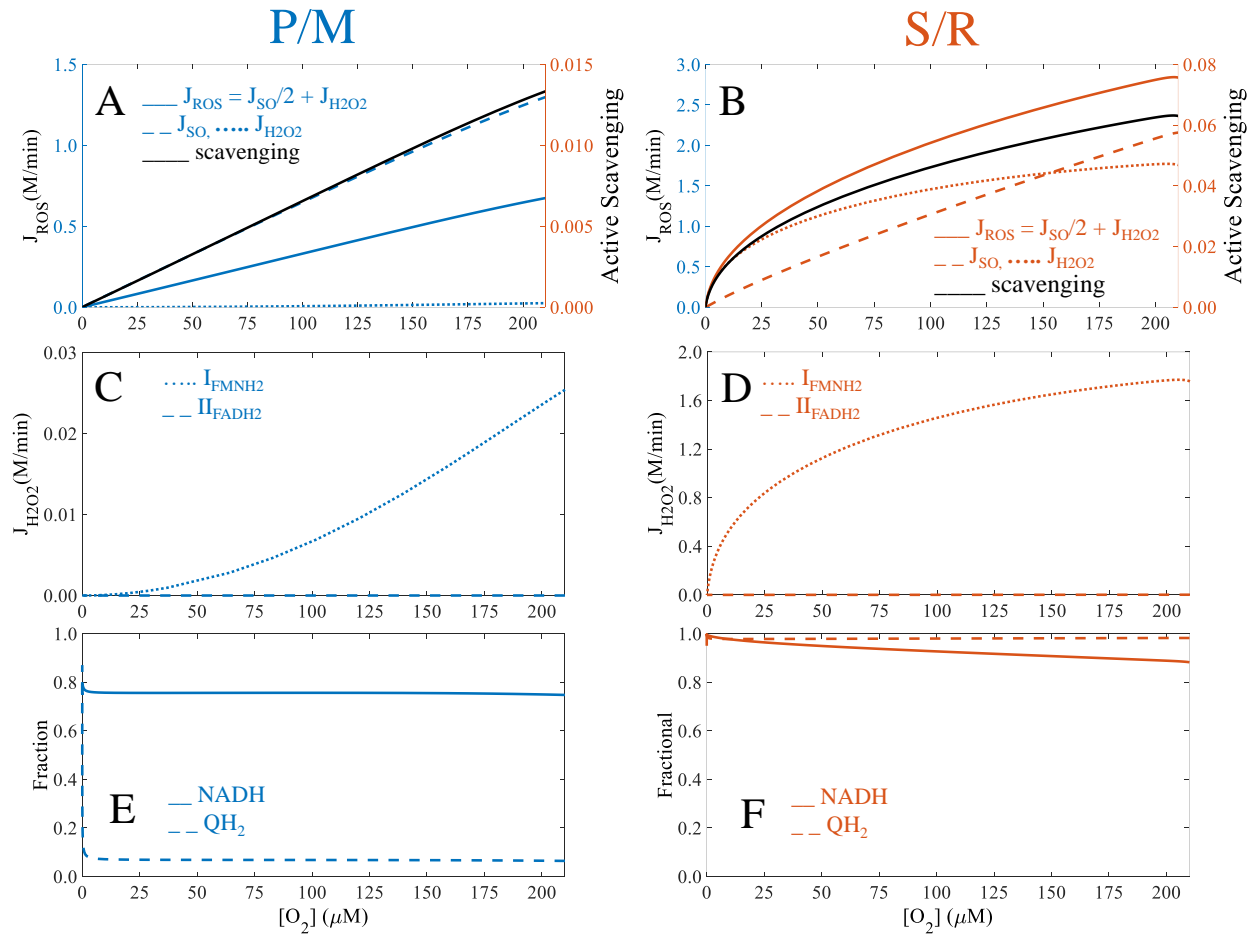


Figure 4.7 Model analysis of site-specific H_2O_2 production and bioenergetics variables critical to mitochondrial ROS production over a range of $[\text{O}_2]$ (μM). To further understand the substrate-specific monotonicity associated with the net $J_{\text{H}_2\text{O}_2}$ on $[\text{O}_2]$ (Fig. 4.5), model analysis was performed to extract additional mechanistic insights. The total ROS, superoxide and hydrogen peroxide fluxes are shown with active scavenging under P/M (A) and S/R (B) simulations. Total ROS flux (J_{ROS} , solid lines) is defined as the sum of hydrogen peroxide flux ($J_{\text{H}_2\text{O}_2}$, dotted lines) and half of the superoxide flux (J_{SO} , dashed lines). The fully reduced flavin of complex I contributes to most $J_{\text{H}_2\text{O}_2}$ under both P/M- (C) and S/R- (D) supported respiration. It also underlies the non-linearity associated with J_{ROS} at low $[\text{O}_2]$ in the S/R simulation. E-F) The model further suggests that the redox states of the NADH and the Q pools are highly sensitive to experimental conditions. Rotenone inhibits QH_2 oxidation at site I_O , which indirectly prevents effective NADH oxidation at site I_F . The NADH pool is, thus, significantly reduced in the S/R simulation, creating a condition conducive for H_2O_2 production.

Regardless of the substrates, most H_2O_2 originates from the fully reduced flavin of complex I (Figs. 4.7B & 4.7D). Interestingly, a similar non-linearity underlies H_2O_2 production by site I_F under S/R-supported respiration (Fig. 4.7D). Model analysis reveals distinguished NADH and Q pool redox states in these simulations, which explains the $J_{H_2O_2}$ profile associated with each substrate combinations. In the P/M simulation, the NADH pool is less reduced, and the Q pool is significantly oxidized (Fig. 4.7C). The presence of rotenone in the S/R simulation prevents quinol oxidation at site I_Q and NADH oxidation at site I_F , maintaining the NADH and Q pools in the mostly reduced states (Fig. 4.7G). The reduced NADH pool maintains the FMN site in the fully reduced state, favoring H_2O_2 production there. Electron flux downstream of site I_Q is unaffected, minimizing H_2O_2 production by the FAD site.

Site-Specific Superoxide Fluxes

As shown in Figure 4.8, the site-specific contributions to total superoxide production are determined by both electron sources (substrates), respiratory states and ETS flux directions. According to model analysis, sites II_Q and II_{FADH_2} do not contribute to total superoxide flux. The superoxide flux values are presented per pair of electrons passing through the ETS by dividing the model outputs by 2. This conversion is to stay consistent with Figure 4.7. The values are also shown in Table 4.6 in addition to the texts below.

During leak state (Fig. 4.8A), site III_{Qp} is the single greatest source of superoxide (0.1899 nmol/mg/min) in mitochondria respiring on P/M. Under these conditions, sites I_Q and I_{FMNH_2} contribute approximately equally to the total superoxide originated from complex I (0.1249 nmol/mg/min). Complex II contributes the least to total superoxide flux, and most of its superoxide arises from the $II_{[3Fe-4S]}$ (0.0835 nmol/mg/min). Under S/R-supported respiration,

P/M, S/R, S, P/M/S

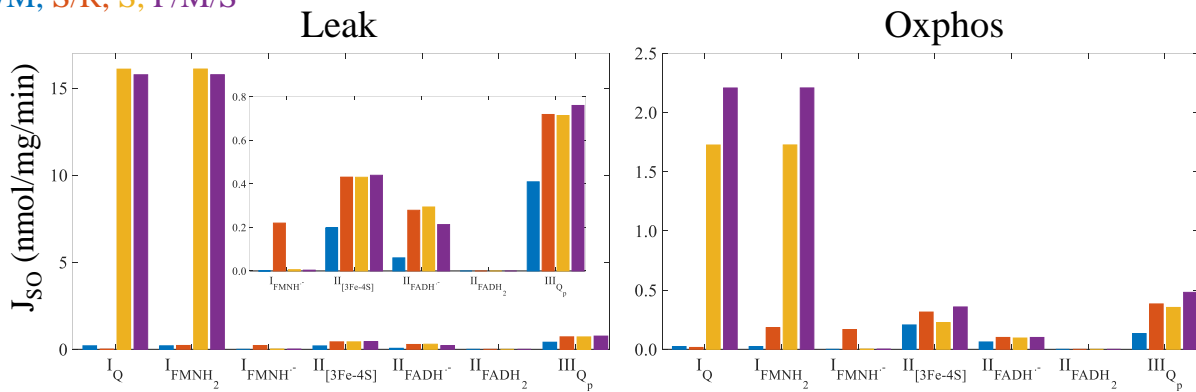


Figure 4.8 Model predictions of superoxide production at ETS redox centers in leak (A) and oxphos (B) states. In non-phosphorylating mitochondria (leak) energized with P/M or S/R, forward electron transport (FET) is favored whereas S and P/M/S favor reverse electron transport (RET). Complex I redox centers include the quinone reductase site (I_Q) and the flavin mononucleotide (I_{FMNH_2} = reduced flavin mononucleotide, $I_{FMNH\bullet}$ = flavin mononucleotide radical). Complex II redox centers are the [3Fe-4S] cluster ($II_{[3Fe-4S]}$) and the flavin adenine dinucleotide ($II_{FADH\bullet}$ = flavin adenine dinucleotide radical). The Q_p site resides in complex III (III_{Q_p}). Overall, superoxide production is lowest under P/M-supported respiration and minimized by phosphorylation. The highly reduced Q pool and a high membrane potential under S- and P/M/S-supported respiration maintain sites I_Q and I_F in the highly reduced states regardless of respiratory states, favoring superoxide production by these sites I_Q and I_F and making complex I the greatest combined source of superoxide.

Table 4.6 Model predictions of site-specific superoxide production (J_{SO} , nmol/mg/min) during leak and oxphos states supported by different substrates. The tabulated J_{SO} are per pair of electrons by dividing the model outputs by 2 to stay consistent with Fig. 4.7. Values less than 10^{-4} are shown as ~ 0 .

State	Leak				Oxphos			
Substrates	P/M	S/R	S	P/M/S	P/M	S/R	S	P/M/S
I _Q	0.1249	~ 0	7.9674	7.5381	0.0171	~ 0	0.9472	1.1906
I _{FMNH₂}	0.1249	0.1388	7.9674	7.5401	0.0171	0.0957	0.9475	1.1909
I _{FMNH₋}	~ 0	0.1388	~ 0	~ 0	~ 0	0.0957	~ 0	~ 0
II _[3Fe-4S]	0.0835	0.1876	0.1870	0.1915	0.0814	0.1317	0.1075	0.1531
II _{FADH₋}	0.0253	0.1404	0.1524	0.1072	0.0244	0.0464	0.0462	0.0491
III _{Qp}	0.1899	0.2833	0.2796	0.3097	0.0634	0.1489	0.1482	0.1983

site III_{Qp} remains the predominant single source of superoxide (0.2833 nmol/mg/min).

However, the II_[3Fe-4S] cluster becomes the second highest contributor to the total superoxide flux (0.1876 nmol/mg/min). Additionally, site II_{FADH•} also becomes an appreciable source of superoxide (0.1404 nmol/mg/min). Superoxide from complex I arises mostly from site I_F in both the radical and fully reduced forms (0.1388 nmol/mg/min per form).

The relative site-specific contributions to total superoxide flux are consistent under S- and P/M/S-supported respiration: $I_Q \approx I_{FMNH_2}$ (as $FMNH_2$) > III_{Qp} > II_[3Fe-4Fe] > II_{FADH•}. The superoxide fluxes at individual redox centers are also comparable. In particular, sites I_{FMNH₂} and I_Q contribute approximately equal amounts to complex I superoxide generation: 7.96 and 7.54 nmol/mg/min under S- and P/M/S-supported respiration, respectively. Superoxide originating from sites II_[3Fe-4S], II_{FADH•} and III_{Qp} are on the same order of magnitude. When S is the substrate, these fluxes are 0.187, 0.1524 and 0.2796 nmol/mg/min, respectively. When P/M/S are present, the fluxes are comparable at 0.1915, 0.1072 and 0.3097 nmol/mg/min, respectively. It is likely that electrons derived from pyruvate metabolism (P/M/S) lead to a slight decrease in superoxide from the FADH• radical and a slight increase in superoxide from site III_{Qp} as NADH-linked substrates favor FET mode.

During oxphos supported by P/M (Fig. 4.8B), site II_[3Fe-4S] becomes the greatest contributor to total superoxide followed by site III_{Qp} (0.0814 vs. 0.0634 nmol/mg/min). Superoxide from complex I originates from both sites I_Q and I_F, mostly as I_{FMNH₂} (0.0171 nmol/mg/min per site). When phosphorylation is supported by S/R, superoxide from site III_{Qp} slightly exceeds that from site II_[3Fe-4S]: 0.1489 vs. 0.1317 nmol/mg/min. However, site I_F is the greatest source of superoxide when superoxide fluxes from the FMNH₂ and FMNH• are

combined (0.0957 nmol/mg/min per redox state). Under conditions that favor RET in phosphorylating mitochondria, complex I remains the greatest source of superoxide with equal contributions from site I_Q and I_{FMNH₂}: 0.94 nmol/mg/min (S) and 1.19 nmol/mg/min (P/M/S). Superoxide fluxes from sites II_[3Fe-4S] and III_{Q_p} are 0.1075 and 0.1482 nmol/mg/min, respectively, in the presence of S. A slight increase is observed when P/M and S are both present: 0.1531 (S) and 0.1983 nmol/mg/min (P/M/S).

Site-Specific Hydrogen Peroxide Fluxes

As hydrogen peroxide results from two-electron redox reactions, only the I_{FMNH₂} and II_{FADH₂} are considered. Regardless of respiratory states and substrate sources, most hydrogen peroxide originate from the I_{FMNH₂} site (Fig. 4.9). The model predicts that J_{H₂O₂} produced by the I_{FMNH₂} site in non-phosphorylating mitochondria is 0.0182 and 1.7105 nmol/mg/min under P/M- and S/R-supported respiration, respectively. Oxphos decreases the membrane potential and subsequently J_{H₂O₂}. Phosphorylation supported by P/M and S/R produces 0.0182 and 1.7105 nmol H₂O₂/mg/min from the I_{FMNH₂} site, respectively. Thus, QH₂-linked substrate (S/R) metabolism in the presence of rotenone enhances leak- and oxphos-state J_{H₂O₂} arising from I_{FMNH₂}.

Also in leak state, RET is predominant when substrates are abundant and inhibitors are absent (S and P/M/S). The model predicts comparable hydrogen peroxide fluxes from I_{FMNH₂} under S- and P/M/S-supported respiration: 15.9336 and 15.0235 nmol/mg/min, respectively. Consequently, most of the decrease in total hydrogen peroxide due to oxphos results from decreased production by this site. However, phosphorylating mitochondria energized by P/M/S produce more hydrogen peroxide from the I_{FMNH₂} site compared to S alone: 2.2690 and 1.8043

P/M, S/R, S, P/M/S

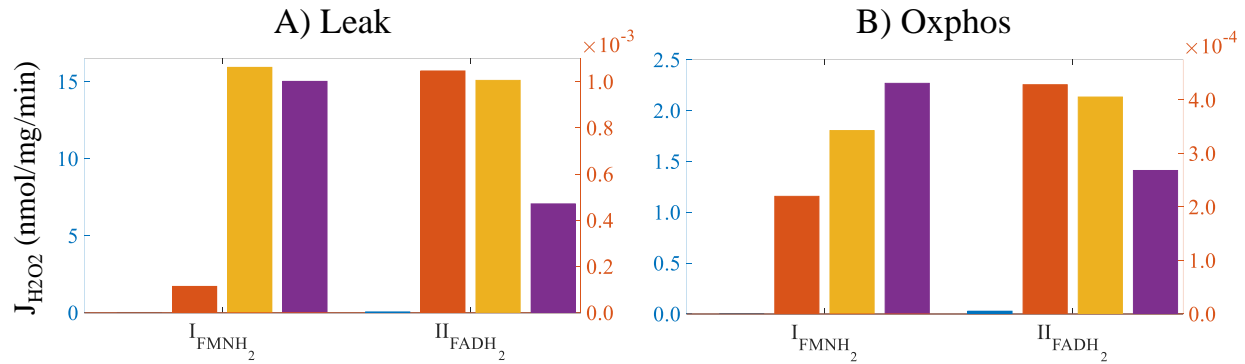


Figure 4.9 Model predictions of hydrogen peroxide production at ETS redox centers at leak (A) and oxphos (B) states. Only the I_{FMNH_2} and II_{FADH_2} are considered as hydrogen peroxide production requires 2 electrons. Left axis values are for I_{FMNH_2} , and right axis values are for II_{FADH_2} in non-phosphorylating mitochondria energized with P/M or S/R, forward electron transport (FET) is favored whereas S and P/M/S favor reverse electron transport (RET). Overall, hydrogen peroxide production is lowest under P/M-supported respiration and minimized by phosphorylation, similar to superoxide production. Regardless of the respiratory states and electron flux directions, most hydrogen peroxide originates from the I_{FMNH_2} .

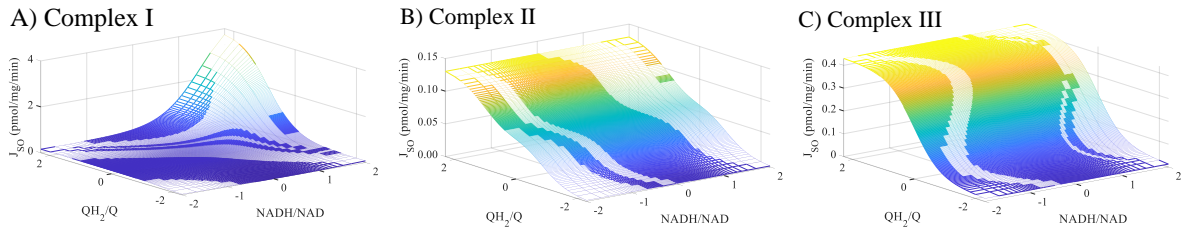
nmol/mg/min, respectively. In the P/M/S simulation, pyruvate metabolism reduces NADH through the Krebs cycle, resulting in a more reduced NADH pool (Fig. S4.2). Consequently, the I_{FMNH_2} site is more reduced under P/M/S-supported respiration, enhancing hydrogen peroxide arising from this site.

Effects of the NADH and Q pools' Reduction States on ROS Production

The corroborated model is further used to explore the effects of the NADH pool's and Q pool's reduction states on the superoxide and hydrogen fluxes (J_{SO} and $J_{H_2O_2}$, respectively) from individual complexes under P/M supported respiration (Fig. 4.10). This simulation exemplifies the utility of model in testing hypotheses that are not experimentally feasible. Specifically, the model is run to 5-minute steady state. All other state variables at the 5-minute steady state are fixed while the NADH/NAD⁺ and QH₂/Q ratios are varied.

In addition to complexes I and III, model analysis reveals appreciable superoxide production by complex II, in contrast to current consensus that it is a negligible source of ROS. Moreover, superoxide fluxes by complexes I, II and III are uniquely sensitive to the redox states of the NADH and Q pools. The reduced NADH and Q pools have a synergistic effect on complex I's superoxide production (Fig. 4.10A). As the NADH pool becomes more reduced, the sensitivity of complex I's superoxide is increased, and vice versa. In contrast, complexes II and III are more sensitive to changes in the Q pool's than the NADH pool's redox state (Figs. 4.10B, C). Hydrogen peroxide originates mostly from complex I in this simulation. Similar to superoxide production, hydrogen peroxide production by complex I peaks when both the NADH and Q pools become mostly reduced (Fig. 4.10D). At any combination of the NADH/NAD⁺ and QH₂/Q ratios, hydrogen peroxide originated from complex I is greater than that arising from complex II. Additionally,

Superoxide



Hydrogen Peroxide

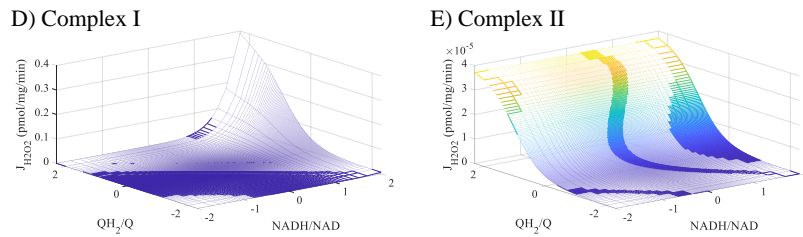


Figure 4.10 Model predictions of superoxide and hydrogen peroxide fluxes (J_{SO} and $J_{H_2O_2}$, respectively) from individual ETS complexes under P/M supported respiration. The state variables at 5-minute steady state are fixed except for the $NADH/NAD^+$ and QH_2/Q ratios. The combination of a mostly reduced Q and NADH pool favors J_{SO} and $J_{H_2O_2}$ by Complex I. Superoxide and hydrogen peroxide originating from complex II are more dependent on the reduction state of the Q pool than that of the NADH pool. Complex III shows a similar relationship between J_{SO} and the Q pool reduction state to that of complex II.

the reduction state of the Q pool exerts greater influence on hydrogen peroxide production by complex II than the NADH reduction state does (Fig. 4.10E).

Effects of Substrate Utilization and Electron Transport Mode on Scavenging Activity

The activity of the scavenging systems – namely, the glutathione and peroxiredoxin systems – to total scavenging activity in response to changes in ROS production remains an enigma for the same reasons that the origins of ROS under native conditions are inconclusive. Due to the lack of quantitative data, the scavenging system is modelled based on the assumptions that it is saturable and responsive to changes in matrix H_2O_2 production. Because regenerating the glutathione and thioredoxin pools indirectly relies on NADH, ROS scavenging has a limited capacity [10]. The responsive nature of the scavenging system to matrix H_2O_2 is necessary to keep net ROS production in the physiology range. In this model, these assumptions were adequate as the model outputs in the calibration and validation stages are consistent with experimental data. Thus, we used the model to predict active scavenging in the experimental conditions simulated in Figure 4.1. The model suggests that scavenging activity is lower in FET mode (Figs. 4.11A, B), which is consistent with lower ROS production (Figs 4.2D, E). The scavenging activity increases significantly under RET mode (Figs. 4.11C, D) to keep up with a significant increase in ROS production (Figs. 4.2F, 4.3B).

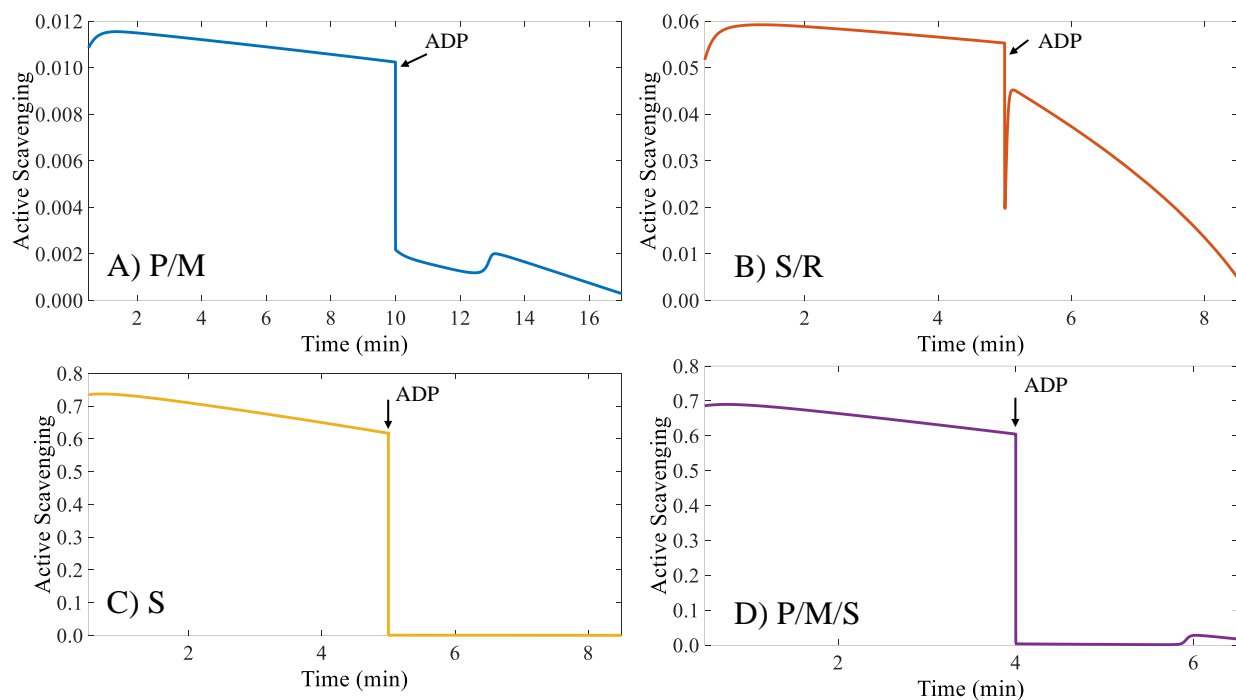


Figure 4.11 Model predictions of active scavenging under different metabolic conditions. Forward electron transport (FET) occurs under P/M- and S/R-supported respiration (A, B). Reverse electron transport occurs under S- and P/M/S-supported respiration (C, D). ADP addition results in maximal oxidative phosphorylation (oxphos state). During oxphos, the scavenging activity decreases regardless of the electron source and transport mode. Under RET mode, the scavenging activity is significantly increased but unable to keep the net $J_{H_2O_2}$ at comparable levels to under FET. The model predictions of active scavenging, thus, together with the changes in $J_{H_2O_2}$ and membrane potential support the assumptions that the scavenging activity is saturable and responds to changes in ROS production.

DISCUSSION

Model Predictions of Site-Specific ROS from the ETS Complexes

Site-specific ROS production has inspired many experimental studies and led to a wealth of experimental data. However, the data are limited to experimental conditions wherein inhibitors are present. The use of different systems, experimental conditions and techniques has also led to discrepancies among these studies. Using simpler systems such as purified enzymes has the advantage that fewer variables need to be accounted for in interpreting experimental results. But the conclusions may not be generalizable. On the contrary, a more intact system affords an environment more similar to *in vivo* conditions but introduce more confounding variables. Additionally, thermodynamic factors such as temperature, buffer ionic strength and buffer pH can all affect enzyme activities but are often neglected. Thus, it is necessary to analyze results obtained under different experimental conditions using a unified framework, including those that appear contradictory. This quantitative framework not only checks for the internal consistency of data but also enables extrapolating to experimentally untestable space.

While several mitochondrial ROS models exist [41,42,50–53], none can reproduce a wide variety of mitochondrial bioenergetic data quantitatively and consistently. These models either lack the biophysical details to simulate the enzymatic reactions associated with both high and low electron flux regimes [42,53] or exclude complex II as a ROS-producing component [50]. Our model includes the submodels of complexes I, II and III each of which contains the biophysical details necessary to simulate a wide variety of bioenergetic data [38–40]. Submodels were calibrated and validated before they are integrated into the ETS-ROS model.

The integrated model was again calibrated (Figs. 4.2, 4.3) and validated (Figs. 4.4, 4.5) before the model was used to generate mechanistic predictions (Figs. 4.7-11). Only processes that are supported by experimental data are explicitly modelled, and sensitivity analysis was performed on the integrated model to refine the adjustable parameters.

Using the corroborated model, we identify the ROS species and their origin (Figs. 4.8, 4.9) under the different metabolic conditions of our experimental data (Fig. 4.2). We found that the III_{Qp} site, site I_{FMNH_2} and site I_{Q} as a semiquinone are the primary sources of superoxide in non-phosphorylating mitochondria energized with P/M (Fig. 4.8, Table 4.5). In non-phosphorylating mitochondria, site I_{F} in the radical form gives rise to considerable amount of superoxide under QH_2 -supported respiration when RET is inhibited (S/R). These model predictions reconcile experimental results regarding complex I from different studies. For example, Galkin and Brandt [30] and Grivennikova & Vinogradov [29] independently concluded that both the fully reduced flavin (FMNH_2) and the flavin radical (FMNH^{\bullet}) can give rise to superoxide. Kussmaul and Hirst also found that site I_{F} is a primary source of superoxide but only when fully reduced [28]. On the other end, Lambert and Brand reported that site I_{Q} is the predominant source of superoxide originating from Complex I [21]. The Ohnishi group found that both sites I_{Q} and I_{F} are ROS sources when they exist in the radical forms [31]. Thus, computational modeling suggests that the differences among experimental data are likely due to different experimental conditions and that even seemingly contradictory results may be true under the right conditions.

Like complex I, the identity and origin of ROS produced by complex II remain unresolved although a consensus until recent years exists that complex II is a negligible source of

mitochondrial ROS. Quinlan *et al.* found that site II_F produces comparable amounts of ROS to site I_Q in the presence of fatty acids [20]. The notion that site II_F produces most ROS from Complex II is shared by Siebels and Drose [34]. However, others contend that significant amounts of ROS originate from the site II_Q [54] and the ISC near the Q site [55]. We used the model to identify conditions that favor ROS production by complex II and the contributions of its redox centers. In particular, the model identifies site II_[3Fe-4S] as the primary source of superoxide arising from complex II. In FET, superoxide arising from site II_{FADH•} becomes more significant only under QH₂-supported respiration (S/R). Thus, our model supports the experimental results that the ISC near the Q site and site II_F give rise to most of complex II's ROS. Moreover, the model predicts that FET in non-phosphorylating mitochondria favors superoxide production by complex III. The bc1 complex also contributes significantly to total superoxide flux in phosphorylating mitochondria although its contribution is more pronounced in FET mode. All these predictions remain experimentally infeasible due to the lack of a robust, reliable method to 1) distinguish superoxide from hydrogen peroxide and 2) directly measure them without interfering with other processes.

CONCLUSIONS

In conclusion, we have developed, analyzed and corroborated a model of mitochondrial ROS that identifies the species-specific ROS originating from the ETS redox centers under varying respiratory states and electron flux directions. Each ROS-producing module is constructed in a thermodynamically faithful manner and tested prior to being unified in a single platform [38–40]. The biophysical details included in the model are supported by experimental data and further refined by the process of sensitivity analysis. Being modular, parsimonious, and consistent, this modeling approach enables the individual modules within the model to work harmoniously with each other in a thermodynamically faithful manner. This approach also facilitates the inclusion of other mitochondrial physiology processes that are related to ROS homeostasis, as mentioned above, when data become available. These qualities distinguish this model from existing models which also attempt to recapitulate mitochondrial ROS homeostasis [41,42] as ours is capable of consistently reproducing experimental data on various aspects of mitochondrial physiology and making predictions that are physiologically appropriate.

APPENDIX

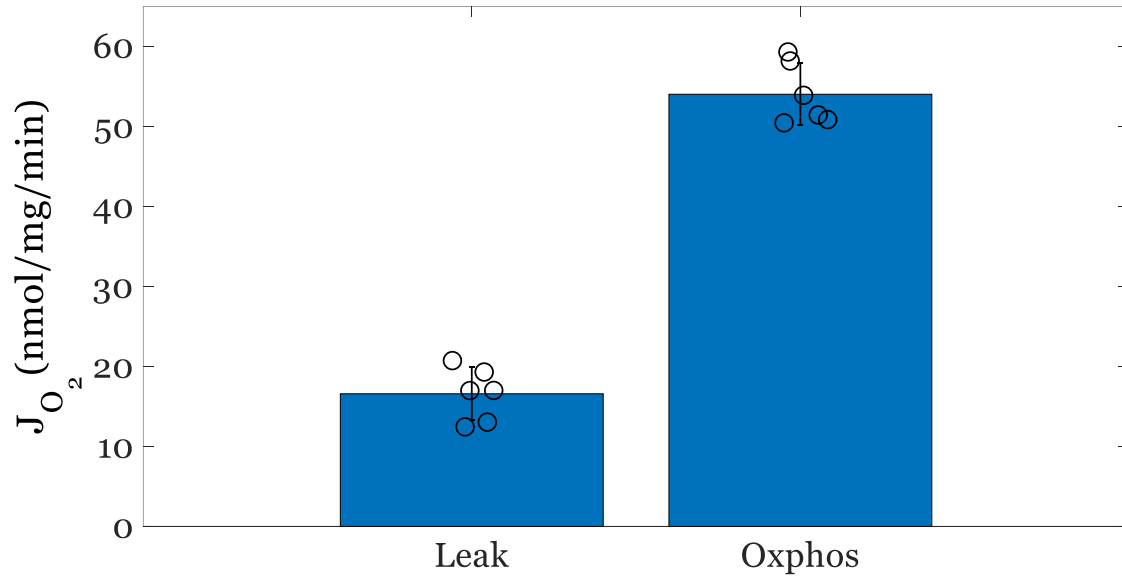


Figure S4.1 L-malate is able to support respiration during leak state and oxphos. Oxygen consumption rates (J_{O_2} , nmol/mg/min) during leak-state and oxphos are quantified using mitochondria isolated from ventricular cardiomyocytes of guinea pigs (0.1 mg/mL). L-malate is the only substrate, and ADP is added to simulate oxidative phosphorylation. Bar plot represents the averaged J_{O_2} values. Individual data points ($n = 6$) consist of 3 biological replicates each of which has 2 technical replicates. Error bars represent the standard deviations.

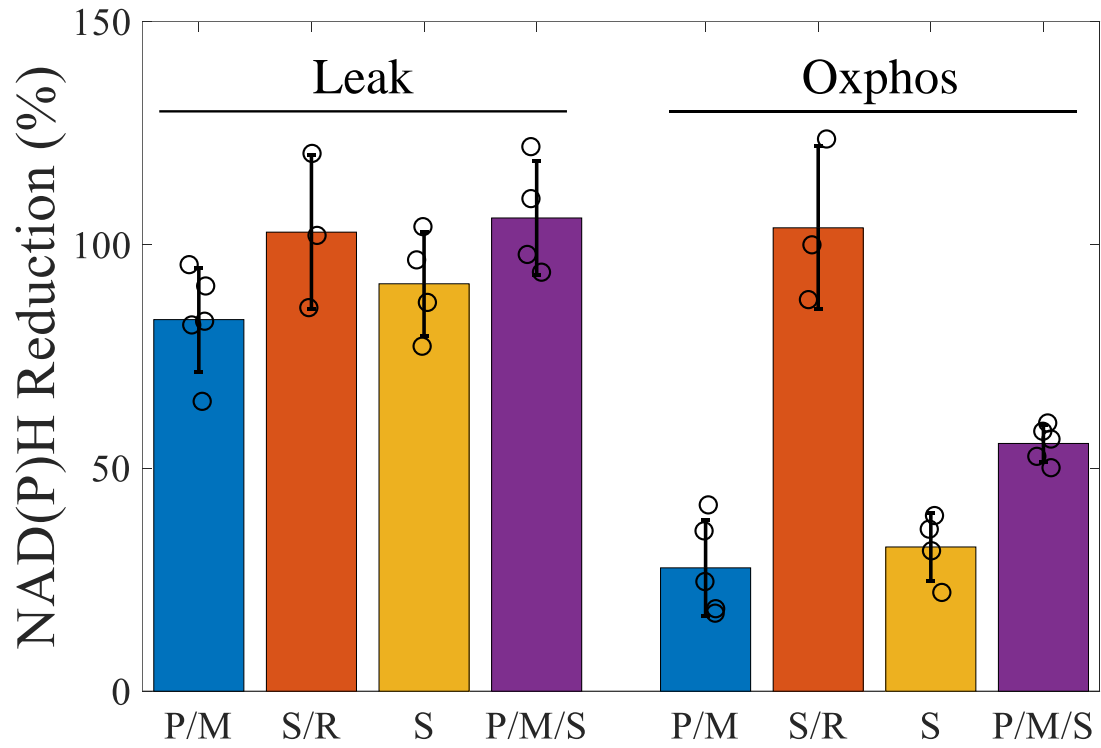


Figure S4.2 NADH redox state was determine during leak and oxphos states using fluorimetry.
 The experimental conditions are identical to our J_{O_2} and $J_{H_2O_2}$ experiments.

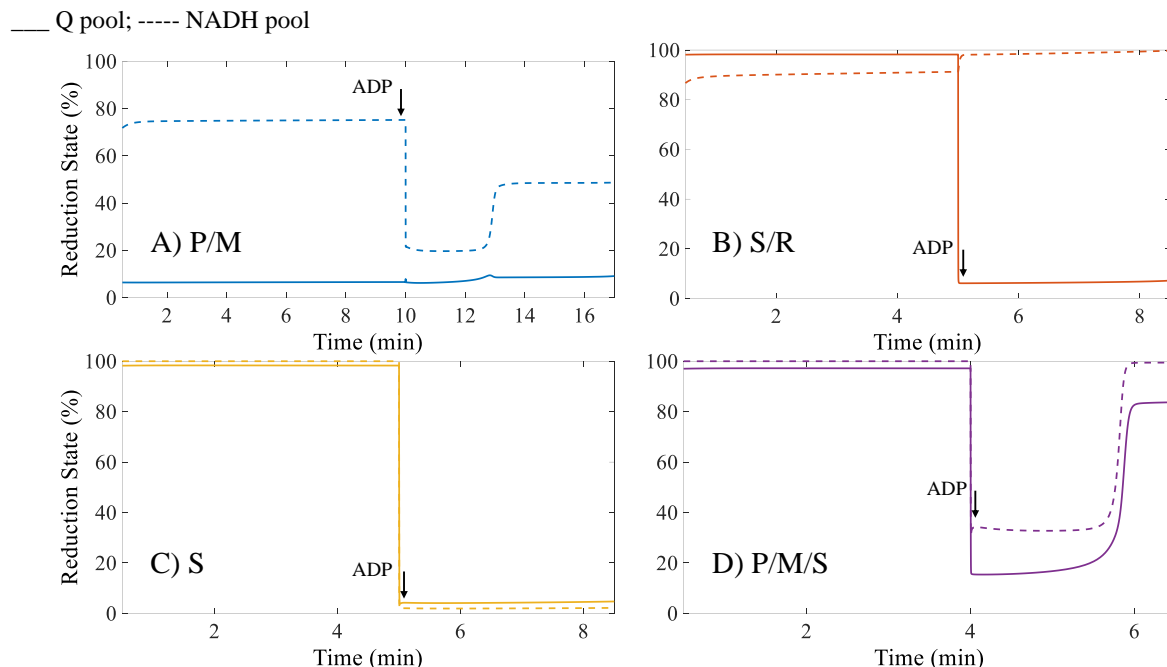


Figure S4.3 Model prediction of the effects of substrate utilization on the reduction states of the Q pool (solid lines) and NADH pool (dashed lines). The reduction state of each species is determined as the ratio of the reduced form and the total pool concentration multiplied by 100 ($([NADH]/[NADH + NAD^+]) \times 100$, and $([QH_2]/[QH_2 + Q]) \times 100$). Forward electron transport (FET) occurs under P/M- and S/R-supported respiration (A-B). Reverse electron transport (RET) occurs under S- and P/M/S-supported respiration (C-D). During leak state (before ADP addition), the NADH pool is mostly reduced in both FET and RET modes regardless of the substrate sources. However, the Q pool is mostly oxidized under P/M-supported respiration. During oxphos state (after ADP addition), the NADH pool becomes more oxidized. The Q pool also becomes more oxidized under S/R-, S- and P/M/S-supported respiration but does not alter significantly under P/M-supported respiration.

REFERENCES

REFERENCES

- 1 Garlid, A.O. *et al.* (2013) Mitochondrial reactive oxygen species: which ROS signals cardioprotection? *American Journal of Physiology-Heart and Circulatory Physiology* 305, H960–H968
- 2 Sena, L.A. *et al.* (2013) Mitochondria Are Required for Antigen-Specific T Cell Activation through Reactive Oxygen Species Signaling. *Immunity* 38, 225–236
- 3 Zhang, Y. *et al.* (2013) ROS play a critical role in the differentiation of alternatively activated macrophages and the occurrence of tumor-associated macrophages. *Cell Research* 23, 898–914
- 4 Padgett, L.E. *et al.* (2015) Loss of NADPH Oxidase–Derived Superoxide Skews Macrophage Phenotypes to Delay Type 1 Diabetes. *Diabetes* 64, 937–946
- 5 Yellon, D.M. and Hausenloy, D.J. (2007) Myocardial Reperfusion Injury. *New England Journal of Medicine* 357, 1121–1135
- 6 Jaeschke, H. and Woolbright, B.L. (2012) Current strategies to minimize hepatic ischemia–reperfusion injury by targeting reactive oxygen species. *Transplantation Reviews* 26, 103–114
- 7 Gutierrez, G. *et al.* (2004) Clinical review: Hemorrhagic shock. *Critical Care* 8, 373
- 8 Ibáñez, B. *et al.* (2015) Evolving Therapies for Myocardial Ischemia/Reperfusion Injury. *Journal of the American College of Cardiology* 65, 1454–1471
- 9 Heusch, G. and Gersh, B.J. (2017) The pathophysiology of acute myocardial infarction and strategies of protection beyond reperfusion: a continual challenge. *European Heart Journal* 38, 774–784
- 10 Murphy, M.P. (2008) How mitochondria produce reactive oxygen species. *Biochemical Journal* 417, 1–13
- 11 Muller, F. (2000) The nature and mechanism of superoxide production by the electron transport chain: Its relevance to aging. *AGE* 23, 227–253
- 12 Ambrosio, G. *et al.* (1993) Evidence that mitochondrial respiration is a source of potentially toxic oxygen free radicals in intact rabbit hearts subjected to ischemia and reflow. *Journal of Biological Chemistry* 268, 18532–18541
- 13 Andreyev, A.Y. *et al.* (2005) Mitochondrial metabolism of reactive oxygen species. 70, 15

- 14 Adam-Vizi, V. and Chinopoulos, C. (2006) Bioenergetics and the formation of mitochondrial reactive oxygen species. *Trends in Pharmacological Sciences* 27, 639–645
- 15 Starkov, A.A. *et al.* (2004) Mitochondrial α -ketoglutarate dehydrogenase complex generates reactive oxygen species. *Journal of Neuroscience* 24, 7779–7788
- 16 Tretter, L. and Adam-Vizi, V. (2004) Generation of reactive oxygen species in the reaction catalyzed by α -ketoglutarate dehydrogenase. *Journal of Neuroscience* 24, 7771–7778
- 17 Bunik, V.I. and Sievers, C. (2002) Inactivation of the 2-oxo acid dehydrogenase complexes upon generation of intrinsic radical species: Radicals upon oxidation of 2-oxo acids. *European Journal of Biochemistry* 269, 5004–5015
- 18 LaNoue, K. *et al.* (1970) Control of Citric Acid Cycle Activity in Rat Heart Mitochondria. *Journal of Biological Chemistry* 245, 102–111
- 19 LaNoue, K.F. *et al.* (1972) Feedback Interactions in the Control of Citric Acid Cycle Activity in Rat Heart Mitochondria. *Journal of Biological Chemistry* 247, 667–679
- 20 Quinlan, C.L. *et al.* (2013) Chapter Twelve - The Determination and Analysis of Site-Specific Rates of Mitochondrial Reactive Oxygen Species Production. In *Methods in Enzymology* 526 (Cadenas, E. and Packer, L., eds), pp. 189–217, Academic Press
- 21 Lambert, A.J. and Brand, M.D. (2004) Inhibitors of the Quinone-binding Site Allow Rapid Superoxide Production from Mitochondrial NADH:Ubiquinone Oxidoreductase (Complex I)*. *Journal of Biological Chemistry* 279, 39414–39420
- 22 Hirst, J. (2013) Mitochondrial Complex I. *Annu. Rev. Biochem.* 82, 551–575
- 23 Wirth, C. *et al.* (2016) Structure and function of mitochondrial complex I. *Biochimica et Biophysica Acta (BBA) - Bioenergetics* 1857, 902–914
- 24 Sun, F. *et al.* (2005) Crystal Structure of Mitochondrial Respiratory Membrane Protein Complex II. *Cell* 121, 1043–1057
- 25 Yankovskaya, V. (2003) Architecture of Succinate Dehydrogenase and Reactive Oxygen Species Generation. *Science* 299, 700–704
- 26 Crofts, A.R. (2004) The Cytochrome bc₁ Complex: Function in the Context of Structure. *Annual Review of Physiology* 66, 689–733
- 27 Ksenzenko, M. *et al.* (1983) Effect of electron transfer inhibitors on superoxide generation in the cytochrome bcl site of the mitochondrial respiratory chain. *FEBS LETTERS* 155, 6

- 28 Kussmaul, L. and Hirst, J. (2006) The mechanism of superoxide production by NADH:ubiquinone oxidoreductase (complex I) from bovine heart mitochondria. *Proceedings of the National Academy of Sciences* 103, 7607–7612
- 29 Grivennikova, V.G. and Vinogradov, A.D. (2006) Generation of superoxide by the mitochondrial Complex I. *Biochimica et Biophysica Acta (BBA) - Bioenergetics* 1757, 553–561
- 30 Galkin, A. and Brandt, U. (2005) Superoxide Radical Formation by Pure Complex I (NADH:Ubiquinone Oxidoreductase) from *Yarrowia lipolytica**. *Journal of Biological Chemistry* 280, 30129–30135
- 31 Ohnishi, S.T. *et al.* (2010) New insights into the superoxide generation sites in bovine heart NADH-ubiquinone oxidoreductase (Complex I): The significance of protein-associated ubiquinone and the dynamic shifting of generation sites between semiquinone and semiquinone radicals. *Biochimica et Biophysica Acta (BBA) - Bioenergetics* 1797, 1901–1909
- 32 St-Pierre, J. *et al.* (2002) Topology of Superoxide Production from Different Sites in the Mitochondrial Electron Transport Chain*. *Journal of Biological Chemistry* 277, 44784–44790
- 33 Quinlan, C.L. *et al.* (2012) Mitochondrial Complex II Can Generate Reactive Oxygen Species at High Rates in Both the Forward and Reverse Reactions*. *Journal of Biological Chemistry* 287, 27255–27264
- 34 Siebels, I. and Dröse, S. (2013) Q-site inhibitor induced ROS production of mitochondrial complex II is attenuated by TCA cycle dicarboxylates. *Biochimica et Biophysica Acta (BBA) - Bioenergetics* 1827, 1156–1164
- 35 Selivanov, V.A. *et al.* (2009) Bistability of Mitochondrial Respiration Underlies Paradoxical Reactive Oxygen Species Generation Induced by Anoxia. *PLOS Computational Biology* 5, e1000619
- 36 Korzeniewski, B. and Zoladz, J.A. (2001) A model of oxidative phosphorylation in mammalian skeletal muscle. *Biophysical Chemistry* 92, 17–34
- 37 Chen, X. *et al.* (2010) Kinetics and Regulation of Mammalian NADH-Ubiquinone Oxidoreductase (Complex I). *Biophysical Journal* 99, 1426–1436
- 38 Bazil, J.N. *et al.* (2014) Determining the origins of superoxide and hydrogen peroxide in the mammalian NADH:ubiquinone oxidoreductase. *Free Radical Biology and Medicine* 77, 121–129
- 39 Manhas, N. *et al.* (2020) Computationally modeling mammalian succinate dehydrogenase kinetics identifies the origins and primary determinants of ROS production. *Journal of Biological Chemistry* 295, 15262–15279

- 40 Bazil, J.N. (2017) Analysis of a Functional Dimer Model of Ubiquinol Cytochrome c Oxidoreductase. *Biophysical Journal* 113, 1599–1612
- 41 Gauthier, L.D. *et al.* (2013) An Integrated Mitochondrial ROS Production and Scavenging Model: Implications for Heart Failure. *Biophysical Journal* 105, 2832–2842
- 42 Gauthier, L.D. *et al.* (2013) A Computational Model of Reactive Oxygen Species and Redox Balance in Cardiac Mitochondria. *Biophysical Journal* 105, 1045–1056
- 43 Brdiczka, D. and Pette, D. (1971) Intra- and Extramitochondrial Isozymes of (NADP) Malate Dehydrogenase. *Eur J Biochem* 19, 546–551
- 44 Nolte, J. *et al.* (1972) Intracellular distribution of phosphoenolpyruvate carboxylase and (NADP) malate dehydrogenase in different muscle types. *Biochimica et Biophysica Acta (BBA) - Enzymology* 284, 497–507
- 45 Duong, Q.V. *et al.* (2020) Calcium overload decreases net free radical emission in cardiac mitochondria. *Mitochondrion* 51, 126–139
- 46 Wollenman, L.C. *et al.* (2017) The effect of respiration buffer composition on mitochondrial metabolism and function. *PLOS ONE* 12, e0187523
- 47 Gnaiger, E. and Group, M.T. (2020) Mitochondrial physiology. *Bioenerg Commun* 2020, 1–1
- 48 Robb, E.L. *et al.* (2018) Control of mitochondrial superoxide production by reverse electron transport at complex I. *Journal of Biological Chemistry* 293, 9869–9879
- 49 Hoffman, D.L. and Brookes, P.S. (2009) Oxygen Sensitivity of Mitochondrial Reactive Oxygen Species Generation Depends on Metabolic Conditions. *Journal of Biological Chemistry* 284, 16236–16245
- 50 Markevich, N.I. and Hoek, J.B. (2015) Computational modeling analysis of mitochondrial superoxide production under varying substrate conditions and upon inhibition of different segments of the electron transport chain. *Biochimica et Biophysica Acta (BBA) - Bioenergetics* 1847, 656–679
- 51 Markevich, N.I. *et al.* (2020) Computational Modeling Analysis of Generation of Reactive Oxygen Species by Mitochondrial Assembled and Disintegrated Complex II. *Front Physiol* 11,
- 52 Markevich, N.I. *et al.* (2020) Hysteresis and bistability in the succinate-CoQ reductase activity and reactive oxygen species production in the mitochondrial respiratory complex II. *Redox Biology* 37, 101630
- 53 Kembro, J.M. *et al.* (2013) Integrating mitochondrial energetics, redox and ROS metabolic networks: a two-compartment model. *Biophys J* 104, 332–343

- 54 Paranagama, M.P. *et al.* (2010) Contribution of the FAD and quinone binding sites to the production of reactive oxygen species from *Ascaris suum* mitochondrial complex II. *Mitochondrion* 10, 158–165
- 55 Grivennikova, V.G. *et al.* (2017) Respiratory complex II: ROS production and the kinetics of ubiquinone reduction. *Biochimica et Biophysica Acta (BBA) - Bioenergetics* 1858, 109–117

CONCLUDING REMARKS

The PhD project presented culminates an integrated computational model of mitochondria that quantitatively recapitulates substrate metabolism and net free radical homeostasis. The model is capable of simulating energy-dependent forward and reverse electron transport modes. For the first time, superoxide and hydrogen peroxide production by the ETC redox centers is quantified under different energetic states across a range of substrate fuels. The fully reduced flavin of complex I contributes to most hydrogen peroxide produced in non-phosphorylating mitochondria energized with pyruvate/malate, succinate/rotenone, succinate and pyruvate/malate/succinate. During reverse electron transport, site I_Q and I_{FMNH₂} become the most significant sites of free radical production as superoxide. During leak state respiration, complex III is the dominant source of free radicals, regardless of substrates. The model also highlights that during forward electron transport, the scavenging system is less than 10% active; however, during reverse electron transport, this system nearly reaches maximal capacity. This finding suggests that during early reperfusion, the limited capacity of the scavenging system precipitates oxidative stress.

Nevertheless, incorporating additional physiological aspects to the current model is necessary to provide a complete *in silico* picture of mitochondrial physiology. The two metabolic modifications are beta oxidation and an expansion of the TCA cycle. Beta oxidation is the major *in vivo* metabolic pathway in cardiac tissue that generates most of the reducing equivalents (NADH and UQH₂) for the ETC. During ischemia, this pathway is “turned off” due to oxygen limitation which results in an extremely reduced NAD⁺ pool [1]. As the regulation of beta oxidation is not well-understood [2–5], additional bioenergetic data such as J_{O₂}, J_{H₂O₂}, membrane potential and NADH redox state using mitochondria from normal and the

reperfused ischemic heart are necessary to characterize this pathway. These experiments can be performed with different fatty acid substrates, especially mono- or polyunsaturated fatty acids [6], to mimic the composition of fats in a healthy and diseased myocardium. It is imperative that the proposed experiments are performed under similar conditions as the other data to enable comparison across data sets. Including beta oxidation in the current model will lead to a more accurate picture of how the matrix and ETC redox environments are metabolically regulated.

In the current model, the TCA cycle is simplified except for the reactions catalyzed by SDH, fumarase and malate dehydrogenase. The reactions catalyzed by the other enzymes are omitted because they were not necessary to reproduce the experimental data used for the current model. In these experiments, calcium was removed from the system; however, calcium does play important roles in energy metabolism. The stimulatory effect of free matrix calcium (in the physiological range, ~ 100 nM) on matrix metabolic enzymes (pyruvate dehydrogenase, isocitrate dehydrogenase and alpha-ketoglutarate dehydrogenase) is essential to reproduce bioenergetic data in the presence of calcium [7,8]. Including these enzymes will be critical to explain how calcium overload in myocardial I/R injury affects metabolism. Thus, reconstructing a full TCA cycle at varied calcium concentrations will enhance the model's ability to explain normal and pathological behavior of mitochondria. A key experiment is to quench non-phosphorylating and phosphorylating mitochondria energized on different substrate combinations in the presence of different calcium levels and quantify the levels of intermediate metabolites.

Lastly, the scavenging system is empirically modelled using a Michaelis-Menten like expression. Although this treatment is sufficient to explain the data, it does not dissect the contributions of the Glutathione and Peroxiredoxin systems to total scavenging. It also limits the model's ability to predict the effects of myocardial I/R injury on these scavenging components. The total scavenging capacity can be indirectly measured via the ability of isolated mitochondria to remove exogenous hydrogen peroxide [9]. In this experiment, a hydrogen peroxide bolus at a known concentration is added to a mitochondria suspension. Then, the amounts of hydrogen peroxide remaining in the buffer at different timepoints are quantified until steady state has been reached. Fitting a curve to the buffer hydrogen peroxide concentrations will enable the determination of the rate constant associated with total mitochondrial scavenging capacity. Such an experiment can be done in the absence of exogenous substrates and the presence of different substrate combinations, as well as varied calcium levels. Doing these experiments under similar conditions to the net ROS measurement experiments will delineate the link between the total scavenging capacity, metabolism and ROS production.

In conclusion, the current model is the first of its kind to consistently reproduce a wide range of bioenergetic data obtained from isolated mitochondria in different respiratory states and fueled by different substrate combinations. Future updates to the model need to account for beta oxidation and other TCA cycle reactions that were simplified in the current model. More importantly, metabolic modifications need to account for the stimulatory and inhibitory effects of calcium at different concentrations. Lastly, to maximize the utility of the model in understanding diseased states such as myocardial I/R injury, the scavenging system needs to be

elaborated. Additional experiments to generate data are necessary to constrain the model parameter space and produce a more complete *in silico* picture of mitochondrial physiology. Such a model can be used to test experimentally infeasible hypotheses and to predict potential outcomes of a pharmaceutical agent on mitochondrial bioenergetics, which guides experimental design and therapeutic development.

REFERENCES

REFERENCES

- 1 Liedtke, A.J. (1981) Alterations of carbohydrate and lipid metabolism in the acutely ischemic heart. *Progress in Cardiovascular Diseases* 23, 321–336
- 2 Schwaiger, M. *et al.* (1985) Retention and clearance of C-11 palmitic acid in ischemic and reperfused canine myocardium. *Journal of the American College of Cardiology* 6, 311–320
- 3 Schwaiger, M. *et al.* (1985) Sustained regional abnormalities in cardiac metabolism after transient ischemia in the chronic dog model. *Journal of the American College of Cardiology* 6, 336–347
- 4 Liedtke, A.J. *et al.* (1988) Changes in substrate metabolism and effects of excess fatty acids in reperfused myocardium. *Circ Res* 62, 535–542
- 5 Lopaschuk, G.D. *et al.* (1990) Glucose and palmitate oxidation in isolated working rat hearts reperfused after a period of transient global ischemia. *Circ Res* 66, 546–553
- 6 Lopaschuk, G.D. *et al.* (2010) Myocardial Fatty Acid Metabolism in Health and Disease. *Physiological Reviews* 90, 207–258
- 7 Denton, R.M. *et al.* (1978) Calcium ions and the regulation of NAD⁺-linked isocitrate dehydrogenase from the mitochondria of rat heart and other tissues. *Biochemical Journal* 176, 899–906
- 8 Denton, R.M. and McCormack, J.G. (1980) On the role of the calcium transport cycle in heart and other mammalian mitochondria. *FEBS Letters* 119, 1–8
- 9 Starkov, A.A. *et al.* (2014) Scavenging of H₂O₂ by mouse brain mitochondria. *J Bioenerg Biomembr* 46, 471–477